Active Heat Transfer Enhancement in Integrated Fan Heat Sinks

by

Wayne L. Staats, Jr.

B.S., University of Wisconsin-Madison (2006)
S.M., Massachusetts Institute of Technology (2008)

Submitted to the Department of Mechanical Engineering
in partial fulfillment of the requirements for the degree of

Doctor of Philosophy in Mechanical Engineering

at the

MASSACHUSETTS INSTITUTE OF TECHNOLOGY

September 2012

Author .....
Department of Mechanical Engineering
August 31, 2012

Certified by .....
J.G. Brisson
Professor of Mechanical Engineering
Thesis Supervisor

Accepted by .....
David E. Hardt
Chairman, Department Committee on Graduate Theses

Active Heat Transfer Enhancement in Integrated Fan Heat Sinks

by

Wayne L. Staats, Jr.

Submitted to the Department of Mechanical Engineering
on August 31, 2012, in partial fulfillment of the
requirements for the degree of
Doctor of Philosophy in Mechanical Engineering

Abstract

Modern computer processors require significant cooling to achieve their full performance. The "efficiency" of heat sinks is also becoming more important: cooling of electronics consumes 1% of worldwide electricity use by some estimates. Unfortunately, current cooling technologies often focus on improving heat transfer at the expense of efficiency. The present work focuses on a unique, compact, and efficient air cooled heat sink which addresses these shortcomings. While conventional air cooled heat sinks typically use a separate fan to force air flow over heated fins, the new design incorporates centrifugal fans directly into the body of a loop heat pipe with multiple planar condensers. These "integrated fans" rotate between the planar condensers, in close proximity to the hot surfaces, establishing a radially outward flow of cooling air. The proximity of the rotating impellers to the condenser surfaces results in a marked enhancement in the convective heat transfer coefficient without a large increase in input power.

To develop an understanding of the heat transfer in integrated fan heat sinks, a series of experiments was performed to simultaneously characterize the fan performance and average heat transfer coefficients. These characterizations were performed for 15 different impeller profiles with various impeller-to-gap thickness ratios. The local heat transfer coefficient was also measured using a new heated-thin-film infrared thermography technique capable of applying various thermal boundary conditions.

The heat transfer was found to be a function of the flow and rotational Reynolds numbers, and the results suggest that turbulent flow structures introduced by the fans govern the transport of thermal energy in the air. The insensitivity of the heat transfer to the impeller profile decouples the fan design from the convection enhancement problem, greatly simplifying the heat sink design process. Based on the experimental results, heat transfer and fan performance correlations were developed (most notably, a two-parameter correlation that predicts the dimensionless heat transfer coefficients across 98% of the experimental work to within 20% relative RMS error).

Finally, models were developed to describe the scaling of the heat transfer and mechanical power consumption in multi-fan heat sinks. These models were assessed against experimental results from two prototypes, and suggest that future integrated fan heat sink designs can achieve a 4x reduction in thermal resistance and 3x increase in coefficient of performance compared to current state-of-the-art air cooled heat sinks.

Thesis Supervisor: J.G. Brisson
Title: Professor of Mechanical Engineering

ACKNOWLEDGEMENTS

First, I acknowledge Professor Brisson for being an inspiring mentor and advisor. He provided me with a unique environment in the Cryogenic Engineering Laboratory to sharpen my research skills. I have, through innumerable discussions and arguments with Professor Brisson, learned a great deal about thermal engineering, but also about physics, engineering, and teaching. I value the rapport we developed over the years and I find his candor and willingness to give honest feedback refreshing.

My committee (Professor Evelyn Wang, Professor Bora Mikić, and Dr. Choon Tan) has been a pleasure to work with. I'm grateful that Professor Evelyn Wang gave me the chance to join the "PHUMP" project and perform this research. Evelyn's door has always been open for discussion, and her tireless devotion to research, teaching and advising has been a source of inspiration. I consider myself fortunate to know Professor Bora Mikić both as a teacher and a committee member. His impressive breadth and depth of heat transfer knowledge reminds me that the learning process never stops. Finally, I appreciate the wise and thoughtful feedback of Dr. Choon Tan, whose turbomachinery and general fluid modeling expertise have led to many productive discussions.

I've had the good fortune of working with smart, talented colleagues in this research: Professors J.G. Brisson, Evelyn Wang, and Jeffrey Lang; postdocs Teresa Peters, Martin Cleary, and Matthew McCarthy; Ph.D. candidate H. Arthur Kariya; S.M. students Jon Allison, Alonso Domínguez, Daniel Hanks, David Jenicek, Catherine Koveal, and Nicholas Roche; and undergraduate researchers Tess Saxton-Fox, Ari Umans, Kai Cao, Jay Sircar, and Kristyn Kadala. These students exhibited a technical perseverance and general *joie de vivre* that made our lab an enjoyable environment.

I'm thankful that the Defense Advanced Research Projects Agency (DARPA) had the foresight to address the thermal management issues that relate to this research. More generally, I'm honored by the responsibility of performing research on behalf of the U.S. taxpayers and glad that our society values science enough to devote our resources to the pursuit of additional knowledge.

I've enjoyed being a part of the Cryogenic Engineering Laboratory at MIT. I'm fortunate that Professor Joseph L. Smith, Jr. was available for discussions and advice. He is a perfect example of a lifelong engineer; he's as comfortable disassembling the helium liquefier, machining, or welding as he is discussing the subtleties of the Second Law. Professor Ernest Cravalho provided me with a teaching assistantship that I found rewarding. I've known several students in the lab, as well, and have enjoyed working with them

or discussing interesting problems: Barbara Botros, Martin Segado, Jake Hogan, Kevin DiGenova, Alonso Domínguez, Teresa Peters, Martin Cleary, Jon Allison, and Gunaranjan Chaudhry (the Grand Integrator). In particular, I enjoyed many productive and stimulating discussions with Martin Segado and appreciated his thoughtful thermal-engineering perspectives. The lab would not be the same without Doris Elsemiller's administrative acumen and colorful personality.

Verily, one of the best aspects of my time at MIT has been the opportunity to befriend many unique but invariably exceptional people (too many to enumerate here). Several of these friends have directly helped in my research. I thank: Joe Petrzelka for wiring and PCB advice; Kevin Cedrone (and the Sloan Automotive Lab) for lending a thermal mass flow meter; Misha Wolfson for developing the MEX interface between MATLAB and the motor controller; Mark Belanger, expert machinist, for managing my favorite shop on the MIT campus (the Edgerton Student Shop); Matt Humbert for many discussions and for helping me cut impellers on the waterjet; Adam Wahab for his tips on soldering surface mount components; and John W. Roberts, Jr. for sharing his expertise and giving advice about tuning closed-loop control systems. I thank Mike Fischer of Engineered Metal Products in Jackson, Wisconsin for his help over the years in laser cutting parts (notably, many of the parts in the circular stator apparatus). Finally, two parts of the Mechanical Engineering Department at MIT deserve a special thanks: the graduate office (Leslie Regan and Joan Kravit) for their advocacy of graduate students, and the Graduate Association of Mechanical Engineers (GAME) for providing forums for fruitful (as well as frivolous) cross-disciplinary discussion (e.g. my personal favorite, GAME coffee hour).

I'm fortunate to have constant support from my family. My father (Wayne L. Staats, Sr.) and sisters (Heidi and Wendy Staats) seem to enjoy talking about my work, and are always willing to provide moral support. My mother, Judy Staats, lives on in my memory. She was a proud, loving mom who always encouraged my academic development. I admire her dedication to teaching, her profession and passion.

Finally, my lovely wife Brooke and daughter Anna have been a constant source of love and support. Brooke has always encouraged me and is my steady horizon in the sometimes tumultuous seas of research. I'm incredibly lucky to have her and I can't imagine a more fulfilling home life.

CONTENTS

THIS PAGE INTENTIONALLY LEFT BLANK

LIST OF FIGURES

THIS PAGE INTENTIONALLY LEFT BLANK

LIST OF TABLES

THIS PAGE INTENTIONALLY LEFT BLANK

CHAPTER 1

INTRODUCTION

As electronics advance, heat generation will continue to limit their performance and require innovative thermal management techniques. Thermal management currently poses a challenge in most advanced electronics, including radar, imaging and telecommunications technologies. Evaporative and forced convection liquid cooling offer high heat fluxes compared to air cooling, but at considerable expense. Indeed, many high-end applications have resorted to pumped liquid, evaporative and spray cooling. Unfortunately, cost and complexity increase in comparison to air-cooled solutions, and reliability often suffers. Another worrisome trend in thermal management is that the solutions employed in modern high-end electronics demand more power than ever before. This power consumption increases operating cost and adds further difficulty in power-limited applications. Therefore, not just the cooling capacity but also the *efficiency* of thermal management systems must improve in order to realize the full potential of modern electronics.

A unique air-cooled heat sink has been proposed to meet the needs of high-power electronics while keeping input power requirements low. This heat sink incorporates a loop heat pipe consisting of a single flat evaporator connected to a multitude of parallel, planar condensers. Impellers driven by an electric motor spin between the condenser layers to force fresh air from a center core radially outward, ultimately serving to take up the thermal power rejected into the evaporator by the electronic device.

Interestingly, the proximity of the impellers to the hot condenser surfaces in this device results in a marked enhancement in the convective heat transfer coefficient without a commensurate increase in input power. In fact, by using integrated centrifugal fans in this fashion, the heat transfer coefficient can be improved by a factor of three compared to pressure-driven flow (in which a separate fan induces flow over the heat transfer surface). This work seeks to develop an understanding of this phenomenon and how to best exploit it in heat sink design. An experimental investigation into the heat transfer and fluid dynamic performance of a single integrated fan heat sink were performed and correlations for the heat transfer as a function of geometry and operating conditions were developed. Additionally, a model was formulated to predict the fan curve of a single layer device based on geometrical parameters. From here, the scaling to multilayer devices was explored, and design methods for multilayer heat sinks of this type were developed. It will be shown that the performance of these multilayer devices is superior to current state of the art air cooled heat sink designs.

This chapter discusses the following:

- The need for better, more efficient air cooled heat sinks
- The current state of the art in thermal management and air cooling
- The main design challenges in developing an air cooled heat sink
- A discussion of convection enhancement techniques, both passive and active
- Two conceptual exercises that demonstrate the design challenges associated with compact air cooled heat sinks
- A new approach to compact air cooled heat exchangers: the integrated fan heat sink
- A review of basic centrifugal fan design tools
- The relevant parameters and dimensional analysis for the integrated fan heat sink
- A survey of currently available heat sinks and fans for thermal management

1.1 Motivation

Computers have become widespread and central to modern life, and worldwide adoption is expected to continue unabated: 4 billion PCs are expected by 2020, up from 592 million in 2002 [1].

Since the invention of the integrated circuit (IC) in the late 1960s the number of components per chip has increased rapidly. An empirical relation called Moore's law — which states that the density of components on ICs doubles about every two years — has held since the IC's invention [2, 3]. This increase in component density, combined with higher clock speeds, has caused the heat dissipation in central processing units (CPUs) to increase from 30 W in the early 1990s [4] to 130 W in 2011 (for an Intel Core i7 CPU [5]).

On a CPU, the power consumption arises from "static" and "dynamic" power. Static power is proportional to the operating voltage and the leakage current through the transistors, and dynamic power is proportional to the clock speed and the square of the operating voltage [6]. Several conclusions can be drawn from this proportionality. First, reducing the operating voltage reduces the power dissipation in the CPU; of course, this is the simplest and first tool chip designers use to reduce the thermal load. After this voltage is reduced as much as possible, the next parameter that can be altered is the clock speed. This illustrates the sacrifice in performance that occurs due to inadequate thermal management. Finally, as the density of transistors increases, the static power will become increasingly significant [6]. This suggests that in the future, thermal solutions will increase in importance, because static power must always be rejected to ambient whenever the CPU is on regardless of clock speed. Thus, ultimately, the speed of ICs (and, by extension, the advancement of computing power) will be limited by thermal management.

Cooling of electronics also has a surprisingly high energy cost, which translates to monetary cost and environmental impact. Data center cooling emissions are expected to rise from 24 to 70 MtCO2e[1] in the same period; emissions from desktop PC electricity

[1] MtCO2e means "million metric tons of CO_2 equivalent." A typical coal power plant in the US emits about 4 MtCO2e per year [7].

consumption are expected to increase from 242 to 309 MtCO2e. Meijer reported that data centers accounted for about 2% of worldwide energy consumption in 2009, and half of this is devoted to cooling [8]. Koomey studied the growth of data center energy consumption from 2005–2010. He concluded that the growth was not as rapid as expected because of new trends in computing (virtualization) and the financial crisis of 2008. Despite this, he estimates that the power use for data centers in 2010 accounted for 1.1–1.5% of worldwide electricity use, and that cooling accounts for about half of this [9]. Any improvements in the efficiency of thermal management solutions would help to reduce some of this energy use.

Considering its economic impact, it is not surprising that computer users and manufacturers are interested in improved thermal management technologies. The International Electronics Manufacturing Initiative (iNEMI) roadmap [10] states:

> "Multi-core processors are now the norm for most computing applications (notebook, desktop, and server). A consequence of the expected demise of the traditional scaling of semiconductors is the increased need for improved cooling and operating junction temperature reduction due to large leakage currents. The consumers demand for thin multifunctional products has led to increased pressure on alternative high density packaging technologies."

In addition, the International Technology Roadmap for Semiconductors (ITRS) [11] predicts that the required thermal resistance for high performance ICs will decrease from its 2009 level of 0.27 K/W to 0.08 K/W in 2024, a more than threefold reduction. This forecast predicts that current air cooling technology will be incapable of meeting the increasingly stringent demands of the ICs: "The high junction-to-ambient thermal resistance resulting from an air-cooled heat sink provides inadequate heat removal capability at the necessary junction temperatures for ITRS projections at the end of this roadmap."

Clearly, there is a broadly recognized need for more effective cooling — in particular, air cooling. Furthermore, the iNEMI roadmap also pointed out another important issue in thermal management solutions: heat sinks are subject to volume constraints. Minimum volume traditionally comes at the expense of thermal performance. These volume constraints are particularly evident in high end applications (e.g. telecommunications, radar, sensing and imaging), which have resorted to more complex liquid cooling, spray cooling, or refrigeration cooling due to the insufficient performance of the current state-of-the-art air cooling solutions [12]. With improved air cooling technology, these complex and power hungry systems could potentially be eliminated. These high end applications can have a larger (~10x) thermal duty than consumer CPUs, but still be constrained to a similar volume envelope.

Finally, new technologies such as LED lighting are certain to require efficient air cooling solutions. With widespread adoption of these new technologies, and the continued pervasiveness of computing technology, any improvements in air cooling have the potential to effect appreciable energy savings, with associated financial and energy security benefits.

1.2 Thermal Management of Electronics

The basic goal of thermal management in electronics is to remove the thermal energy that is dissipated within a component, and ultimately reject this energy to the ambient surroundings. This involves heat transfer:

- from the junction into a heat spreader
- from the heat spreader into a finned structure
- into the room housing the electronic components
- from the room to the environment outside, (e.g. by using an air conditioner, if necessary).

Each of these steps poses a unique set of challenges; however, this work focuses on the heat transfer between the heated surface and the ambient air.

Various physical phenomena can be used to provide cooling to the heated surface. Anandan surveyed the methods used in high heat flux thermal management [13]. These include natural convection and radiation, forced air convection, forced liquid convection, and evaporation. The physics of these processes ultimately set limits on their performance; their ranges of heat flux can be seen in Fig. 1-1. The heat flux typically associated with air cooling goes to about 15,000 W/m^2. Given that the heat flux from an Intel Core i7 processor is ~100,000 W/m^2, the need to enhance the heat transfer (e.g. by adding fins) associated with pure air cooling becomes evident.

Although physical phenomena involving liquids are capable of higher heat fluxes, air cooling offers simplicity and ease of integration. An air cooled heat sink can be a self contained unit that doesn't require any fluid connections. This means that the heat sink always remains dry near the electronics, which can be damaged by some cooling fluids. Some installation sites, such as an office, are simply not equipped to handle liquid cooling with external connections. The simplicity of air cooling inherently reduces its installed cost in a system. This is evidenced by the widespread use of air cooling; Sathe pointed out that the adoption of CMOS technology led to more emphasis on overall system cost, increasing the commercial appeal of air cooled heat sinks [14]. Bar-Cohen identified air cooled heat sinks as technology that will play a "pivotal role" in thermal management [15].

The Defense Advanced Research Projects Agency (DARPA) identified a need for compact, efficient air cooled heat sinks; the current state-of-the-art is inadequate to meet the

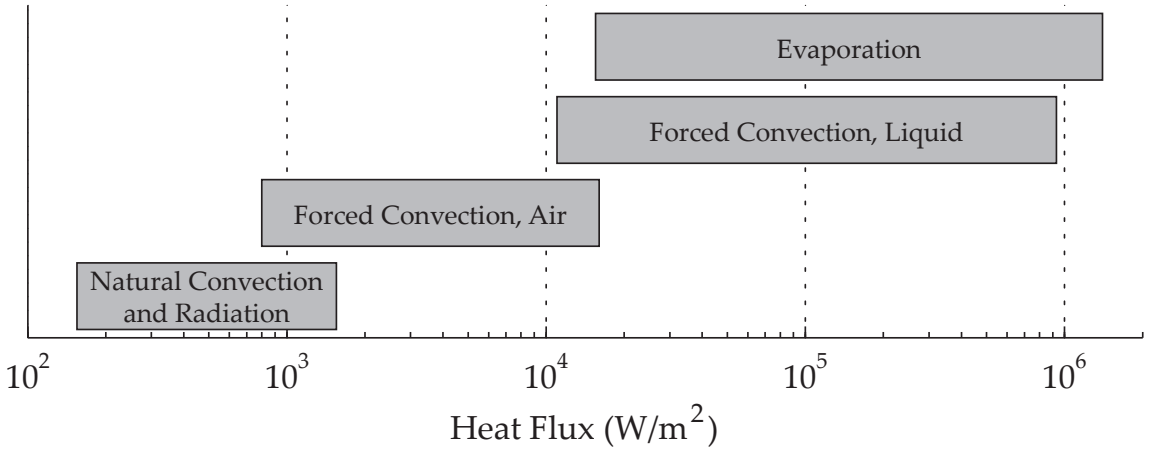

Figure 1-1: Different physical phenomena have characteristic ranges of heat flux (adapted from [13]). Thermal management in high end applications often resorts to evaporation or forced liquid convection, but air cooling tends to be much simpler and more convenient.

thermal management needs of many high performance systems [12]. As a result, these applications have resorted to "exotic liquid-cooled manifolds, spray-cooled enclosures, and vapor-compression refrigeration." With improvements in air cooling, simpler heat sinks could replace these bulky and complex solutions. To accomplish this, DARPA set forth a list of goals in its Microtechnologies for Air-Cooled Exchangers (MACE) program. These goals are shown in Table 1.1, and include a 4x improvement in the overall thermal resistance and a 3x improvement in the coefficient of performance while remaining bounded by the same 102 mm cubical envelope. These metrics will be referenced subsequently in this work to demonstrate the efficacy of the integrated fan heat sink. It will be shown below in Section 1.5 that these goals are a significant challenge that pushes the boundaries of air cooling technology.

1.3 Air Cooled Heat Sink Design

A conventional air cooled heat sink consists of a heated surface, extended surfaces to increase the effective convection area, and most often a fan to force a flow of air over the extended surfaces. A commercially available heat sink (Noctua NH-D14) is shown in Fig. 1-2 In this case, cylindrical heat pipes are in contact with the heated surface to bring thermal energy to the extended surfaces with minimal temperature drop. This thermal energy flows from the heat pipes into the fins, where it is transferred through convection into the stream of air induced by the two fans.

Conventional finned heat sinks have been studied by many investigators. Tuckerman and Pease [17] studied a microchannel heat sink etched on silicon and minimized thermal resistance by choosing the appropriate channel width, fin width and aspect ratio subject to contraints on the geometry and pressure drop. Knight et al. [18] developed an analytical method to minimize thermal resistance of a heat sink with pressure driven flow in a closed finned channel by varying the geometry. Teertstra et al. [19] developed an analytical model to calculate the Nusselt number for a plate fin heat sink as a function of geometry and flow properties. Bejan [20] illustrates a heat sink optimization using entropy generation minimization (EGM), a method whereby the entropy production is quantified and ascribed to the various loss producing mechanisms, and the free parameters are altered to minimize the overall entropy generation rate (for an overview of the method, see [21]). Culham and Muzychka [22] presented a method similar to that of Bejan, where the geometry of plate fin heat sinks is optimized by minimizing the entropy generation rate. Their method also allowed for the incorporation of real fan performance data in the model. Similarly, Khan et al. [23] applied EGM techniques to optimize a pin fin heat sink. Bar-Cohen and

Table 1.1: DARPA MACE Program Goals

	State of the Art	DARPA MACE Goal
Thermal Power Input	1000 W	1000 W
Inlet Air Temperature	30 C	30 C
Overall Thermal Resistance	0.2 K/W	**0.05 K/W** (4x improvement)
Electrical Power Input	100 W	33 W
Coefficient of Performance	10	**30** (3x improvement)
Envelope Dimensions	102mm × 102mm × 102mm	102mm × 102mm × 102mm

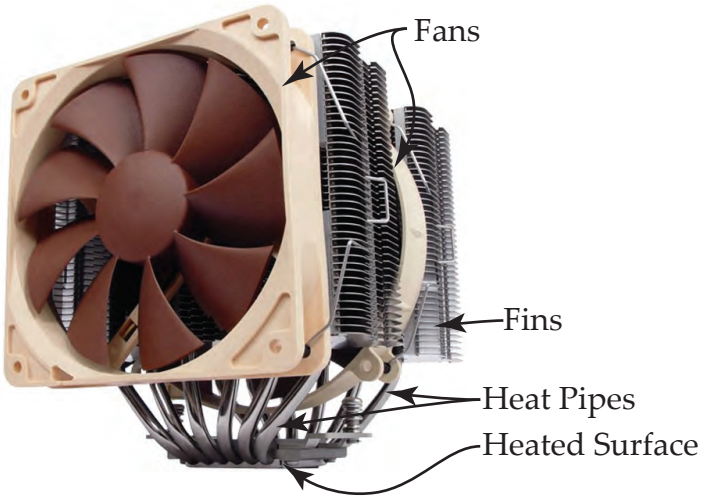

Figure 1-2: A conventional heat sink employs one or more fans and an array of fins. In this particular example, cylindrical heat pipes are used to improve the heat transfer from the base to the extended surfaces (adapted from [16]).

Iyengar [24,25] presented methods of optimizing a parallel plate heat sink. Their methods accounted for the energy used in the manufacture of the heat sink and the cooling energy used over the expected life of the computer in which it resides; their optima sometimes differed from the EGM optima, since the latter did not account for manufacturing energy. Furukawa and Yang [26] performed a numerical analysis of a plate fin heat sink in natural convection, and found their optimum design predictions to be very close to those of Bejan, Culham and Muzychka, and others.

Several recent studies have shown that finless designs can provide improved performance in small heat sinks. Egan et al. [27] looked at a miniature, low profile heat sink with and without fins and used particle image velocimetry to detail flow structures and heat transfer. Stafford et al. [28] studied forced convection cooling on low profile heat sinks with and without fins and showed that heat transfer rates of the finless designs were better than their finned counterparts.

A fundamentally different approach to air cooling was developed by Koplow [29]. The "Sandia Cooler", or "air bearing heat exchanger" (ABHE), consists of a rotating disc atop a circular stator plate. The top of the disc has fins that extend upward and act as impeller blades to draw air in axially and discharge it radially. The air gap between the disc and the stator was very thin. This thinness combined with the high shear rates reduce the thermal resistance of the air gap. The ABHE exploits the slow boundary layer development that occurs in an accelerating reference frame (a phenomenon studied experimentally by Cobb in 1956 [30]). The performance of the Sandia Cooler is significantly better than traditional air cooled heat sinks; this will be discussed more in Section 1.9.

1.3.1 Design Compromises

Heat sink design involves compromises between the important figures of merit (viz. thermal resistance, pumping power, and volume). First, the thermal performance and the volume occupied by the heat sink present conflicting goals. This tradeoff is evident form a simple energy balance on a single stream heat exchanger. The heat transfer from in a heat

exchanger is

$$\dot{Q} = UA\Delta T = \frac{\Delta T}{R}, \tag{1.1}$$

where U is the overall heat transfer coefficient, A is the surface area, ΔT is an appropriate average temperature difference between the heated surface and the cooling air[2], and R is the thermal resistance. The UA product, which is the inverse of the thermal resistance R, represents the effective size of the heat exchanger. Therefore, for a specified heat transfer rate and maximum surface-to-ambient temperature difference the UA product can be estimated. This also illustrates that any enhancement in the heat transfer coefficient can manifest itself as a reduction in the total surface area needed for cooling. Generally, UA corresponds to the overall volume of the heat sink (since the fins that comprise the surface cannot be excessively crowded due to pumping considerations). Thus, the designer must choose between low thermal resistance and overall volume.

The second major design challenge is the balance between thermal and hydraulic performance. As mentioned above, the desirable maximization of UA leads to a multitude of closely spaced surfaces (to increase A) with high velocity fluid flow (to increase U). However, moving a fluid through small passages at high speed requires a large pumping power input. The pumping power requirement is the product of the total pressure[3] loss and the volume flow through the device:

$$\dot{W} = \dot{V}\Delta p_{\mathrm{t}} \tag{1.2}$$

In general, increasing $\dot{W}$ produces a higher velocity in the system, leading to reduced thermal resistance.

1.3.2 Performance Evaluation Criteria of Heat Sinks

Determining the appropriate figure of merit for a heat sink is a difficult task because of the variety of objectives in heat sink design. For example, total heat transfer, surface heat flux, thermal resistance, work input, and overall volume may be either constraints, or quantities to optimize in a heat sink.

The mean heat transfer coefficient, referenced to the inlet temperature difference, is a common metric. One can quickly relate the base-to-ambient temperature difference to the total heat transfer by using the inlet-temperature-difference mean heat transfer coefficient:

$$h_{\mathrm{ITD}} = \frac{\dot{q}''}{\Delta T_{\mathrm{in}}} = \frac{\dot{Q}}{\Delta T_{\mathrm{in}} A_{\mathrm{h}}}, \tag{1.3}$$

where $\dot{q}''$ is the surface heat flux, $\dot{Q}$ is the total heat transfer rate, A_{h} is the heated surface area, and ΔT_{in} is the average temperature difference between the heated wall and the ambient. Care must be exercised in using this as a metric, because the temperature scale causes it to be different in magnitude compared to the conventionally defined mean h (or h_{LMTD}), which references the log-mean temperature difference between the wall and the flow.

The overall thermal resistance (R) is also commonly used to evaluate heat sinks. The thermal resistance is analogous to electrical resistance (where ΔT and $\dot{Q}$ are analogous to

[2]Typically this average is the log-mean temperature difference $\Delta T_{\mathrm{lm}} = \frac{\Delta T_{\mathrm{in}} - \Delta T_{\mathrm{out}}}{\ln(\Delta T_{\mathrm{in}}/\Delta T_{\mathrm{out}})}$

[3]The total pressure p_{t} is defined as the sum of the static pressure p and the dynamic pressure $\frac{\rho v^2}{2}$, where ρ is the density and v is the velocity.

voltage and current, respectively). In heat sinks, the temperature scale in R is typically the base-to-inlet temperature difference (ΔT_{in}):

$$R = \frac{\Delta T_{\text{in}}}{\dot{Q}}. \tag{1.4}$$

R is the reciprocal of $h_{\text{ITD}} A_{\text{h}}$, the heat sink's overall conductance.

The effectiveness, introduced above, is the ratio of the heat transfer to the maximum possible heat transfer in the heat sink. This occurs when the air flow reaches the wall temperature. Thus,

$$\epsilon = \frac{\dot{Q}}{\dot{Q}_{\text{max}}} = \frac{\dot{Q}}{\dot{m} c_p \Delta T_{\text{in}}}, \tag{1.5}$$

where ΔT_{in} is the maximum temperature difference in the heat sink, which occurs at the inlet. The effectiveness gives a dimensionless measure of the fluid's temperature rise in the heat sink, and couples the heat transfer and mass flow rates.

The volume of the heat sink (V) can be nondimensionalized by the heat input surface area (A_{h}) for the heat sink to give a measure of the heat sink's compactness. This normalized volume ($\widetilde{V}$) is given by

$$\widetilde{V} = \frac{V}{A_{\text{h}}^{3/2}}. \tag{1.6}$$

Some of these parameters can be related to each other; these relations are shown for convenience in Table 1.2.

1.3.3 Pipe Flow Example

At this point, an example problem that demonstrates the basic scaling of heat transfer and pumping power will be analyzed. Despite the fact that heat sinks usually have complex flow geometries, the analysis of a well known heat transfer topology (namely, pipe flow) leads to insights into the basic scaling of the problem. However, in typical pipe flow analysis the scaling of heat transfer and pumping power are seldom examined together. This scaling shows a large pumping power penalty for high velocities (even though they result in high heat transfer coefficients). The need to reduce the typical velocity through the heat sink results in a design having larger cross sectional flow area and results in larger overall volumes.

In this exercise (shown in Fig. 1-3), cool air flows through a circular, smooth duct, cooling the walls which are at a constant temperature. The pumping power and heat transfer will be calculated for a variety of Reynolds numbers. For simplicity, the flow is

Table 1.2: Relationships Between the Thermal Parameters

	h_{ITD}	R	ϵ	$\dot{q}''$
h_{ITD}	—	$h_{\text{ITD}} = \frac{1}{R A_{\text{h}}}$	$h_{\text{ITD}} = \frac{\epsilon \dot{m} c_p}{A_{\text{h}}}$	$h_{\text{ITD}} = \frac{\dot{q}''}{\Delta T_{\text{in}}}$
R	$R = \frac{1}{h_{\text{ITD}} A_{\text{h}}}$	—	$R = \frac{1}{\dot{m} c_p \epsilon}$	$R = \frac{\Delta T_{\text{in}} A_{\text{h}}}{\dot{q}''}$
ϵ	$\epsilon = \frac{h_{\text{ITD}} A_{\text{h}}}{\dot{m} c_p}$	$\epsilon = \frac{1}{\dot{m} c_p R}$	—	$\epsilon = \frac{\dot{q}'' A_{\text{h}}}{\dot{m} c_p \Delta T_{\text{in}}}$
$\dot{q}''$	$\dot{q}'' = h_{\text{ITD}} \Delta T_{\text{in}}$	$\dot{q}'' = \frac{\Delta T_{\text{in}} A_{\text{h}}}{R}$	$\dot{q}'' = \epsilon \dot{m} c_p \Delta T_{\text{in}} A_{\text{h}}$	—

assumed to be hydrodynamically and thermally fully developed[4].

The pumping power depends on the Reynolds number of the cooling flow. The frictional drag can be calculated with the Darcy-Weisbach equation,

$$\Delta p = f \frac{L}{d_\mathrm{h}} \frac{\rho v^2}{2}, \tag{1.7}$$

where f is the Darcy friction factor, L is the length in the streamwise direction, d_h is the hydraulic diameter, ρ is the fluid density and v is the velocity. The friction factor can be determined analytically for fully developed laminar flow ($f\,\mathrm{Re} = 64$ for circular ducts), when $\mathrm{Re} < \mathrm{Re}_\mathrm{crit}$, or with an empirical correlation for turbulent flow. For circular duct flow in a smooth tube, Petukhov's formula[5] [31] gives an accurate estimate of f for turbulent flow. Thus, the equations to calculate the friction factor are

$$f = \begin{cases} \frac{64}{\mathrm{Re}}, & \text{if } \mathrm{Re} \leq 2300 \text{ (laminar)} \\ (0.790 \ln \mathrm{Re} - 1.64)^{-2}, & \text{if } \mathrm{Re} > 2300 \text{ (turbulent)} \end{cases}. \tag{1.8}$$

Re is the Reynolds number, defined as

$$\mathrm{Re} = \frac{\rho v d_\mathrm{h}}{\mu}, \tag{1.9}$$

where μ is the fluid's dynamic viscosity. In turbulent flow, the velocity profile changes very rapidly near the wall, and turbulent eddies render the core of the flow relatively uniform in temperature and velocity. In contrast to laminar flow, energy and momentum are rapidly transported in this turbulent core without much influence from the wall. This makes the flow relatively insensitive to the shape of the duct, so the round duct correlations can also be used with reasonable accuracy for other geometries.

The heat transfer coefficient can be estimated in a similar fashion to the friction factor. For laminar flow, the Nusselt number is a constant depending on the flow geometry (3.66 for circular ducts with constant temperature walls); for turbulent flow, Gnielinski's

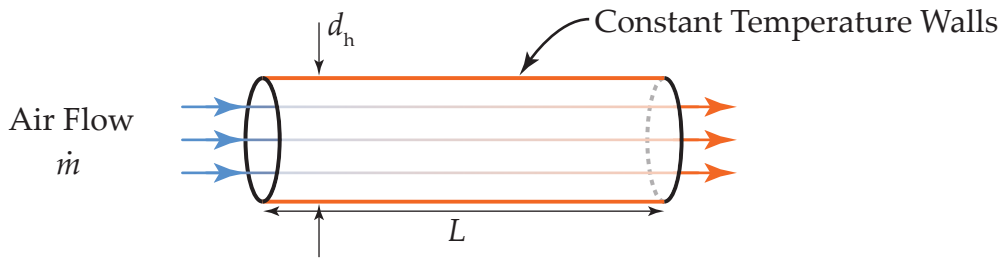

Figure 1-3: A simple, single stream air cooled heat exchanger conceptual exercise demonstrates the scaling typically encountered in the design of an air cooled heat sink.

[4]The main scaling of the problem is not appreciably affected by the entry length because, in general, developing flow correlations use a Reynolds analogy in calculating the Nusselt number and friction factor.

[5]Strictly speaking, Petukhov's formula is valid for $\mathrm{Re} > 10^4$; however, using it for $\mathrm{Re} > 2300$ produces an error of less than 10% in the friction factor compared to a Moody chart.

formula gives accurate results. Thus, the Nusselt number was calculated as

$$\mathrm{Nu} = \begin{cases} 3.66, & \text{if } \mathrm{Re} \leq 2300 \text{ (laminar)} \\ \frac{(f/8)(\mathrm{Re}-1000)\mathrm{Pr}}{1+12.7(f/8)^{1/2}(\mathrm{Pr}^{2/3}-1)},, & \text{if } \mathrm{Re} > 2300 \text{ (turbulent)} \end{cases}. \tag{1.10}$$

The Nusselt number (Nu) can be thought of as a dimensionless heat transfer coefficient:

$$\mathrm{Nu} = \frac{hd_\mathrm{h}}{k}, \tag{1.11}$$

where h is the convective heat transfer coefficient and k is the thermal conductivity of the fluid. In Eq. 1.10, Pr is the Prandtl number, which is a ratio of momentum and thermal diffusivities:

$$\mathrm{Pr} = \frac{\nu}{\alpha} = \frac{c_p \mu}{k}, \tag{1.12}$$

where ν, α, and c_p, are the kinematic viscosity, thermal diffusivity, and isobaric specific heat of the fluid. Finally, to calculate the heat transfer, the temperature rise of the fluid stream must be accounted for. The effectiveness-N_TU method is a mathematically convenient way to calculate the total heat transfer. The number of transfer units ($\mathrm{N_{TU}}$) is defined as

$$\mathrm{N_{TU}} = \frac{UA}{\dot{m}c_p}, \tag{1.13}$$

which is merely a dimensionless expression of a heat exchanger's effective conductance UA. The effectiveness (ϵ), defined in Eq. 1.5, is related to the number of transfer units in a single stream heat exchanger as

$$\epsilon = 1 - \exp(-\mathrm{N_{TU}}). \tag{1.14}$$

With these equations, the thermal resistance and pumping power in a hypothetical single stream, circular duct heat sink were calculated (Fig. 1-4). In this problem, the duct was assumed to have hot, constant temperature walls with a fluid-to-wall temperature difference of 50 °C at the inlet. In Fig. 1-4, the pumping power and heat transfer are plotted over the range of $500 < \mathrm{Re} < 10000$ and normalized by their values at $\mathrm{Re} = 10000$. The tubes were 10 diameters long (although the result shown in Fig. 1-4 was insensitive to d_h and L/d_h in this calculation for $L/d_\mathrm{h} <\sim 1000$).

The rate of increase in the pumping power is striking; it increases by a factor of about 2000 while the heat transfer only increases by a factor of about 10. The coefficient of performance, defined as the ratio of heat transfer to pumping power, decreases as the Reynolds number increases, except for a minuscule increase near the turbulent transition at $\mathrm{Re} = 2300$. This illustrates the somewhat counterintuitive scaling of the pumping power and heat transfer, and underscores the challenge associated with heat transfer enhancement: turbulence does improve heat transfer, but is often accompanied by a severe pumping power increase. This scaling tends to push a design toward larger cross sectional flow area to reduce the local Reynolds number, thereby accepting the lower heat transfer coefficients associated with laminar flow. There has been research that shows a clear benefit to destabilizing the flow to reduce the critical Reynolds number and generate turbulent-like structures (e.g. a von Kármán vortex street) at Reynolds numbers that would normally indicate laminar flow. This destabilized flow yields some enhancement in

the heat transfer with a minimal pumping cost [32].

1.4 Heat Transfer Enhancement Techniques

Heat transfer enhancement is a basic thermal engineering challenge: to maximize the heat transfer coefficient from a fixed heat transfer area and cooling mass flow rate, or equivalently to minimize the temperature difference between a heated surface and the stream of air that cools it. Much research has been devoted to various forms of heat transfer enhancement. Bergles [33] gives a comprehensive review that discusses the two classes of enhancement techniques — passive and active — and their various incarnations in single and multiphase cooling. One common difficulty in the various methods is achieving an enhancement in the heat transfer rate without an excessive pumping power increase. The basic reason for this is that many enhancement methods work by inducing a turbulent transition. Turbulent heat transfer's effectiveness is attributable to the advective action of small eddies in the flow. These eddies, while serving to transport thermal energy and augment the heat transfer rate, are also responsible for enhanced transfer of momentum. This increase in the effective viscosity increases the drag and pumping power requirement.

A formal statement of this parallel enhancement of heat transfer and fluid friction is

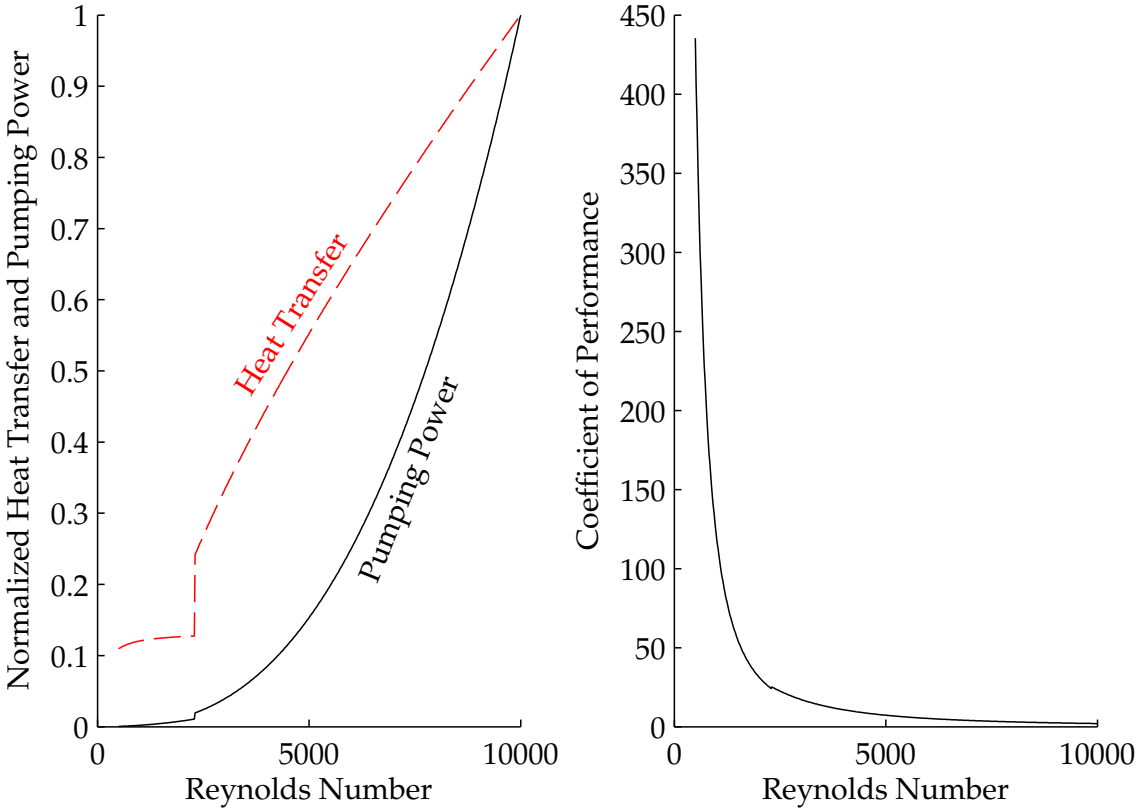

Figure 1-4: The coefficient of performance decreases with increasing Reynolds number. This can be seen by examining the pumping power and heat transfer; the pumping power increases more rapidly than the heat transfer as the Reynolds number increases.

called the Reynolds analogy.

$$\mathrm{St} = \frac{C_f}{2}\mathrm{Pr}^{-2/3}, \tag{1.15}$$

where St is the Stanton number ($\mathrm{St} = \frac{\mathrm{Nu}}{\mathrm{RePr}}$), C_f is the skin friction coefficient of the flow ($C_f = \frac{\tau_s}{(1/2)\rho v^2}$; τ_s is the shear stress on the wall), and Pr is the Prandtl number ($\mathrm{Pr} = \frac{c_p \mu}{k}$). This expression is valid for Prandtl numbers near unity; more complicated expressions allow for nonunity Prandtl numbers (e.g., see Rubesin et al. [34]).

1.4.1 Passive Enhancement

Passive techniques generally consist of modifying or adding structures to a heated surface, with the intention of extending the surface or altering the flow field of the cooling fluid. Single phase enhancement techniques include rough surfaces, extended surfaces, displaced enhancement devices, and swirl flow devices. Rough surfaces increase the heat transfer by causing separation and more violent turbulent eddies, and also by finning effects on the scale of the roughness. These two effects are difficult to separate.

Extended surfaces are used in compact heat exchangers to achieve high surface area to volume ratios. Louvered, perforated, wavy, or offset strip fins are commonly used. These fins exploit the high heat transfer associated with developing flow by forcing the boundary layer to restart at each louver or offset. This can produce 50–100% enhancement compared to flat fins. These compact heat exchangers have been widely studied, and a more detailed discussion can be found in Bergles [33].

Displaced enhancement devices and swirl flow devices are common enhancement techniques for internal flows. Displacement enhancement devices include twisted tapes, meshes, rings, discs, or mixer elements that act as fins and disrupt the flow. These are not commonly used in turbulent flow because of the high pressure drops they introduce. More recently, self-oscillating reeds have been demonstrated to enhance the heat transfer coefficient by a factor of up to 2.5 with only a modest (50%) increase in the pressure drop [35]. Swirl flow devices such as inlet vortex generators and twisted-tape inserts enhance the heat transfer by (1) increasing the flow path length, (2) causing secondary flows, and (3) acting as fins.

Karniadakis et al. [32] studied flow destabilization in a parallel plate channel using flow obstructions. They determined that the minimum-dissipation heat transfer enhancement problem is equivalent to a flow destabilization problem: by producing a lower critical Reynolds number (a less stable flow), the same Nusselt number can be achieved at a lower Reynolds number, which reduces the pumping power to achieve equivalent heat transfer.

1.4.2 Active Enhancement

The review by Bergles [33] discusses a number of active enhancement methods (viz. stirring, surface scraping, and rotating surfaces).

Surface scraping is commonly used to enhance the heat transfer in viscous liquids. In this method, a scraper moving in close proximity to the wall mechanically removes the fluid adjacent to the wall, allowing fresh bulk-temperature fluid to replace the fluid that was warmed by the wall. Scraping is generally useful in laminar flow, where the boundary layer introduces a significant impediment to the convective heat transfer. In laminar flow, the boundary layer grows slowly and the heat transfer across the boundary layer (from the

wall to the freestream or bulk flow) can be approximated to first order by assuming the boundary layer is stagnant and applying Fourier's Law:

$$\dot{Q}_{\text{bl}} \approx \frac{k\Delta T}{\delta_{\text{bl}}}, \tag{1.16}$$

where δ_{bl} is the boundary layer thickness. This explains the high heat transfer coefficients observed in developing flow, where the boundary layer is very thin. Part of the boundary layer can also be physically removed and replaced with fresh fluid from the core of the flow. After this removal, transient conduction into the fluid proceeds until a fresh packet of fluid restarts the process. This can be implemented with, for example, a mixing propeller or a screw.

This phenomenon is prevalent in some industrial applications such as polymer, pharmaceutical, and asphalt processing [36]. For example, polymer extrusion screws exhibit this behavior in the small clearance space between the screw and the wall. This mechanical enhancement can increase the heat transfer coefficient significantly. The heat transfer coefficient for rapid renewal, when the transient conduction penetration depth is thin, is

$$h = 2\sqrt{\frac{k\rho c_p}{\pi}}\sqrt{f}, \tag{1.17}$$

where f is the frequency of surface renewal. This model of the convective enhancement is referred to as "penetration theory" or "surface renewal theory" in the literature [37, 38]. An alternate approach is to assume the heat transfer occurs through a stagnant film of thickness δ, which is related to the clearance between the scraper blade and the heated surface. The heat transfer coefficient of the stagnant film is

$$h = \frac{k}{\delta}, \tag{1.18}$$

where δ is the film thickness.

While most research in mechanical augmentation has focused on viscous fluids, Hagge and Junkhan [38] studied mechanical augmentation of heat transfer in air. They placed a rotating 2-bladed scraper on a heated flat plate in a wind tunnel. They found that the surface renewal theory gave a reasonable estimate of the experimental data for normally-laminar flows, but the full data set was better represented by assuming that a turbulent flow between the blade and the surface was established. The most significant enhancement was observed when the scraper operated in a flow that would otherwise have been laminar. This applies to the integrated fan, where the superficial Reynolds number of the flow through the channel most often suggests laminar flow. Indeed, significant enhancement was observed experimentally in the integrated fans studied in the present work.

1.5 Compact Heat Sinks: Conceptual Designs

In this section some of the challenges of creating a compact, high COP air cooled heat sink will be examined by studying two hypothetical topologies. In these two examples, compact heat exchanger designs are devised that use some form of heat transfer enhancement combined with a loop heat pipe with planar condensers. Ultimately, both of these examples illustrate the balance between thermal resistance, pumping power, and overall

volume.

First, a heat sink with radially outward flow between parallel disc condensers was analyzed. Radially outward flow has some fluid dynamical features that result in enhanced heat transfer coefficients even below the critical Reynolds number predicted by circular duct flow. In this geometry, the stationary discs were assumed to be isothermal, as would be nearly the case if the discs were comprised of planar heat pipe condensers. Furthermore, this geometry offers a straightforward comparison to the integrated fan heat sink which will be discussed in Section 1.6. Next, a linear through-flow heat exchanger incorporated into a stack of parallel heat pipe condensers was analyzed. This heat exchanger had offset strip fins in the air flow channels to passively enhance the convective heat transfer. Offset strips represent a well established convective heat transfer enhancement technique often used in compact heat exchangers.

In comparing these approaches with the integrated fan introduced in Section 1.6, it will be shown that these modular solutions – that is, where a separate fan drives air flow over heated surfaces – do not take advantage of some desirable physical phenomena. In fact, using either of these hypothetical heat exchanger topologies to meet the goals discussed in Section 1.2 proved to be very difficult.

1.5.1 Radially Outward Flow

A heat sink comprised of a loop heat pipe (an evaporator at the base and a multitude of parallel, planar disc shaped condensers with a central air inlet core) and radially outward air flow between the condensers was analyzed. The fluid dynamics of radially outward results in periodic oscillating flow in certain regimes, yielding an enhancement of the convective heat transfer coefficient. Additionally, this topology will later be used to directly show the benefit of adding integrated fans between the condenser layers.

The hydrodynamic and thermal behavior of radially outward flow between parallel discs has been studied extensively because of its interesting fluid dynamics and practical utility (e.g. in turbomachinery and bearings). Mochizuki and Yang [39, 40] and Mochizuki et al. [41] performed experimental studies on the heat transfer and fluid dynamics of radially outward flow between two parallel axisymmetric discs. They determined that the radially outward flow has several distinct flow regimes: (1) fully laminar from the inlet to the outlet; (2) laminar, with an internal region of separation and oscillating flow; (3) laminar/oscillating with a turbulent transition, and a reverse transition back to laminar before the outlet; and (4) turbulent throughout the entire passage [41]. This periodic oscillating flow produces a significant increase in the heat transfer coefficient compared to Poiseuille flow or even slug flow.

Suryanarayana [42] performed an experimental study on the heat transfer in radial outflow between parallel discs held at uniform temperature, both stationary and rotating, with an inlet radius r_1 and outer radius r_2 separated by a gap of breadth b_g (similar to the geometry shown in Fig. 1-5). Suryanarayana's correlation is in a convenient power law form for the mean Nusselt number over the disc. The geometries of interest in the present work (in particular r_1/r_2 and b_g/r_2) are within Suryanarayana's experimentally characterized range. Accordingly, the average Nusselt number for the radial flow ($\mathrm{Nu}_{\mathrm{rf}}$) can be calculated using his correlation for stationary plates as

$$\mathrm{Nu}_{\mathrm{rf}} = \frac{h_{\mathrm{LMTD}} b_g}{k} = 0.0332 \mathrm{Re}_{b_g}^{0.782}, \tag{1.19}$$

where h_{LMTD} is the average heat transfer coefficient based on the log mean temperature difference between the heated plate and the air and $\mathrm{Re}_{b_\mathrm{g}}$ is the Reynolds number based on the plate spacing (b_g) and the log mean velocity. The correlation was based on data with $300 < \mathrm{Re} < 5000$. The Nusselt number in the Suryanarayana correlation, Eq. (1.19), uses the plate spacing as the length scale, which is important to note because it differs from the hydraulic diameter $d_\mathrm{h} = 2b_\mathrm{g}$, which is more commonly used in Nusselt number correlations. Furthermore, in contrast to many heat transfer coefficients reported in heat sink literature, which define the heat transfer coefficient using the temperature difference between the wall and the inlet temperature, Suryanarayana's heat transfer coefficient in Eq. (1.19) references the log mean temperature difference:

$$h_{\mathrm{LMTD}} = \frac{\dot{Q}}{A\Delta T_{\mathrm{LM}}}, \tag{1.20}$$

where A is the surface area of the air flow channel. The log mean temperature difference ΔT_{LM} for this heat sink is defined as

$$\Delta T_{\mathrm{LM}} = \frac{(T_\mathrm{w} - T_\mathrm{in}) - (T_\mathrm{w} - \overline{T}_\mathrm{o})}{\ln\left(\frac{T_\mathrm{w} - T_\mathrm{in}}{T_\mathrm{w} - \overline{T}_\mathrm{o}}\right)}, \tag{1.21}$$

where T_w is the wall temperature, T_in is the inlet air temperature, and $\overline{T}_\mathrm{o}$ is the average outlet temperature.

The Reynolds number in Suryanarayana's correlation (Eq. (1.19)), $\mathrm{Re}_{b_\mathrm{g}}$, is defined as

$$\mathrm{Re}_{b_\mathrm{g}} = \frac{\rho U_{\mathrm{ave}} b_\mathrm{g}}{\mu} \tag{1.22}$$

where U_{ave}, the log mean velocity, can be calculated as in [42] as

$$U_{\mathrm{ave}} = \frac{\dot{m}}{2\pi\rho b_\mathrm{g}} \frac{\ln(r_2/r_1)}{r_2 - r_1}, \tag{1.23}$$

where $\dot{m}$ is the mass flow rate in the flow channel.

The number of transfer units, a dimensionless heat exchanger size, can be calculated as

$$N_{\mathrm{TU}} = \frac{h_{\mathrm{LMTD}} A n}{\dot{m} c_p}, \tag{1.24}$$

where n is the number of air flow layers in the heat sink, A is the wetted surface area per air flow layer, and c_p is the isobaric specific heat of the air. The effectiveness of the heat exchanger can be calculated using Eq. 1.14; the actual heat transfer is calculated using ϵ as

$$\dot{Q} = \epsilon \dot{m} c_p \Delta T_{\mathrm{in}}, \tag{1.25}$$

where ΔT_{in} is the difference between the wall temperature and the inlet air temperature.

In addition to the heat transfer, the pumping power required to drive air radially outward through the parallel plates can determined in several steps. In essence, the fan is used to bring stagnant, atmospheric pressure air to a pressure and velocity sufficient to drive the flow through the parallel disc channels; the work requirement of the fan can then be determined for a specified mass flow rate.

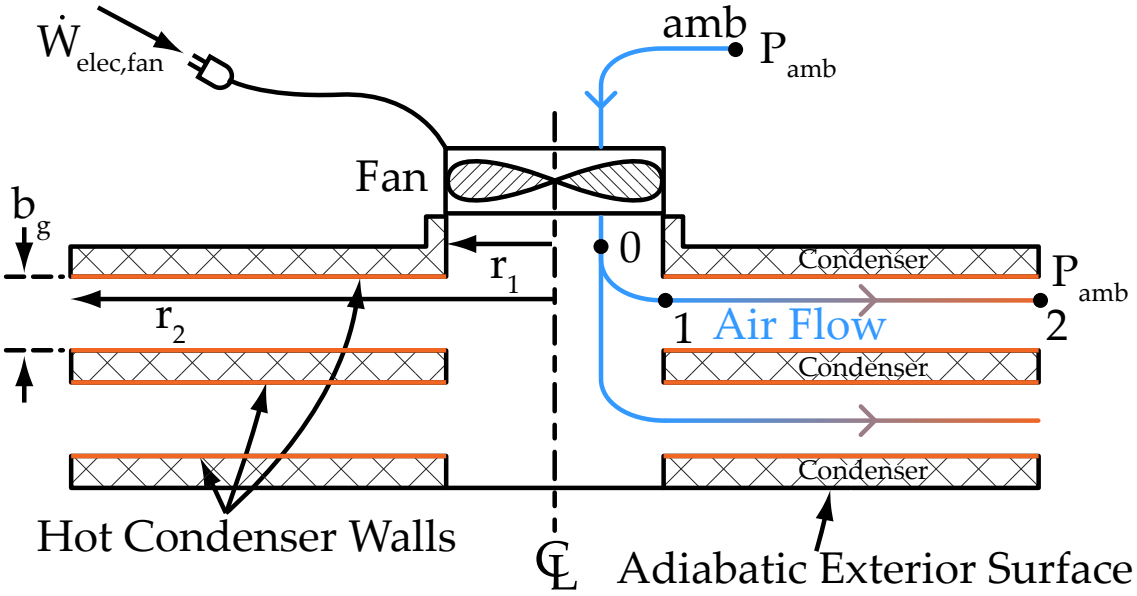

Figure 1-5: A schematic of the radial flow model. A fan forces air axially into a parallel plate gap where it then flows radially outward, providing convective cooling to the heated walls.

First, the pressure difference between points 1 and 2 in Fig. 1-5 is calculated using an expression derived by Moller [43]. Moller determined an approximate solution for the pressure distribution of a turbulent radial outflow in a parallel plate gap by using an integral solution to the momentum equation. Moller also derived a laminar solution; however, the error introduced by using the turbulent solution in regions where the composite laminar-turbulent solution was appropriate was found to be small for the cases considered in this work. Therefore, for simplicity, the turbulent solution was used for all Re; this has the form

$$p_1 - p_2 = \frac{\dot{m}^2}{2\rho b_g^4}\left[\frac{-16}{63\pi^2}\left(\frac{b_g}{r_2}\right)^2\left(\left(\frac{r_2}{r}\right)^2 - 1\right) + \cdots \right.$$
$$\left. 0.007089\frac{b_g \mu^{0.25}}{\dot{m}^{0.25}}\left(\frac{1}{r^{0.75}} - \frac{1.682}{(2r_2)^{0.75}}\right)\right]. \tag{1.26}$$

For the geometries investigated in this work, the flow from point 1 to point 2 experiences a static pressure *increase* due to the increasing cross sectional area. Since the flow exits the parallel plate gap into atmospheric conditions as a jet, the pressure at the exit (p_2) is atmospheric. The pressure upstream of the parallel plate gap entry (that is, point 0 in Fig. 1-5) is determined using the head loss equation, modeling the flow from 0–1 as an area change and a bend:

$$\frac{p_0}{\rho} + \frac{v_0^2}{2} - \left(\frac{p_1}{\rho} + \frac{v_1^2}{2}\right) = (K_b + K_{ac})\frac{v_1^2}{2} \tag{1.27}$$

where v_0 and v_1 are the velocities at points 0 and 1, and K_b and K_{ac} are the minor losses associated with the right angle bend and the area change, respectively. The turning loss is

assumed to be $K_b = 1$, which is typical of a sharp right angle bend [44]. The area change loss is given by Fay [44] as

$$K_{ac} = \begin{cases} 0.4\left(1 - \frac{A_1}{A_0}\right), & \text{if } A_1 \leq A_0 \text{ (contraction)} \\ \left(1 - \frac{A_0}{A_1}\right)^2, & \text{if } A_1 > A_0 \text{ (expansion)} \end{cases} \tag{1.28}$$

where A_0 and A_1 are the flow areas at points 0 and 1, given by

$$\begin{aligned} A_0 &= \pi r_1^2 \\ A_1 &= 2\pi r_1 b_g n, \end{aligned} \tag{1.29}$$

where n is the number of flow channels (2 channels are shown in Fig. 1-5). Rearranging Eq. (1.27) gives the pressure difference from point 0 to point 1 as

$$p_0 - p_1 = (1 + K_b + K_{ac})\frac{\rho v_1^2}{2} - \frac{\rho v_0^2}{2} \tag{1.30}$$

Mass conservation can be used to simplify Eq. (1.30) by eliminating v_0 and v_1, giving the pressure difference as a function of the mass flow rate as

$$p_0 - p_1 = \frac{\dot{m}^2}{2\rho}\left[\frac{(1 + K_b + K_{ac})}{A_1^2} - \frac{1}{A_0^2}\right] \tag{1.31}$$

Finally, the ideal work required to bring stagnant air at atmospheric pressure (point "amb" in Fig. 1-5) to the pressure and velocity at point 0 in Fig. 1-5, determined using the conservation of energy, is

$$\dot{W}_{f,fan} = -\dot{m}\left(\frac{p_{amb} - p_0}{\rho} - \frac{v_0^2}{2}\right) \tag{1.32}$$

where $\dot{W}_{f,fan}$ is the useful work delivered to the fluid (air) by the fan. Eliminating v_0 and reformulating in terms of the mass flow rate using continuity, Eq. (1.32) becomes

$$\dot{W}_{f,fan} = \frac{\dot{m}^3}{2\rho^2 A_0^2} - \frac{\dot{m}(p_{amb} - p_0)}{\rho} \tag{1.33}$$

Equations (1.33), (1.31) and (1.26) can be solved to determine the mechanical power input required by the fan to yield an arbitrary mass flow rate. This power estimate represents the power input to pump air through the system with a lossless fan.

In this heat sink, the tradeoff between thermal resistance, COP, and volume can be studied by solving for $\dot{W}_{f,fan}$, $\dot{Q}$, and the volume V. $\dot{W}_{f,fan}$ can be calculated as described in the previous paragraph; $\dot{Q}$ can be determined from Eqs. 1.19, 1.24, and 1.25. The volume can be calculated as

$$V = \left[n_{layers}(b_g + b_{cond}) + b_{evap}\right]A_{base}, \tag{1.34}$$

where n_{layers} is the number of air flow layers, b_{evap} and b_{cond} are the breadths of the evaporator and a condenser, and A_{base} is the surface area of the heat sink's base.

First, the thermal resistance and pumping power are shown in Fig. 1-6. In this plot, the radial flow heat sink was simulated with 1–15 layers, with each layer having a gap breadth (b_g) of 1 mm. The inner and outer diameters of the disc-shaped condensers were

0.04 and 0.10 m to allow it to fit in the envelope specified by the DARPA MACE requirements[6]. Mass flow rates ranging from the minimum required flow ($\dot{m} = \dot{Q}/(c_p \Delta T_{\text{in}})$) to 75 g/s were simulated. The condensers and evaporator were assumed to be 2.5 and 17 mm thick, respectively, based on realistic planar loop heat pipe component sizes [45, 46]. The evaporator volume plus the volumes of the condensers and air flow gaps were added to determine the total heat sink volume, and this was normalized to the heated area $A_{\text{h}} = \pi r_2^2$:

$$\widetilde{V} = \frac{V}{A_{\text{h}}^{3/2}}, \tag{1.35}$$

where $\widetilde{V}$ is the normalized volume. The 15-layer stack occupied a volume of 0.55 L, which corresponds to a normalized volume of 0.78. The maximum volume and normalized volume in the DARPA requirements are 1 L and 1 (assuming the entire square base is heated), respectively.

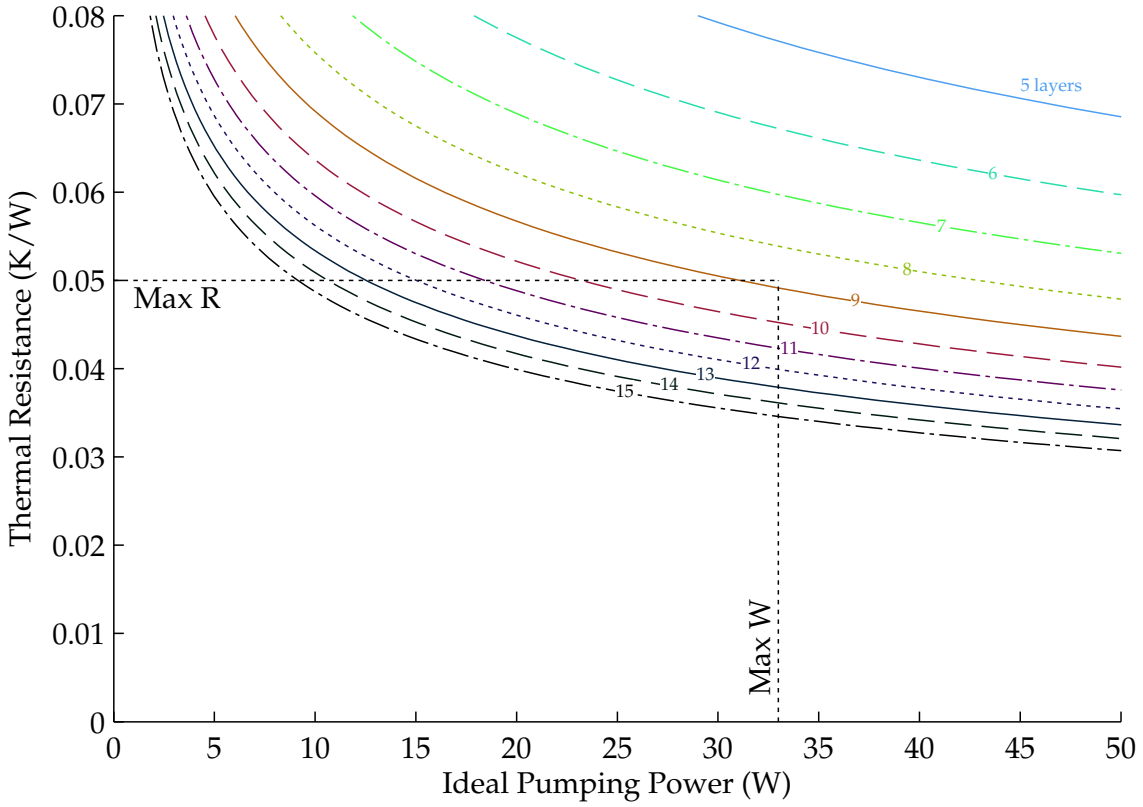

Figure 1-6: A hypothetical radial outflow heat pipe cooler was used to demonstrate the typical tradeoff between thermal performance, COP, and volume. In this heat sink, parallel condensers of a heat pipe bound an outward radial flow of air. With a 10 layer device, the maximum pumping power and thermal resistance requirements set forth by DARPA can be met; however, no penalty for the fan efficiency is considered. Since these efficiencies would not be likely to exceed 40%, the metrics seem very difficult to achieve with this topology.

[6]The inner diameter was selected to produce the best results; increasing the inner diameter improved the pumping power at the expense of heat transfer area. The gap breadth was also selected by comparing several gap spacings and selecting the spacing that produced the best R vs. $\dot{W}$ curves.

While several designs of the radial flow heat sink appear capable of meeting the metric, the simulation described above is very optimistic. First, no penalty for the fan efficiency was accounted for. Since fans sized for these flow rates are typically less than 30% (see Sec. 1.9.1), this essentially pushes all of the operating points over the maximum power specification. Second, the volume of the fan was not accounted for; this can be on par with the heat sink volume. The Xcelaero Squall 50 (see Sec. 1.9.1), for example, occupies a volume of 0.49 L. This volume would increase the size of the radial flow heatsink above the maximum volume specification. This conceptual exercise demonstrates the difficulty of developing a heat sink that is both thermodynamically efficient and compact.

1.5.2 Stacked Offset Strip Fin Heat Sink

In this subsection, a second heat sink concept is examined to demonstrate that even by using elaborate compact heat exchanger technology paired with planar heat pipes, the DARPA thermal, COP, and volume requirements are difficult to satisfy. It will be shown that, using established passive heat transfer enhancement techniques, no obvious solution to the compact air cooled heat sink problem emerges. The integrated fan approach, which will be introduced in Sec. 1.6, proves to be a more compact and efficient solution.

A widely used compact heat exchanger enhancement is the offset strip fin; a diagram of this geometry can be seen in Fig. 1-7. In offset strip fin heat exchangers, corrugated fins are formed to create small flow passages. These passages only extend a short distance in the streamwise direction before they are interrupted by another identical row that is offset by a half-pitch. In this arrangement, the boundary layer is constantly restarting at each new row of fins, forcing the boundary layer to remain thin.

Manglik and Bergles conducted a survey of experimental data for offset strip fin heat exchangers that comprised 18 fin geometries; they developed an empirical correlation that spans the turbulent transition, and is valid from $120 \leq \mathrm{Re}_{d\mathrm{h}} \leq 10^4$ [47]. The hydraulic diameter in this geometry is defined as

$$d_\mathrm{h} = \frac{4A_\mathrm{c}}{A_\mathrm{s}/l} = \frac{4shl}{2(sl+hl+th)+ts}, \tag{1.36}$$

where A_c is the cross sectional area, A_s/l is the surface area per unit length, and s, h, l and t are defined in Fig. 1-7. Dimensionless ratios can be formed from the lengths defining the unit cell:

$$\alpha = \frac{s}{h} \tag{1.37}$$

$$\delta = \frac{t}{l} \tag{1.38}$$

$$\gamma = \frac{t}{s}. \tag{1.39}$$

The average Fanning friction factor and the Colburn j-factor are correlated as

$$f_\mathrm{F} = a_1 \mathrm{Re}^{a_2} \alpha^{a_3} \delta^{a_4} \gamma^{a_5} \left[1 + a_6 \mathrm{Re}^{a_7} \alpha^{a_8} \delta^{a_9} \gamma^{a_{10}}\right]^{0.1} \tag{1.40}$$

and

$$j = b_1 \mathrm{Re}^{b_2} \alpha^{b_3} \delta^{b_4} \gamma^{b_5} \left[1 + b_6 \mathrm{Re}^{b_7} \alpha^{b_8} \delta^{b_9} \gamma^{b_{10}}\right]^{0.1}, \tag{1.41}$$

where a_i and b_i are constants given in Table 1.3.

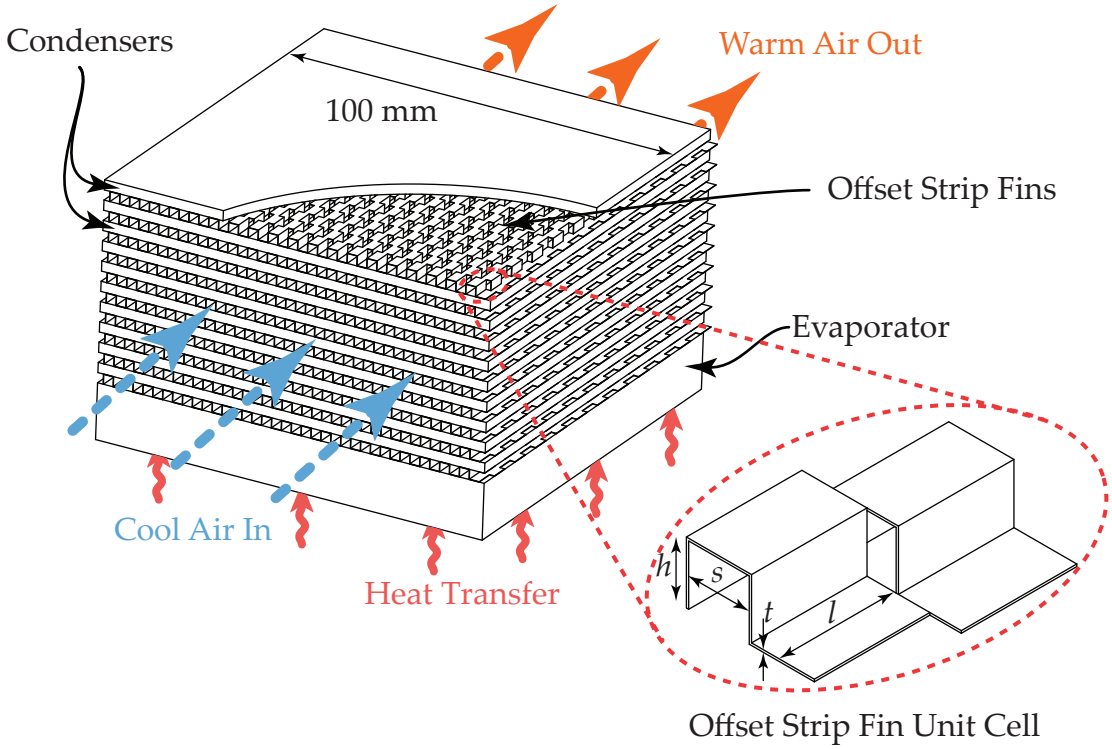

Figure 1-7: A hypothetical offset strip fin heat pipe cooler was used to demonstrate the typical tradeoff between thermal performance, COP, and volume. In this heat sink, parallel condensers and offset strip fins transfer heat to a stream of air provided by a fan (not shown). While the heat sink itself can be relatively compact, the combined volume of the heat sink and fan is significantly larger.

Table 1.3: Constants in Eqs. 1.40 and 1.41

i	a_i	b_i
1	9.6243	0.6522
2	-0.7422	-0.5403
3	-0.1856	-0.1541
4	0.3053	0.1499
5	-0.2659	-0.0678
6	$7.669 \cdot 10^{-8}$	$5.269 \cdot 10^{-5}$
7	4.429	1.34
8	0.92	0.504
9	3.767	0.456
10	0.236	-1.055

The Fanning friction factor (the dimensionless wall shear stress) is related to the Darcy friction factor (the dimensionless pressure drop per unit length) by a factor of 4:

$$f = 4f_{\mathrm{F}}. \tag{1.42}$$

The Colburn j-factor is defined as

$$j = \mathrm{StPr}^{2/3} = \frac{\mathrm{Nu}}{\mathrm{RePr}^{1/3}}, \tag{1.43}$$

where $\mathrm{St} = \frac{\mathrm{Nu}}{\mathrm{Re}\cdot\mathrm{Pr}}$ is the Stanton number.

With these equations the Nusselt number and Darcy friction factor can be predicted a priori from the heat sink geometry and flow rate. From here, the pressure drop and heat transfer can be calculated. The pressure drop is given by the Darcy-Weisbach equation (originally shown in Eq. 1.7) as

$$\Delta p = f\frac{L}{d_{\mathrm{h}}}\frac{\rho v^2}{2}, \tag{1.44}$$

where L is the total length of the channel. The mean heat transfer coefficient (h_{m}) is calculated from the definition of the Nusselt number as

$$h_{\mathrm{m}} = \frac{\mathrm{Nu}\,k}{d_{\mathrm{h}}}, \tag{1.45}$$

where k is the thermal conductivity of the air. To account for the changing temperature of the air stream, the effectiveness-N_{TU} method is employed. The number of transfer units is calculated as

$$N_{\mathrm{TU}} = \frac{h_{\mathrm{m}}A_{\mathrm{s,tot}}}{\dot{m}c_p}, \tag{1.46}$$

where $A_{\mathrm{s,tot}}$ is the total surface area of the offset strip fins, $\dot{m}$ is the mass flow rate of air through the heat sink, and c_p is the isobaric specific heat of the air. Inherent assumptions in using this method are (1) the flow is equally distributed among the parallel flow channels (this can be difficult to achieve in practice); and (2) the properties of the air do not change significantly as the air's temperature increases. Recalling (see Eq. 1.14) that the effectiveness for this single-stream heat exchanger is

$$\epsilon = 1 - \exp\left(-N_{\mathrm{TU}}\right), \tag{1.47}$$

the total heat transfer is given by

$$\dot{Q} = \epsilon\left(\dot{m}c_p\Delta T_{\mathrm{in}}\right), \tag{1.48}$$

where the parenthetical expression represents the maximum possible heat transfer that can be rejected into the air flowing at mass flow rate $\dot{m}$. When the effectiveness is 1, temperature of the air reaches the wall temperature and the temperature profile is said to "pinch."

The base area was set to 0.1 by 0.1 m, the maximum specified in the DARPA specifications, and the height of the channel was set to 2.5 mm. It was assumed that a 2.5 mm condenser would serve as an isothermal wall to separate each offset strip fin flow channel. The offset strip fin geometry was chosen using the best performing geometry in [47]. The

thermal resistance and pumping power are plotted in Fig. 1-8. The specifications (maximum R and $\dot{W}$) from the DARPA MACE program are shown as black dashed lines. At first glance, it seems that several designs have potential to meet the metric. However, like the radial flow heat sink in the previous section, the pumping power calculated here is the *ideal* power, which is at least 3 times lower than the actual input power, due to the fan efficiency. The volume also exceeds the DARPA metric starting at 13 layers, and this does not include any provision for a fan. As mentioned in the previous section, the volume of the fan can be significant. Additionally, the flow characteristics (Δp vs. $\dot{V}$, the system flow resistance) of each system reveal an additional challenge. The least restrictive of these flow passages, the 15 layer version, has a pressure drop of 118 Pa and a flow rate of 17.6 L/s when its thermal resistance reaches 0.05. Finding a fan that can meet this relatively stringent requirement for a compact heat sink is another challenge for the designer.

Thus, while the thermal and COP requirements seem attainable with this topology, the separate fan makes the volume requirement difficult to meet. Even with significantly effort to enhance the convective heat transfer and increase the hot surface area using planar heat pipes, the heat sink is still bulky in comparison to the DARPA goals. The topic of the present work (i.e. the integrated fan heat sink, which will be introduced in the next section) uses the volume it occupies more effectively, and in subsequent chapters will be shown to have the potential to exceed the DARPA goals in all respects.

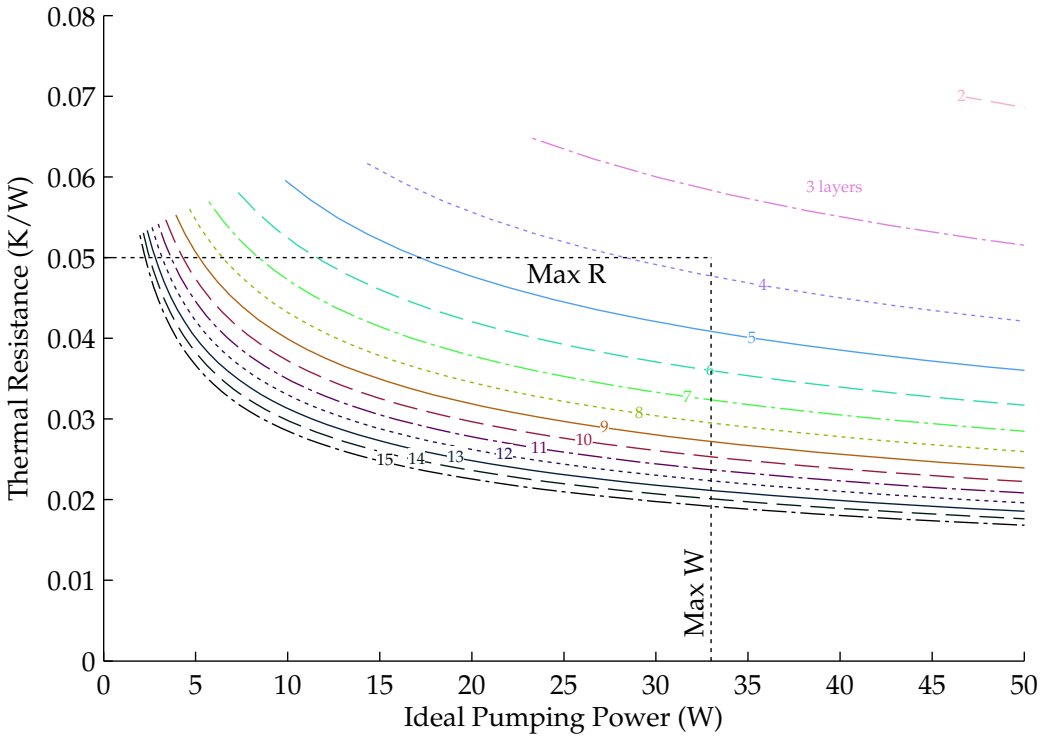

Figure 1-8: The hypothetical parallel plate heat exchanger with offset strip fins performs better than the radial outflow heat exchanger; however, it would be very difficult to meet the DARPA volume requirement. The 15 layer version occupies more volume than the specification and does not include a fan, which would add considerable additional volume.

1.6 The Integrated Fan Heat Sink

1.6.1 Basic Design

The typical approach in an air cooled heat sink design is to use a discrete, separate fan to force air flow over a finned heat sink (see, for example, Fig. 1-2). This approach has been very extensively studied and optimized, but it is ultimately limited because of the convective heat transfer coefficient between the air and the fins, and the unfavorable scaling of pumping power and heat transfer. One common approach is to use passive convection enhancement techniques (e.g. roughened surfaces; dimpled, corrugated or louvered fins) to essentially increase the UA product without increasing the physical size of the heat sink. Two approaches of this variety were analyzed in Section 1.5, and were shown to This work focuses on a new, alternate approach: the integration of one or more fans into the heat sink, placing the fans in close proximity with the fins. A diagram of this topology can be seen in 1-9.

This integrated fan heat sink approach has a number of advantages. First, in addition to pumping air through the heat sink, the fans in this arrangement serve to enhance the convective heat transfer coefficient from the hot surfaces. In essence, the fans act as an *active* heat transfer enhancement mechanism while also performing the task of pumping enough air through the heat sink to meet the required thermal duty. Second, heat sinks with a thermal duty in the 1 kW range are sized such that, for reasonable motor speeds (under 10000 rpm), centrifugal fans are likely to be the most efficient design. This can be

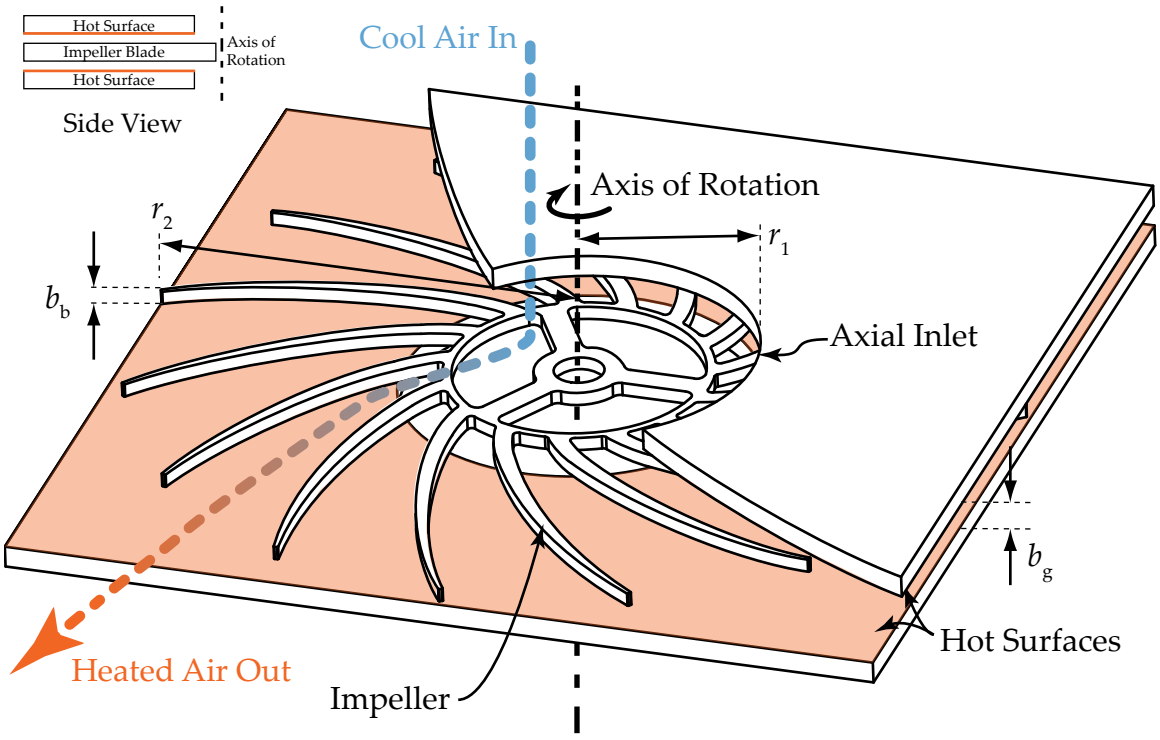

Figure 1-9: In contrast to a traditional air cooled heat sink in which a fan forces air flow over a finned heat sink, an integrated fan heat sink incorporates fans directly into the heat sink, placing the fan blades in close proximity to the heated surfaces.

seen using a dimensionless[7] parameter called the specific speed (N_s), which is a performance parameter for turbomachinery [48], and is defined as

$$N_s = \frac{\omega \dot{V}^{1/2}}{(gH)^{3/4}}, \tag{1.49}$$

where ω is the angular velocity of the fan, $\dot{V}$ is the volume flow of air, ρ is the density of the air, g is the gravitational constant ($\sim 9.81 \text{m/s}^2$) and H is the "head." The head is related to the pressure rise of the fan by $\Delta p = \rho g H$. Figure 1-10 shows that for a particular value of N_s an optimal machine topology can be chosen. For a 0.1 m diameter fan (a design that would fit in the envelope detailed in the DARPA guidelines), the Euler turbomachinery equation and first order loss estimates (see Sec. 1.7) can be used to predict the head and volume flow for a given speed. At 5000 rpm, a specific speed of 0.4 was calculated; referring once again to Fig. 1-10, this suggests that a centrifugal fan is the most appropriate topology in this application.

1.6.2 Implementation in a Loop Heat Pipe

To create a compact heat sink, the integrated fan makes for a natural complement to planar heat pipes (e.g. Ding et al. [49], Kariya [45], Hanks [46]).

A loop heat pipe with multiple parallel condensers and integrated centrifugal fans was developed [45, 46, 50]. This heat sink, referred to by the rather unfortunate name "PHUMP," is a loop heat pipe with impellers driving air radially outwards across a multitude of parallel plate condensers (Figure 1-11). Heat transfer into the bottom of the device causes the working fluid, water, to evaporate and travel up the vertical pipes into the parallel condensers. Heat is removed from the condensers by convective heat transfer to the

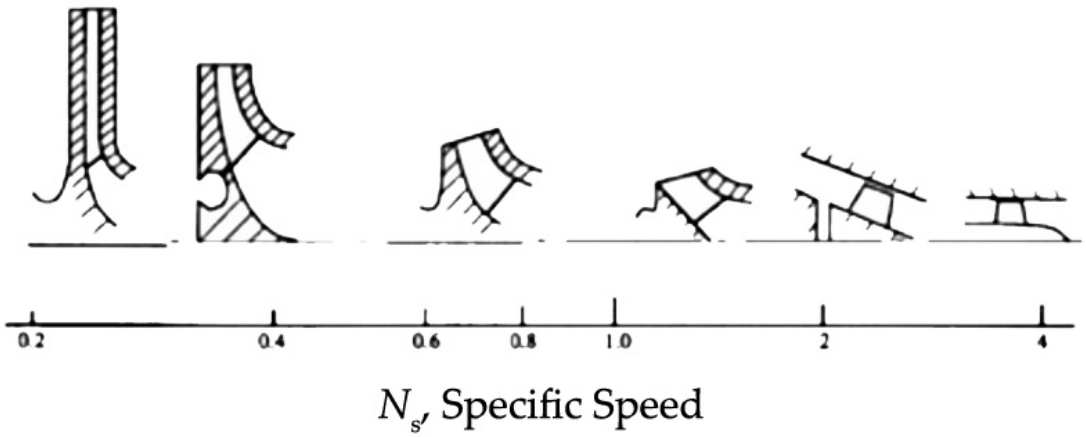

Figure 1-10: The specific speed is a dimensionless performance parameter that describes turbomachinery and serves as a design guideline for selection of optimal topology. For a fan in the diameter range of the PHUMP, and a reasonable rotational speed (~5000 rpm), the specific speed is about 0.4. This specific speed suggests that a centrifugal fan would yield the best results (Figure from [48]).

[7] Unfortunately, a common practice in industry is to express the specific speed in a dimensional form through the use of inconsistent units in its definition. In this work, the universal, dimensionless form is used.

air flow. Fresh, cool air is drawn in through the inlet at the top. This configuration exploits the tremendous heat transfer coefficient associated with evaporation to achieve a high heat flux at the evaporator base. Although the heat transfer coefficient from the condensers to the air is much lower than in the evaporator, the large thermal power input from the evaporator is distributed among the parallel condensers. By parallelizing the condensers, their overall thermal resistance is greatly reduced. Finally, a practical advantage is that the device is self-contained, using the surrounding air as the heat exchange fluid and therefore requiring no external fluid connections.

1.7 Centrifugal Fan Analysis and Design

1.7.1 Ideal Performance

The performance of an ideal fan can be determined by applying the conservation of angular momentum to the impeller:

$$\frac{\Delta p_t}{\rho} = (u_2 c_{u2} - u_1 c_{u1}), \tag{1.50}$$

where Δp_t is the total pressure rise across the fan, u is the blade speed ($u = \omega r$) and c is the absolute fluid velocity. Subscripts 1 and 2 refer to the inlet and the outlet of the impeller, respectively. Equation 1.50 is known as the Euler turbomachinery equation. The

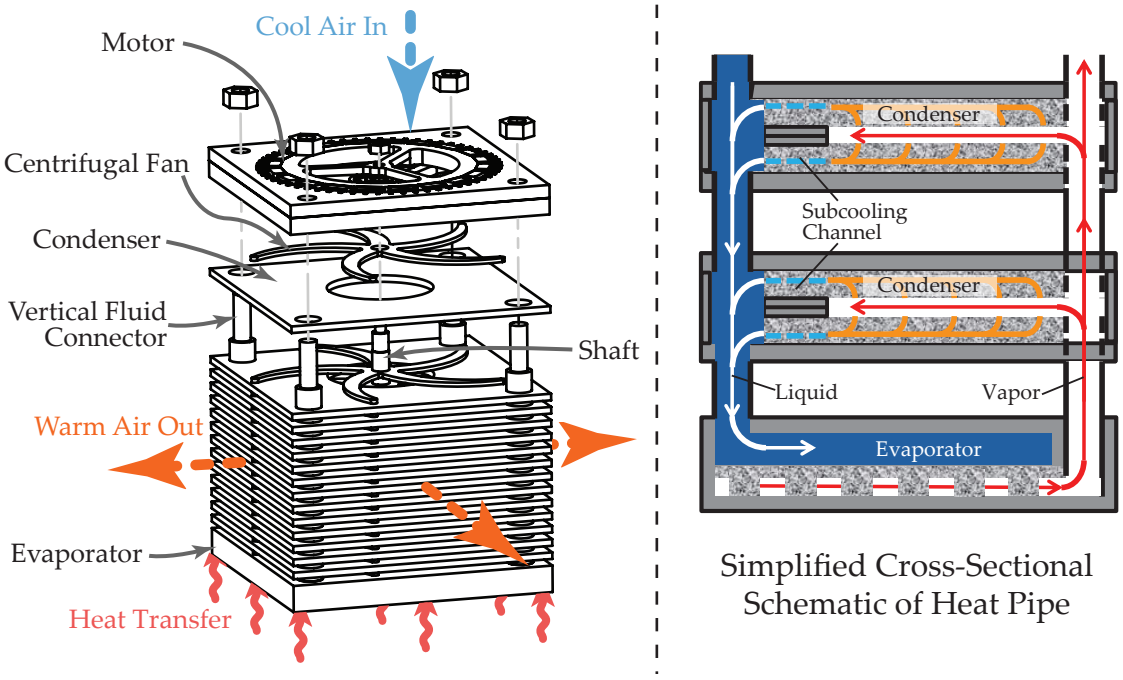

Figure 1-11: An implementation of an integrated fan heat sink, called the PHUMP, consists of a series of centrifugal fans operating in parallel to cool the condensers of a loop heat pipe. The heated surface on the bottom is the evaporator of the heat pipe. A compact, low profile brushless DC motor atop the device powers the fans. The simplified schematic (adapted from Hanks [46]) shows the internal heat pipe structure. The workings of the heat pipe are described in detail by Kariya [45] and Hanks [46].

tangential component of the absolute velocity at the inlet to the impeller, c_{u1}, is often neglected because the flow in the inlet section is radial (i.e. the upstream effect of the blades is very small and the incoming flow is irrotational). Of course, the inlet tangential velocity is important in fans with inlet guide vanes; however, in this work the fans did not have inlet guide vanes. Accordingly, the second term in Eq. 1.50 vanishes. The Euler equation thus simplifies to

$$\frac{\Delta p_t}{\rho} = u_2 c_{u2} \tag{1.51}$$

Epple showed that the Euler equation can be combined with geometrical relations from the velocity triangle and expressed in terms of three parameters: the total-to-static head coefficient ψ_{ts}, the flow coefficient ϕ, and the exit angle β_2 (90° corresponds to radial blades):

$$\psi_{ts} = \frac{1}{2}\left[1 - \left(\frac{\phi}{\sin\beta_2}\right)\right]. \tag{1.52}$$

The head and flow coefficients are the dimensionless pressure rise and volume flow; they are defined in Sec. 1.8.

In an ideal impeller, the flow follows the blades perfectly, and its direction at the outlet (in the relative frame) is determined by the exit angle of the blade. Due to a number of loss mechanisms, the ideal pressure rise predicted by the Euler equation overpredicts the actual pressure rise at a certain flow. Or, in other words, for a given power input, an impeller imparts less angular momentum to the flow than the Euler equation predicts.

It is convenient to work in a reference frame that rotates with the fan. However, the important velocities in the Euler equation refer to the stationary frame. The transition from the rotating to the stationary frame can be visualized using a velocity triangle, as shown in Fig. 1-12. Here, at any point, the absolute velocity c (i.e., in the fixed reference frame) is the vector sum of the relative velocity w and the local velocity of the fan blade $u = \omega r$. If the flow in the relative frame is assumed to follow the blade contour, the relative velocity exits at the exit angle β_2.

The meridional velocity is related to the volume flow rate through the system as

$$c_m = w_m = \frac{\dot{V}}{A_c} \tag{1.53}$$

where A_c is the local cross sectional area, $\pi d b_g$.

A trigonometric relationship between the meridional velocity, the blade angle, and the magnitude of the relative velocity can be determined from the velocity triangle:

$$|w| = w_m / \sin\beta \tag{1.54}$$

$$w_u = w_m / \tan\beta \tag{1.55}$$

w_u, the component of w in the tangential (u) direction, is of interest because it can be subtracted from u to obtain c_u, which appears in the Euler equation:

$$c_u = u - w_u \tag{1.56}$$

The Euler quantities are an upper bound on the performance of a fan. However, several unavoidable losses degrade the performance predicted by the Euler equation. These losses arise from both inviscid and viscous phenomena.

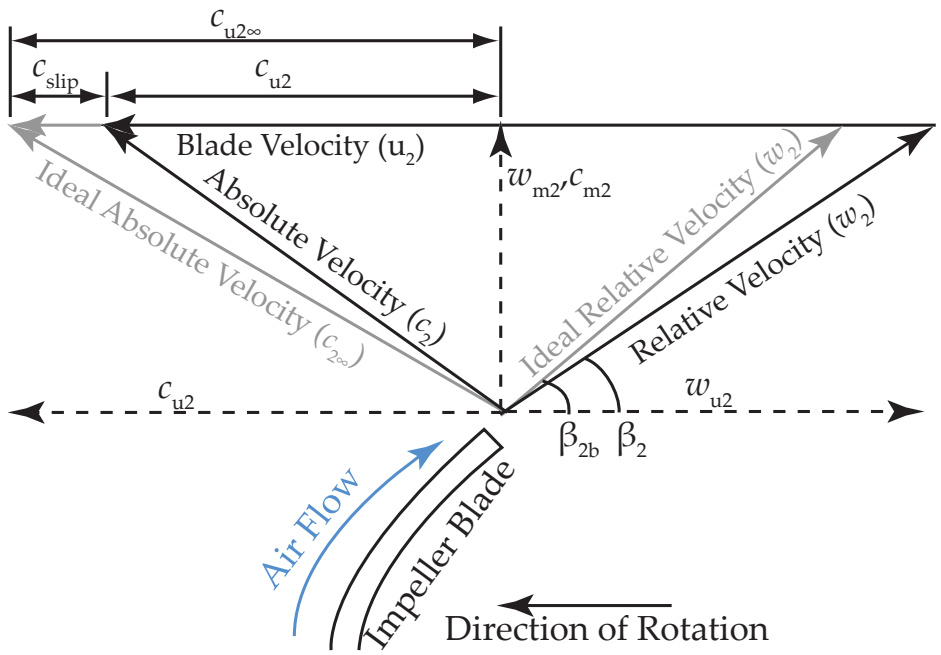

Figure 1-12: The velocity triangle shows the relationship between the absolute velocities (c) and the relative velocities (w).

1.7.2 Losses

Departure from the ideal predictions of the Euler turbomachinery equation occurs from several mechanisms. First, slip loss accounts for the imperfect guiding of the flow by a finite bladed impeller, causing the flow to leave the fan at an a shallower angle than the blade. Second, incidence or "shock" loss at the entry occurs at operating points other than the design point, when the flow angle at the entry does not match the blade angle and impacts the blade at the entry. Friction loss arises from dissipative interactions between the fluid and the fan (e.g. leakage from the pressure side to the suction side of the blade). These losses all act to reduce the theoretical pressure rise calculated by the Euler equation.

The Euler equation requires some assumption about the tangential velocity of the fluid exiting the fan. In the ideal prediction, all of the flow exiting the impeller is assumed to follow the contour of the blade and leave at the exit angle. The reduction in the angular momentum associated with deviation from the blade is accounted for with a quantity called the slip factor. The slip factor (σ_s) is

$$\sigma_s = 1 - \frac{c_{slip}}{u_2} \tag{1.57}$$

where c_{slip} is the slip velocity and u_2 is the blade velocity at the exit plane. c_{slip} is the difference between the actual absolute tangential outlet velocity and the ideal prediction of the absolute tangential outlet velocity.

In essence, the slip factor is a measure of how close the tangential velocity at the exit approaches the blade tip speed. The ideal tangential exit velocity, determined purely by the operating point and the blade geometry, is reduced by a slip velocity. A number of effects, both inviscid and viscous, contribute to this slip. The dominant effect is often an

inviscid phenomenon known as the "relative eddy." Helmholtz's third theorem states that the flow irrotational flow entering the impeller must remain irrotational [51]; therefore, in a reference frame rotating with the impeller, the entry flow (irrotational in the fixed frame) must have a rotation rate equal and opposite to that of the reference frame. The relative eddy results in a circular motion in the rotating frame that tends to speed up the flow on the suction side of each blade and retard the flow on the pressure side. When superimposed on the through flow, the result is a nonuniform velocity profile at the exit plane which causes the flow to exit at an angle to the blades (i.e. the blades do not guide the flow perfectly and the absolute tangential outlet velocity is less than the ideal value).

A number of formulas have been developed to predict the slip factor. Stodola proposed a slip factor based on a slip velocity using assumed values of the relative eddy size and location [52–54]. Additionally, Wiesner developed an empirical relation based on an extensive set of industrial data, and showed the slip factor can be approximated as

$$\sigma_s = 1 - \frac{\sqrt{\sin\beta}}{Z^{0.7}}, \tag{1.58}$$

where β is the exit angle and Z is the number of blades in the impeller.

More complicated slip factor relations have subsequently been developed; Von Backstrom [55] developed a unified slip factor theory, based on a single relative eddy in the impeller rather than a relative eddy in each blade passage. Qiu et al. [54] thoroughly reviewed the slip factor correlations in 2011 and developed a unified slip factor model that works at off-design conditions and accounts for passage variation and blade turning.

In addition to slip, frictional loss and incidence loss (also called "shock loss") also result in significant degradation of the Euler predicted pressure rise. Frictional loss tends to increase parabolically with the volume flow [52] as

$$\Delta p_f = C\dot{V}^2, \tag{1.59}$$

where C is a constant. The frictional pressure loss increases monotonically with the volume flow. The incidence loss also varies parabolically with the volume flow, but is not monotonic over the operating range of the impeller; at one point on the fan curve, the incidence loss vanishes. The results of these losses can be seen qualitatively in the fan curve shown in Fig. 1-13.

1.8 Dimensional Analysis

The functional dependencies of the heat sink can, to some extent, be postulated using the Buckingham Pi theorem. This method is described in most fluid mechanics textbooks (e.g. White [56], Dixon [53], Wright [57], Boyce [58], Brennen [48], Lewis [59]). The Buckingham Pi theorem systematically combines the relevant parameters of a system into a set of dimensionless "Π groups." This set of Π groups represents the minimum number of parameters necessary to fully describe the system (provided the relevant parameters are all properly accounted for). A planned set of experiments can be limited to vary these dimensionless groups, reducing the dimension of the parameter space required to characterize the problem.

The basic procedure is as follows:

1. Identify the n parameters relevant to the problem and their dimensions

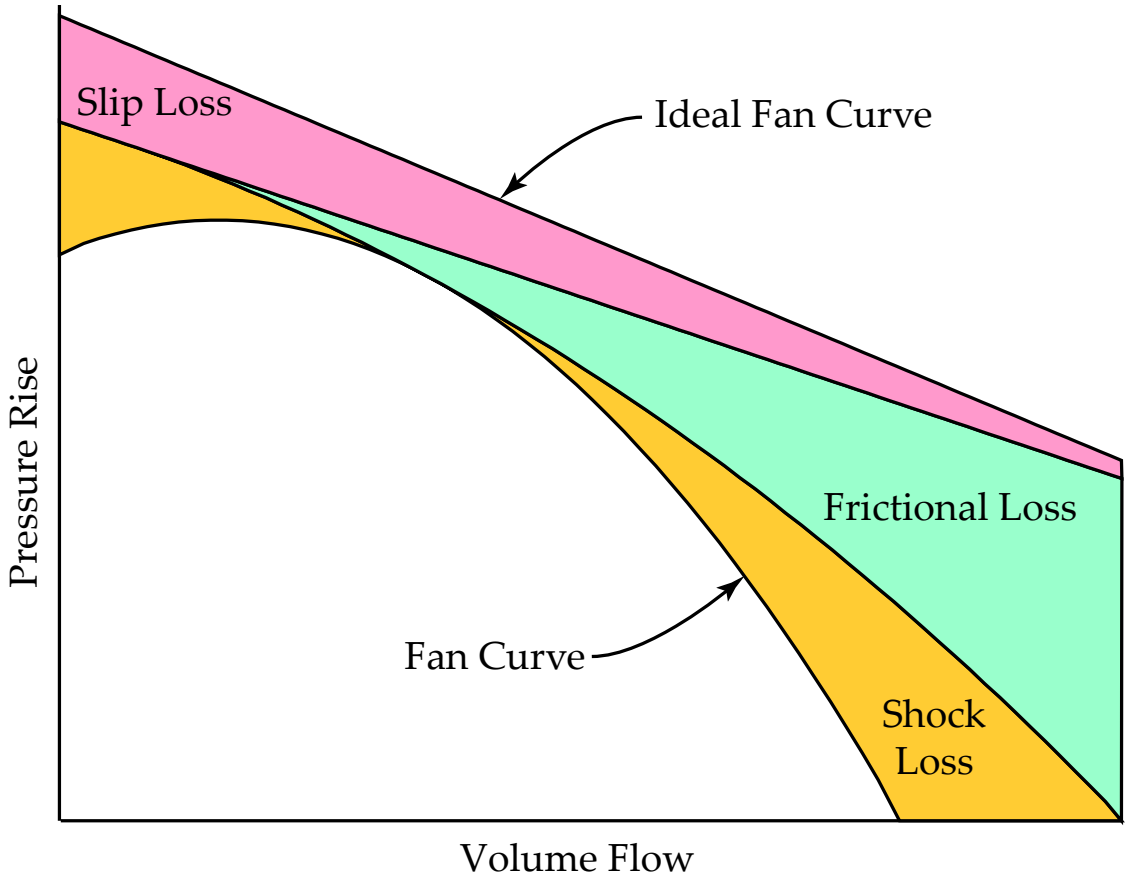

Figure 1-13: The ideal fan performance curve, calculated from the Euler equation, is reduced by several losses: slip, frictional and shock.

2. Choose m of these parameters, where m is the number of unique dimensions represented by the n parameters. The set of m parameters must encompass all of the unique dimensions, and cannot themselves be arranged to form a dimensionless group.

3. Form Π groups by combining the remaining $n - m$ parameters with the m repeating parameters. The powers of the m repeating parameters must be chosen to give dimensionless Π groups .

The problem of interest can then be described by the relationships between the Π groups.

1.8.1 Relevant Parameters

Fan Parameters

The parameter selection and dimensional analysis of the fan is similar to analyses such as Wright [57]. First, the fluid properties are relevant to the performance of any fluid machine. Since this work focuses on fans, the flow can be considered incompressible and the relevant fluid properties are the density ρ and the dynamic viscosity μ.

The operating parameters of the fan are the rotational speed ω, volume flow rate $\dot{V}$, the total-to-static pressure rise Δp_{ts} and the power input $\dot{W}$. Any two of these may be somehow controlled in an experiment, while the other two are resulting performance parameters.

Finally, several parameters that describe the geometry of the system must be included. The primary geometrical parameter is the outer diameter of the impeller, d_2. The breadth of the impeller blade, b_{b}, and the breadth of the gap between the parallel plates, b_{g} are also important parameters. In addition, the number of blades and the exit angle play a role in the performance of the system.

Heat Sink Parameters

In addition to the parameters discussed above, several factors related to the heat transfer are important in describing the system. Two additional fluid properties must be specified: the thermal conductivity k and the isobaric specific heat c_p.

The operating point, in terms of the heat transfer, can be described by the heat transfer rate into the system, $\dot{Q}$, and the temperature difference between the inlet fluid and the heated walls, ΔT_{in}. Experimentally speaking, one of these may be set and the other results from the performance of the device. Finally, no new geometrical parameters must be specified, as these are identical to those specified for the fan performance.

Table 1.4 summarizes the relevant parameters and their dimensions. Several additional geometrical parameters are included in the table as dimensionless ratios. The system's sensitivity to these parameters will be investigated and discussed.

Table 1.4: Relevant Parameters and Dimensions

	Parameter	Dimension
Fluid Properties	ρ	ML^{-3}
	μ	$\mathrm{ML}^{-1}\mathrm{T}^{-1}$
	k	$\mathrm{MLT}^{-3}\Theta^{-1}$
	c_p	$\mathrm{L}^2\mathrm{T}^{-2}\Theta^{-1}$
Operating Properties	ω	T^{-1}
	$\dot{V}$	$\mathrm{L}^3\mathrm{T}^{-1}$
	Δp_{ts}	$\mathrm{ML}^{-1}\mathrm{T}^{-2}$
	$\dot{W}$	$\mathrm{ML}^2\mathrm{T}^{-3}$
	$\dot{Q}$	$\mathrm{ML}^2\mathrm{T}^{-3}$
	ΔT_{in}	Θ
Geometry	d_2	L
	$\mathrm{AR} = b_{\mathrm{b}}/d_2$	1
	$\mathrm{FR} = b_{\mathrm{b}}/b_{\mathrm{g}}$	1
	$\mathrm{IR} = d_1/d_2$	1
	β_2	1

1.8.2 Dimensionless Groups

Table 1.4 shows 14 unique parameters, 3 of which are already dimensionless geometrical ratios. Since there are four unique dimensions involved in the parameters (Mass M, Length L, Time T, and Temperature Θ), the remaining 11 parameters can be reduced to $11 - 4 = 7$ dimensionless groups. ρ, ω, d_2 and k were chosen as repeating parameters. Proceeding with the Buckingham Pi theorem, the Π groups are as follows:

$$\begin{aligned}
\Pi_1 &= \frac{\mu}{\rho\omega d_2^2} \\
\Pi_2 &= \frac{\dot{V}}{\omega d_2^3} \\
\Pi_3 &= \frac{\Delta p_{\text{ts}}}{\rho\omega^2 d_2^2} \\
\Pi_4 &= \frac{\dot{W}}{\rho\omega^3 d_2^5} \\
\Pi_5 &= \frac{\rho\omega d_2^2 c_p}{k} \\
\Pi_6 &= \frac{\dot{Q}}{\rho\omega^3 d_2^5} \\
\Pi_7 &= \frac{\Delta T k}{\rho\omega^3 d_2^4}
\end{aligned} \tag{1.60}$$

The Π groups may be multiplied against constants, against each other, or raised to powers to form alternate, equally valid dimensionless groups. For convenience, several such transforms were applied to the groups in Eq. 1.60 to recast them into commonly used groups. The first Π group can be inverted to form the rotational Reynolds number:

$$\Pi_1^{-1} = \text{Re}_\omega = \frac{\rho\omega d_2^2}{4\mu} \quad \textbf{Rotational Reynolds Number}. \tag{1.61}$$

This form of the Reynolds number takes the familiar form of $\frac{\rho v L}{\mu}$, with the characteristic length and velocity being the outlet radius of the fan and the impeller tip speed.

Three common turbomachinery performance parameters have forms similar to Π_2, Π_3 and Π_4. The volume flow is often nondimensionalized by a characteristic velocity and a reference area. The tip speed $\omega d_2/2$ is a good (and very prevalent) choice for the characteristic velocity. The reference area is chosen to be the area at the exit plane of the fan (i.e. $\pi d_2 b_g$). This choice incorporates both the diameter and the breadth of the gap. A common reference area that sometimes appears in literature (e.g. White [56]) is d_2^2; this is an unfortunate choice for a centrifugal fan because the breadth does not affect the nondimensionalization, which does not make physical sense. In this work, the exit plane area $\pi b_g d_2$ is used as the reference area. Proceeding with the nondimensionalization, Π_2 is multiplied by $(b_g/d_2)^{-1}$ and a constant, and the volume flow becomes the flow coefficient:

$$\Pi_2 (b_g/d_2)^{-1} (\pi/2)^{-1} = \phi = \frac{\dot{V}}{(\omega d_2/2)(\pi b_g d_2)} \quad \textbf{Flow Coefficient}. \tag{1.62}$$

Similarly, the pressure rise is nondimensionalized by comparing it to a reference pressure. This reference pressure simply takes the form of the dynamic pressure ($1/2\rho v^2$)associated with the tip speed $\omega d_2/2$. For mathematical convenience, however, the 1/2 is omitted from this pressure[8]. Indeed, Π_3 multiplied by a constant becomes the total-to-static head coefficient:

$$\Pi_3(1/4)^{-1} = \psi_{\text{ts}} = \frac{\Delta p_{\text{ts}}}{\rho(\omega d_2/2)^2} \quad \textbf{Total-to-static Head Coefficient}. \tag{1.63}$$

An important feature of the head coefficient lies in its subscript, which stands for "total-to-static." This signifies that the total-to-static pressure rise of the impeller is the quantity of interest; that is, the difference between the static pressure at the exit of the impeller and the *total* pressure at the inlet to the impeller. The static pressure is the pressure exerted by a quiescent fluid; the total pressure is the sum of the static pressure and the dynamic pressure $\rho v^2/2$, where v is the local velocity. This distinction is sometimes important, especially at higher flow rates. Epple discusses the utility of using total-to-static metrics for impeller rating in great detail [51], but essentially these quantities best represent the practical use of a fan. The static pressure is appropriate at the outlet because the dynamic pressure is lost at the outlet. On the other hand, at the inlet, the static pressure can be difficult to measure on a test apparatus. In contrast, on a flow bench with a large plenum upstream of the inlet there is a small loss in total pressure between the plenum and the inlet. Also, the large area ratio between the plenum and the inlet renders the dynamic pressure in the plenum negligible, so a measurement of static plenum pressure gives the total pressure at the inlet. Indeed, Epple found that the total-to-static metrics were more universally descriptive of an impeller's performance. It's worth mentioning that an unsubscripted head coefficient (Ψ) generally refers to the "total" or "total-to-total" head coefficient, meaning that the total pressure at both the inlet and outlet is referenced. The dynamic pressure at the outlet is usually lost and is almost never measurable. If it is anticipated that the exit dynamic pressure can be mostly recovered, the total-to-total head coefficient may be of more interest. Japikse and Baines discuss the merits of these performance criteria in more detail [60].

Another interpretation of the flow coefficient and the head coefficient is a ratio of velocities at the exit plane of the fan. When normalized to the blade tip speed, the flow and head coefficients represent the meridional and tangential components of the absolute exit velocity, respectively [51].

Next, the power coefficient is recovered from Π_4 by multiplying by a constant. The power coefficient compares the mechanical power input to the impeller to a reference power. This reference power is the product of the reference volume flow (in the flow coefficient) and the reference pressure rise (in the head coefficient):

$$\Pi_4(\pi/8)^{-1} = \xi = \frac{\dot{W}}{\rho(\omega d_2/2)^3(\pi b_{\text{g}} d_2)} \quad \textbf{Power Coefficient}. \tag{1.64}$$

Three parameters are related to the thermal behavior of the system. First, Π_5 and Π_1

[8]Some authors choose to retain the 1/2, so some care must be taken when comparing the head coefficient to other publications. This definition used in this work permits another interpretation based on the velocity triangle; the total head coefficient is a ratio of the outlet tangential velocity to the blade tip speed, and the total-to-static head coefficient is analogously defined but with the total-to-static pressure replacing the total pressure.

can be multiplied to get the Prandtl number, which characterizes the ratio of momentum diffusivity to thermal diffusivity:

$$\Pi_5\Pi_1 = \mathrm{Pr} = \frac{c_p\mu}{k} \quad \textbf{Prandtl Number}. \tag{1.65}$$

Second, Π_6 and Π_3 can be combined to give a dimensionless heat transfer into the system. The coefficient of performance simply compares the heat transfer rate to the mechanical power input:

$$\Pi_6\Pi_3^{-1} = \mathrm{COP} = \frac{\dot{Q}}{\dot{W}} \quad \textbf{Coefficient of Performance}. \tag{1.66}$$

It is important to note that the COP is often greater than 1; it is not an efficiency, but merely a dimensionless expression of the heat transfer per unit work transfer in a heat pump. The third thermal parameter is the mean dimensionless heat flux (a combination of Π_6 and Π_7):

$$\Pi_6\Pi_7^{-1} = \Phi_\mathrm{m} = \frac{\dot{Q}}{d_2\Delta T k} \quad \textbf{Dimensionless Heat Flux}. \tag{1.67}$$

The dimensionless heat flux quantifies the heat transfer conductance (i.e. the heat transfer rate per temperature difference) or resistance of the system. Often, the Nusselt number serves this purpose, but a subtle difference warrants a change in nomenclature from Nu_m to Φ_m (a detailed discussion of the differences in the behaviors of these two dimensionless parameters can be found in Shah and London [61]). The temperature difference in Φ_m is between the wall temperature and the *inlet* fluid temperature. In contrast, Nu_m generally uses the logarithmic mean temperature difference:

$$\Delta T_\mathrm{lm} = \frac{\Delta T_1 - \Delta T_2}{\ln\left(\Delta T_1/\Delta T_2\right)}, \tag{1.68}$$

where ΔT_1 and ΔT_2 are the wall-to-fluid temperature difference at the inlet and outlet, respectively. The outlet temperature, of course, depends on the heat transfer into the system, the heat transfer conductance of the system, and the capacity flow rate of fluid through the system. Thus, the temperature scale in Nu_m is seldom known a priori, whereas in Φ_m the temperature scale is simply ΔT_1, which is a design parameter and is often specified a priori. From a rating perspective, Nu_m is satisfactory, but for design purposes Φ_m can simplify the problem considerably.

Several other dimensionless parameters warrant discussion, although the parameters above are sufficient to describe the problem. First, the efficiency of the fan is a useful metric that compares the power delivered to the air ($\dot{V}\Delta P_\mathrm{ts}$) to the mechanical power input. Again, the total-to-static quantities are used for their consistency.

$$\eta_\mathrm{ts} = \frac{\dot{V}\Delta p_\mathrm{ts}}{\dot{W}} \quad \textbf{Fan Efficiency} \tag{1.69}$$

The efficiency is defined in terms of the total-to-static pressure difference because (1) this pressure difference is directly measured in the experimental apparatus, and (2) the total-to-static efficiency is known to be a useful performance metric in centrifugal fan design [51]. Since the flow, head, and power coefficients were defined with a consistent

reference area and characteristic velocity, the efficiency can also be expressed as

$$\eta_{\text{ts}} = \frac{\phi\psi_{\text{ts}}}{\xi}. \tag{1.70}$$

The heat sink, of course, can be thought of as a single stream heat exchanger, and several heat exchanger design tools prove to be useful. First, the effectiveness ϵ (defined in Eq. 1.5) is the ratio of the heat transfer to the maximum possible heat transfer. The maximum heat transfer occurs when the temperature of the air stream reaches the wall temperature:

$$\epsilon = \frac{\dot{Q}}{\dot{m}c_p(T_{\text{w}} - T_1)}, \tag{1.71}$$

where $\dot{m}$ is the mass flow rate of air, and T_{w} and T_1 are the wall and inlet temperatures.

Often associated with the effectiveness is a ratio of the streamwise temperature change of the fluid and the characteristic temperature difference from the wall to the fluid. This ratio is known as the number of transfer units (also defined in Eq. 1.13):

$$N_{\text{TU}} = \frac{UA}{\dot{m}c_p}, \tag{1.72}$$

where U is the overall conductance and A is the heat transfer surface area. The UA product is simply the inverse of the thermal resistance R.

Three of the geometrical parameters in Table 1.4 are referred to by shortened names for convenience. First, the aspect ratio (AR) is defined as

$$\text{AR} = \frac{b_{\text{b}}}{d_2}, \tag{1.73}$$

the ratio of the blade breadth to the outer diameter. Next, the fill ratio (FR) is a measure of how much the impeller fills the parallel plate gap, namely

$$\text{FR} = \frac{b_{\text{b}}}{b_{\text{g}}}. \tag{1.74}$$

The inlet ratio (IR) is the ratio of the inner diameter (d_1) to the outer diameter (d_2),

$$\text{IR} = \frac{d_1}{d_2}. \tag{1.75}$$

To summarize, the dimensionless groups (excluding geometrical ratios) are as follows: Re_ω, ϕ, ψ_{ts}, ξ, Pr, COP, and Φ_{m} .

1.9 Performance of Commercially Available Solutions

A number of commercially available heat sinks were examined to determine the current level of performance one could reasonably expect in an air cooled heat sink. A review website, Frostytech [62], performed thermal testing on many heat sinks. Their test setup consisted of a 30 by 30 mm copper heater block embedded in an insulator and heated with a precision power resistor. An embedded thermocouple measured the temperature of the

block. A 150 W load was applied to the heater block and the temperature rise of the block above ambient was measured. The results for 20 heat sinks are summarized in Table 1.5. The thermal resistance R, electrical power consumption $\dot{W}_{\text{elec}}$, overall volume occupied, and the normalized volume (defined in Eq. 1.35). The normalized volume ($\widetilde{V} = V/A^{3/2}$) is a dimensionless measure of how much volume a heat sink occupies compared to the surface area over which the heat load is applied. For reference, a cube with one surface heated would have a normalized volume of 1 (although a heat sink with a normalized volume of 1 isn't necessarily cubical, since the heated area need not be square). The intent of examining this parameter was to appropriately penalize excessive bulk while maintaining a fair comparison metric between heat sinks with different thermal duties.

The thermal resistance and normalized volume of the surveyed heat sinks are shown in Fig. 1-14. In this plot, points closer to zero on both axes are desirable (small, with low thermal resistance). A tradeoff between thermal resistance and volume is evident; the lower volume heat sinks have a higher thermal resistance. The PHUMP's predicted performance can be seen as a significant improvement compared to the traditional heat sinks. The Sandia Cooler (version 1, as discussed in Section 1.3) also occupies a position far from the commercially available heat sinks; the volume is lower and thermal resistance is higher compared to the PHUMP.

1.9.1 Fans

Air cooled heat sinks rely on either natural or forced convection to reject heat to the ambient temperature surroundings. In stationary applications, forced convection heat sinks

Table 1.5: Commercially Available Heat Sinks Surveyed [62]

Num.	Manufacturer	Model	$\Delta T\|_{\dot{Q}=150\text{W}}$ (K)	R (K/W)	$\dot{W}_{\text{elec}}$ (W)	Volume (L)	$\widetilde{V} = VA^{-3/2}$
1.	Spire	Thermax Eclipse II (2 fans)	12.6	0.084	8.4	3.07	113.7
2.	Tuniq	Tower 120 Extreme	14.1	0.094	1.9	2.23	82.6
3.	Noctua	NH-D14	14.5	0.097	2.3	3.52	130.2
4.	Spire	Thermax Eclipse II	14.5	0.097	4.2	2.56	94.7
5.	Thermaltake	Frio	14.5	0.097	12.0	2.66	98.6
6.	Prolimatech	Megahalems (80CFM)	15.0	0.100	1.9	2.02	74.9
7.	3Rsystem	Iceage 120 Boss II	15.4	0.103	4.6	1.93	71.5
8.	Titan	TTC-NK85TZ	15.5	0.103	3.8	2.07	76.7
9.	Zaward	Vapor 120	15.6	0.104	5.4	1.43	53.0
10.	Thermolab	BADA	16.0	0.107	4.9	1.49	55.0
11.	Sunbeamtech	Core-Contact Freezer	16.1	0.107	3.4	1.99	73.7
12.	Zalman	CNPS10X Quiet	16.5	0.110	3.0	2.00	73.9
13.	Zalman	CNPS10X Flex (80CFM)	16.5	0.110	1.9	1.94	71.7
14.	Zalman	CNPS10X Performa	16.6	0.111	2.4	1.95	72.2
15.	Spire	Thermax II (SP67951)	16.7	0.111	4.2	1.86	68.9
16.	Noctua	NH-C14	14.1	0.094	1.2	3.26	120.7
17.	Zalman	CNPS8900 Extreme	21.7	0.145	4.8	0.88	32.5
18.	Evercool	HPL-815	27.7	0.185	3.6	0.45	16.8
19.	Silverstone	NT07-AM2	51.0	0.408	2.2	0.30	5.5
20.	Scythe	Kozuti SCKZT-1000	32.9	0.219	2.4	0.46	16.9

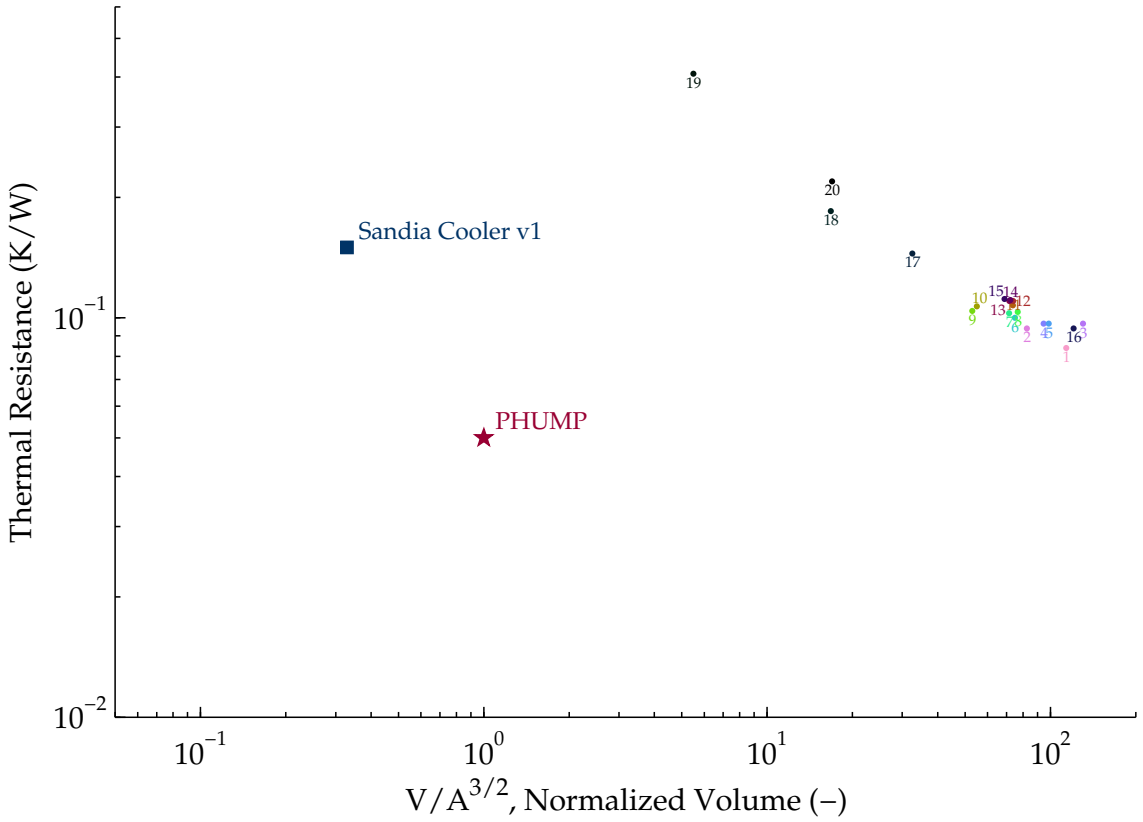

Figure 1-14: Twenty commercially available heat sinks were surveyed and compared to the anticipated performance of the PHUMP. The Sandia cooler is also shown for reference.

use fans[9] to induce the air flow over the heat sink. These fans are typically modular units that are completely separate from the heat sink.

Fans come in many forms. The tube axial fan — an axial fan contained in a small venturi section to reduce tip vortices — is found in the majority of air cooled heat sink applications [65]. Vane axial fans have vanes to remove the swirl from the fan exhaust. They are more efficient, but are costlier and occupy a deeper volume envelope for a given fan diameter.

The minimum required air flow can be calculated from an energy balance on the air flowing through the heat sink:

$$\dot{V} = \frac{\dot{Q}}{\rho c_p \Delta T_{\text{in}}}, \tag{1.76}$$

where $\dot{V}$ is the volume flow of air, $\dot{Q}$ is the heat transfer rate from the heat sink, ρ and c_p are the density and isobaric specific heat of the air, and ΔT_{in} is the temperature difference between the heated surface and the ambient air. This represents the minimum flow rate because the heat transfer was assumed to be effective enough to raise the air stream to the

[9] There is no universally agreed upon standard on what distinguishes a fan from a blower or a compressor. In industrial parlance, a compressor's intent is to increase the fluid's pressure, while a fan's intent is to move the fluid [63]. Alternatively, the pressure ratio can be used as a guide: pressure ratios less than 1.1 are called fans, between 1.1 and 1.2 are called blowers, and more than 1.2 are called compressors [64]. A pump designates a fluid machine that handles a liquid. All of the machines developed in this work have a low pressure ratio and seek mainly to move air, and thus are referred to as fans.

same temperature as the heated surface. For heat sinks with heat rejection rates in the range of 100–1000 W, the required air flow is approximately $(2-20)\cdot 10^{-3}\mathrm{m}^3/\mathrm{s}$.

A number of fans with flow rates in this range were chosen from Digi-Key (an electronics components distributor [66]) for analysis, to demonstrate the performance of current commercially available offerings. These fans are summarized in Table 1.6. The fan curves (Δp vs. $\dot{V}$) were extracted from the manufacturers' datasheets using graphical data reverse engineering software [67]. The nominal power consumption was given on the datasheet, although it was generally ambiguous to which operating point the nominal power referred. The fan overall fan efficiency is defined as

$$\eta_{\mathrm{fan,o}} = \frac{\dot{V}\Delta P}{\dot{W}_{\mathrm{elec}}}, \tag{1.77}$$

where $\dot{W}_{\mathrm{elec}}$ is the electrical power input to the fan. The overall efficiency curves for the fans surveyed were estimated by calculating the hydraulic power $\dot{V}\Delta P$ from the fan curves and dividing by the nominal power consumption. The fan and efficiency curves can be seen in Fig. 1-15. The peak efficiency of the surveyed fans was 42% (Xcelaero Squall 50); this was a specialized vane axial fan. The next highest efficiency in the survey was 23.8%. More commonly, the maximum efficiency was around 20% or less. It is worth noting, also, that the calculated efficiencies[10] are probably higher than the operational efficiency. The reason for this suspected overprediction is the ambiguity of the nominal power specified in the datasheets. For example, if the nominal power refers to a point near the free delivery volume flow, the hydraulic power would be much lower, and the efficiency would be overpredicted everywhere else in the fan's operation. Reported efficiency in other sources [29] suggests that generally, these types of fans have a very low efficiency (as low as 5%). The motor efficiency of small fans, most of which are powered by brushless DC motors, is typically 40–60% [29, 68].

The efficiency of the currently available fans for electronics cooling is important for comparison to the designs discussed in the present work. In subsequent chapters, the results of this survey will be revisited.

1.10 Summary

The increasingly stringent demands of modern electronics have pushed air cooled heat sinks to the limits of what is possible with current designs; some applications have exceeded the capabilities of air cooling and resorted to more exotic and costly solutions. The challenge in designing air cooled heat sinks is balancing the thermal resistance, pumping power, and overall volume. With current technology, minimizing any two of these parameters usually occurs in concert with an unacceptable increase in the third. An integrated fan heat sink was introduced which is compact, exploits active heat transfer enhancement, and has the potential to be thermally efficient.

In what follows, an experimental study of this integrated fan heat sink topology is described. Its characteristics were found to be an improvement over the current state of the art.

[10] The efficiency curve for the Xcelaero Squall 50 was provided by the manufacturer. The other efficiency curves were calculated with Eq. 1.77.

Table 1.6: Commercially Available Fans Surveyed

Manufacturer	Part Number	Digi-Key Part No.	$\dot{W}_{elec}$ (W)	Speed (rpm)
Delta	AHB1548EH	603-1101-ND	25	4000
Delta	AHB1548SH	”	21	3700
Delta	AHB1548VH	”	18	3400
Delta	AFC0948DE–TP20	603-1188-ND	29	7500
Delta	FFB1012EHE	603-1074-ND	26	5000
Sunon	PMD4809PMB1–A	259-1423-ND	12	4900
Sunon	PMD4809PMB2–A	”	7.7	4400
Sunon	PMD1209PMB3–A	”	5.6	3800
Delta	FFB0912SH	603-1066-ND	8.3	4100
Delta	BFB1024M (centrifugal)	BFB1012M-A-ND	6.2	3200
Xcelaero	Squall 50	—	66	13000

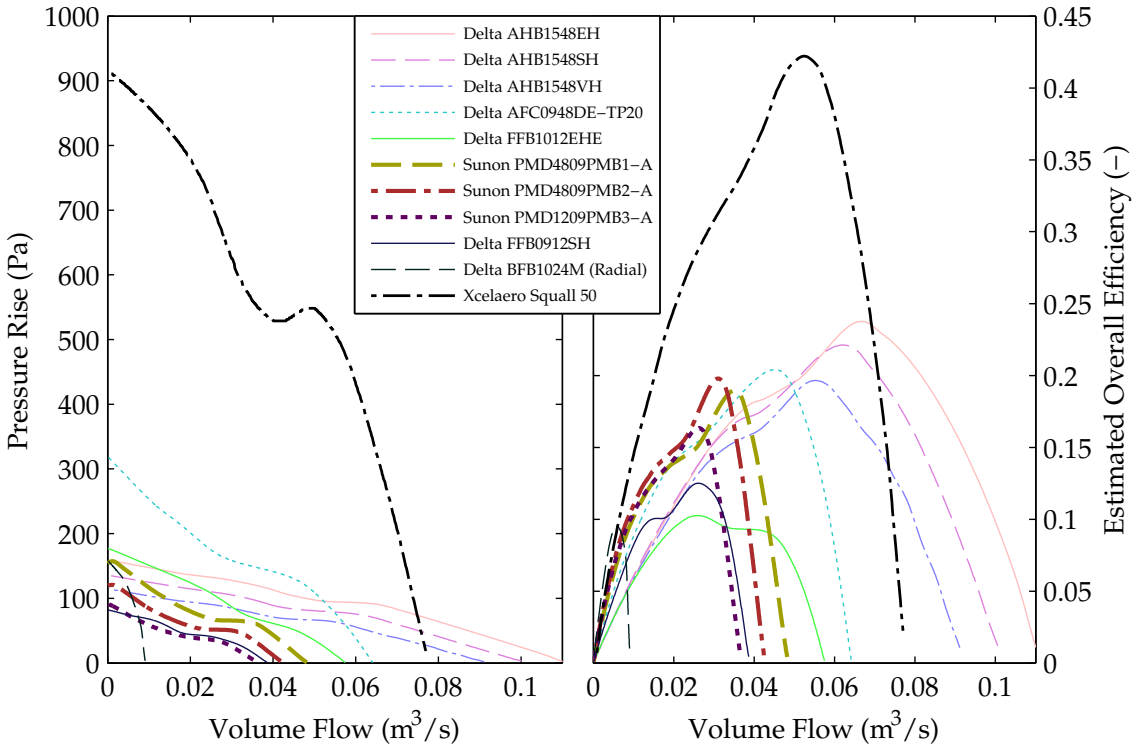

Figure 1-15: 11 commercially available fans used for thermal management of electronics were selected from an electronic components distributor. The fan performance data was extracted from the manufacturer provided datasheets. The efficiency curves were estimated by (1) computing the hydraulic power from the fan curve, and (2) dividing the hydraulic power by the nominal electrical power consumption stated on the datasheet. No estimation was required for the Xcelaero Squall 50 because the manufacturer provided a measured efficiency curve. The highest efficiency of the fans surveyed was calculated to be 24%, except for the Squall 50 which was significantly higher than the others at 42%.

CHAPTER 2

EXPERIMENTAL SETUP

Experiments were performed to gain insight into the complex fluid dynamics of the fan, with respect to both the pumping performance and the heat transfer. Two apparatuses were used to characterize the fans in this work. An apparatus with square stator plates and four corner support posts allowed the characterization of a geometry that one may expect in a heat pipe application; in fact, this apparatus was intended to mimic the geometry anticipated in the heat pipe described in Chapter 1. The square stator apparatus consisted of stator plates that could be heated, so the fan performance as well as the overall heat transfer performance could be characterized.

Additionally, a flow bench apparatus with circular stator plates provided information about the fully unshrouded impellers operating in axisymmetric system. This circular apparatus provided the bulk of the experimental data. The instrumented portion of this apparatus was modular so that three different types of experiments could be performed: (1) fan characterization, i.e. determination of the dimensionless fan curves; (2) average heat transfer characterization, in a manner analogous to that of the square stator apparatus; and (3) local heat transfer characterization, in which a novel infrared (IR) thermography method was used to characterize the local heat transfer coefficient. In each of these three experiment types the fan being characterized was the only motive force for the air in the system.

A number of impeller geometries were characterized. The impeller described in [50] was characterized, and often used as a baseline since this impeller was ultimately designed for use in the PHUMP. Several other 5-blade impellers with varying exit and entry angles were also characterized. Next, a series of radial (i.e. $\beta = 90°$) blade impellers with varying number of blades was tested. Next, 15-bladed logarithmic spiral impellers with blade angles of 75, 60, 45 and 30 degrees were characterized. Each impeller geometry was also tested with several fill ratios. The 90 degree blades were also tested with various inner and outer diameters. These geometries provided a rough idea of the parameter space describing the impeller shape; the variations in the impeller shapes tested were motivated by the parameters identified by dimensional analysis.

2.1 Square Stator Apparatus

An apparatus designed to closely mimic the anticipated heat pipe geometry in the PHUMP was constructed, so that the effect of the corner post regions would be included in the characterized impeller designs. In this experimental apparatus, shown in Fig. 2-1 (schematic) and Fig. 2-2 (picture), dry nitrogen from a building supply passed through a rotameter and into an inlet section with the same diameter as the fan inlet (colloquially known as the chimney section). Two flow straightening screens in the top of this chimney section uniformized the velocity profile upstream of the fan inlet. The static pressure difference between the chimney and ambient was measured with three pressure sensors of various ranges[1]. Finally, the air entered the parallel plate gap in which the impeller rotated, and was discharged radially to the surrounding ambient air.

The square stator apparatus had heated stator plates, so two types of tests could be performed: a fan characterization, in which the plates were unheated; and a heat transfer characterization, which consisted of a subset of the operating points in the fan characterization, but with the stator plates held at a constant elevated temperature. The fan characterization test measured the fan curves and power consumption at various rotational speeds. The heat transfer characterization measured these quantities, as well as the average heat transfer coefficient of the air flowing over the plate. The following section describes this experimental apparatus and the fan and heat transfer characterizations.

2.1.1 Description of Apparatus

The square stator apparatus consisted of two copper stator plates attached to an aluminum support structure and ultimately to an optical breadboard on a lab workbench. An aluminum platform on the support structure had four acetal studs installed into threaded holes. A square piece of balsa wood and the lower copper stator were installed on the aluminum platform, with the studs passing through holes in the four corners of the balsa wood and copper. Additionally, an aluminum tube in the center held two bearings and a rotating shaft, driven on the bottom by a DC motor. The shaft extended up past the lower stator; the impeller was sandwiched axially between two shaft collars installed on the shaft. The upper stator was separated from the lower stator by precision shim washers on the acetal studs. The chimney section was situated atop the upper stator. The chimney and the upper stator were held in place with hex nuts threaded onto the acetal studs. The space between the upper stator and the chimney was fitted with a silicone gasket to minimize leakage flow.

The upper stator plate was removable since it was only secured with four hex nuts; the gap between the stator plates was set by precision shim washers on each of the four studs. The location of the shaft collars and impeller was chosen to ensure that the impeller was centered between the plates.

Nitrogen was supplied to the apparatus from the building supply; it passed through a forward pressure regulator, a throttle valve, a rotameter, and finally entered the chimney section. The regulator isolated the system from small fluctuations in the pressure of the building nitrogen supply. The throttle valve controlled the flow rate of nitrogen, which was read from the rotameter. In this arrangement, most of the pressure drop (~300 kPa)

[1] This configuration provided adequate range for the full range of tests, while still maintaining excellent sensitivity at low pressure differences. Cross-checking of the sensors also provided some level of error detection.

occurred across the throttle valve; consequently, the variations in the fan inlet pressure (~0-1 kPa) had a negligible effect on the flow rate through the system. Thus, the volume flow could be set to a constant value (irrespective of the fan operating point) by adjusting the valve only once per required flow rate. This property was important because the tests were designed so that the only intervention necessary was the adjustment of the valve to test various flow rates.

Pressure Measurement

Three pressure sensors were used to measure the pressure difference between the inlet to the impeller and the ambient. The sensor characteristics can be seen in Table 2.1. Each sensor was of the differential, bidirectional, piezoresistive strain gauge variety. One tap of each sensor was connected to the chimney tap; the second tap was open to ambient pressure. The chimney tap was split three ways to expose the chimney pressure to all three sensors simultaneously. Table 2.1 shows that the range and uncertainty of each sensor are

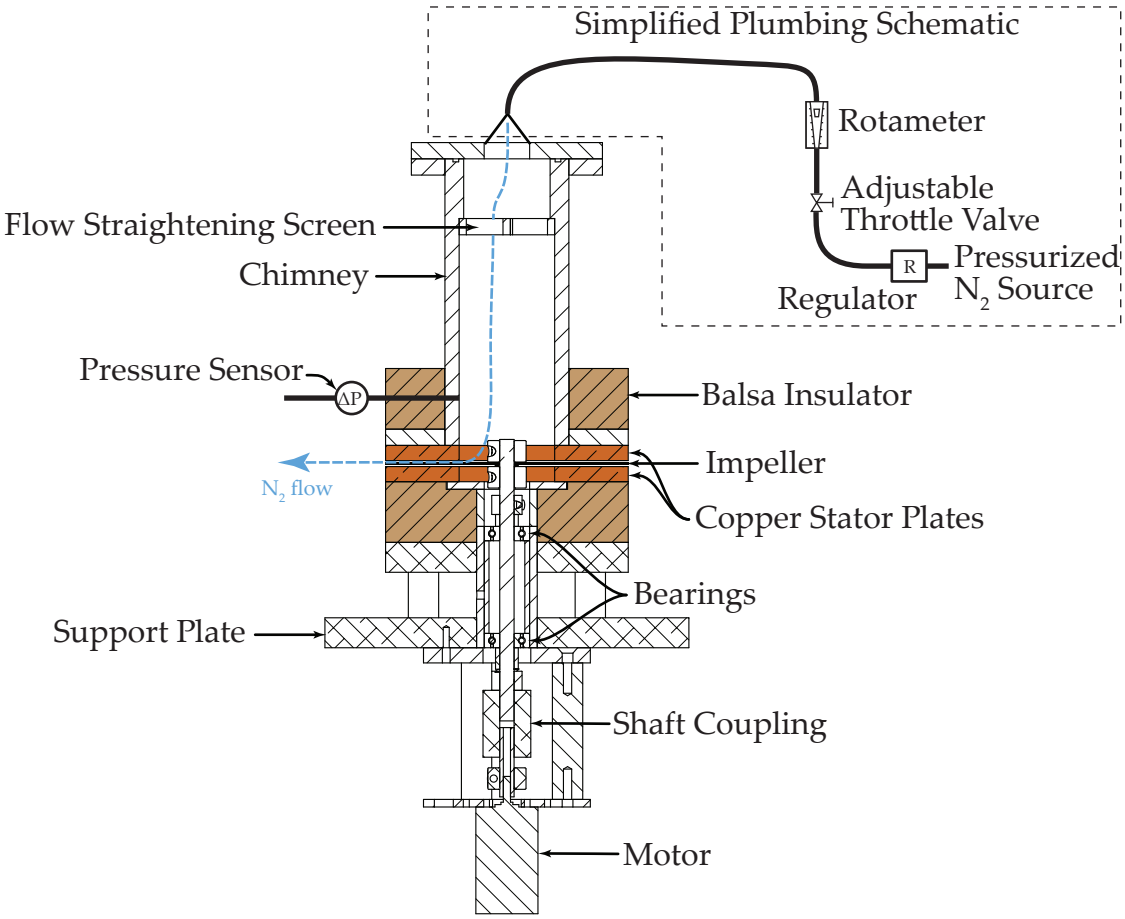

Figure 2-1: In the square stator apparatus, nitrogen from a pressurized source flowed into the fan section where it was discharged radially by the impeller. The pressure rise from the eye region to the ambient was measured, as was the volume flow through the system. The apparatus also had heated copper stator plates that were used to measure the heat transfer coefficient of the air flow in the stator gap.

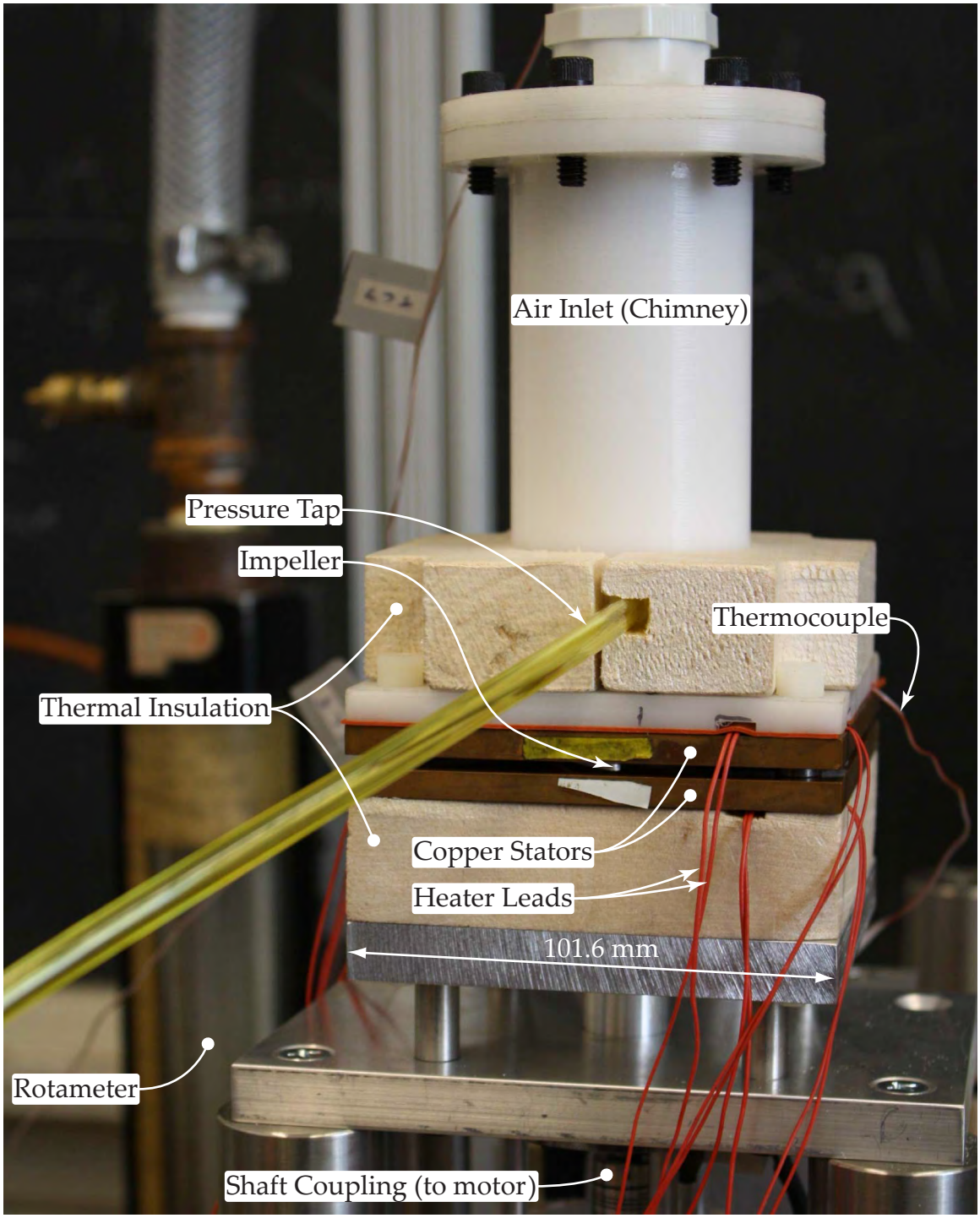

Figure 2-2: The square stator apparatus was used for fan characterization and heat transfer characterization. The thermal insulation, made of balsa wood, minimized the heat loss from copper plates.

related; by using all three sensors simultaneously, low absolute uncertainty was achieved in the narrower ranges, while still maintaining the capability of measuring the widest range. Also, error checking was performed in any overlapping range by comparing the readings from multiple sensors.

A calibration test was performed to ensure that the sensors were functioning properly. In this test, a 2 L plastic bottle was modified to have two ports in the cap. The first port went to the three pressure sensors while the second port went to a syringe. By displacing the plunger of the syringe, the volume of the container changed, thereby changing the pressure. The output of the three sensors was recorded, and the calibration curves shown in Fig. 2-3 were generated. The markers indicate the measured voltage associated with each sensor, and the "true" pressure reading, taken to be the pressure calculated from pressure sensor 2[2]. The dashed lines are the manufacturer-provided calibration curves associated with each sensor and the shaded regions are the nominal uncertainty bounds indicated in Table 2.1, also from the manufacturer's datasheets. The excellent agreement between the data points and their respective calibration curves indicated that PS1 and PS3 were in good agreement with PS2.

The calibration curves represented a linear relationship between the differential pressure reading and the measured voltage from the sensor:

$$\Delta P_i = G_i V_i + O_i, \tag{2.1}$$

where G_i is the gain and O_i is the offset for sensor i. The values of G_i and O_i and the nominal uncertainty for each sensor are given in Table 2.1. In practice, the signals from the pressure sensors were measured in many samples for each operating point and the mean value was taken to be the actual pressure. A less conservative but practical estimate of the uncertainty in the pressure measurement was determined from the standard deviation of these samples[3]:

$$\delta\Delta P_i = \text{stdev}(\Delta P_i) \tag{2.2}$$

Equation 2.2 provides an experimental estimate of the uncertainty; this is more an indicator of the sensor's precision rather than its overall accuracy, because it inherently discards long term variation in the measured signal. The uncertainty from the manufacturer's datasheet includes long term effects, and is generally much higher than the estimate from Eq. 2.2. As a side note, the standard deviation operator in this work is defined as (see, e.g.,

Table 2.1: Pressure Sensors in the Square Stator Apparatus

Label	PS1	PS2	PS3
Manufacturer	Honeywell	All Sensors	Honeywell
Model Number	DC002NDC4	1 INCH-D-4V	ASDXL05D44D
Range (Pa)	± 498	± 249	± 1245
Nominal Uncertainty	1.5% FS (15 Pa)	0.25% FS (1.3 Pa)	2.5% FS (62 Pa)
Gain G_i (Pa/V)	249.1	124.5	622.7
Offset O_i (Pa)	-560.5	-280.2	-1557

[2]Pressure sensor 2 was used as the true measurement because it had the lowest nominal uncertainty. PS2 was also calibrated by the manufacturer.

[3]The lowercase delta (δ) preceding a symbol means "uncertainty in" throughout this work.

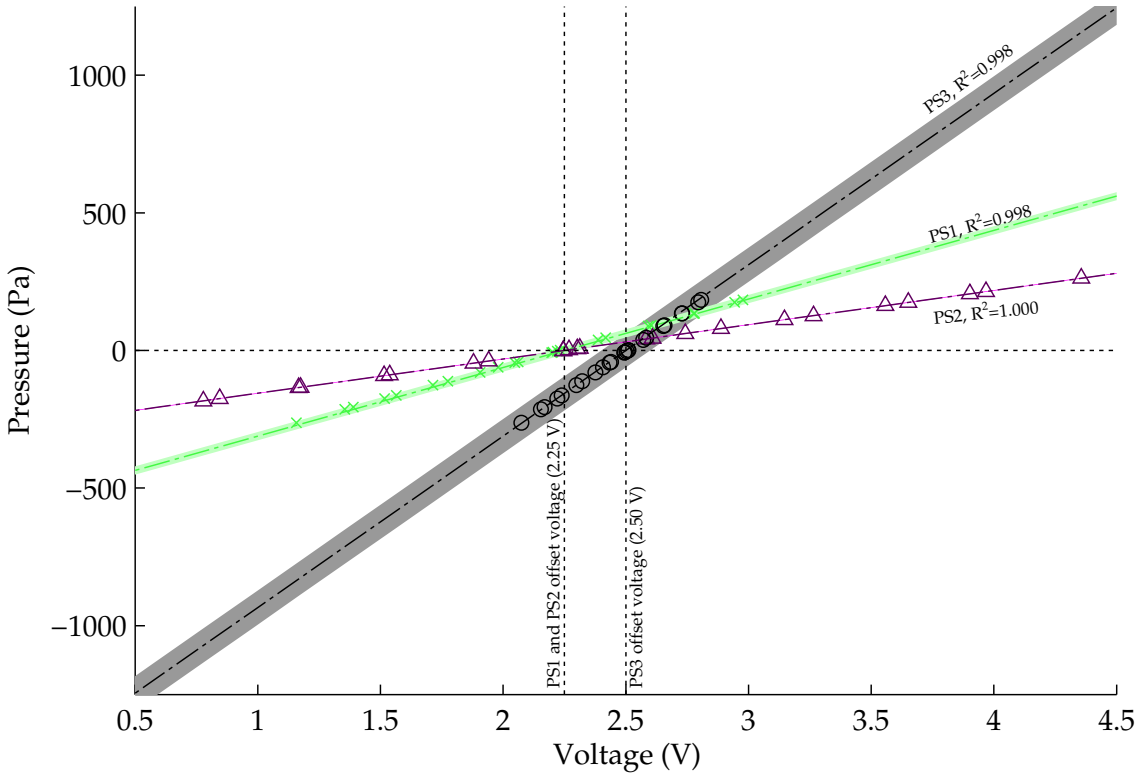

Figure 2-3: The pressure sensors were attached to a common reservoir whose pressure was varied. The data markers show the pressure of the reservoir (as measured by sensor 2) as a function of the voltage output of each sensor. The lines represent the manufacturer-provided calibration curves; the shaded regions surrounding each line represents the uncertainty bounds according to the manufacturer-specified uncertainty. The high R^2 values indicate good agreement between the pressure sensors in the range measurable by sensor 2.

Bevington [69]):

$$\text{stdev}(x) = \left(\frac{1}{n-1} \sum_{i=1}^{n} (x_i - \overline{x})^2 \right)^{\frac{1}{2}}, \tag{2.3}$$

where x is a sample, n is the number of elements in x, and $\overline{x}$ is the (arithmetic) sample mean.

Motor Control and Power Measurement

The impeller's rotation was driven by a DC motor (Maxon 339152). An integrated 500-count encoder (Maxon 225778) provided the speed measurement, and a controller (Maxon 390003) held the speed constant irrespective of the load torque on the impeller. The motor controller also provided a measurement of the electric current going to the motor. Both the control and measurement signals were exchanged via a USB connection to the data acquisition computer.

The motor controller was capable of driving either a brushless DC or a brushed DC motor. In these experiments, a brushed DC motor was used. The motor controller was powered by a 24 V supply, giving the motor the ability to run at speeds up to about 9500

rpm. The controller used the feedback signal from the encoder on the motor to perform closed loop speed control. Speed commands were issued to the motor controller from LabVIEW to bring the impeller to the desired operating point; actual speed and motor current measurements from the motor controller were sent as inputs to LabVIEW to determine the shaft power.

The motor's torque output (M) was related to the electric current (I) by the torque constant K_T of the motor:

$$M = K_\mathrm{T} I \tag{2.4}$$

For the motor in this work, $K_\mathrm{T} = 20.8\,\mathrm{mNm/A}$ according to the manufacturer's datasheet. The measured motor power was calculated as the product of the torque and the rotational speed:

$$\dot{W}_\mathrm{meas} = M\omega \tag{2.5}$$

The measured motor power included losses associated with the motor and bearings. These losses are independent of the fan performance, and must be subtracted from the measured power to determine the mechanical power consumption associated with the fan. The procedure used to account for these losses is discussed in Section 2.1.2.

The uncertainties associated with the speed and torque measurements were estimated by taking the standard deviation of the samples comprising the mean measurement:

$$\delta\omega = \mathrm{stdev}(\omega) \tag{2.6}$$

$$\delta M = \mathrm{stdev}(M) \tag{2.7}$$

Volume Flow Measurement

A rotameter (Fischer & Porter 10A3565A housing, FR1-35-G-10/83 tube) was used to measure the volume flow rate through the system. The rotameter reads in a scale with integer increments from 0–100. The manufacturer's datasheet specifies ranges in the volume flow that depend on which interchangeable float is used in the rotameter. Two floats were used in this work (Fischer & Porter 1-GUSVT-611 and 1-GNSVGT-68); their ranges, for the standard reference gas of air at 21 °C and 101.3 kPa, were (respectively) 3.23×10^{-3} m^3/s (6.9 cfm) and 17.5×10^{-3} m^3/s (37 cfm). The rotameter had a linear output, so the calibration curve took a form reminiscent of the pressure sensor curves but with no offset:

$$\dot{V}_\mathrm{raw} = G_{\mathrm{r},i} \cdot \mathrm{rot}, \tag{2.8}$$

where $\dot{V}_\mathrm{raw}$ is the raw volume flow reading, rot is the 0–100 value read from the rotameter scale and $G_{\mathrm{r},i}$ is the gain associated with float i. The volume flow reading is termed "raw" because of the inherent assumption that the measured conditions are identical to the rotameter's calibration conditions. A correction factor is introduced to account for the difference in density between the measured fluid and the fluid with which the rotameter was calibrated. In a given rotameter, the volume flow depends on the annular area between the float and the wall (A_fw); a constant (c) dependent on the geometry, gravity, and the float density; and the fluid density (ρ) [70]:

$$\dot{V} = \frac{cA_\mathrm{fw}}{\sqrt{\rho}}. \tag{2.9}$$

At the same reading on the rotameter scale, cA_{fw} is constant, meaning that $\dot{V}\sqrt{\rho}$ is also constant for a given reading. Knowing this, the corrected volume flow ($\dot{V}$) is related to the raw volume flow calculated in 2.8 as

$$\dot{V} = \dot{V}_{\mathrm{raw}}\sqrt{\frac{\rho_{\mathrm{cal}}}{\rho_{\mathrm{in}}}}, \tag{2.10}$$

where ρ_{cal} is the calibration density associated with the rotameter and ρ_{in} is the density of the fluid passing through the rotameter during the test. The density ρ_{in} was calculated using the measured inlet temperature and the ideal gas law. In this work, the correction was quite small since the (1) pressure of the nitrogen passing through the rotameter was nearly atmospheric (the fans only lower the pressure in the chimney by about 1 kPa at most), (2) the difference between the ambient temperature and the standard temperature was typically less than 10 K (3% of the absolute temperature), and (3) nitrogen has a density very close to that of air.

Temperature Measurement

Type-J thermocouples (Omega 5TC-TT-J-30-36) were used to measure temperatures in various parts of the system. A thermocouple input board (National Instruments 9213 in a cDAQ-9172 chassis) with built in cold junction compensation amplified and measured the voltages from the thermocouples and converted these voltages to temperatures. The uncertainty associated with the thermocouples was stated to be 1.1 K based on the manufacturer's datasheet, but in practice the uncertainty was lower. In an ice bath test with five thermocouples, none of the thermocouples deviated by more than 0.05 K from the correct ice point. Excellent agreement was also observed with a silicon diode thermometer (LakeShore DT-470) at room temperature, whose accuracy was 32 mK. Thus, the thermocouple uncertainty in this work was estimated to be ±0.05 K.

Heater Control

Each copper plate was heated by four polyimide film heaters (Omega KHLV-102/(10)-P) wired in parallel, with an overall equivalent resistance of 10.2 Ω. To best mimic the surface of a condenser, a constant temperature boundary condition on each plate was desired. The temperature of each copper plate was measured as the average temperature of two thermocouples situated in small holes drilled into the sides of the copper plates. The LabVIEW data collection program implemented PID control of the heaters to maintain the copper plate temperature at a constant value.

The control output from the data acquisition system determined how much power was delivered to each heater. This control signal ranged from 0–5 V. An amplifier circuit, shown in Fig. 2-4 and Fig. 2-5, used a non-inverting power operational amplifier circuit to apply a gain to this control signal. The resultant signal, boosted from 0–5 V at low current to 0–40 V at high current, drove the heaters.

The voltage applied to each heater was measured during operation by using a resistive voltage divider to reduce the 0–40 V signal down to the 0–10 V range of the analog input board. The actual voltage was related to the measured voltage in this voltage divider by a simple linear fit,

$$V_{\mathrm{out},i} = G_{\mathrm{v},i}V_{\mathrm{meas},i} + O_{\mathrm{v},i}, \tag{2.11}$$

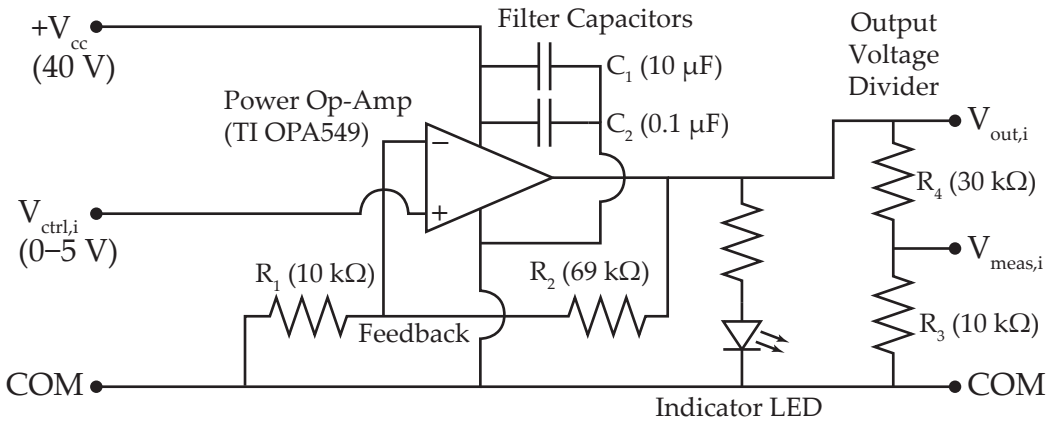

Figure 2-4: A power op-amp boosted the 0–5 V signal from the data acquisition system to a 0–40 V signal at the current levels required by the heaters (the gain in this non-inverting op-amp circuit is given by $V_{out} = V_{ctrl}(1 + R_2/R_1)$ — about 8). A voltage divider on the output allowed the analog input board to measure the voltage applied to the heaters by reducing the signal into the board's 0–10 V range. An indicator LED provided a visual indication of when the heaters were powered. For clarity only one channel from the two channel amplifier is shown.

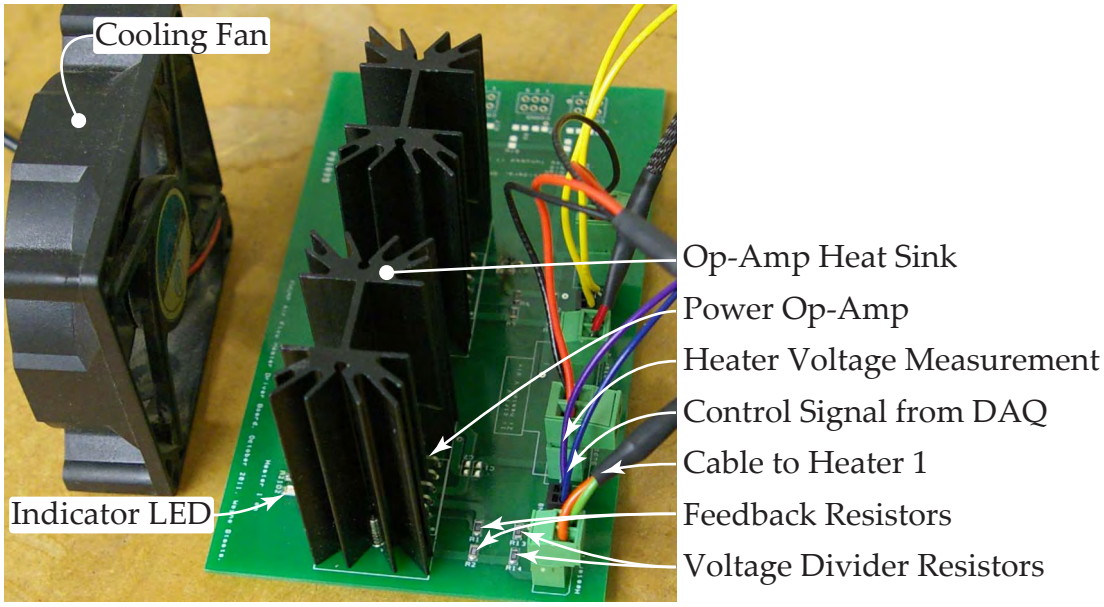

Figure 2-5: A printed circuit board of the schematic in Fig. 2-4 amplified the control signal from the data acquisition system and provided voltage measurements (proportional to the heater voltages) to the data acquisition system.

where V_{out} is the voltage applied to the plate, V_{meas} is the voltage measured by the data acquisition system, G_v and O_v are the gain and offset of the voltage divider and the subscript i refers to either plate 1 or 2, corresponding to the upper and lower plate respectively. The calibration curves for the voltage dividers dividers were measured by applying a voltage from a power supply across the V_{out} terminal and COM. V_{meas} was read using the data acquisition system, for several applied voltages, and a linear fit was applied to the data. The estimated uncertainty in V_{out} was taken to be the standard deviation of the error between (1) the applied voltage from the power supply and (2) the voltage calculated using the calibration constants and the voltage divider output (V_{meas}). The calibration constants obtained using this method, and the expected uncertainty are shown in shown in Table 2.2.

The electrical power delivered to plate i is dissipated in the heaters and manifests itself as thermal input power ($\dot{Q}_{in,i}$):

$$\dot{Q}_{in,i} = V_{out,i}^2 / R_i, \tag{2.12}$$

where R_i is the resistance of the heater on plate i, at the operating temperature.

The uncertainty of the thermal input power arises from both the applied voltage and the resistance of the plate. The resistance was measured using a digital multimeter with a four wire resistance measurement and is estimated to have an uncertainty of

$$\delta R_i = 0.01\Omega \tag{2.13}$$

The uncertainty in the applied voltage arises from the uncertainties in the voltage divider and in the data acquisition hardware that reads V_{meas}. By virtue of the calibration method described above, both of these uncertainties are included in the $\delta V_{out,i}$ values specified in Table 2.2.

The uncertainty in thermal power due to uncertainty in applied voltage and resistance is calculated, assuming the uncertainties are independent, as

$$\delta\dot{Q}_{in,i} = \sqrt{\left(\frac{\partial \dot{Q}_{in,i}}{\partial V_i}\delta V_i\right)^2 + \left(\frac{\partial \dot{Q}_{in,i}}{\partial R_i}\delta R_i\right)^2}, \tag{2.14}$$

which simplifies to

$$\delta\dot{Q}_{in,i} = \sqrt{\left(\frac{2V_i}{R_i}\delta V_i\right)^2 + \left(\frac{V_i^2}{R_i^2}\delta R_i\right)^2}. \tag{2.15}$$

2.1.2 Fan Characterization

Fan curves were measured by setting the volume flow of nitrogen through the system (read by the rotameter) and measuring the resultant pressure rise from the chimney tap to ambient (measured by the pressure sensors) at a variety of rotational speeds (set and

Table 2.2: Heater Voltage Divider Characteristics

	Upper Stator ($i = 1$)	Lower Stator ($i = 2$)
Gain $G_{v,i}$ (-)	3.960	3.950
Offset $O_{v,i}$ (V)	0.023	-0.063
Uncertainty $\delta V_{out,i}$ (V)	± 0.055	± 0.047

measured by the motor controller). Each fan was characterized at 1 krpm increments from 0 to 9 krpm. By this method, fan curves at a multitude of rotational speeds were measured. Since the supply was pressurized, it was possible to measure operating points where the inlet pressure was higher than the outlet pressure; these points do not have a practical motivation in heat sink applications, so they were not analyzed. However, the setup's ability to measure the true free delivery point distinguishes it from many comparable flow bench setups that only use the fan being tested to motivate flow through the system.

Experimental Procedure

The following procedure was used to characterize the fan performance (i.e. the pressure rise and the mechanical power required vs. volume flow):

1. The system was run at 8 krpm for several minutes to allow the bearings to warm up.
2. A bearing loss test was performed (with no impeller installed on the shaft) by running the system at several rotational speeds and measuring the power input from the motor. This step was performed periodically to ensure that the losses did not drift over time, but not necessarily prior to each fan characterization. The details of the bearing loss characterization are discussed in Section 2.1.2.
3. The impeller to be characterized was installed on the shaft. The upper plate and chimney were removed to expose the shaft. The impeller was placed onto the shaft; the spacing above the lower plate was determined with by placing precision shims on a shaft collar at the same axial position as the lower stator surface. A second shaft collar with a compliant washer secured the impeller in place above the precision shims.
4. The fan curve test was performed. A series of volume flows were imposed on the system; at each volume flow, a series of rotational speeds were set. This double-nested loop scheme produced a series of fan curves (ΔP vs. $\dot{V}$) for the various rotational speeds tested. This procedure was as follows:
   (a) The valve upstream of the rotameter, which determined the flow rate through the system, was set to produce the desired flow rate. The rotameter reading was recorded.
   (b) The motor was set to a series of rotational speeds. At each speed, after a 4 second settling period, 11 seconds of data were recorded at a sampling rate of 20 Hz. The motor controller data (i.e. rotational speed and motor current) was taken at a different sampling rate; the motor controller yielded 100 samples over the collection period. These data were subsequently averaged to produce one data point per operating point.
   (c) The valve was adjusted to the next operating point, and the previous steps were repeated until the conclusion of the test.

The raw data (i.e. voltages from each pressure sensor, reading from the rotameter scale, speed and current from the motor controller) was processed for each operating point according to the calibrations described above. Additionally, to determine the mechanical power consumption associated with each fan, a correction was necessary to remove the parasitic power draw associated with the inefficiencies of the motor and bearings.

Bearing Power Loss

The shaft in the square stator apparatus was supported by a pair of self aligning, double row ball bearings (SKF 126TN9), oiled with spindle oil designed for use in high speed spindle bearings, as would be found in a milling machine. Originally, the bearings were packed with grease; to reduce the bearing friction, the grease was removed using a penetrating oil (WD-40), and was replaced with the lighter spindle oil. The bearings consume some power that must be subtracted from the motor output power to determine the shaft power input to the impeller. These losses were characterized as follows. The system was run at 8 krpm with no impeller for five minutes to warm up the bearings. Next, the power dissipated in the bearings was determined by running the motor, with no impeller attached to the shaft, at various speeds and measuring the motor power output. Each operating point consisted of 11 seconds worth of data which produced 100 samples from the motor controller. Speeds between 0 and 9 krpm were characterized at 1 krpm increments. The speeds were taken in the following order to make hysteresis evident in post processing: $\omega = [0, 2, 4, 6, 8, 9, 7, 5, 3, 1]$ krpm. The bearing power ($\dot{W}_{\text{brg}}$) was observed to vary quadratically with the rotational speed, suggesting that viscous friction is the dominant loss mechanism in the bearings:

$$\dot{W}_{\text{brg}} \propto \omega^2 \tag{2.16}$$

$\dot{W}_{\text{brg}}$ also includes other losses such as windage on the shaft.

Some representative experimental data is shown in Fig. 2-6.

The power required to rotate the shaft was plotted as a function of the rotational speed and a parabolic fit forced through the origin was applied:

$$\dot{W}_{\text{brg}} = K_{\text{b},1}\omega^2 + K_{\text{b},2}\omega. \tag{2.17}$$

Figure 2-6 shows the bearing losses and the parabolic fits. Although the points shown in Fig. 2-6 comprise a span of several months, the bearing losses remained reasonably consistent.Using this fit, the shaft power ($\dot{W}$) was calculated by subtracting the bearing power loss from the measured motor power

$$\dot{W} = \dot{W}_{\text{meas}} - \dot{W}_{\text{brg}}. \tag{2.18}$$

2.1.3 Heat Transfer Characterization Procedure

For some of the fans, the heat transfer from the stators to the air was characterized. This process consisted of heating the stator plates and performing a modified fan characterization test in which the thermal energy transferred to the air from the heated stators was measured.

To perform this characterization, the parallel stator plates were made of copper; the surfaces opposite the airflow were heated with polyimide film insulated heaters (Omega KHLV-102/(10)-P). Each plate housed two type-J thermocouples embedded in separate wells. Insulation minimized the heat loss on the outside of the film heaters. A custom-built linear amplifier circuit drove the heaters for each plate independently. The temperature of the plates was chosen, and a PID control system varied and recorded the power required to maintain the set temperature. Thermocouples also measured the inlet nitrogen temperature and the ambient temperature.

A data acquisition system (National Instruments cDAQ-9172 with 9213, 9201, 9263

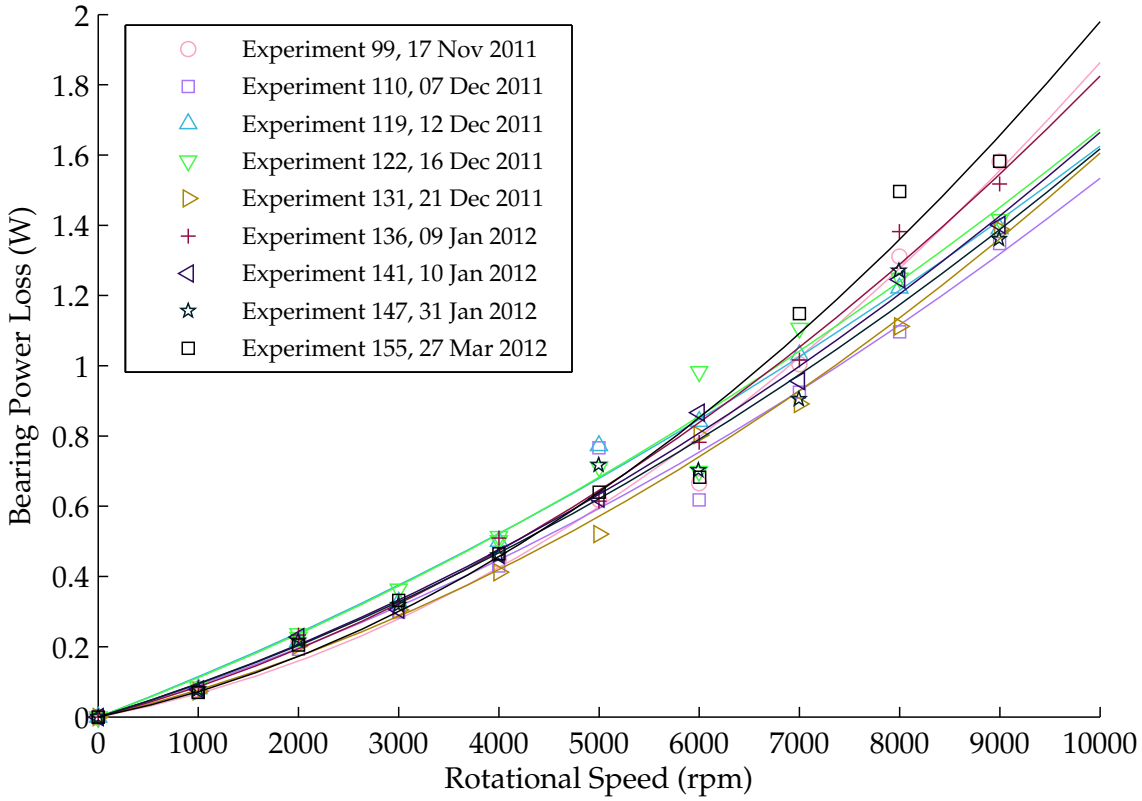

Figure 2-6: The power consumed in the bearings varied quadratically with the rotational speed. The bearing losses were measured periodically to account for variations in the bearing power loss over time. Markers indicate experimental data; lines are parabolic fits to the data set of the same color.

modules) collected the data from the thermocouples, pressure sensors, motor controller and heater driver. A LABVIEW program directed the data collection, issued commands to the motor controller, and performed the PID heater control.

In the operation of the PHUMP, the condensers are expected to operate at 80 °C . Accordingly, the temperature of the copper plates in this work was set to 80 °C . The resistance R_h of the film heaters (4 per plate in parallel) was measured at 80 °C . The voltage V applied to the heaters was measured, and the thermal power delivered to each plate was calculated as

$$\dot{Q} = \frac{V^2}{R_h} - \dot{Q}_{loss} \tag{2.19}$$

The heat loss ($\dot{Q}_{loss}$) occurs due to several mechanisms. Heat leaks from the heaters to the ambient through the insulation on the outer surface of the copper plates, and also due to natural convection from the edges. Most of the heat loss occurs through the insulation; this loss was determined experimentally by running the system with no nitrogen flow and no rotation of the impeller. At this operating point, the heat transfer from the plates to the air in the gap is minimized and most of the heat input to each plate goes through the insulation and the edges. Since the plates were held at constant temperature throughout the test, it was reasonable to expect that this heat loss was constant for all of the operating points.

Each geometry tested underwent the following procedure. The copper plates were brought to 80 °C and the system was allowed to come to thermal equilibrium. With no flow through the system, five rotational speeds were characterized: 0, 3, 5, 7 and 9 krpm. Five minutes of data was collected at each of these operating points; sufficient time (5 minutes[4]) was allowed prior to data collection at each point to ensure the system reached steady state. Next, the valve was opened to set the flow rate to 20 on the rotameter scale, and the same series of rotational speeds were tested at this flow rate. Five flow rates, equally spaced between 0 and 100 on the rotameter scale, were included in the characterization.

2.2 Circular Stator Apparatus

An apparatus was constructed to characterize the fundamental, generalized form of the fully unshrouded integrated fan, which consisted of the impeller and two annular stator plates. This apparatus has several notable differences compared to the square stator apparatus. First, the circular stator apparatus directly measures the total-to-static pressure difference, because the pressure tap upstream of the fan is located in an area where the cross sectional area is large enough to make the flow's dynamic pressure negligible. Second, the mass flow measurement is electronically measured using an hot wire anemometer-based flow meter; this method is more accurate and informative than the rotameter. Third, in the circular stator apparatus, the fan being characterized is the only force moving air through the apparatus, and thus flows at or beyond the free delivery flow rate cannot be characterized. To characterize the fan curve in restricted flow regions, a throttle valve upstream of the fan restricted the flow in the system, effectively providing a higher system resistance for the fan to work against. In this way, the fan's operation closely resembled the actual operating conditions that one would expect in a real flow system.

The circular stator apparatus was designed with a modular test section that could perform three types of tests, described in further detail below (Section 2.2.1). These tests were: fan characterization (Section 2.2.2), heat transfer characterization (Section 2.2.3), and local heat transfer characterization (Section 2.2.4).

2.2.1 Description of Apparatus

A schematic of the circular stator apparatus can be seen in Fig. 2-7; a 3-D model can be seen in Fig. 2-8. Air flow entered the system at the top, passed through the air filter (K&N R-1050) and then through the mass flow sensor. The air flow then passed through a modified automotive throttle body (a butterfly valve). After the throttle, the air entered a cylindrical plenum whose entry contained a baffle plate to minimize jetting of the air flow from the throttle valve; a thermocouple situated near the baffle plate measured the temperature of the inlet air. A screen just downstream of the baffle plate served to smooth out small variations in the flow. A pressure tap in the plenum wall was located downstream of the screen. The motor that drove the fan was also situated within the plenum. Finally, the air entered the parallel plate gap in which the fan rotated, and was discharged to the ambient pressure surroundings. A static pressure tap was situated at the outlet of the parallel plate gap.

The details of each portion of the experimental apparatus are discussed below.

[4]During initial experiments, the system took about 2-3 minutes to reach steady state. The waiting period was set to 5 minutes to minimize the potential for premature data collection.

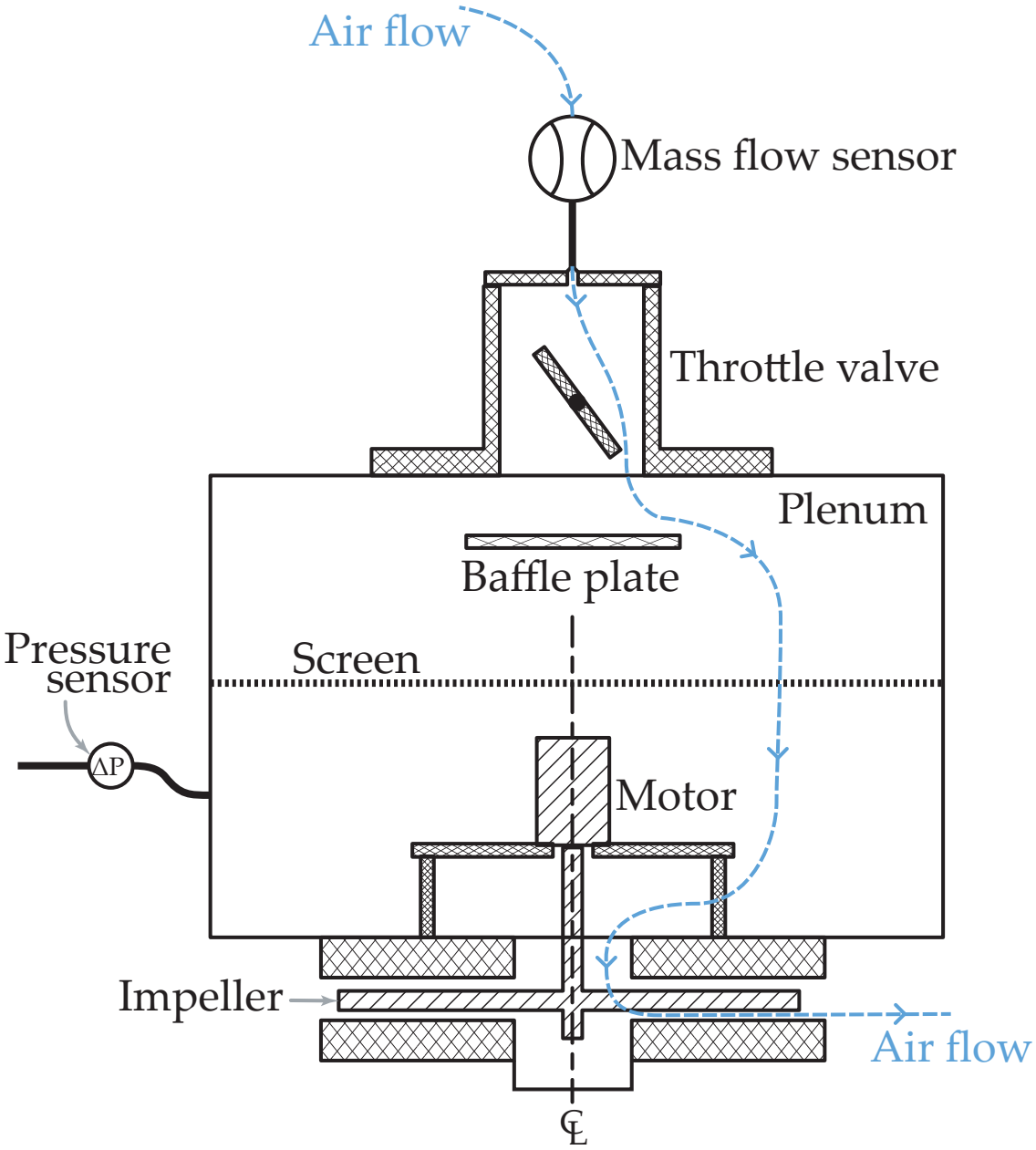

Figure 2-7: The circular stator apparatus. The pressure upstream of the fan was measured in the plenum, where the dynamic pressure is very small. The bottom of the parallel plate gap was blocked so that all of the fan's air flow entered through the mass flow sensor.

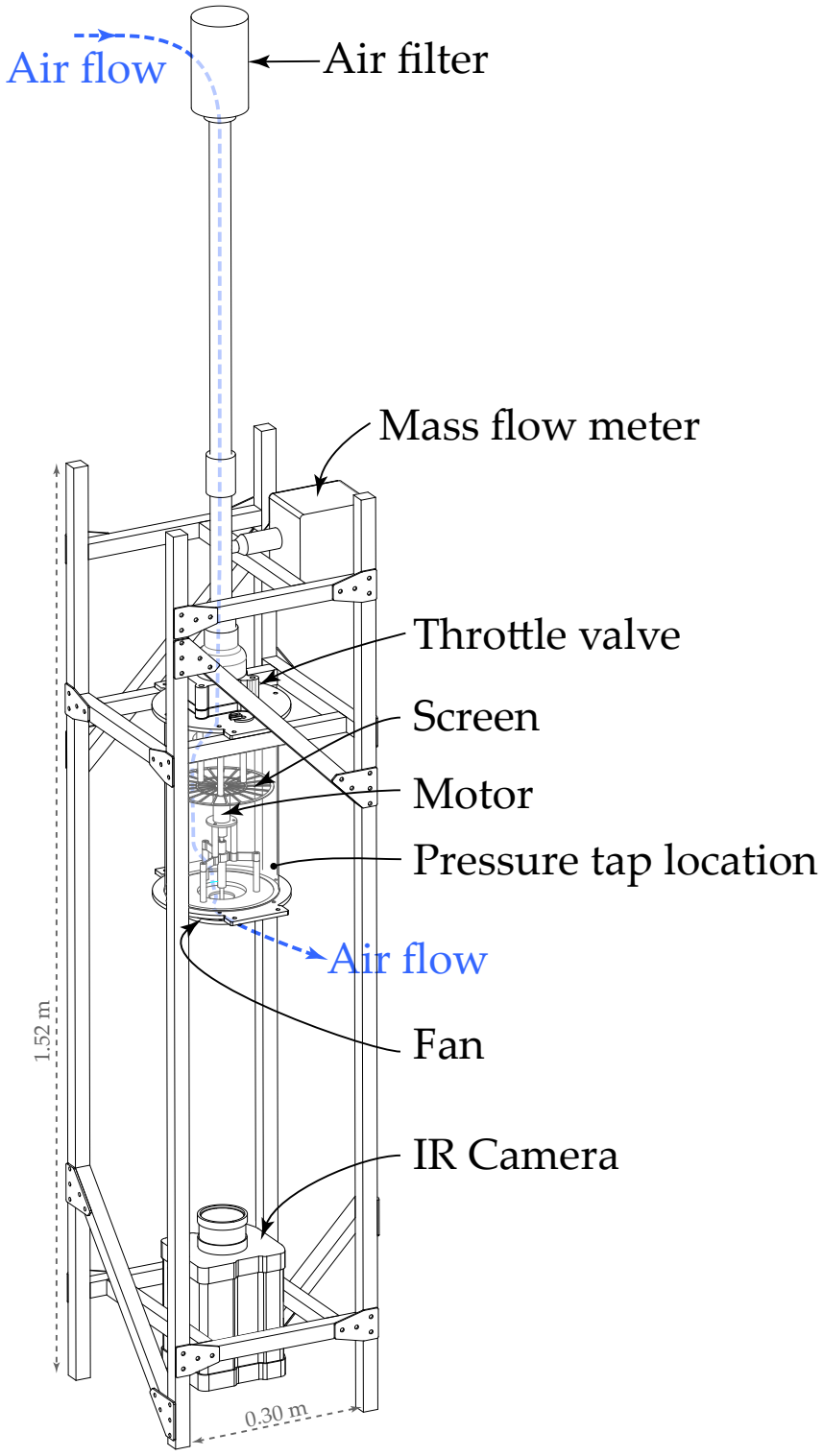

Figure 2-8: A 3-D model of the circular stator apparatus. Air flow entered the top of the apparatus and flowed through the mass flow meter, throttle valve, plenum, and finally into the fan inlet. The fan discharged the air to the ambient surroundings. An IR camera was used for the local heat transfer coefficient tests described in Section 2.2.4.

Data Acquisition Hardware

Several pieces of hardware were used to communicate between the experiment and the computer. A multifunction DAQ board (Measurement Computing USB-2537) with 32 differential 16-bit analog inputs read the voltage signals from the various sensors in the experiment. Two 16-bit, 16-channel analog output boards (Measurement Computing USB-3106) allowed the computer to control various aspects of the experiment (e.g. the throttle position and the power signals for the heated plates). A thermocouple input board (NI 9213 module in a NI cDAQ-9172 chassis) was used to read temperature signals from the system.

Mass Flow Meter

The mass flow meter was a hot-wire anemometer type meter (Eldridge Products, Inc. Master-Touch 8689MPNH-SSS-133). The mass flow meter contained circuitry that linearized the output to a 0–5 V signal that was read by the analog input board. The range of the mass flow meter was configurable, and was set to 11.3 g/s for most of the experiments. The measurement uncertainty was estimated to be 1% of the reading plus 0.5% of the full scale based on the manufacturer-provided instruction manual.

Throttle Valve

After exiting the mass flow meter, the air passed through a butterfly valve modified to be driven by a servo (Turnigy MG90S) so that its position could be controlled from the data acquisition computer. The data acquisition computer sent a signal to the analog output board, commanding a voltage ranging from 0–5 V. An Arduino microcontroller [71] was used to remap the 0–5 V signal to the appropriate servo language commands that would result in a throttle angle ranging from 0 (fully closed) to 90 (wide open) degrees. The Arduino maintained the servo at the commanded throttle angle until a different command was sent by the analog output board; this arrangement required very little of the DAQ computer's resources during a test. For convenience, the throttle position was referred to as a number ranging from 0 (fully closed) to 1 (wide open), whose values map linearly to the throttle angle.

The throttle and servo can be seen in Fig. 2-9. The throttle was mounted to the plenum with four screws. A laser cut steel spacer plate (the throttle mount) separated the throttle slightly from the top of the plenum and provided a mounting point for the servo bracket. To minimize leakage into the plenum, silicone gaskets were cut to fit the interfaces between the throttle, the throttle mount, and the top of the plenum. A silicone reducing boot fit over the barbed upper lip of the throttle valve, forming an air tight seal to the plumbing on the mass flow meter.

Plenum

The plenum consisted of a polycarbonate cylinder sandwiched between two laser cut aluminum plates, clamped together with threaded rod. Silicone gaskets between the aluminum and polycarbonate formed an air tight seal. The upper aluminum plate had a hole equal in diameter to the inner diameter of the throttle mount; a silicone gasket also ensured minimal leakage at the interface to the throttle. Two slotted poly(methyl methacrylate) (PMMA) discs and some silicone RTV sealant were used to pass wires (for the motor

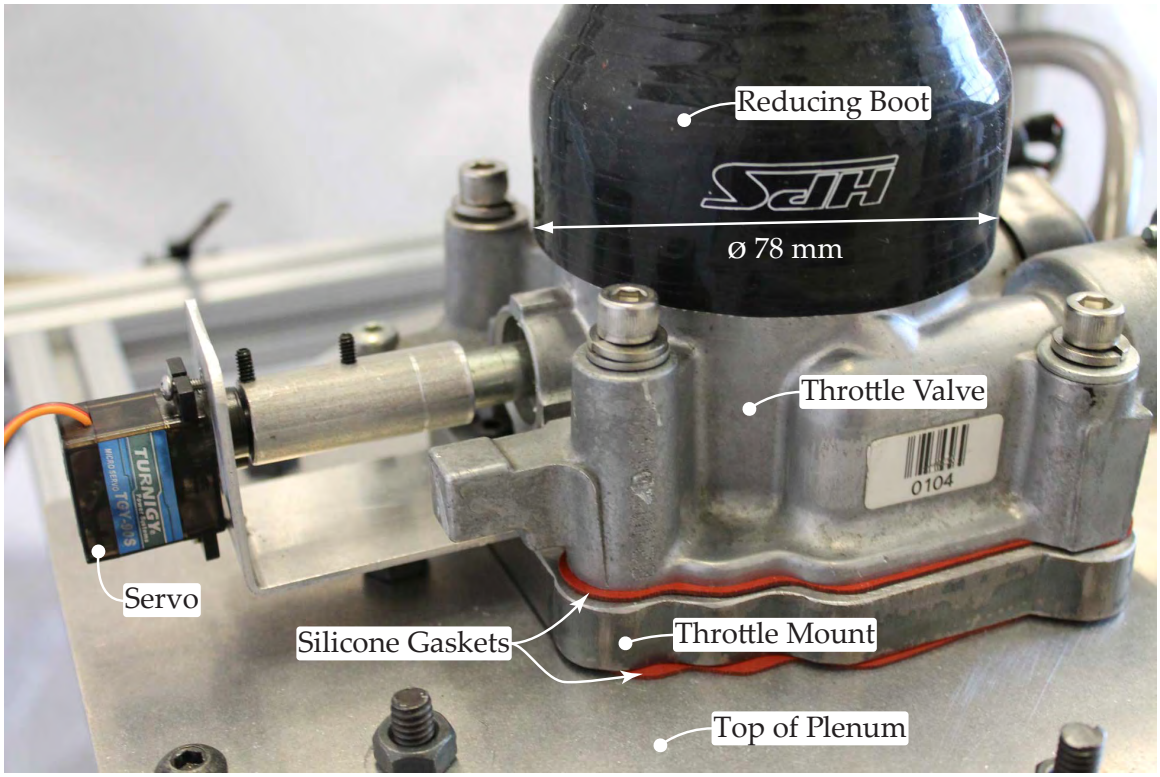

Figure 2-9: An automotive butterfly throttle valve was modified to be driven by a servo, so the valve could be actuated by the data acquisition computer.

power, motor encoder, and inlet temperature thermocouple) from the outside to the inside of the plenum while maintaining an air tight seal, as shown in Fig. 2-10.

A three-spoked, raised structure was mounted to the inside face of the plenum's bottom aluminum plate. The motor, bearing assembly, and shaft onto which the fans mounted were supported by this structure. The motor's output shaft connected to a helical beam coupling and a 6 mm diameter precision drive shaft. Two 6 mm ID / 10 mm OD radial ball bearings mounted in a 12.7 mm OD machined aluminum tube supported the shaft. By mounting the motor inside the plenum, the stator plates and the impeller could be changed without disturbing the motor or bearings.

To ensure perpendicularity between the impeller shaft and the outer bottom face of the plenum, a dial test indicator was mounted on the shaft. The probe of the indicator was placed against the bottom face of the aluminum plate and the shaft was rotated. The tri-spoked motor mount plate was shimmed until the shaft could rotate without the dial test indicator moving, indicating perpendicularity. This procedure was very similar to tramming a milling machine [72]. Once the shaft was perpendicular to the bottom plenum face, the upper stator face was automatically perpendicular to the shaft as well, as long as the upper stator face could be installed parallel to the plenum face. This was a simple matter of checking the flatness of the modular stator pieces that attached to the plenum face.

The motor mount served to raise the motor far enough away from the fan's inlet that minimal air blockage occurred. A brief CFD showed that indeed, the blockage associated with the motor and motor mount supports was negligible. The three motor mount stand-

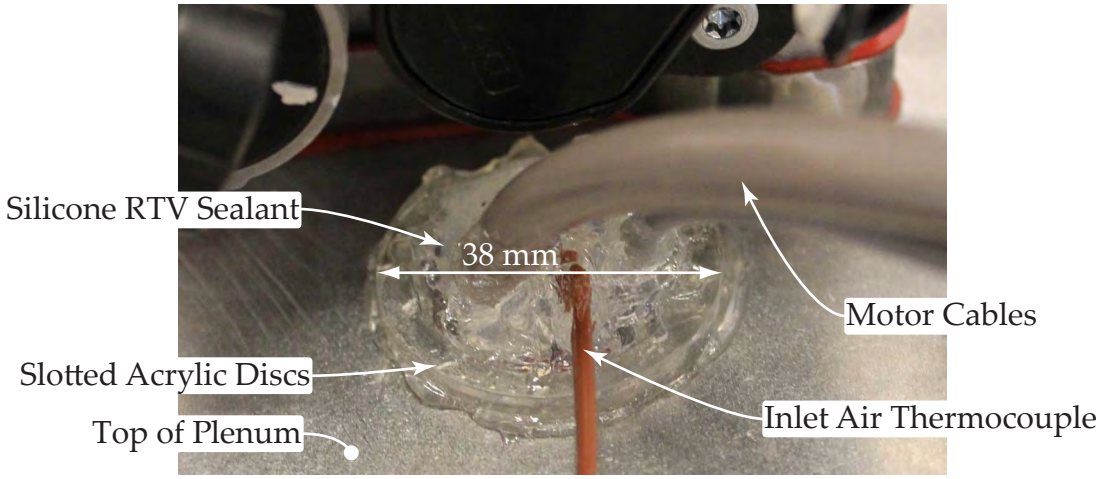

Figure 2-10: Two slotted PMMA discs and some silicone RTV sealant were used to pass the motor cables and the inlet air thermocouple into the plenum.

offs were also placed far enough from the inlet that their effect on the inlet flow was very small.

Pressure Sensors

The pressure sensors used in the circular stator apparatus were identical models to PS1 and PS3 in the square stator apparatus above. To avoid confusion, the sensors in the circular stator apparatus will be referred to as PS4 and PS5. The 5V excitation for each sensor was provided using a precision voltage reference IC attached to a small custom PCB. This precision reference ensured a very consistent excitation voltage for the sensors while allowing a flexible power supply voltage. PS4 and PS5 can be seen in Fig. 2-11.

PS4 had a lower range (±500 Pa) than PS5 (±1250 Pa). It was observed that at zero flow and no rotation of the impeller, PS4 was reading -10 Pa. Therefore, the offset in the calibration curve of PS4 was increased by 10 Pa to zero the reading of PS4. With this adjusted calibration curve, the readings of PS4 and PS5 were compared in several fan curve tests. Indeed, the readings were consistent and differed by less than 20 Pa for the entirety of PS4's range. Since the uncertainty of PS5 is greater than this difference, the sensors can be said to have satisfactory agreement.

The pressure tap in the plenum measured the static pressure, but since the velocity in the vicinity of the pressure tap was negligible, the pressure reading was essentially equal to the total pressure. The inner diameter of the plenum was 164 mm. If the baffle plate and screen make the velocity profile uniform, then the dynamic pressure in the plenum is

$$P_{\text{dyn}} = \frac{1}{2}\rho\left(\frac{\dot{V}}{A_{\text{c}}}\right)^2, \tag{2.20}$$

where A_{c} is the plenum's cross sectional area. For a volume flow rate ($\dot{V}$) of $9.6\times10^{-3}\text{m}^3/\text{s}$ (corresponding to the maximum range of the mass flow meter), the dynamic pressure in the plenum can be calculated to be about 0.1 Pa, which is much smaller than the resolution of the most accurate pressure sensor in the experiment and orders of magnitude smaller than the pressure rise across the fan. Therefore, the pressure measurement in the

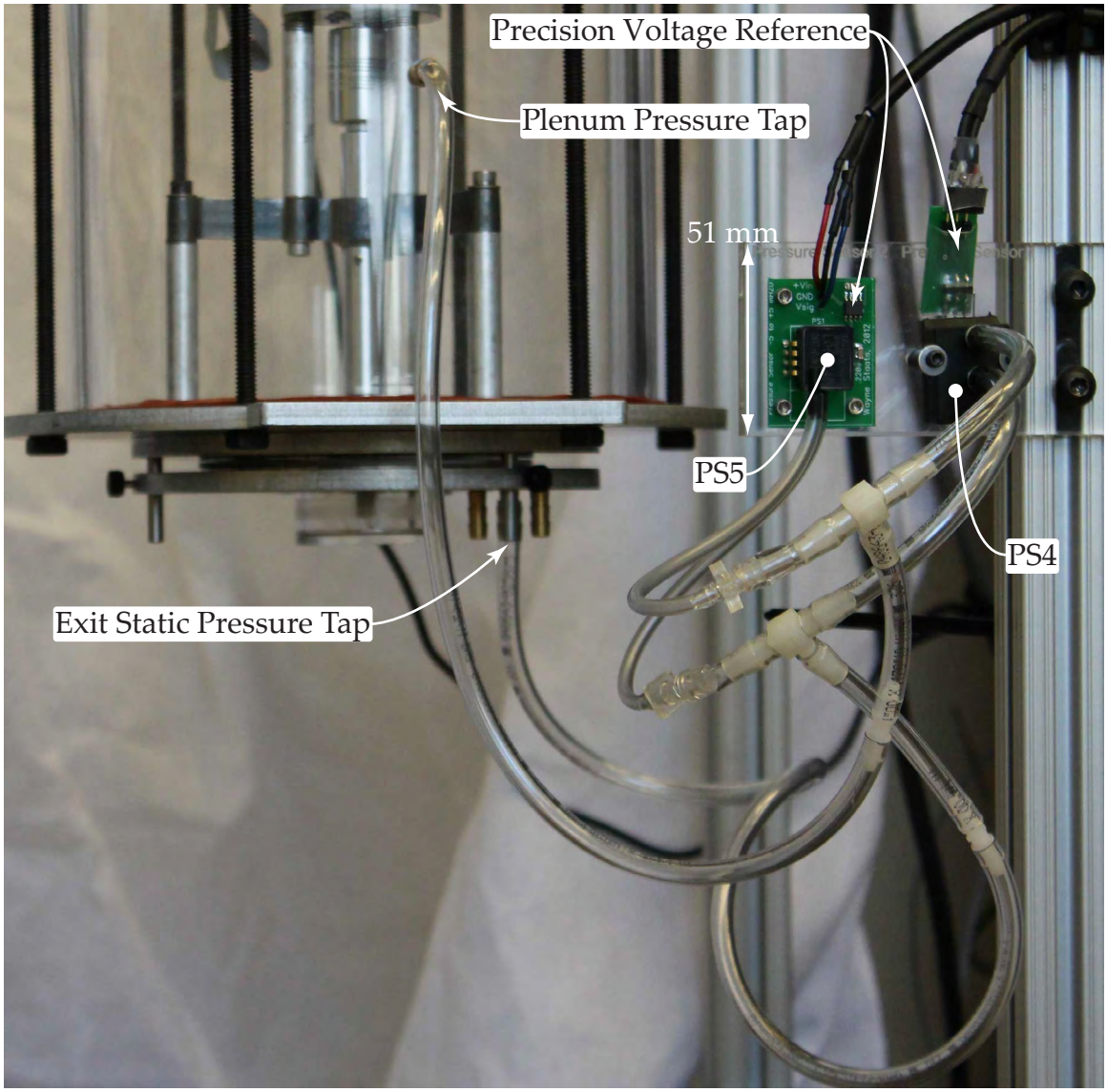

Figure 2-11: Pressure sensors 4 and 5, used in the circular stator apparatus, measured the pressure difference between the plenum and the exit of the fan.

plenum was assumed to always be equal to the upstream total pressure. The location of the upstream total pressure tap in the plenum can be seen in Fig. 2-11 and Fig. 2-12.

The total pressure tap from the plenum was connected to the low pressure tap of PS4 and PS5. Their high pressure taps were connected to a static pressure tap at the outlet of the fan channel. In the square stator apparatus, the high pressure tap was left open to the ambient surroundings; in practice, this should be the same since the exit of the fan is essentially a jet outlet and thus has the same pressure as the surroundings. However, in the circular stator apparatus there was sometimes a small radial length along which some pressure recovery was possible before truly reaching the ambient surroundings. To be rigorous and measure the true static pressure at the fan exit, a static pressure tap was installed perpendicular to the lower stator immediately next to its outer diameter. This tap was connected to the high pressure tap of PS4 and PS5.

Motor Control

The motor control was accomplished in a manner similar to the square stator apparatus, using the same motor and controller. However, on the software side, the circular stator apparatus was slightly different. In the square stator apparatus, the Maxon EPOS2 controller was accessed via LabVIEW; in the circular stator apparatus, the DAQ was performed with MATLAB, so a MEX file was created to access the C libraries of the EPOS2 motor controller. Functionally, this had no effect on the control.

The motor current had a considerable amount of variance during normal operation. A test was performed where the motor, with no impeller on the shaft, was driven at a constant speed of 5 krpm and its current measured from the motor controller. A single sample was taken at a rate of about 1 Hz. The power at each point was calculated from these current and speed measurements. The uncertainty associated with this measurement was high; the mean was 0.587 W and the standard deviation was 0.581 W (99%). This signal-to-noise ratio was deemed unacceptable.

To improve the measurement uncertainty, 4000 samples were taken during each measurement of the current. The sample mean of this set of measurements was the steady-state current measurement. The uncertainty associated with this mean current value is the standard error (SE), which is related to the sample standard deviation (σ) and the number of samples (n) by

$$\mathrm{SE} = \frac{\sigma}{\sqrt{n}}. \tag{2.21}$$

This suggested that the uncertainty of the mean current could be reduced by taking more

Table 2.3: Pressure Sensors in the Circular Stator Apparatus

Label	PS4	PS5
Manufacturer	Honeywell	Honeywell
Model Number	DC002NDC4	ASDXL05D44D
Range (Pa)	± 498	± 1245
Nominal Uncertainty	1.5 % FS (15 Pa)	2.5 % FS (62 Pa)
Gain G_i (Pa/V)	249.1	622.7
Offset O_i (Pa)	-560.5+10.3	-1557

Figure 2-12: A photograph of the plenum section, showing the location of the upstream total pressure tap.

samples. This reduced uncertainty was verified by running another test, which measured the power at each point using this averaging scheme. Each measurement was taken to be the mean value of 4000 samples. The standard deviation using this method was reduced to 0.034 W (6% of the mean value). The tradeoff in this approach was that each sample took about 13 seconds to acquire, compared to about 3 ms for a single sample. Figure 2-13 shows a comparison to the single sample method and the averaging method, applied to the raw motor current measurements from the motor controller.

2.2.2 Fan Characterization

Tests to determine the fan curves (without testing the heat transfer) were performed because more detailed fan data could be gathered in less time (a fan curve test consisted of 109 operating points and took about 50 minutes, while a heat transfer test consisted of 25 operating points and took about 2 hours and 43 minutes). In the circular stator apparatus, every operating point was in quadrant I of a pressure rise vs. volume flow plot (i.e. $\Delta p_{ts} > 0$ and $\dot{V} > 0$). This is because the fan was the only apparatus moving air through the sys-

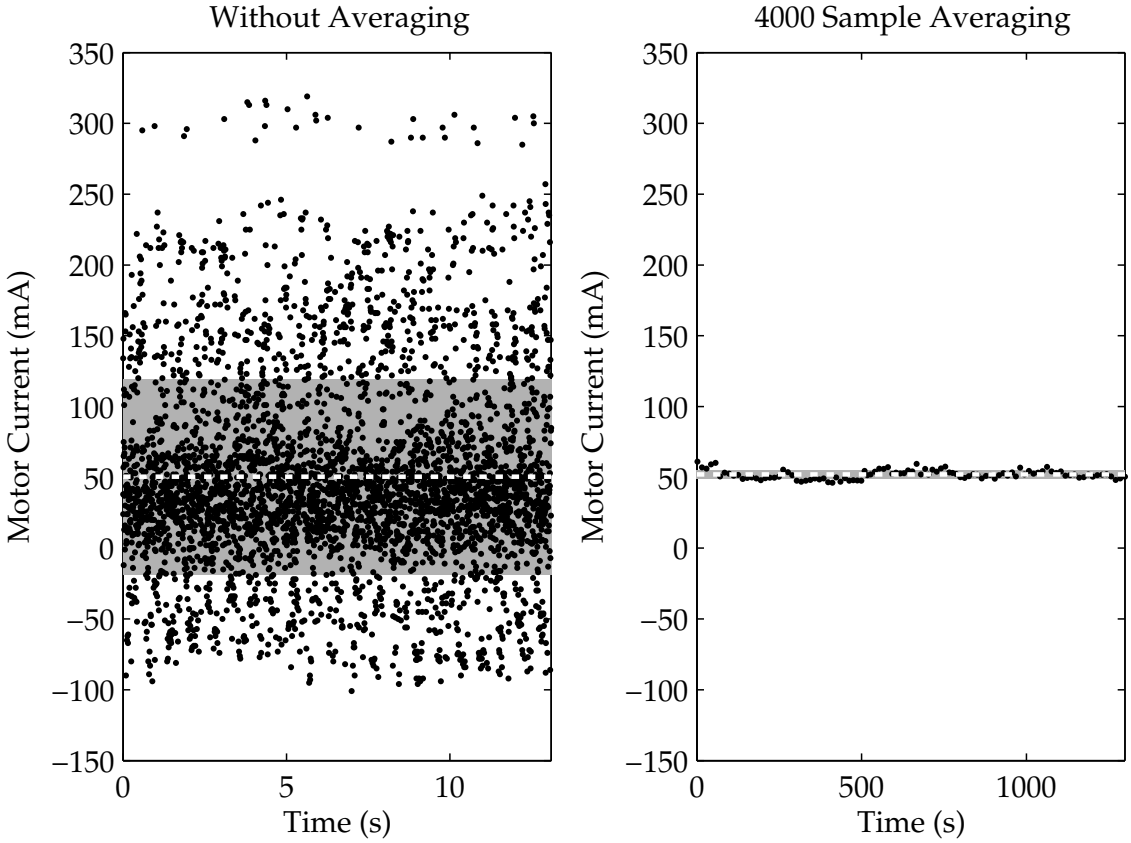

Figure 2-13: The motor current measured from the motor controller had significant fluctuations with time, yielding an unacceptable signal-to-noise ratio. By taking many samples to comprise each measurement, the uncertainty associated with the motor current measurement was significantly reduced. The dashed white line on each plot indicates the mean motor current and the shaded region represents the uncertainty bounds, defined by the sample standard deviation.

tem, and therefore no auxiliary pressure source could force flow across the fan. This was desirable because every operating point tested was representative of a realistic, practical operating point. Figure 2-14 shows the contrast in the data collection procedures of the square and circular stator apparatuses.

Impeller Installation

First, an aluminum clamp style shaft collar was installed on the impeller shaft. The location of this shaft collar determined the axial position of the impeller, and therefore its positioning was critical to the alignment of the impeller between the stator plates. To accurately set the shaft collar position and install the impeller, the following steps were performed. Some of these steps can be seen in Fig. 2-15.

1. The distance from the end face of the shaft to the face of the upper stator plate (i.e. the shaft protrusion length) was measured. A precision ground steel bar of known thickness was placed coincident to the upper stator plate, and the depth gauge measured the distance between the end face of the shaft to the steel bar. The thickness of the bar was added to this measurement to determine the shaft protrusion length.

2. The breadth of the gap between the upper stator plate and the top face of the impeller (b_{si}) was calculated as:

$$b_{si} = \frac{b_g - b_b}{2}, \tag{2.22}$$

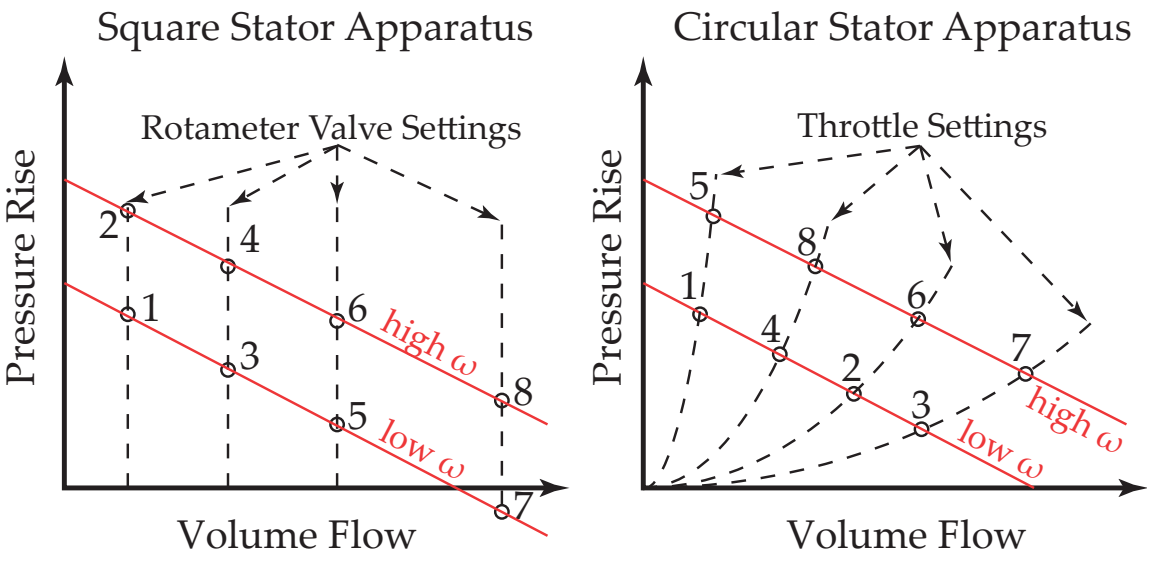

Figure 2-14: Fan performance curves were characterized in different orders in the square and circular stator apparatuses. In the square stator apparatus, the volume flow was set with the valve immediately upstream of the rotameter, and the rotational speed was varied for each volume flow, resulting in data points collected in the order shown. In the circular stator apparatus, the servo actuated throttle valve changed the system resistance as the rotational speed was held constant, which gives a different collection order compared to the square apparatus. All of the data in the circular stator apparatus was in quadrant I of the ΔP vs. $\dot{V}$ curve; some data in the square stator apparatus was in quadrant IV, which is not of practical interest in heat sink design.

where b_g is the gap breadth and b_b is the breadth of the impeller blade.

3. The stator-impeller gap breadth was subtracted from the shaft protrusion length. This represented the shaft collar installation length (L_{sc}), measured from the end face of the shaft.

4. A depth gauge was set to L_{sc}, and a custom built tool (the "shaft collar tool") transferred the depth gauge's measurement to the impeller shaft. The shaft collar was tightened as it was held against the shaft collar tool. Frames (a)–(d) of Figure 2-15 show the shaft collar tool and the process of transferring the depth gauge measurement to the shaft collar.

5. The impeller was installed by placing it on the shaft and pushing it against the aluminum shaft collar. Another shaft collar (a steel set screw shaft collar) was installed below the impeller. A compliant silicone ring glued to the top of the steel shaft collar maintained contact pressure against the impeller, ensuring that the upper face of the impeller was always coincident with the aluminum shaft collar. This can be seen in

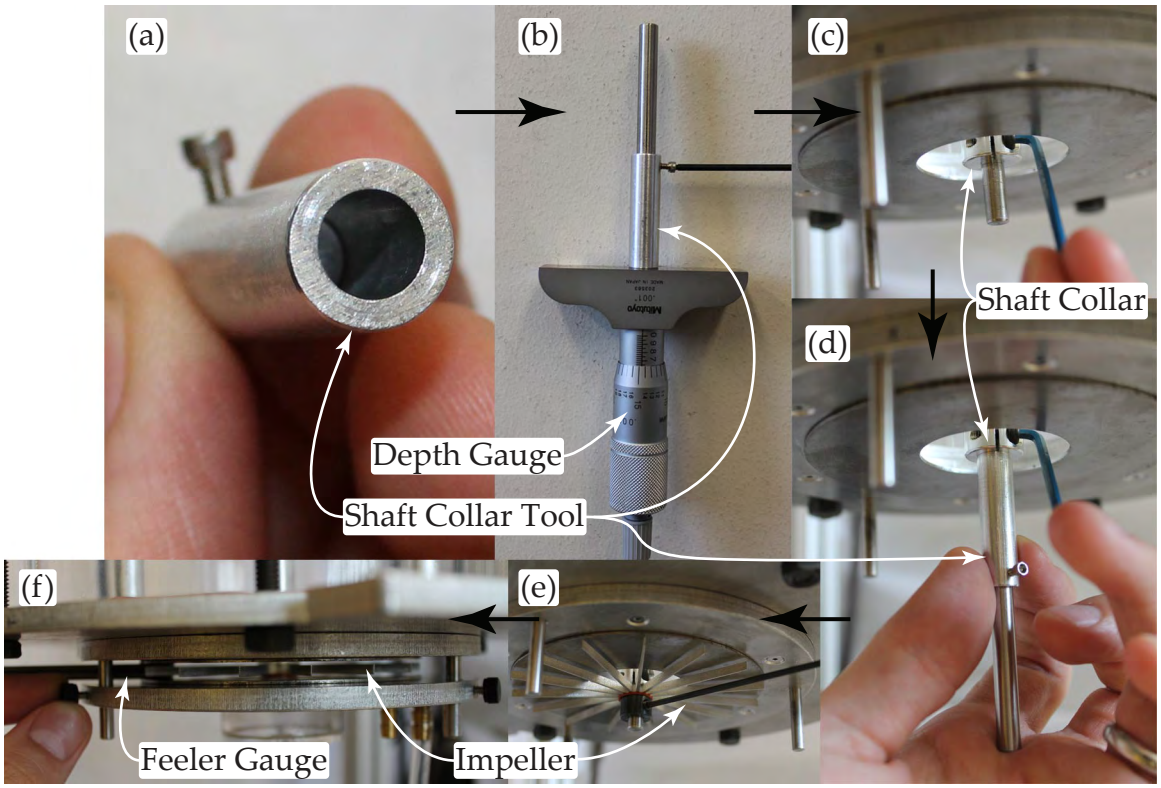

Figure 2-15: Accurate placement of the impeller between the stators was very important, especially when the fill ratio was high. (a) A custom built shaft collar tool made the impeller placement systematic and accurate. (b) The depth of the well in the shaft collar tool was set by placing it over a depth gauge set to the desired shaft collar installation length. (c) The shaft collar defining the impeller position was loosened, and (d) locked in place after its position was set by placing the shaft collar tool on the end of the shaft. (e) The impeller was installed on the shaft, and a second shaft collar underneath the impeller locked it in place. (f) Feeler gauges were used to set the stator gap breadth; the three thumb screws were tightened, setting the gap breadth to the thickness of the feeler gauges.

frame (e) of Fig. 2-15.

6. The lower stator plate was installed. The lower stator plate, also made of mild steel, was mounted magnetically to the bottom support plate, which had three precision reamed holes equispaced near its outer perimeter. These holes fit onto three dowel pins installed in the upper support plate. The reamed holes in the bottom support plate had cross drilled holes with thumb screws so that the plate could be locked in an axial position by tightening the thumb screws.

   To set the lower stator plate in the proper location, feeler gauges were selected so their thickness added to b_g. The feeler gauges were inserted between the upper and lower stators near each of the three dowel pins, and the lower stator plate was moved into position so the feeler gauges contacted each stator. The thumb screws were then tightened to lock the position of the lower stator plate. Each screw was set and locked sequentially; this was done once to get the lower stator very close to the correct position and the process repeated to ensure that the stator was exactly b_g below the upper stator plate.

7. The location of static pressure tap at the outlet was checked, and moved if necessary. This location could be changed to one of three possible locations depending on the outer diameter of the stators/impeller being tested (d_2).

After installation of the impeller, the test procedure to measure the fan curve was executed.

Experimental Procedure

The fan curve measurement process in the circular stator apparatus is described below. The entire test consisted of a sequence of rotational speed set points and a sequence of throttle valve set points. The sequence of rotational speeds was [1, 3, 5, 7, 9, 8, 6, 4, 2] krpm. The sequence of throttle positions was [0, 0.1, 0.18, 0.3, 0.4, 1, 0.35, 0.25, 0.225, 0.15, 0.125, 0.075]. As in the square stator apparatus experiments, these sequences of set points followed an up-then-down pattern to make hysteresis evident in post processing.

1. The rotational speed of the impeller was set to zero and the pressure difference between the outlet static pressure tap and the pressure tap in the plenum was measured by PS4 and PS5. The readings of PS4, PS5 and the mass flow meter were recorded. Their readings were an average value of 10 seconds of data collected at a rate of 1000 Hz.

2. The rotational speed was set to 1 krpm, the first in the sequence of rotational speed set points. The throttle position was set to 0, the first in the sequence of throttle set points. The voltage readings from pressure sensors and mass flow meter were recorded.

3. The actual rotational speed and the current being used by the motor were recorded from the motor controller. These readings were an average value of 4000 data points, which took about 13 seconds to record. The methodology behind this is discussed in Section 2.2.1.

4. The throttle was set to the next position in the sequence of throttle set points; a brief equilibration time elapsed and then the voltages from the pressure sensors and mass flow meter were recorded.

5. Steps 3–4 were repeated until each throttle set point was tested at the current rotational speed.

6. The rotational speed was set to the next speed in the sequence of rotational speed set points.

7. Steps 3–6 were repeated until each rotational speed in the sequence was tested.

This test procedure, performed for each impeller geometry and gap breadth, yielded the voltages from PS4 and PS5, the mass flow rate, the current consumed by the motor, and the rotational speed at each operating point. This data was subsequently processed (the appropriate calibration curves were applied to the raw data) into meaningful operating parameters. An example of this processed data can be seen in Fig. 2-16. These results are typical: the fan curves, unique at each rotational speed, are most often linear, although they were sometimes observed to be slightly parabolic. This will be discussed in greater detail in Chapter 5.

2.2.3 Heat Transfer Characterization

The heat transfer coefficient of a fan was characterized by performing a fan characterization test with heated copper stator plates. The plates were heated to a constant temperature and held at this temperature by a closed loop control system. The power required to maintain the plate temperature was measured at each operating point.

The copper heater plate assembly can be seen in Fig. 2-17 and Fig. 2-18. Each stator plate consisted of two 3.2 mm thick plates of copper, cut into an annular shape on a waterjet cutter. Four polyimide film heaters (Electro-Flex Heat KH-0.5X2-10-28-A) were bonded to one of the copper plates. The space around the rectangular-shaped heaters was filled by some additional copper pieces cut from a thin copper plate of roughly the same thickness as the heaters. Next, the remaining annular plate was adhered to the top of the film heaters and copper filler pieces with silver-filled thermally conductive epoxy. Thermocouple wells were formed by cross drilling small (~1 mm) diameter holes in two locations about 90 degrees apart on the side of one of the copper plates. The ensemble at this point formed a copper-heater-copper sandwich structure. This sandwich structure was epoxied to a polyetherimide frame, which served to provide structural support and thermal insulation (with minimal contact with the copper assembly to reduce the heat leak to the surroundings). This frame structure was analogous to the stator support plates in the fan characterization experiments; it contained the necessary bolt pattern to mount to the lower face of the plenum.

The stator plate assemblies were designed to have isothermal copper regions so that the heat loss to ambient would occur from the same temperature as that measured by the thermocouples. The reason for this is as follows. If the plates are held at constant temperature, the heat loss to ambient should be independent of the heat flux into the air flow stream. However, several assumptions are inherent in this statement. First, the copper is assumed to be isothermal. This turns out to be a reasonable assumption, because the Biot number of the copper is very low ($\mathrm{Bi} < 10^{-3}$). A finite element model of the plates also

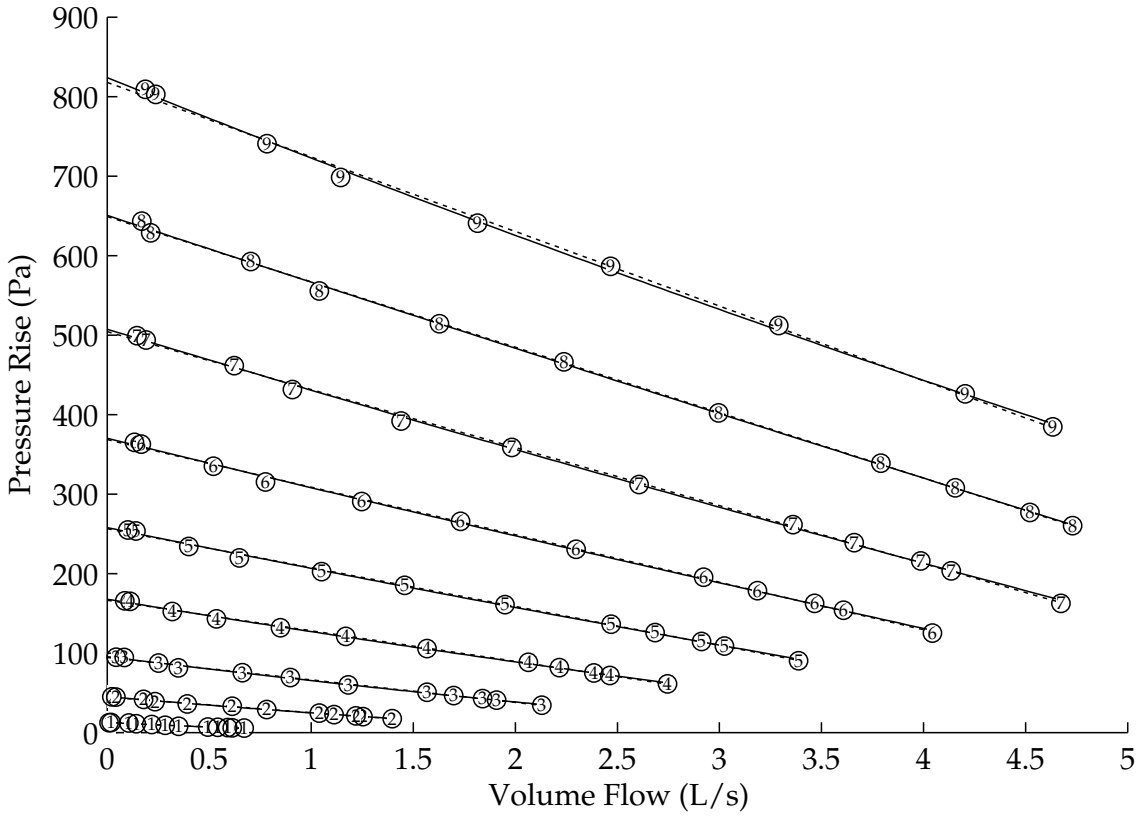

Figure 2-16: An example of some raw fan curves measured with the circular stator apparatus. These data were taken on a 15-blade fan with $b_b = 1.6\,\text{mm}$, $b_g = 2.6\,\text{mm}$, $d_1 = 40\,\text{mm}$, $d_2 = 100\,\text{mm}$, and 60° exit angle. The numbers in each marker indicate the rotational speed in krpm. The solid lines are parabolic fits to each rotational speed; the dashed lines are linear fits. Most of the experiments were satisfactorily represented by a linear fit.

confirmed that there were negligible temperature gradients in the lateral direction of the copper, and that the copper satisfactorily spreads the heat input of the heaters. Second, the heat leak from the copper to the ambient is assumed to originate from the same temperature. By embedding the heaters in the copper plates this assumption is much more valid compared to installing the heaters on the top side of a single copper plate. In this second (hypothetical) case, the heat loss to ambient can occur from a different temperature than that of the plate, because at high heat loads the thermal resistance between the heater and the plate causes the heater to have a higher temperature. Thus, error would be introduced if one were to assume the heat loss occurs uniformly from the measured copper plate temperature.

The stator plates were driven by the same amplifier board as in the heat transfer experiments in the square stator assembly. The voltage applied to the heaters (all four heaters of each plate were wired in parallel) was measured with the same resistive divider as in the square stator assembly. However, the data acquisition system was as described in Section 2.2.1.

The control system in the circular stator apparatus heat transfer characterization test was improved over the analogous test in the square stator apparatus. While the square apparatus used PID control, this circular apparatus used PI control but with a filtered input

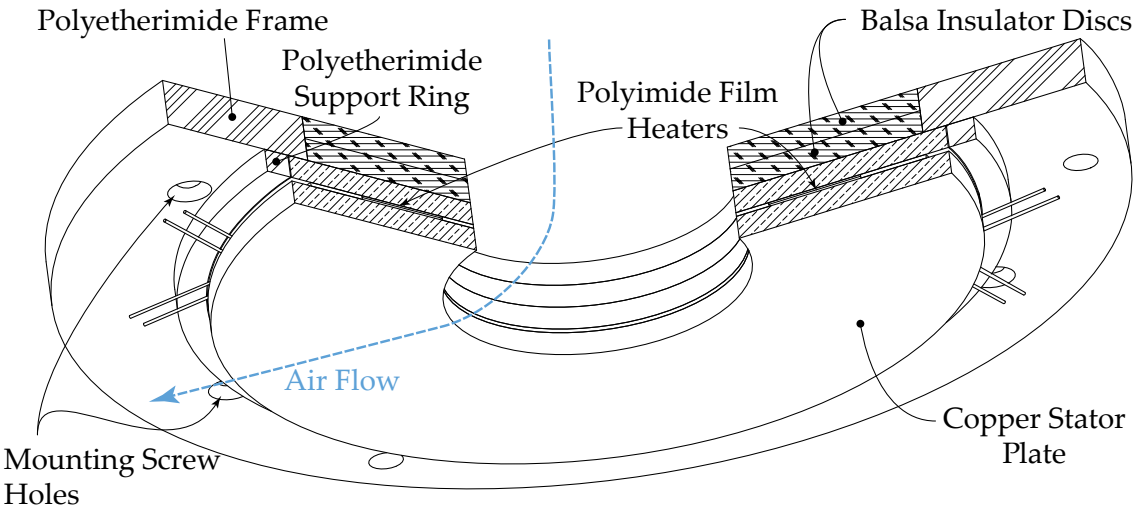

Figure 2-17: The circular stator apparatus used a sandwich structure comprised of copper plates with polyimide heaters to measure the average heat transfer coefficient. The copper plates encased the heaters and a copper foil spacer and were glued together with silver-filled, thermally conductive epoxy. A polyetherimide support structure was then adhered with conventional epoxy to the copper plates; this allowed the heater assembly to mount to the bottom of the plenum. Balsa insulator discs minimized the heat loss from the copper opposite the airflow. This is a view of the upper stator plate from below, with a cutaway to show the internal structure of the assembly.

signal. The readings from the two thermocouples on each stator plate were averaged for each stator. The error (the difference between this average temperature and the set point) signal was then passed through a 10^{th} order lowpass FIR filter. This filtering reduced the system's tendency to change the control signal too quickly and become unstable[5]. The response of the circular apparatus was fast, and the control system was robust and free of instability.

Experimental Procedure

The heat transfer characterization experiments were performed using the following procedure:

1. The impeller was installed in an identical manner to the fan characterization experiments. This is described in Section 2.2.2.

2. The heaters were turned on. The impeller was held stationary and the throttle valve was closed. The system was allowed to reach the set point temperature, and the control system maintained the plates at this temperature until steady state conditions were reached. The system was deemed to be at steady state when both the temperature and the heat input were constant. Generally, it took about 5 minutes for the system to reach steady state after a change in the fan operating point, and slightly longer upon the initial startup.

   This first point was used to determine the heat loss from the system. With no air flow between the stators or rotation of the impeller, all of the power input from the

[5] An additional parameter in the PID control served this purpose in the square stator apparatus.

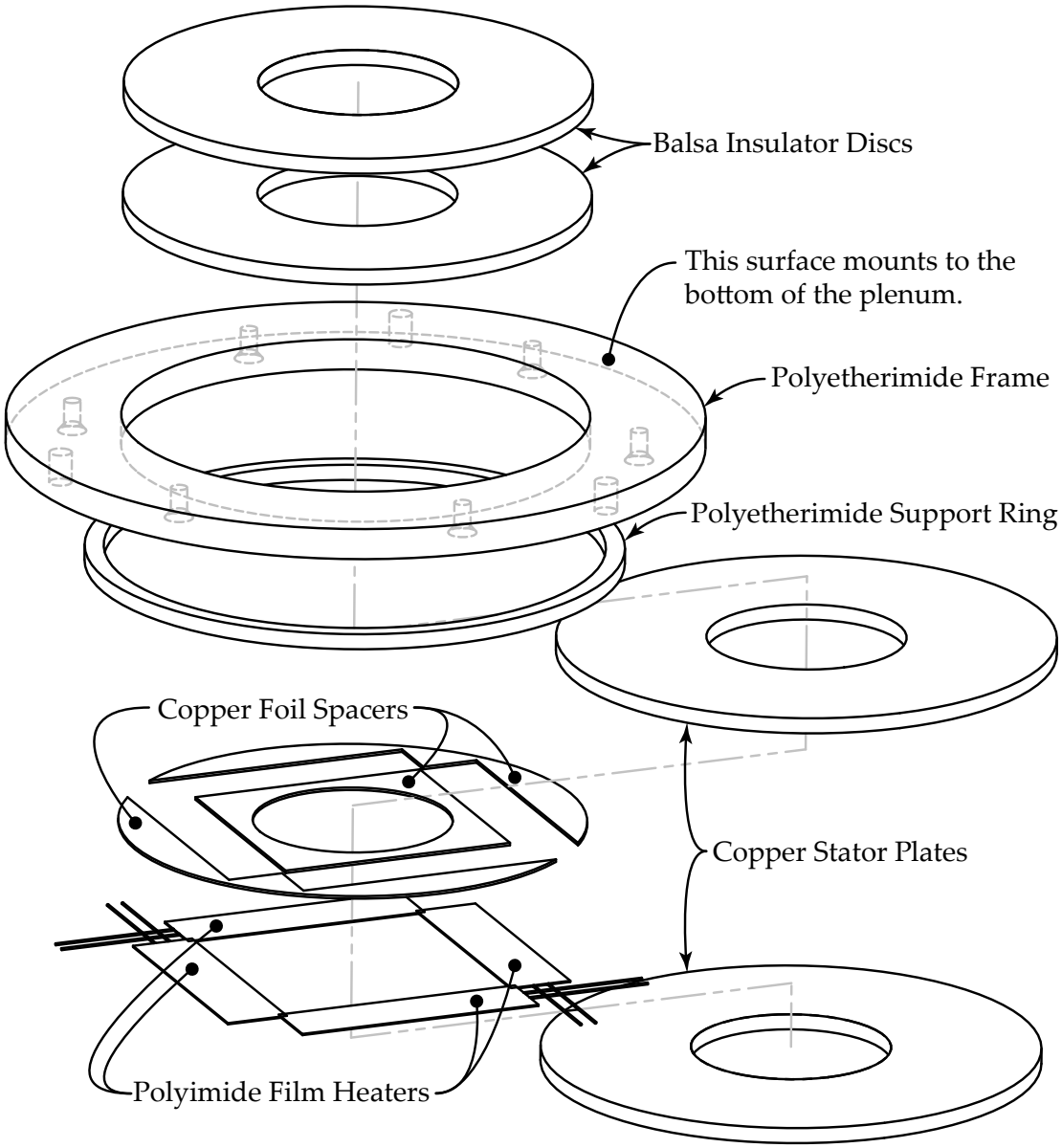

Figure 2-18: This exploded view of the circular heater apparatus shows the polyimide film heaters and the copper foil spacers.

heaters left the system in the form of heat loss. As in the square stator heat transfer characterization, since the plates remained at the same temperature for all of the operating points, the heat loss was assumed to be constant throughout each test.

3. The procedure of the fan curve test was followed, as described in Section 2.2.2. In the heat transfer characterization, fewer rotational speeds and throttles were characterized due to the much longer equilibration times. At each operating point, the fan parameters and also the thermal power input for each plate was recorded for 5 minutes.

2.2.4 Local Heat Transfer Characterization

The heat transfer characterization tests served a practical purpose and gave useful information about the heat transfer capabilities of integrated fan heat sinks. However, the experiments only yielded *averaged* information about the heat transfer; the exact variation of the heat transfer coefficient with radius cannot be extracted from the experiments described in Section 2.2.3. Knowledge of this local variation in the heat transfer coefficient is important in some applications. For example, consider a heat pipe design such as the PHUMP where the condensers are cooled by integrated fans. A designer may wish to calculate the temperature of certain critical regions of a condenser (e.g. dedicated zones to subcool the condensed liquid before it returns to the evaporator). With accurate knowledge of the local variation in the heat transfer coefficient, appropriate boundary conditions can be applied to a model of the condenser internals, allowing a designer to tailor the heat pipe internals to best match the cooling air flow.

To characterize the local heat transfer coefficient, a heated thin film infrared thermography method was used. Heated thin film IR thermography methods are typically limited to a constant heat flux boundary condition, but in heat pipe applications the condenser exposed to the air flow approximates a constant temperature boundary condition. A new variation of this method was developed, which used discrete, independently controllable zones and allowed for freedom to set different heat transfer boundary conditions.

Heated Thin Film Infrared Thermography Background

In the heated thin film IR thermography method, a thin material is heated by electric current to create a known distribution of heat generation. The thin material acts as a wall for the flow of interest; the flow removes the generated heat by forced convection. An IR camera records the temperature distribution in the wall. Due to the thinness of the material, the temperature is uniform across the film and the camera can view the side of the film opposite the forced convection flow. The combined knowledge of the heat generation rate and the wall temperature as functions of position allows one to deduce the local heat transfer coefficient. Care must be taken to subtract energy fluxes other than the convection being characterized. These auxiliary energy flows occur due to lateral conduction in the film, radiation, and natural convection on the side opposite the forced convection flow. A detailed explanation of these corrections can be found in Stafford [73]; the details of this loss accounting in this work are described in Section 2.2.4.

The IR thermography method has been used in previous work. Astarita used printed circuit boards (PCBs), the traces of which had a tortuous path that covered the entire surface, to give a uniform heat flux. He studied the variation of the Nusselt number on the wall of a rectangular U-shaped duct [74] and showed that the PCB must be thin enough

to have a low Biot number (negligible temperature gradients across the thickness of the material). The anisotropy of the fiberglass/copper composite structure must be accounted for in calculating the conduction loss. Astarita, in a subsequent work, studied the heat transfer from a rotating disc. The heated surface in this study was also a PCB. Special care was taken in post processing to correct for the disc's rotation during the line scan of the thermal image. Stafford et al. conducted a number of studies that use thin film IR thermography. They studied the heat transfer of the exit flow of an axial fan impinging onto a flat heated plate [73, 75, 76]. The heated plates were tensioned stainless steel foils; a constant heat flux boundary condition was imposed in this setup. They outlined a procedure for calculating the lateral conduction through the plate. If not accounted for, significant errors were observed to occur in the calculation of the heat transfer coefficient. Stafford et al. also studied the heat transfer and flow field in a small centrifugal fan heat sink, using IR thermography and particle image velocimetry [77]. This system had a centrifugal fan pumping air radially outward into a vaneless diffuser where most of the heat transfer occurred. In all of these studies, constant heat flux was the heat transfer boundary condition tested.

Description of Apparatus

In this work, thin PCBs were used as the heated film, acting as the stator plates in the fan setup. A PCB was attractive for this purpose for several reasons. First, professional PCB fabrication businesses can make high quality boards economically and quickly. Second, a PCB can be made out of fiberglass that is thermally thin but still rigid enough to act as a structural element. If a thin metal foil were used instead, it would have to be tensioned to maintain its flatness, which would be difficult in the annular geometry of the integrated fan. Third, fine grained control over the heater geometry can be attained because the PCB trace tolerances are very tight. For example, the manufacturer of the PCBs in this work specifies a minimum trace width and minimum trace spacing of 0.15 mm. Finally, using a PCB allows the use of practical features such as vias (plated holes that provide a connection from one side of the PCB to the other) and pads. As will be discussed below, one iteration of the PCBs included some thermocouples soldered to pads, which were used to corroborate the IR camera's temperature measurements.

One drawback of the heated thin film method is traditionally the lack of control over how the heat transfer into the fluid is distributed. This limits the experiment to a single boundary condition (often this boundary condition is constant heat flux, but could be different depending on the PCB trace design). In order to reduce this limitation and test different boundary conditions, the PCB was split into 12 annular zones that were independently controlled. This arrangement was designed so the constant temperature boundary condition could be approximated by varying the power dissipated in each zone. Each of the 12 heated zones on the top[6] of each PCB contained a spiral shaped trace. Connections to provide power to the trace were on side of the PCB opposite the spirals, and connectivity was achieved through two vias. The power leads were soldered directly to the back side of the PCB and strain relieved by potting the soldered connections with epoxy. A picture of the PCB design can be seen in Fig. 2-19. The upper and lower stator PCBs were identical, and were constructed of 0.50 mm thick FR4 fiberglass with gold plated copper traces.

Each stator PCB was supported by a black acetal homopolymer frame. The frame was

[6]The side of the heated stator PCB exposed to the air flow in the stator gap is referred to as the top side.

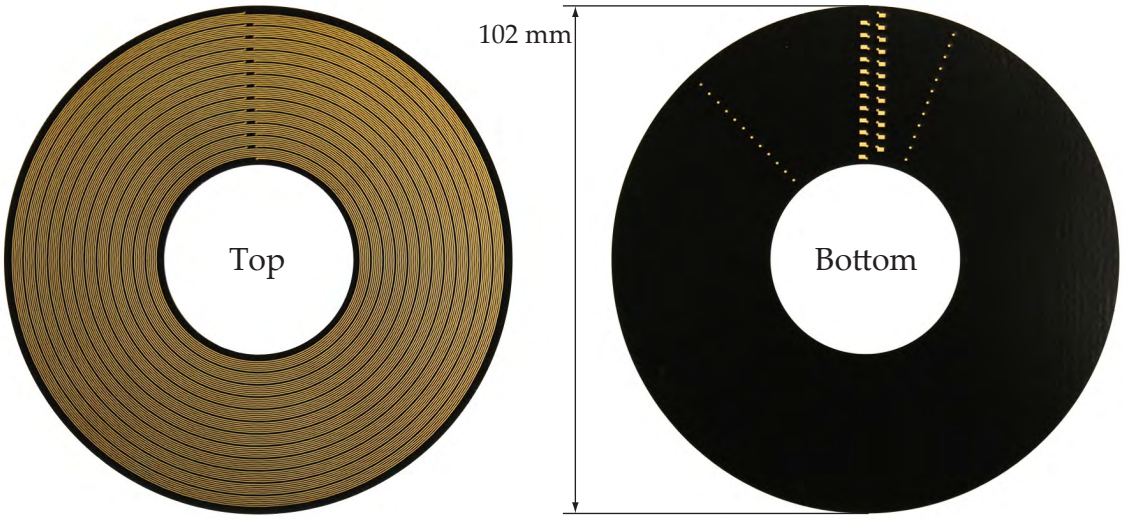

Figure 2-19: A photograph of the heated thin film PCB, showing the top and bottom side of the board. The bottom side was coated with black soldermask; the top side had no soldermask. The spiral-shaped copper traces on the top side were gold plated to reduce corrosion.

designed to have a very small contact region with the PCB along the outer periphery to minimize conduction loss from the PCBs to the support frame. The support frames had the same hexagonal 6-bolt pattern as the structures in the fan characterization and heat transfer characterization tests, so it could be attached to the bottom of the plenum. It also used a similar pattern of 3 dowel pins pressed into the top support. A matching hole pattern with cross drilled thumb screws in the lower stator support frame fixed the position of the lower stator. The breadth of the stator gap was set by using feeler gauges to space the PCBs prior to tightening the thumb screws, in the same procedure as described in Section 2.2.2. A diagram of the stator PCB support structure can be seen in Fig. 2-20

A PMMA end cap for the lower stator PCB prevented air from entering the bottom PCB hole. This was important because any leakage into the eye region would bypass the mass flow meter, and the mass flow measurement would thus underpredict the actual air flow in the stator gap. This end cap consisted of three thin rings and a disc, laser cut from 6.4 mm sheet stock, and adhered together in a stack with silicone sealant. This fabrication method allowed the annular ring that adhered to the lower stator PCB to be very thin to minimize thermal leakage.

Two iterations of the stator PCBs were constructed. In the first iteration, the original intent was to solder surface mount connectors to the PCB for the power connections and also for a series of resistance temperature detectors (RTDs). The connectors proved to be unreliable and difficult to work with, so the wires were soldered directly to the PCB and strain relieved with epoxy. The RTDs were surface mount, 100 Ω, platinum RTDs and were arranged in an Anderson loop [78] with a single voltage excitation for each stator. It was found that the temperature measurement of the board was very susceptible to noise. Ultimately, the RTDs were not used and the temperature reading was obtained from the thermal camera image.

In the second iteration of the stator PCBs, the RTDs were eliminated and small circular pads were placed on the back side of each heater zone (see Fig. 2-19). One 36 AWG type-J

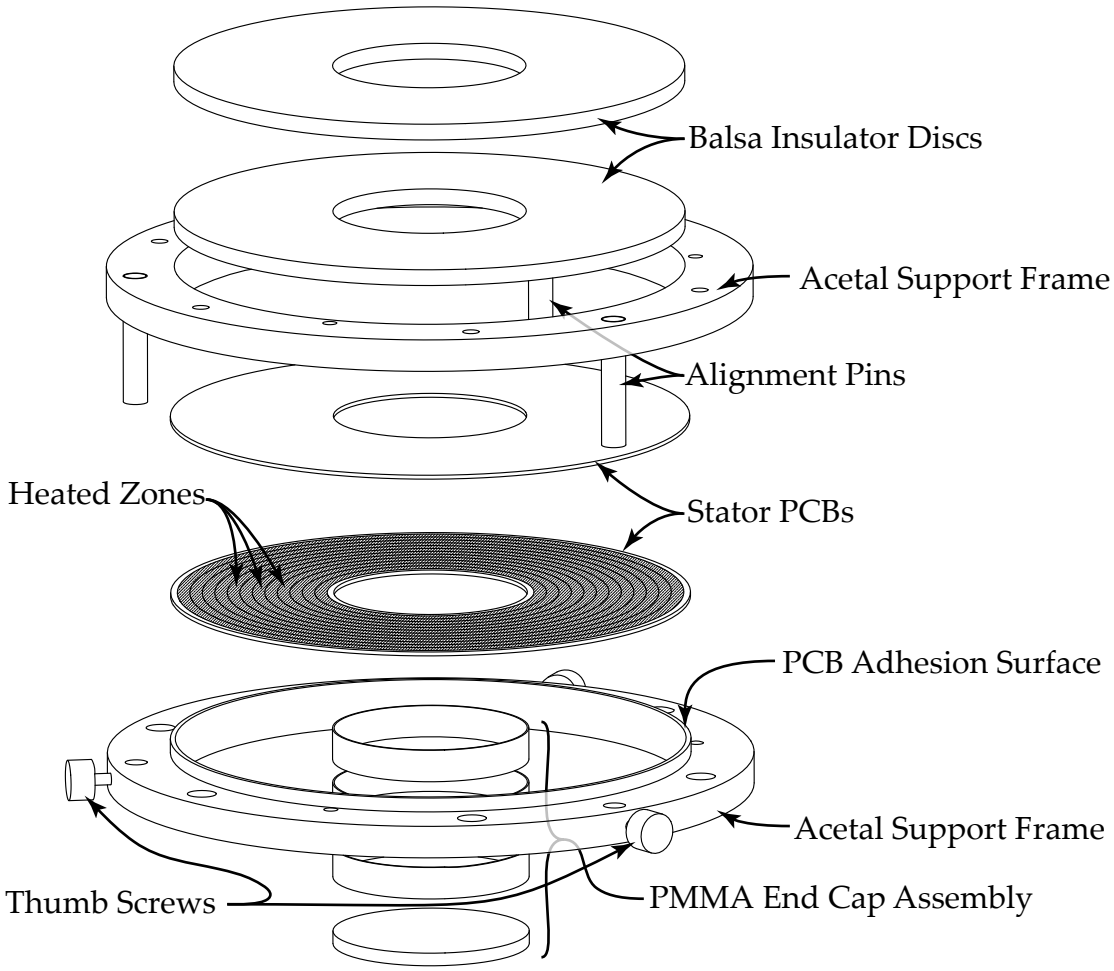

Figure 2-20: The heated stator PCBs were each adhered to an acetal support frame. The upper support frame attached to the lower face of the plenum and had two annular balsa wood discs for thermal insulation. It also had alignment pins pressed into a three hole pattern; the lower support frame could slide along these pins and lock into place with thumb screws. A PMMA end cap assembly adhered to the lower stator PCB blocked air flow from entering the center hole on the bottom, ensuring that all of the fan's air supply flowed through the plenum.

thermocouple was soldered to each of these pads (one per heater channel), placing them in good thermal contact with the PCB. The thermocouples were strain relieved and insulated with a small dab of epoxy; care was taken to ensure that a small length (10 mm) of the thermocouple was held against the PCB so the junction was not cooled by the thermocouple leads. A second row of thermocouple pads on the bottom side of the PCBs served as a backup in case of damage to the first row. These backup pads were not needed in the experiments. The acetal support frames in this second iteration were slightly modified as well. In the first iteration, there was a lip on the outer edge of the frame running around the perimeter of each PCB to center the PCB in the frame. In the second version, this lip was eliminated and replaced with three dowel pins to center the PCB. This change was to ensure that the PCB did not "oil can," or bow in the center. In both cases, cyanoacrylate adhesive secured the PCB to its acetal frame.

The spiral traces on each stator PCB were driven by a custom built amplifier board. The basic idea of this amplifier was similar to the two-channel heater driver described in Section 2.1.1. However, two main differences in this application led to a different amplifier design. First, the impedance of the spiral PCB traces (2–5 Ω) was lower compared to the polyimide film heaters used in the two-channel configuration. This meant that a comparatively low voltage was needed to drive the same current through the heater. Second, each channel only comprised approximately 1/12 of the power budget of each stator, making the power per channel about 1/12 of the two-channel amplifier described above. Finally, many more channels were used (24 compared to 2), so concerns such as cost, packaging, and ease of construction were more significant. To recap, these 12-channel amplifiers were designed to operate on a low voltage (8 V), high current (50 A) power supply, to amplify a 0–5 V analog signal voltage from the data acquisition system, and to boost the current of this signal voltage to drive the low-impedance heater traces. A schematic of a single channel from one of the 12-channel amplifiers is shown in Fig. 2-21.

Each channel of the amplifier board consisted of a unity gain op-amp and a transistor in a common collector configuration. The collector of the transistor was at $+V_{cc}$ and the emitter, which was fed back to the inverting input of the op-amp, was maintained at the control voltage by the op-amp. The inverting input of the op-amp used feedback from the

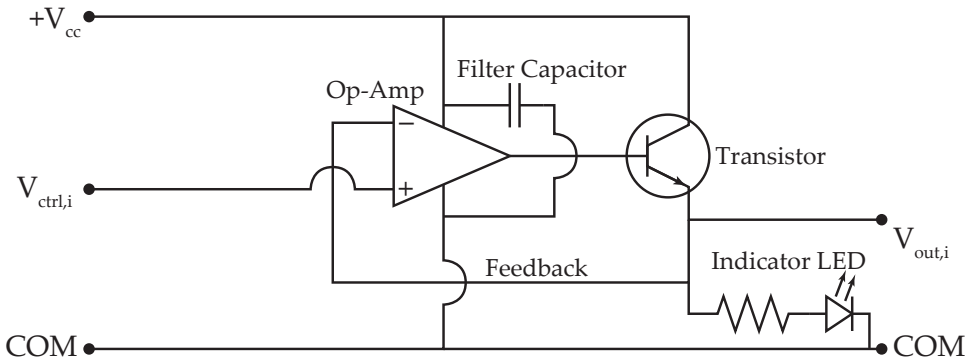

Figure 2-21: Each heated PCB was powered by a custom built 12-channel amplifier. Each channel of these amplifier boards consisted of an op-amp and a transistor. The feedback of the op-amp was connected to the emitter of the transistor.

emitter of the transistor to ensure that the voltage applied to the heater remained at the control voltage. The transistor amplified the current output from the op-amp. Another way to view the circuit is as a unity-gain amplifier that only exposes the control signal to the extremely high input impedance of the op-amp, but provides a low output impedance to the system to match the low impedance of the heaters. The amplifier boards were fabricated by a printed circuit board company; a picture of the boards in operation can be seen in Fig. 2-22. Waterjet cut copper heat sinks and DC computer fans provided cooling to the transistors to prevent them from overheating.

Experimental Procedure

Initially, an experiment was performed to test the capability of the amplifier boards and the heated stator plates, and to demonstrate the exquisite control over the heat input and PCB temperature. First, the rotational speed of the impeller was set to 5 krpm and the throttle valve was closed. The power input (heat flux) of each channel was set to approximately produce a constant, elevated temperature on the plate. Next, the heat flux to each channel was individually, in sequence, set to double the value needed to maintain the plate at constant temperature. The result of this can be seen in Fig. 2-23. The thermal images have a color mapping that corresponds to the local temperature. It can be seen that each channel had a distinct, identifiable location in the thermal image, and that heat spreading

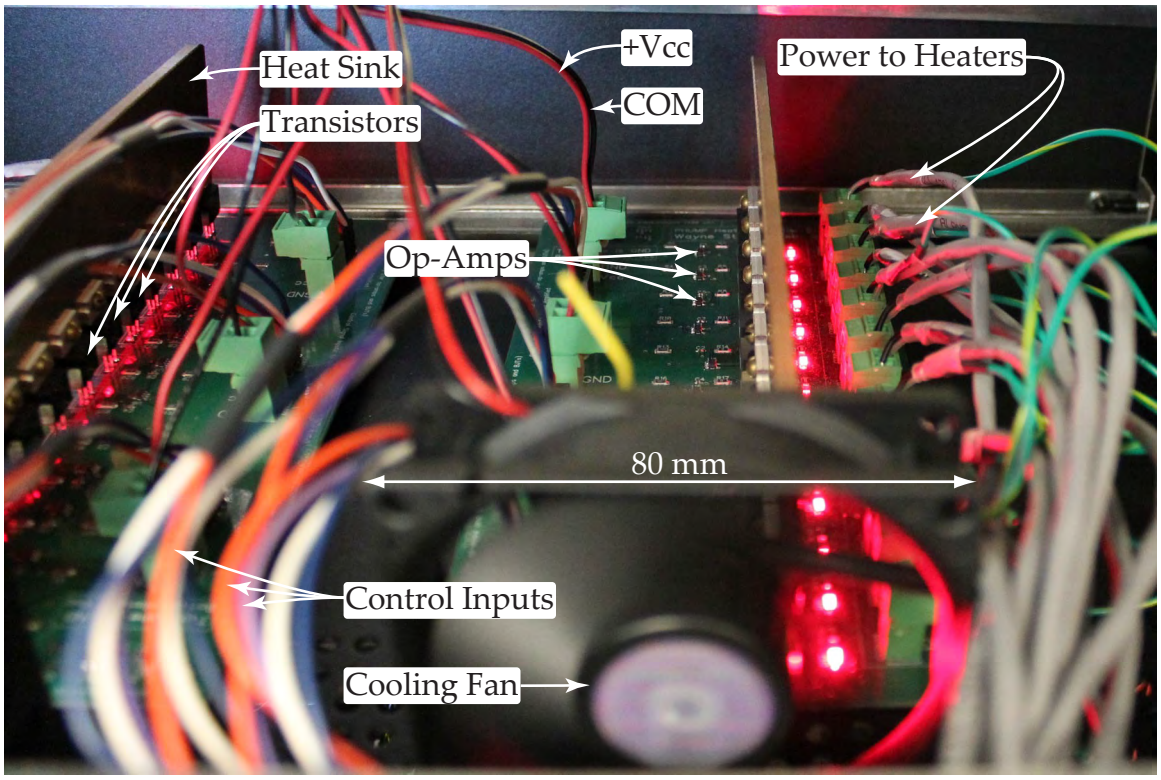

Figure 2-22: The 12-channel amplifier boards that drove the heated stator PCBs consisted of mostly surface mount components. A copper heat sink provided cooling to the transistors, along with two computer cooling fans. An indicator LED provided visual confirmation that voltage was being applied to each channel. The amplifier boards were housed in a rack mount chassis.

in the lateral direction wasn't excessive. In some of the operating points a slight smearing of the temperature profiles occurred, causing temperature gradients to arise in the tangential direction. This mostly occurred in the vicinity of the power input leads. In post processing, a pie-slice-shaped area surrounding the leads and amounting to about 1/4 of the total annular area was ignored to ensure the results weren't affected by this artifact of the experimental setup.

The resistance of the PCB traces were measured on a digital multimeter (Hewlett-Packard 34401A) using a 4-wire resistance measurement. These resistances were measured in two locations: directly on the upper PCB surfaces and at the end of each power lead, where it plugged into the amplifier board. This was done to separate the trace resistance from the resistance of the leads, so the leads could be accounted for when calculating how much voltage to apply to achieve a desired power dissipation in the PCB trace. The voltage applied to each zone was calculated as follows. First, the desired heat flux in a zone (q'') was multiplied by the zone's surface area (A_{zone}) to determine the power input required, namely

$$\dot{Q}_{\text{zone}} = q'' A_{\text{zone}}, \tag{2.23}$$

where the area A_{zone} is simply the zone's radial width dr_{zone} times the circumference at its midpoint:

$$A_{\text{zone}} = dr_{\text{zone}} 2\pi \bar{r}_{\text{zone}}. \tag{2.24}$$

In Eq. 2.24, $\bar{r}_{\text{zone}}$ is the arithmetic mean radius of the zone. Next, the current I_{zone} required to produce the necessary power $\dot{Q}_{\text{zone}}$ was calculated as

$$I_{\text{zone}} = \sqrt{\frac{\dot{Q}_{\text{zone}}}{R_{\text{zone}}}}, \tag{2.25}$$

where R_{zone} is the resistance of the heater trace in the zone, not including the leads from the amplifier board. Finally, the voltage output needed at the amplifier channel (V_{chan}) associated with the zone was calculated as

$$V_{\text{chan}} = I_{\text{zone}}(R_{\text{zone}} + R_{\text{wire}}), \tag{2.26}$$

where R_{wire} is the resistance of the wire running from the amplifier board to the heater trace in the zone. This procedure ensured that the correct amount of power was applied to the heater trace to give the desired heat flux. In the experiments, this heat flux was chosen either as a bulk value applied to the entire plate at once (constant q'' boundary condition); or, as different values for each zone (selected to produce a constant temperature boundary condition).

The experimental procedure of the local heat transfer test was very similar to that of the heat transfer characterization test described in Section 2.2.3. However, in addition, at each operating point a thermal image was recorded. The thermal camera (FLIR SC6000) was positioned at the bottom of the structural frame that held the circular stator apparatus, looking up at the bottom of the lower stator PCB. Once the thermal camera image was observed to be time invariant the thermal image was recorded, the pressure sensors, mass flow meter and motor controller measurements were made, and subsequently the operating point was changed. The order of operating points was identical to that of the heat transfer characterization test.

Post Processing

The thermal camera images were recorded in a format (FLIR Public Format) that contains the temperature information at each pixel. These images were exported to a CSV file that was imported to MATLAB for processing. The following procedure was used to process this raw temperature matrix into meaningful results that could be analyzed:

1. The temperature matrix was spatially low-pass filtered. This was accomplished using three two-dimensional convolutions of the temperature matrix with a 2-D FIR filter (similar to a 3-pixel wide Gaussian blur).

2. The scale factor for the image was determined by measuring a known distance (in pixels) in the thermal image. The outer diameter of the acetal frame was used for this measurement because it had very easily identifiable, crisp edges.

3. The center of the stator was located in the thermal camera image. This was done with a circle detection algorithm. First, a pixel location was chosen that was near the center. Next, a double nested loop iterated through the X- and Y- pixels in the vicinity of the starting point. At each test point, a region bounded by two concentric circles was defined. These circles represented the eye and the outer edge of the stator PCB. Their diameters, in pixels, were calculated using the scale factor and their measured physical dimensions. Next, the average temperature in the bounded region was calculated. Since the hottest regions were located on the stator PCB, the center point whose bounded region had the highest average temperature was likeliest to be the center. This was confirmed to be a reliable method for finding the center point, and ensuring that any small changes in the camera's field of view between operating points would not affect the post processing.

4. The coordinates were transformed so that origin was coincident with the center of the stator PCBs. Dimensional values were assigned to each pixel. The radius and angle from the positive X-axis were also calculated for each pixel.

5. The losses enumerated in Stafford [73] were calculated. These losses were:

   (a) Lateral conduction through the PCB. This was calculated using the equations outlined in [73], which are based on Fourier's law. The derivatives $\frac{dT}{dx}$ and $\frac{d^2T}{dx^2}$ (and their analogs in the y- direction) were computed numerically using an 8-tap FIR derivative filter to avoid noise amplification. The thermal conductivity of the PCB was assumed to be 0.27 $\mathrm{W/m \cdot K}$ based on the PCB manufacturer's datasheet for the FR4 substrate.

   (b) Radiation loss to the surroundings. This was calculated using the Stefan–Boltzmann law, assuming an emissivity of 0.95 for the black soldermask on the bottom of the PCB.

   (c) Natural convection on the bottom of the lower stator PCB. This was determined experimentally by analyzing the data at a calibration operating point, where power was applied to the stators but the impeller was stationary and the throttle valve was closed. In this configuration, no heat could be transferred to the air flow between the stator plates because the mass flow through the system was zero. Thus, all of the heat input was lost to natural convection and radiation. A natural convection heat transfer coefficient was calculated for the pixels in

each zone, based on the zone's heat input and temperature difference to ambient during this calibration. The quantities in these calibration points were circumferentially averaged so that the natural convection heat transfer coefficient became a function of radius only.

6. The forced convection heat flux at each pixel was calculated by subtracting the various losses from the experimentally set heat input at each pixel. The heat generation depended on the zone in which each pixel was located, and was recorded for each operating point in the test.

7. The heat fluxes and the PCB temperature were circumferentially averaged at each radius, and the forced convection heat transfer coefficient (h_{fc}) as a function of radius was determined by

$$h_{\mathrm{fc}}(r) = \frac{q''_{\mathrm{fc}}(r)}{T(r) - T_{\mathrm{amb}}}, \tag{2.27}$$

where $T(r)$ is the circumferentially averaged temperature of the PCB, T_{amb} is the ambient temperature, and $q''_{\mathrm{fc}}(r)$ is the circumferentially averaged forced convection heat flux.

2.3 Geometries Tested

Several impeller geometries, shown in Fig. 2-24, were characterized. The impellers all have extruded (i.e. 2-D) geometry, so they can be manufactured using processes such as waterjet cutting, laser cutting, wire EDM, or punching. This 2-D, planar geometry is a natural choice for planar heat pipes since the condensers between which the impellers rotate are typically flat.

The impellers were first cut from sheet metal on a waterjet cutter. The material was aluminum (6061-T6 alloy), chosen for its ease of manufacture, flatness, and stiffness. Next, the center hole was reamed to the appropriate size (6 mm). After this, the impellers were deburred by wet sanding the flat surfaces using a flat, ground glass surface covered with 120 and subsequently 240 grit sandpaper. A flat aluminum disc was used to apply a small amount of pressure to the top of the impellers during sanding. The sanding served to deburr and smooth the impellers, but the flatness was not guaranteed by this process; a bowed impeller would spring back to its original shape after the sanding pressure was removed. To ensure that the impellers were flat, a stress relieving process was performed, similar to the procedure used by Banner to flatten duralumin (2000 series aluminum) [79]. The impeller was placed between two pieces of flat, 6.4 mm thick borosilicate glass plates, and heated in an oven to 230 °C . They were held at this temperature for approximately 45 minutes and then allowed to slowly cool to room temperature, still held between the glass plates.

According to the Euler equation (Eq. 1.52), the exit angle and outer diameter should be important geometrical parameters. The dimensional analysis in Section 1.8.2 also suggested that the fill ratio and inlet ratio should be significant. Therefore, these parameters were varied in the experimentally characterized impellers.

First, an impeller that was developed by Allison [50] was adopted as a performance baseline against which other impellers could be compared. This impeller, referred to as "Fan 1," was originally devised for a similar heat sink; its design was based on CFD and

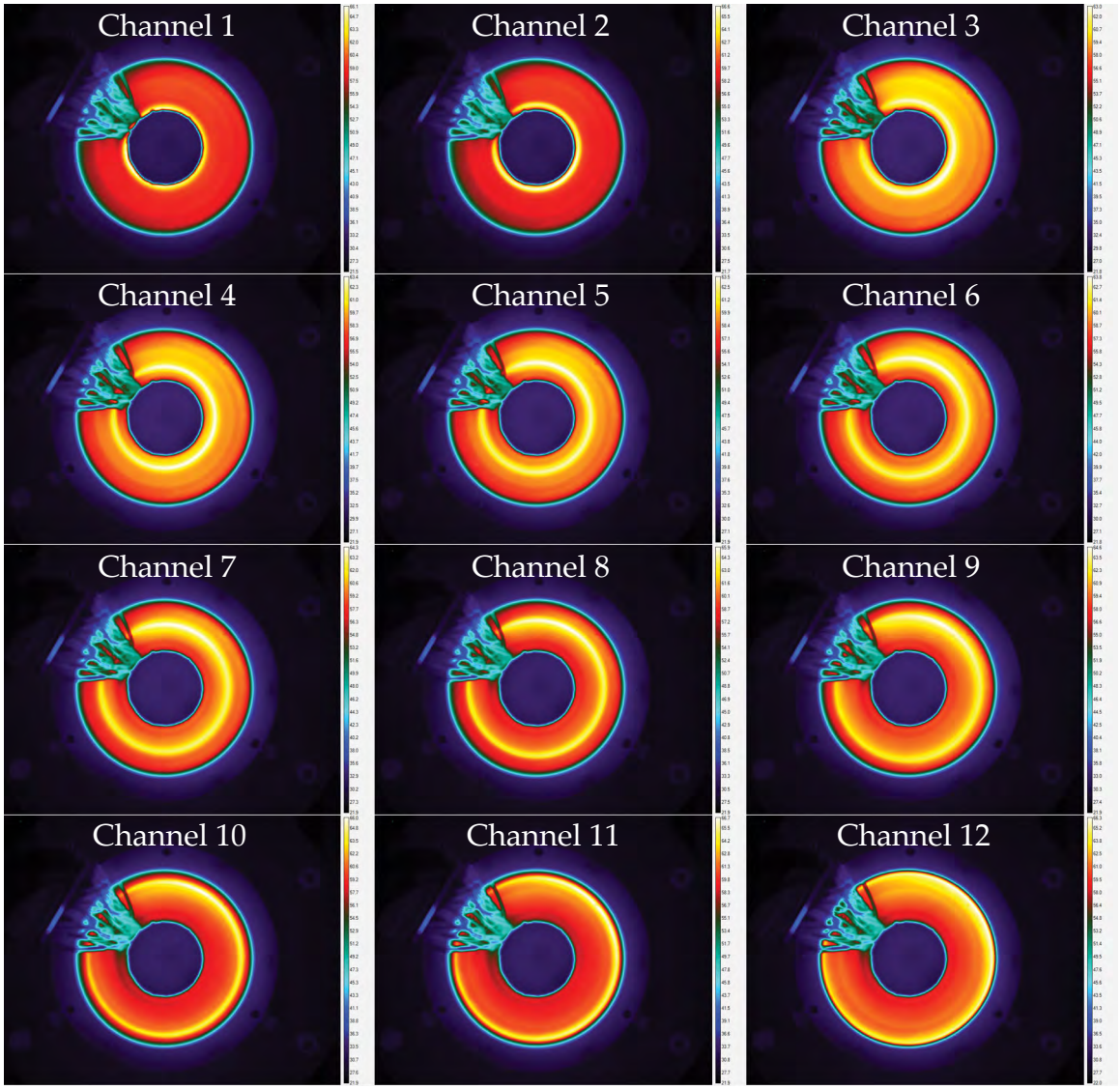

Figure 2-23: A test was performed to (1) determine the location of each heated channel on the thermal image and (2) demonstrate the control capability of the independent channels. These thermal images, taken from below the lower stator, show the temperature field on the lower stator. The impeller speed was set to 5 krpm in the counterclockwise direction, and the heat flux from each channel was set so the stator had a constant temperature. Next, the heat flux in each channel was individually, and in sequence, doubled so its temperature would increase relative to the other channels.

experiments at the free delivery condition. The blade was backswept at an angle that changed linearly from 90 degrees at its root to 42 degrees at its tip; the blade had the thickness profile of the aft portion of a NACA 0011 airfoil, presumably to reduce the likelihood of flow separation. Fan 1 was designed for performance at the free delivery point of the fan curve; it was not tested at points in the fan curve with higher pressure rise. Thus, its performance was unknown for the bulk of its operating range prior to the experimental characterization in this work.

Fans 2 and 3 were 5-bladed, constant blade width, and had exit angles of 45 and 70 degrees, respectively. The entry angles were designed to minimize incidence loss at the inlet at the Euler-predicted point of maximum efficiency, at 5 krpm. The volume flow at this 5 krpm, maximum efficiency point was estimated based on the Euler equation. Fan 4 was a 7-bladed design motivated by a CFD study of the entry and exit angle in a constant blade width impeller. The square stator apparatus was used to characterize only Fans 1–4.

Fans 5–7 had radial (90 degree) blades with 15, 10, and 5 blades. For structural reasons their blades had a very slight linear taper, becoming thinner toward the blade tip. Fans 14 and 15 were identical to Fan 5 but were scaled to an outer diameter of 75 and 120 mm, respectively (except for the center hole, which remained 6 mm in diameter). Fans 8 (15-bladed) and 10 (20-bladed) also had radial blades but contained an open inner region, with 3 spokes emanating from the center shaft hole and connecting to a support ring. The support ring kept the inlet eye and stator gap entry unobstructed and also improved the structural integrity of the impeller blades. This feature proved to be important in multilayer stacks of fans, to avoid starvation of the layers in the center of the stack.

Structurally, radial blades have an important advantage over backswept blades: the centrifugal force on the blades results in predominantly tensile stress. For the impeller sizes of interest in this work, the blades were very stiff in tension even with the small cross sections shown in Fig. 2-24. In contrast, the weight of each blade causes a *bending*

Table 2.4: Fan Characteristics

Fan	Exit Angle (°)	Number of Blades	Outer Diameter (mm)
1	42.5	5	100
2	45	5	100
3	70	5	100
4	30	7	100
5	90	15	100
6	90	10	100
7	90	5	100
8	90	15	100
9	-	-	100
10	90	20	100
11	75	15	100
12	60	15	100
13	45	15	100
14	90	15	75
15	90	15	120
16	30	15	100

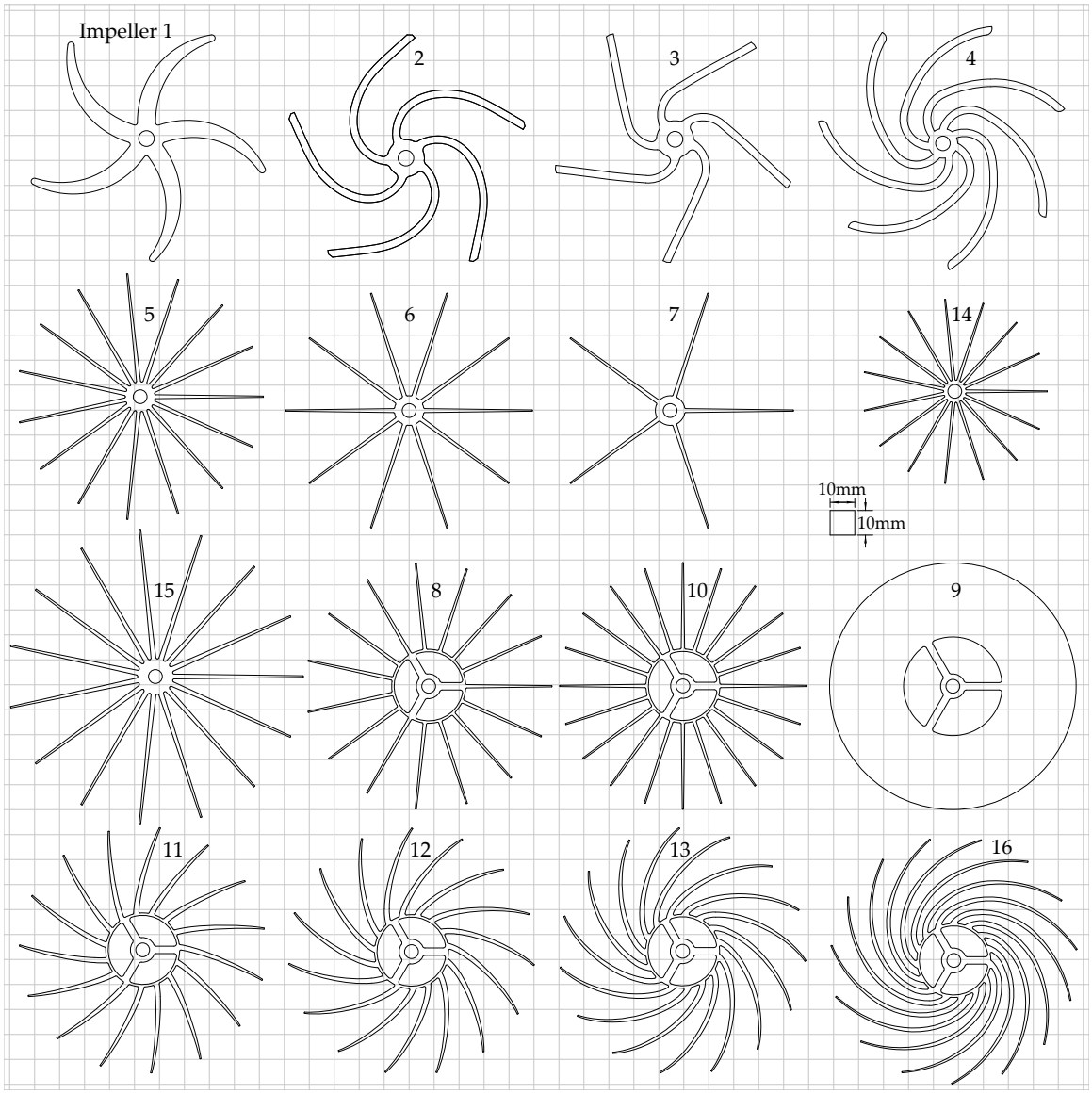

Figure 2-24: The fans characterized in this work, shown to scale on a 10 mm grid. The number by each impeller was used as an identifier.

stress in backswept impellers. The deflection that results from this bending stress can be quite substantial in a long, thin blade. For example, the outer diameter of an abandoned impeller design expanded by several millimeters during operating at speeds of 5 krpm and above. Interestingly, the deflection in these fully unshrouded impellers is *much* more pronounced than in conventional impellers because they lack of the structural support of a shroud. This effect can probably be exploited to design impellers whose diameter (and blade angle) changes with the rotational speed; for example, a fan of smaller diameter could have an "emergency" mode at a higher speed, where diameter would expand. This would increase the flow rate significantly at the expense of a large power requirement. In this work, however, the deflection of the blades was seen as a nuisance to be minimized. In fact, in the square stator apparatus excessive deflection could result in the impeller tips scraping the four corner posts. Therefore, the support ring in Fans 8, 10–13, and 16 served two important purposes: (1) it reduced the length of the cantilevered portion of the blades, thereby reducing its deflection under centrifugal bending; and (2) it allowed the blades to begin at a larger circumference, giving more space for thicker blade roots (i.e. stiffer blades) without excessively blocking the inlet eye. Again, this minimization of the eye blockage is important when multiple fan layers are stacked and share a common inlet.

Fan 9 was a viscous disc pump, also sometimes referred to as a Tesla pump [80, 81]. The performance of Fan 9 was very poor, and thus the idea was not pursued to the same extent as the other impellers. Fans 11–13 had 15 backswept blades originating from the support ring. Their blades followed a logarithmic spiral and had a thickness distribution roughly proportional to r^{-2}, in order to reduce the centrifugal bending force. The blade angles of Fans 11–13 were 75, 60, and 45 degrees, respectively.

Table 2.5 lists the experiments performed; it includes the experimental reference identifier (EID), the apparatus used, the type of test performed, and the major geometrical parameters. The geometrical parameters listed in Table 2.5 are also shown in Fig. 2-25. Some of the fans listed are designated "1w," which means that the profile of Fan 1 was tested with wiper blades, which will be discussed in Section 4.5.1. Finally, Fig. 2-26 shows a graphical summary of the experiments performed, indicating the impeller number, gap breadth, and type of experiment performed.

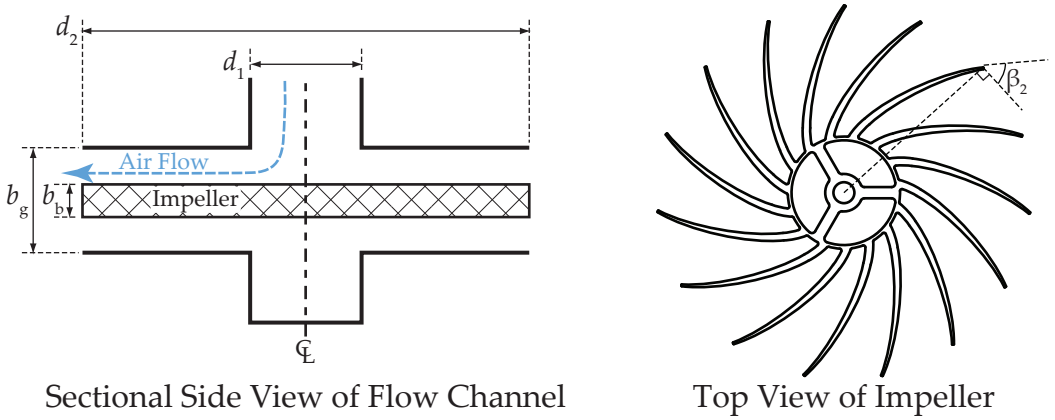

Figure 2-25: A schematic cross section of an integrated fan showing the gap breadth (b_g), the blade breadth (b_b), and the inner and outer diameters (d_1 and d_2), and a top view of an impeller showing the exit blade angle (β_2).

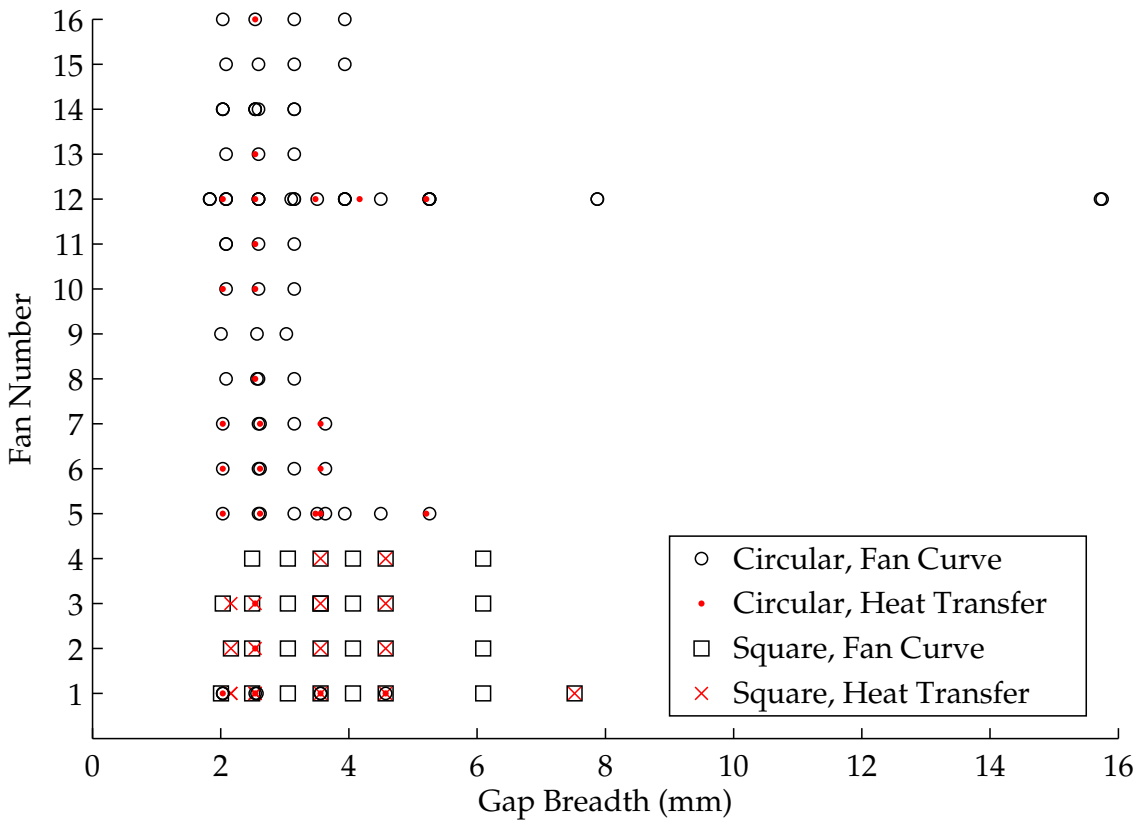

Figure 2-26: The experiments performed on the circular and square stator apparatuses, shown in graphical form.

Table 2.5: Fan Characterizations Performed

EID	Apparatus	Exp. Type	Fan	d_2 (mm)	d_1 (mm)	b_b (mm)	b_g (mm)
64	Square	Bearing Loss	-	-	-	-	-
65	Square	Bearing Loss	-	-	-	-	-
66	Square	Bearing Loss	-	-	-	-	-
68	Square	Bearing Loss	-	-	-	-	-
71	Square	Bearing Loss	-	-	-	-	-
72	Square	Bearing Loss	-	-	-	-	-
73	Square	Bearing Loss	-	-	-	-	-
76	Square	Bearing Loss	-	-	-	-	-
77	Square	Bearing Loss	-	-	-	-	-
79	Square	Bearing Loss	-	-	-	-	-
81	Square	Bearing Loss	-	-	-	-	-
84	Square	Bearing Loss	-	-	-	-	-
91	Square	Bearing Loss	-	-	-	-	-
99	Square	Bearing Loss	-	-	-	-	-
110	Square	Bearing Loss	-	-	-	-	-
113	Square	Bearing Loss	-	-	-	-	-

(continued on next page)

(continued from previous page)

EID	Apparatus	Exp. Type	Fan	d_2 (mm)	d_1 (mm)	b_b (mm)	b_g (mm)
119	Square	Bearing Loss	-	-	-	-	-
122	Square	Bearing Loss	-	-	-	-	-
131	Square	Bearing Loss	-	-	-	-	-
136	Square	Bearing Loss	-	-	-	-	-
141	Square	Bearing Loss	-	-	-	-	-
147	Square	Bearing Loss	-	-	-	-	-
188	Square	Bearing Loss	-	-	-	-	-
75	Square	Fan Curve	1	100	40	1.52	2.01
69	Square	Fan Curve	1	100	40	1.52	2.49
86	Square	Fan Curve	1	100	40	1.52	3.05
87	Square	Fan Curve	1	100	40	1.52	3.56
88	Square	Fan Curve	1	100	40	1.52	4.06
63	Square	Fan Curve	1	100	40	1.52	4.57
127	Square	Fan Curve	1	100	40	1.52	6.10
115	Square	Fan Curve	1	100	40	6.50	7.52
89	Square	Fan Curve	2	100	40	1.52	2.16
70	Square	Fan Curve	2	100	40	1.52	2.49
90	Square	Fan Curve	2	100	40	1.52	3.05
120	Square	Fan Curve	2	100	40	1.52	3.56
125	Square	Fan Curve	2	100	40	1.52	4.06
92	Square	Fan Curve	2	100	40	1.52	4.57
128	Square	Fan Curve	2	100	40	1.52	6.10
93	Square	Fan Curve	3	100	40	1.52	2.03
74	Square	Fan Curve	3	100	40	1.52	2.49
94	Square	Fan Curve	3	100	40	1.52	3.05
95	Square	Fan Curve	3	100	40	1.52	3.56
121	Square	Fan Curve	3	100	40	1.52	3.56
96	Square	Fan Curve	3	100	40	1.52	4.06
97	Square	Fan Curve	3	100	40	1.52	4.57
129	Square	Fan Curve	3	100	40	1.52	6.10
67	Square	Fan Curve	4	100	40	1.52	2.49
123	Square	Fan Curve	4	100	40	1.52	3.05
112	Square	Fan Curve	4	100	40	1.52	3.56
124	Square	Fan Curve	4	100	40	1.52	4.06
126	Square	Fan Curve	4	100	40	1.52	4.57
130	Square	Fan Curve	4	100	40	1.52	6.10
82	Square	Fan Curve	1w	100	40	2.54	2.67
85	Square	Fan Curve	1w	100	40	2.54	2.67
137	Square	Fan Curve	1w	100	40	2.54	3.05
132	Square	Fan Curve	1w	100	40	2.54	3.56
138	Square	Fan Curve	1w	100	40	2.54	4.06
139	Square	Fan Curve	1w	100	40	2.54	4.57
140	Square	Fan Curve	1w	100	40	2.54	6.10
149	Square	Fan Curve	1w	100	40	4.57	5.08

(continued on next page)

(continued from previous page)

EID	Apparatus	Exp. Type	Fan	d_2 (mm)	d_1 (mm)	b_b (mm)	b_g (mm)
148	Square	Fan Curve	1w	100	40	4.57	5.59
142	Square	Fan Curve	1w	100	40	4.57	6.10
143	Square	Fan Curve	1w	100	40	4.57	6.60
144	Square	Fan Curve	1w	100	40	4.57	7.11
104	Square	Heat Transfer	1	100	40	1.52	2.16
105	Square	Heat Transfer	1	100	40	1.52	2.16
100	Square	Heat Transfer	1	100	40	1.52	2.54
145	Square	Heat Transfer	1	100	40	1.52	2.54
146	Square	Heat Transfer	1	100	40	1.52	2.54
117	Square	Heat Transfer	1	100	40	1.52	3.56
116	Square	Heat Transfer	1	100	40	1.52	4.57
114	Square	Heat Transfer	1	100	40	6.50	7.52
102	Square	Heat Transfer	2	100	40	1.52	2.16
98	Square	Heat Transfer	2	100	40	1.52	2.54
118	Square	Heat Transfer	2	100	40	1.52	3.56
106	Square	Heat Transfer	2	100	40	1.52	4.57
103	Square	Heat Transfer	3	100	40	1.52	2.16
101	Square	Heat Transfer	3	100	40	1.52	2.54
133	Square	Heat Transfer	3	100	40	1.52	3.56
107	Square	Heat Transfer	3	100	40	1.52	4.57
134	Square	Heat Transfer	4	100	40	1.52	3.56
108	Square	Heat Transfer	4	100	40	1.52	4.57
83	Square	Heat Transfer	1w	100	40	2.54	2.67
135	Square	Heat Transfer	1w	100	40	2.54	3.56
109	Square	Heat Transfer	1w	100	40	2.54	4.57
193	Circular	Bearing Loss	-	-	-	-	-
206	Circular	Bearing Loss	-	-	-	-	-
207	Circular	Bearing Loss	-	-	-	-	-
208	Circular	Bearing Loss	-	-	-	-	-
218	Circular	Bearing Loss	-	-	-	-	-
219	Circular	Bearing Loss	-	-	-	-	-
220	Circular	Bearing Loss	-	-	-	-	-
221	Circular	Bearing Loss	-	-	-	-	-
222	Circular	Bearing Loss	-	-	-	-	-
223	Circular	Bearing Loss	-	-	-	-	-
224	Circular	Bearing Loss	-	-	-	-	-
190	Circular	Fan Curve	1	100	40	1.52	2.03
200	Circular	Fan Curve	1	100	40	1.52	2.03
237	Circular	Fan Curve	1	100	40	1.52	2.03
189	Circular	Fan Curve	1	100	40	1.52	2.54
230	Circular	Fan Curve	1	100	40	1.52	2.57
191	Circular	Fan Curve	1	100	40	1.52	3.56
197	Circular	Fan Curve	1	100	40	1.52	3.56
192	Circular	Fan Curve	1	100	40	1.52	4.57

(continued on next page)

(continued from previous page)

EID	Apparatus	Exp. Type	Fan	d_2 (mm)	d_1 (mm)	b_b (mm)	b_g (mm)
278	Circular	Fan Curve	5	100	40	1.57	2.03
231	Circular	Fan Curve	5	100	40	1.57	2.59
204	Circular	Fan Curve	5	100	40	1.57	2.62
279	Circular	Fan Curve	5	100	40	1.57	3.15
215	Circular	Fan Curve	5	100	40	1.57	3.63
290	Circular	Fan Curve	5	100	40	3.12	3.51
293	Circular	Fan Curve	5	100	40	3.12	3.94
294	Circular	Fan Curve	5	100	40	3.12	4.50
297	Circular	Fan Curve	5	100	40	3.12	5.26
277	Circular	Fan Curve	6	100	40	1.57	2.03
232	Circular	Fan Curve	6	100	40	1.57	2.59
209	Circular	Fan Curve	6	100	40	1.57	2.62
280	Circular	Fan Curve	6	100	40	1.57	3.15
213	Circular	Fan Curve	6	100	40	1.57	3.63
276	Circular	Fan Curve	7	100	40	1.57	2.03
233	Circular	Fan Curve	7	100	40	1.57	2.59
210	Circular	Fan Curve	7	100	40	1.57	2.62
281	Circular	Fan Curve	7	100	40	1.57	3.15
214	Circular	Fan Curve	7	100	40	1.57	3.63
241	Circular	Fan Curve	8	100	40	1.57	2.08
216	Circular	Fan Curve	8	100	40	1.57	2.57
225	Circular	Fan Curve	8	100	40	1.57	2.59
282	Circular	Fan Curve	8	100	40	1.57	3.15
217	Circular	Fan Curve	9	100	40	1.55	2.57
275	Circular	Fan Curve	9	100	40	1.55	2.01
283	Circular	Fan Curve	9	100	40	1.55	3.02
238	Circular	Fan Curve	10	100	40	1.57	2.08
226	Circular	Fan Curve	10	100	40	1.57	2.59
284	Circular	Fan Curve	10	100	40	1.57	3.15
239	Circular	Fan Curve	11	100	40	1.57	2.08
240	Circular	Fan Curve	11	100	40	1.57	2.08
227	Circular	Fan Curve	11	100	40	1.57	2.59
285	Circular	Fan Curve	11	100	40	1.57	3.15
242	Circular	Fan Curve	12	100	40	1.57	1.83
243	Circular	Fan Curve	12	100	40	1.57	1.83
235	Circular	Fan Curve	12	100	40	1.57	2.08
260	Circular	Fan Curve	12	100	40	1.57	2.08
228	Circular	Fan Curve	12	100	40	1.57	2.59
261	Circular	Fan Curve	12	100	40	1.57	2.59
244	Circular	Fan Curve	12	100	40	1.57	3.15
245	Circular	Fan Curve	12	100	40	1.57	3.15
246	Circular	Fan Curve	12	100	40	1.57	3.94
247	Circular	Fan Curve	12	100	40	1.57	3.94
248	Circular	Fan Curve	12	100	40	1.57	5.26

(continued on next page)

(continued from previous page)

EID	Apparatus	Exp. Type	Fan	d_2 (mm)	d_1 (mm)	b_b (mm)	b_g (mm)
249	Circular	Fan Curve	12	100	40	1.57	5.26
250	Circular	Fan Curve	12	100	40	1.57	7.87
251	Circular	Fan Curve	12	100	40	1.57	15.72
291	Circular	Fan Curve	12	100	40	3.12	3.51
292	Circular	Fan Curve	12	100	40	3.12	3.94
295	Circular	Fan Curve	12	100	40	3.12	4.50
296	Circular	Fan Curve	12	100	40	3.12	5.26
252	Circular	Fan Curve	12	100	50	1.57	1.83
253	Circular	Fan Curve	12	100	50	1.57	2.08
254	Circular	Fan Curve	12	100	50	1.57	2.59
255	Circular	Fan Curve	12	100	50	1.57	3.10
256	Circular	Fan Curve	12	100	50	1.57	3.94
257	Circular	Fan Curve	12	100	50	1.57	5.25
258	Circular	Fan Curve	12	100	50	1.57	7.87
259	Circular	Fan Curve	12	100	50	1.57	15.75
236	Circular	Fan Curve	13	100	40	1.57	2.08
229	Circular	Fan Curve	13	100	40	1.57	2.59
286	Circular	Fan Curve	13	100	40	1.57	3.15
272	Circular	Fan Curve	14	75	40	1.57	2.03
273	Circular	Fan Curve	14	75	40	1.57	2.03
270	Circular	Fan Curve	14	75	40	1.57	2.54
271	Circular	Fan Curve	14	75	40	1.57	2.54
234	Circular	Fan Curve	14	75	40	1.57	2.59
269	Circular	Fan Curve	14	75	40	1.57	3.15
267	Circular	Fan Curve	14	75	50	1.57	2.03
266	Circular	Fan Curve	14	75	50	1.57	2.54
268	Circular	Fan Curve	14	75	50	1.57	3.15
262	Circular	Fan Curve	15	120	50	1.57	2.08
263	Circular	Fan Curve	15	120	50	1.57	2.59
264	Circular	Fan Curve	15	120	50	1.57	3.15
265	Circular	Fan Curve	15	120	50	1.57	3.94
274	Circular	Fan Curve	16	100	40	1.55	2.03
288	Circular	Fan Curve	16	100	40	1.55	2.54
287	Circular	Fan Curve	16	100	40	1.55	3.15
289	Circular	Fan Curve	16	100	40	1.55	3.94
201	Circular	Heat Transfer	1	100	40	1.52	2.03
195	Circular	Heat Transfer	1	100	40	1.52	2.54
196	Circular	Heat Transfer	1	100	40	1.52	3.56
198	Circular	Heat Transfer	1	100	40	1.52	4.57
202	Circular	Heat Transfer	2	100	40	1.52	2.54
203	Circular	Heat Transfer	3	100	40	1.52	2.54
307	Circular	Heat Transfer	5	100	40	1.57	2.03
205	Circular	Heat Transfer	5	100	40	1.57	2.62
311	Circular	Heat Transfer	5	100	40	1.57	3.56

(continued on next page)

(continued from previous page)

EID	Apparatus	Exp. Type	Fan	d_2 (mm)	d_1 (mm)	b_b (mm)	b_g (mm)
314	Circular	Heat Transfer	5	100	40	3.12	3.48
304	Circular	Heat Transfer	5	100	40	3.12	5.21
308	Circular	Heat Transfer	6	100	40	1.57	2.03
212	Circular	Heat Transfer	6	100	40	1.57	2.62
312	Circular	Heat Transfer	6	100	40	1.57	3.56
309	Circular	Heat Transfer	7	100	40	1.57	2.03
211	Circular	Heat Transfer	7	100	40	1.57	2.62
313	Circular	Heat Transfer	7	100	40	1.57	3.56
298	Circular	Heat Transfer	8	100	40	1.57	2.54
310	Circular	Heat Transfer	10	100	40	1.57	2.03
299	Circular	Heat Transfer	10	100	40	1.57	2.54
300	Circular	Heat Transfer	11	100	40	1.57	2.54
306	Circular	Heat Transfer	12	100	40	1.57	2.03
301	Circular	Heat Transfer	12	100	40	1.57	2.54
315	Circular	Heat Transfer	12	100	40	3.12	3.48
316	Circular	Heat Transfer	12	100	40	3.12	4.17
305	Circular	Heat Transfer	12	100	40	3.12	5.21
302	Circular	Heat Transfer	13	100	40	1.57	2.54
303	Circular	Heat Transfer	16	100	40	1.55	2.54

2.4 Summary

To understand the performance of fully unshrouded centrifugal fans, a number of experiments were performed. Two main apparatuses — the square stator apparatus and the circular stator apparatus — were constructed. Each apparatus could perform tests to measure the fan performance (pressure rise and power consumption versus volume flow) and the heat transfer performance (heat transfer coefficient). Additionally, the circular stator apparatus was constructed with the ability to characterize the local heat transfer coefficient in the air flow using a unique variation of the heated thin film IR thermography method.

A number of impeller geometries were characterized in the experimental apparatuses. 16 impeller profiles were tested with various stator gap breadths, blade breadths, inner and outer diameters. This allowed a number of dimensionless geometrical parameters to be explored, including the blade exit angle, number of blades, fill ratio, inlet ratio and aspect ratio; the experimental data was used to provide a sound basis for insight into how these unique fans can be exploited in thermal fluid systems. Ultimately, this understanding is based on direct measurements of the fans' performance, and thus can be relied upon to yield accurate performance predictions.

THIS PAGE INTENTIONALLY LEFT BLANK

CHAPTER 3

CFD ANALYSIS

In this chapter, some attempts at modeling integrated fans using computational fluid dynamics (CFD) are discussed. Integrated fans have some features that commonly result in difficulties for CFD solvers. As such, the success of modeling these fans using CFD programs was uncertain. To determine whether CFD could yield satisfactory predictions, several benchmark simulations were performed and compared with experimental data (which will be discussed in greater detail in Chapter 4). A CFD model of an experimentally characterized fan was tested with three turbulence models and with different mesh sizes. Based on the mesh size estimates of this study, a second study was conducted to compare the heat transfer predictions of these turbulence models. Finally, a third study tested another experimentally characterized fan design with a more complicated impeller profile and various fill ratios.

CFD simulations were also used to qualitatively explore some of the parameter space of the integrated fans. Several studies were performed to investigate the effect of the number of blades and various geometrical ratios defining the fan. These studies are presented to demonstrate how CFD of integrated fans can provide useful insights and ultimately result in better fan design.

It will be shown that CFD models using relatively low-computational-cost modeling approaches can give reasonable agreement with experimental data in the pressure rise and mechanical power predictions. On the other hand, with respect to the heat transfer, reasonable agreement was achieved only under certain conditions. Fortunately, it will be shown in Chapter 4 that the heat transfer is relatively independent of the impeller profile, and depends mostly on the operating point (i.e. the channel Reynolds number and rotational Reynolds number). The fan's ability to reach an operating point is independent of the heat transfer into the system, and can be simulated in CFD without any need to represent the heated surfaces. The success of CFD in predicting the fan's operating point suggests that it can be used in combination with empirical heat transfer correlations to design integrated fans.

3.1 Model Description

The integrated fans were modeled using ANSYS CFX [82], a commercially available CFD software package. For computational efficiency, the impeller was modeled using a rota-

tionally symmetric portion of the fan and stator, as shown in Fig. 3-1. The model shown in Fig. 3-1 is a wedge-shaped[1] portion of a circular fan, with the impeller blade situated in the middle of domain. The effects of blockages in the exit plane (e.g. the corner posts in the square stator apparatus) were not included in the model.

The model was comprised of two domains: a fixed domain and a rotating domain that contained the impeller blade. The rotating domain had slightly different governing equations that account for the centrifugal and Coriolis forces. The two domains were joined using a "frozen rotor" condition, which treats the fixed and rotating domains' relative positions as fixed. At the interface between the domains, the components of velocity (accounting for the frame change) are continuous and the pressure is equal. The frozen rotor condition is one of the simplest and most robust frame change models; in situations with strong rotor-stator interactions, however, the frozen rotor model can be problematic [83, 84]. These modeling problems arise due to the rotor-position-dependence inherent in devices rotor-stator interactions, which is ignored with the frozen rotor model. In these cases, a different frame-change model would be appropriate. In the integrated fan simulations, the frozen rotor model was used because the rotor-stator interactions are not position-dependent in the axisymmetric domain. This axisymmetric topology of the CFD model is similar to that of the circular stator apparatus, allowing for side-by-side comparisons to experimental data.

At the inlet and outlet, the model mostly followed the ANSYS "best practices" guidelines, which recommend a mass flow or velocity inlet and a static pressure outlet as numerically robust boundary conditions [83]. Figure 3-2 shows the various boundary conditions in the model. A normal velocity was prescribed at the inlet and a static pressure "opening" was applied at the outlet. Openings are similar to outlets, but in contrast to an outlet the direction of the flow is not specified; this distinction is important in the more restricted operating regimes of the fans, when a recirculatory zone establishes itself at the exit plane of the impeller, and can cause the outlet of the model to have a tangential velocity component. The inlet and the outlet each had a small "calming section" so the interface between the stationary and rotating domains was not too close to either the inlet or the outlet. The side walls of the wedge-shaped domains had rotationally periodic boundary conditions. The two flat walls near the outlet of the model were modeled as free slip walls, and the remaining boundary conditions in the model were no-slip, hydraulically smooth walls.

Analogous to the experiments discussed in Chapter 2, two main types of simulations were performed: (1) adiabatic (and unheated) stator fan characterizations and (2) isothermal (above ambient temperature) stator heat transfer characterizations. The quantities of interest in characterizing the fan were the total-to-static head coefficient (ψ_{ts}) and the power coefficient (ξ) as functions of the flow coefficient (ϕ). These were determined in the simulations by calculating the total pressure at the inlet and the torque on the impeller blade.

The total pressure at the inlet was determined through an area average on the inlet plane at the conclusion of a simulation and the net mass flow rate was known a priori through the specification of the velocity; the static pressure at the outlet opening was specified as an input parameter. The torque on the impeller about the rotational axis was determined by integrating the torque contributions due to forces on the boundary defining the blade. Once the torque was determined, the mechanical power was simply

[1] For impellers with curved blades, the edges of the domain followed the same curve that defined the blade shape.

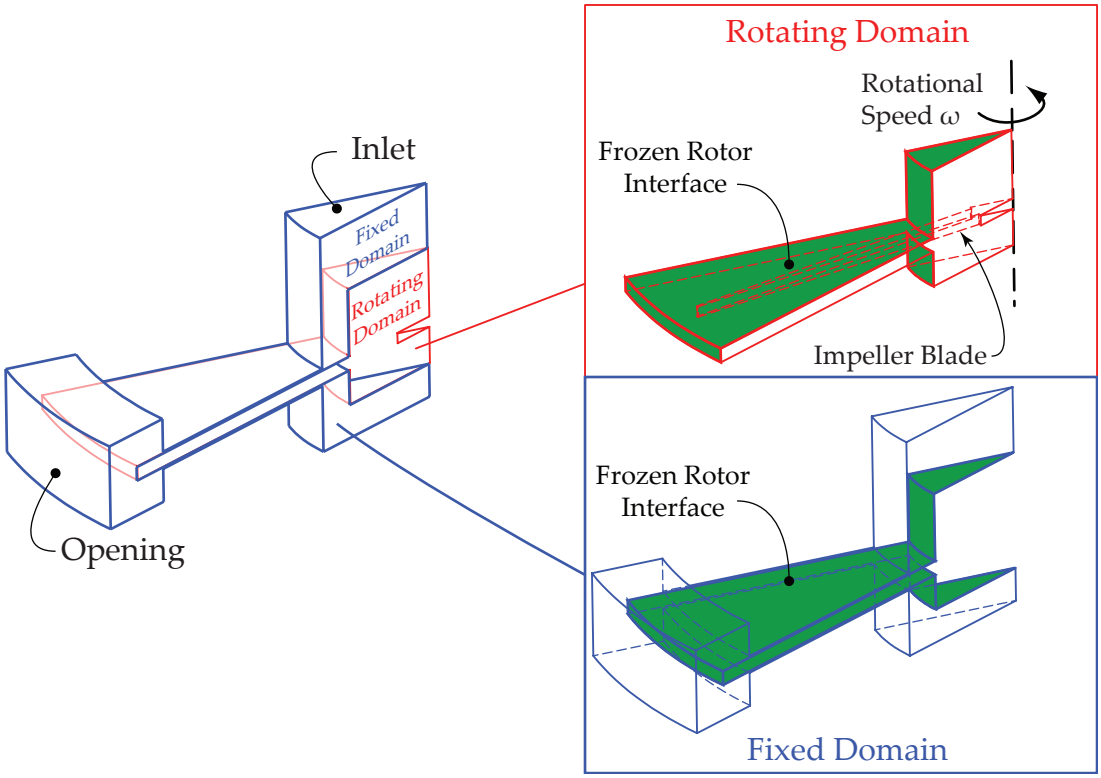

Figure 3-1: The CFD models consisted of an axisymmetric segment of a fan with a single impeller blade. The model was comprised of a stationary and a rotating domain which were joined with a frozen rotor condition, meaning that the relative positions of the two domains were treated as fixed. In this reference-frame-change model, pressure and velocity (accounting for the change in reference frame) are continuous across the interface. The side walls are treated with a rotationally periodic boundary condition so pressure and velocity are identical on the opposite walls (see Fig. 3-2).

calculated as the product of the torque and the rotational speed. Fan curves and power curves were determined at a fixed rotational speed by running several simulations, each with a different velocity at the inlet, and calculating the inlet total pressure and torque for each simulation. The dimensionless parameters were calculated according to their definitions in Section 1.8.2.

In the heat transfer characterizations, the no-slip wall boundary condition on the stator walls was set to a constant temperature (50 K above the inlet temperature). The heat transfer tests used the same procedure as the fan curve tests for determining the fan curves but also included, in post-processing, the integration of the heat flux on the stator walls to determine the total heat transfer into the system. The heat transfer characterizations required the addition of the energy equation in the fluid model. Changes in density associated with the increasing temperature were accounted for by using an ideal gas model for the air.

3.2 Benchmarking

The fans studied in this work have features that suggest CFD analysis may be difficult. Several disparate length scales are important in the problem. The diameter, for example,

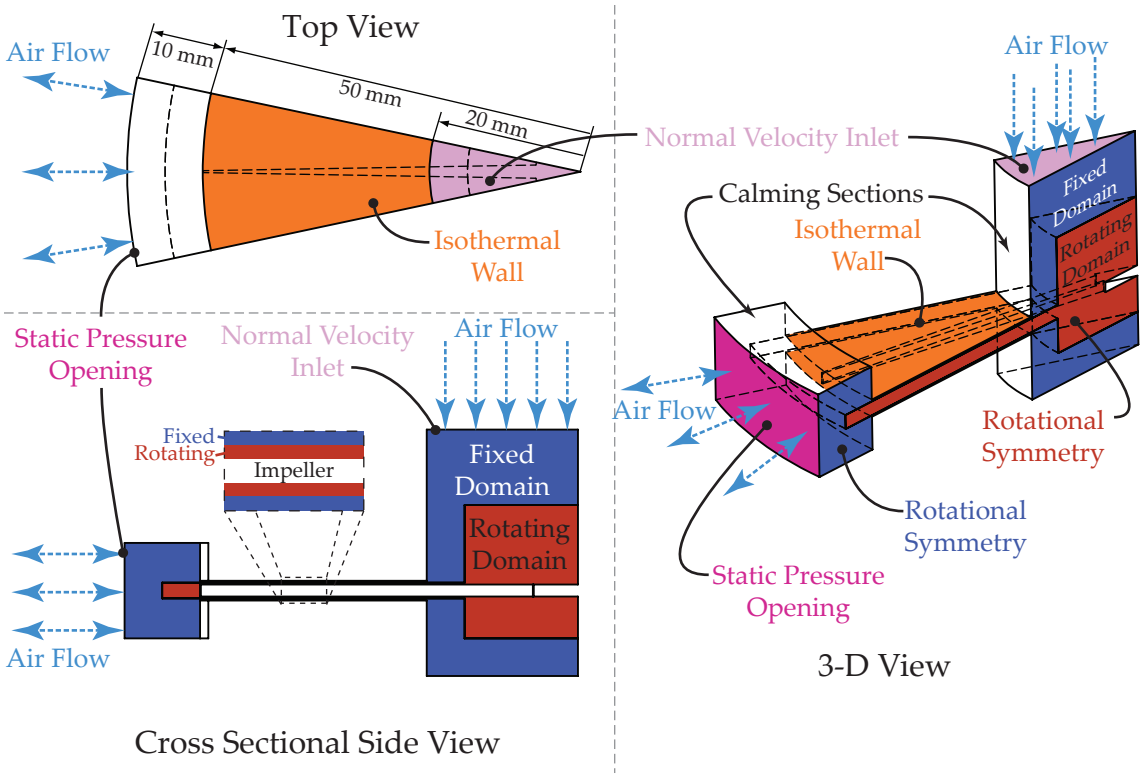

Figure 3-2: The CFD models consisted of a stationary and rotating domain. The inlet boundary condition was a normal velocity inlet, and the outlet boundary condition was a static pressure opening (meaning that the flow direction is not specified). The sides of the wedge-shaped domains had rotationally periodic conditions that allowed flow to pass to the opposite side of the domain. For the heat transfer tests, the stator walls had an isothermal no-slip wall that was 50 K above the inlet air temperature. The cross sectional side view (which cuts through the center of the impeller blade) shows a close-up view of the stator gap, and the fixed-rotating interface in that region.

is a fundamental parameter in the Euler turbomachinery equation; simultaneously, the gap between the impeller and the wall has a strong effect on the tip leakage from the pressure to the suction side of each blade. The ratio of these length scales was commonly 200:1 or greater. Separation on the suction side of the blade is also known to be an important effect in centrifugal fans. Unfortunately, prediction of separation is a challenging phenomenon to model, and many turbulence models do not properly capture these physics. In this section, some CFD modeling attempts are discussed, some of which achieved good agreement with experimental data. Efforts to determine satisfactory turbulence models, boundary conditions, and mesh size are outlined.

3.2.1 Turbulence Models

Several classes of simulations capable of simulating turbulence are prevalent in modern CFD. Direct numerical simulation (DNS) simulates the entire flow field to the resolution of the smallest eddies at great computational cost. Large eddy simulation (LES) is similar to DNS but uses a filtering scheme to lower the number of computations. The Reynolds Averaged Navier-Stokes (RANS) methods add several conservation equations for effective

transport properties (e.g. viscosity) and have the greatest computational efficiency of these approaches.

Common RANS methods include the $k-\epsilon$, $k-\omega$, and Shear Stress Transport (SST) models. The $k-\epsilon$ model is widely used and often shows up as the default turbulence model in commercial CFD software. However, this model is known to fail at predicting separation and near-wall phenomena. Conversely, the $k-\omega$ model excels at predicting near-wall conditions but does not predict freestream phenomena as accurately. The SST model combines the $k-\epsilon$ and $k-\omega$ models with a blending function, and shows better agreement with experimental data under a variety of conditions [85, 86].

RANS models are much less computationally intensive, and therefore find more widespread use than DNS or LES. To determine whether RANS models are capable of simulating integrated fans, several benchmark tests were performed. Three turbulence models (laminar/none, $k-\epsilon$, and SST) were compared to experimental data from the circular stator apparatus. Three mesh sizes were used for each turbulence model, with two different refinement levels[2] in the stator gap region.

Figure 3-3 shows the results of these benchmark tests. In Fig. 3-3, the solid black circles are experimental data (for Fan 5 with $b_\mathrm{b} = 1.6\,\mathrm{mm}$ and $b_\mathrm{g} = 2.0\,\mathrm{mm}$) with a best-fit curve; the CFD results are indicated with markers whose shape and color correspond to the number of elements, as indicated by the legend. The 7k, 43k, and 142k trials had a refinement of 1, while the 16k, 83k, and 239k trials had a refinement of 2. The best-fit curve for the head coefficient was chosen to be a line[3]. For the efficiency, the best-fit curve for the experimental data was a rational function,

$$\eta_\mathrm{ts} = \frac{\phi\psi_\mathrm{ts}}{\xi} = \frac{\phi(\psi_\mathrm{ts,max} - C_\mathrm{r}\phi)}{\xi_0 + C_\mathrm{w}\phi}, \tag{3.1}$$

where $\psi_\mathrm{ts,max}$, C_r, ξ_0, and C_w are the coefficients determined from linear fits to the fan and power curves. This function was determined from the definition of the efficiency (Eq. 1.70) in terms of the dimensionless parameters that define the fan ($\eta_\mathrm{ts} = \phi\psi_\mathrm{ts}/\xi$); the linear fits for the fan and power curves will be discussed in more detail in Section 4.2.3. The function for predicting the experimentally observed efficiency (Eq. 3.1) represents a curve that resembles a parabola, but does not necessarily have symmetry about a constant-ϕ (vertical) line. This skewed nature of the efficiency curve means that the point of best efficiency need not be located at $\phi = \phi_\mathrm{max}/2$ even though the maximum hydraulic power is developed at this point on the fan curve.

The errors in the CFD predictions were quantified using the relative root-mean-squared error (rRMSE), defined as

$$\mathrm{rRMSE} = \sqrt{\frac{1}{n}\sum_{i=1}^{n}\left(\frac{x_\mathrm{p,i} - x_\mathrm{m,i}}{x_\mathrm{m,i}}\right)^2}, \tag{3.2}$$

where $x_\mathrm{m,i}$ is the measured quantity and $x_\mathrm{p,i}$ is the correlation-predicted quantity for data point i of an experiment with n data points. Figure 3-4 shows the rRMSE for each of the simulations shown in Fig. 3-3, assuming that the correct value for a data point is the coordinate (ψ_ts or η_ts) indicated by the best-fit line of the experimental data. As expected,

[2] Refinement is a feature of the CFD meshing software that allows a local increase in the mesh density near certain locations (in this case, in the region bounded by the stator walls).

[3] The observation of linear fan curves is discussed in Chapter 4.

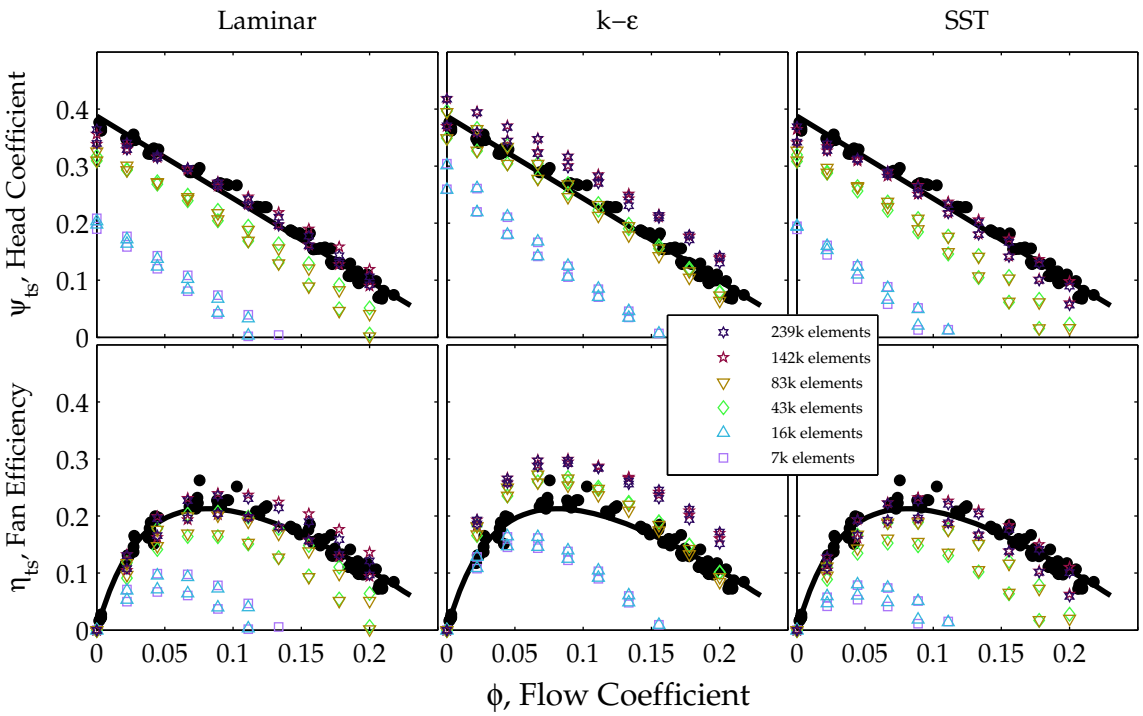

Figure 3-3: Three turbulence models (laminar, $k-\epsilon$, and SST) with various mesh sizes were compared to some experimental data (solid black circles with a best-fit line) for Fan 5, with a blade breadth of $b_b = 1.6\,\text{mm}$ and a gap breadth of $b_g = 2.0\,\text{mm}$. The shape and color of the markers (as indicated in the legend) corresponds to the number of elements; as the number of elements increased, the CFD models more closely approximated the experimental data (with the exception of the $k-\epsilon$ model, which slightly overpredicted the fan curve and the efficiency). Overall, the fan behavior was captured by all three of the turbulence models, as long as the number of elements in the mesh was sufficiently high.

the trends in Fig. 3-3 and 3-4 suggest that increasing the number of elements reduces the error between the simulated and experimentally determined fan performance curves. The exception to this improvement was the increase in error of the $k-\epsilon$ model beyond 43k elements.

Based on initial simulations, the laminar and SST model seem to provide good predictions of the fan and efficiency curves. Next, their effectiveness in predicting the heat transfer was studied. In this next set of benchmarks, 3 values of the fill ratio ($\text{FR} = b_b/b_g = [0.44, 0.61, 0.78]$) with the same 15-blade impeller (Fan 5, $d_2 = 100\,\text{mm}$, $d_1 = 40\,\text{mm}$, $b_b = 1.6\,\text{mm}$) were simulated using the laminar, $k-\epsilon$, and SST turbulence models including the energy equation, and an isothermal boundary condition on the stator walls (with the wall at 50 K above the inlet air temperature: $T_{\text{wall}} - T_{\text{in}} = 50\,\text{K}$). The number of elements in these simulations ranged from 105–114k elements in accordance with the findings from the fan curve benchmarks above.

The results of these heat transfer benchmarks are shown in Fig. 3-5. The laminar model sometimes has accurate predictions, but most of the time the agreement with the experimental data only occurs at low rotational speeds and low Reynolds numbers. It also does not predict significant enhancement between the 3 and 7 krpm curves, which is contrary to the experimental observations. This suggests that the laminar model is not completely

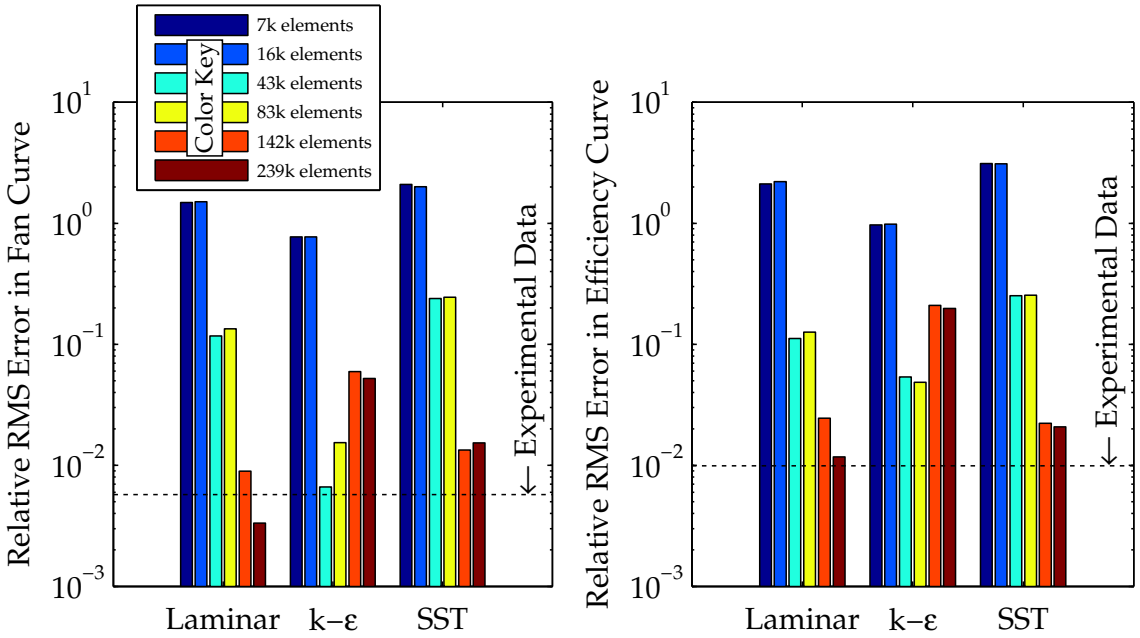

Figure 3-4: The error of the three turbulence models compared in Fig. 3-3 was quantified using the relative RMS error (rRMSE). For each turbulence model, the 6 bars indicate the number of elements, sorted in ascending order from left to right (the number of elements is indicated in the color key). The "correct" value in calculating the error (using Eq. 3.2) was determined from the best-fit curves in Fig. 3-3. Therefore, the experimental data also had an associated error; this error is indicated with the black dashed line. The laminar and SST models most closely predict the experimental data, provided the number of elements is sufficient.

capturing the physics of the heat transfer in the system, despite the agreement in its computed fan performance curves. Additionally, the $k-\epsilon$ model does not agree with the experimental heat transfer data; in general, its computed dimensionless heat flux was off by about 100% at a given Reynolds number. Finally, the SST model shows satisfactory agreement with the experimental data, especially at higher channel Reynolds numbers. At low Re, its computed dimensionless heat flux is in accord with the 7 krpm experiment with a fill ratio of FR = 0.4 (the lower right plot in Fig. 3-5).

To further explore the validity of using the SST model, 4 experimentally-characterized fans were simulated (including the energy equation to estimate the heat transfer) and their results compared with analogous experiments. These fans had the profile of Fan 1, with $d_2 = 100\,\text{mm}$, $d_1 = 40\,\text{mm}$, $b_\text{b} = 1.5\,\text{mm}$, and variable fill ratios (FR = $[0.33, 0.43, 0.60, 0.71]$). Fan 1 has a different geometry than Fan 5 (which was used in the benchmark tests above). Fan 1 only has 5 blades, while fan 5 has 15 blades. This decrease in the number of blades makes the flow passage wider and results in less flow guidance by the blade (and thus a higher slip factor). Fan 1 also has a curved blade, compared to the straight blade in Fan 5. These features were tested to ensure that reasonable predictions could be obtained for various integrated fan geometries.

Meshes with about 150k elements were used in these simulations of Fan 1. For each fan, 15 linearly spaced values of the flow coefficient were simulated. At each of these points, a random rotational speed between 3 and 9 krpm was specified; the inlet velocity was calculated from this combination of flow coefficient and rotational speed. The

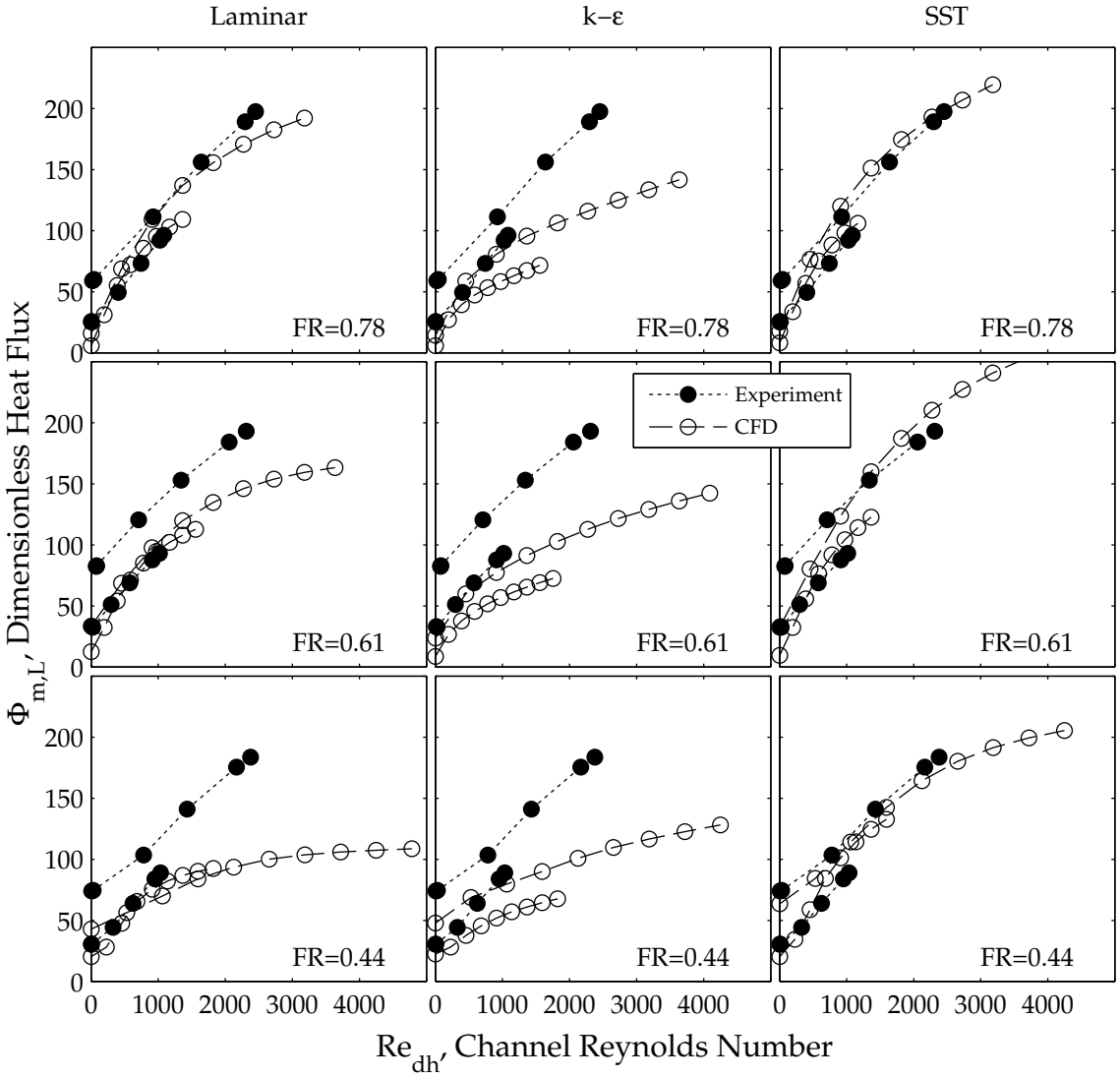

Figure 3-5: The dimensionless heat flux in several integrated fans was calculated using CFD simulations (hollow data markers) and compared to experimental data (solid data markers). Three fill ratios (FR = $[0.44, 0.61, 0.78]$) were tested using the laminar, $k-\epsilon$, and SST turbulence models. The experimental data is shown for rotational speeds of 3 and 7 krpm; the CFD simulations were run at corresponding speeds (the lower of the two curves comprising each data set is the 3 krpm speed). The SST model seems to be the most accurate for predicting the heat transfer. The $k-\epsilon$ model consistently underpredicts the experimental data; the error associated with the laminar model increases at the higher rotational speeds and Reynolds numbers.

fan curves are shown in Fig. 3-6 for the CFD results (represented by hollow markers), and the experiments with corresponding geometry (represented with solid markers). In comparing the simulation results with the experimental data, it can be seen that the CFD computed the trends in the fan and efficiency curves, although the computations were less accurate at the higher fill ratios. Despite having randomly varying rotational speeds, the CFD-computed curves are quite consistent, indicating that the dimensionless parameters effectively removed the dependence on rotational speed from the fan curves.

Despite this satisfactory agreement between the CFD-computed fan performance curves and the experimental data, a potential pitfall of modeling integrated fans is demonstrated in this study as well. Figure 3-7 shows the heat transfer predictions of the CFD model (hollow markers) compared with experimental data (solid markers). The CFD, in this case, clearly fails to provide the trend in the experimentally observed behavior. This shows that a satisfactory fan performance curve from a CFD simulation does not always indicate that the CFD is capable of computing the correct trend in the heat transfer; thus, designers must be cautious of accepting CFD results as valid based solely on agreement in the fan performance curves.

In this chapter, several turbulence models (laminar, $k-\epsilon$, and SST) were tested and compared to experimental data for integrated fans (in particular, for Fan 5). It was shown that, of these models, the laminar and SST models achieved better agreement with experimental data for predicting the fan curves. For predicting the heat transfer, however, the SST model computations captured the essential physics better than the laminar or $k-\epsilon$ models, which showed serious flaws when compared against experimental results. The

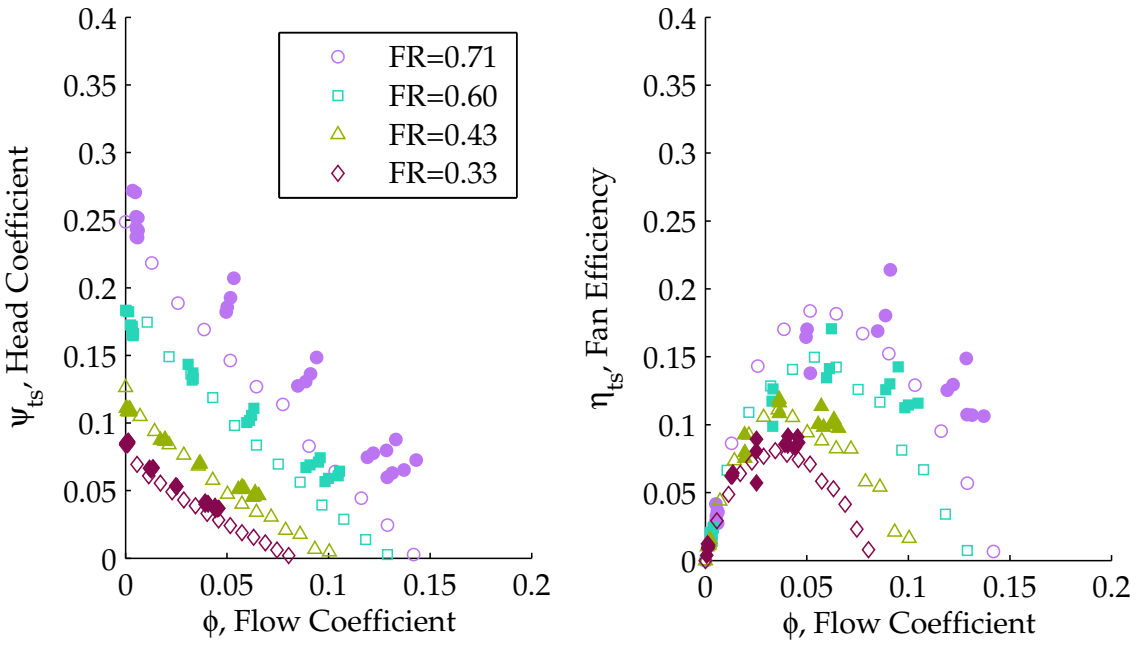

Figure 3-6: A CFD model of Fan 1 (d_2 = 100 mm, d_1 = 40 mm, b_b = 1.5 mm, FR = [0.33, 0.43, 0.60, 0.71]) that used the SST turbulence model computed the trends in the fan and efficiency curves. The solid markers indicate experimental data; the hollow markers represent the CFD results for the corresponding geometry. The marker type indicates the fill ratio (see legend).

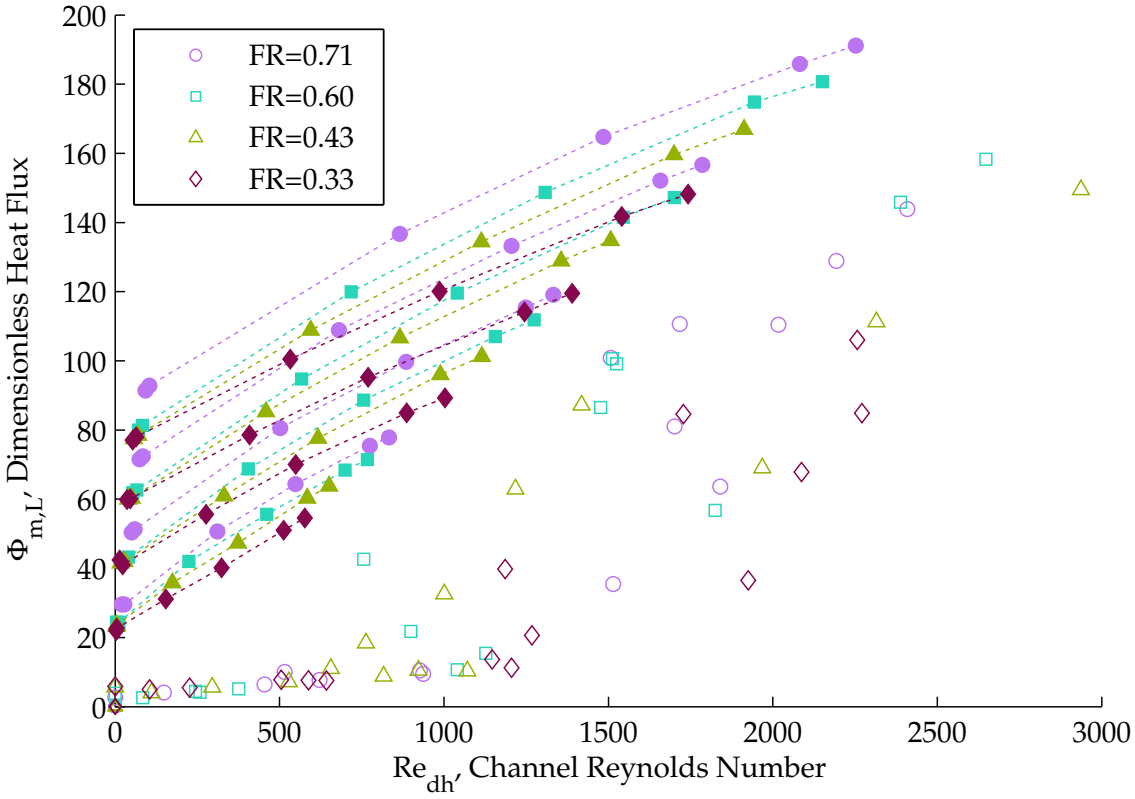

Figure 3-7: The CFD model of Fan 1 (d_2 = 100 mm, d_1 = 40 mm, b_b = 1.5 mm, FR = [0.33, 0.43, 0.60, 0.71]) that used the SST turbulence model predicted the trends in the fan and efficiency curves, as was shown in Fig. 3-6. However, the heat transfer was not satisfactorily predicted by the model. The solid markers indicate experimental data; the hollow markers represent the CFD results for the corresponding geometry. The marker type (see legend) indicates the fill ratio. The experimental data and CFD comprised a range in rotational speeds from 3–9 krpm. The failure of these CFD models to predict the heat transfer shows that satisfactory agreement in the predicted fan curves does not necessarily guarantee fidelity in the heat transfer.

SST model, though capable of computing the heat transfer and fan curves in the benchmark tests, failed to adequately compute the heat transfer in a second benchmark test despite correctly computing the trends in the fan curves. Thus, when performing simulations of integrated fans, great care must be taken in interpreting the results, since agreement in the fan physics do not always mean that the heat transfer will be computed successfully.

In Chapter 4, it will be shown that the heat transfer depends on the operating point of the fan (rotational speed and volume flow), and does not have a noticeable, direct dependence on the profile of the impeller. In other words, the heat transfer can be decoupled from the fan design; the fan design determines the operating point (flow rate for a given rotational speed and system resistance), and the operating point determines the heat transfer. This result is quite fortuitous, because the CFD predicts the flow performance (fan and efficiency curves) of integrated fans much more reliably than the heat transfer.

3.3 Parametric Studies

To illustrate how CFD can be used in the design process for integrated fans, several parametric studies are discussed. These studies were performed to investigate the effects of some basic geometry changes on the pressure rise and power characteristics of some integrated fans. To experimentally characterize all of these variations would be very time consuming and costly. For example, to perform experiments where the inlet diameter (d_1) varies would require multiple duplicate sets of heated plates, as well as the additional time of conducting the experiments. In these parametric studies, the effect of the number of blades, the fill ratio (FR = b_b/b_g), and inlet ratio (IR = d_1/d_2) were examined in three separate studies. First, fans with blades identical to those of Fan 5 were simulated with a varying number of blades. Next, Fan 1 was simulated with varying fill ratio, inlet ratio, aspect ratio, and scale factors. Finally, the inlet ratio was explored further with Fan 5.

3.3.1 Number of Blades

As discussed in Section 1.7, the number of blades is expected to have an effect on the fan performance; adding blades to a fan allows it to better guide the flow and reduce the size of the relative eddy and the variation in velocity across the blade passage. However, at a certain point, the flow blockage introduced by the finite-width blades reduces the pressure rise and outweighs the flow guiding benefit. To determine the optimal number of blades in Fan 5, several sets of CFD simulations were performed on fans with varying numbers of blades. Each of these fans shared the same individual blade shape as Fan 5 and had a fill ratio of FR = b_b/b_g = 1.5 mm/2.5 mm = 0.6; the only change between the fans in these simulations was the number of blades (Z). Figure 3-8 shows the results of these simulations. Clearly, noticeable improvements in both the fan curve and the efficiency curve occur until about 16 blades. The maximum head and flow coefficients (the intercepts of the fan curve) are shown in the upper right plot in Fig. 3-8 as functions of the number of blades. From this plot, an optimum number of blades appears to occur around $Z = 16$. Similarly, the maximum efficiency is shown in the lower right plot of Fig. 3-8. An optimum in this plot seems to occur at $Z = 15$.

This parametric study of the number of blades shows how, in the early part of a design, CFD can be useful in solving simple problems such as determining the number of blades to use in a fan design.

3.3.2 Fan 1 Parameters

Some of the geometrical ratios were studied by performing simulations of 72 design variations of Fan 1 (see Fig. 2-24 for the impeller profile). The base design had an impeller diameter of 100 mm, an inlet diameter of 40 mm, a blade breadth of 1.5 mm and a gap breadth of 2.5 mm. In dimensionless terms, this equates to a fill ratio of FR = 0.6, an aspect ratio of AR = b_b/d_2 = 0.015, and an inlet ratio of IR = d_1/d_2 = 0.4. The 72 designs included variations in the fill ratio (FR = $[0.6, 0.7, 0.8]$), the aspect ratio (AR = $[0.015, 0.025]$), the inlet ratio (IR = [0.30.40.50.6]), and scales (scale = $[0.8, 1, 1.2]$). Changing the scale meant simply applying a uniform scale factor to the base geometry. For example, the 1-scale design had a base diameter of d_2 = 100 mm, and the 0.8-scale design had $d_2 = 0.8 \cdot 100 =$ 80 mm. The scale was varied to confirm the choice of dimensionless parameters and ensure consistency at several different sizes.

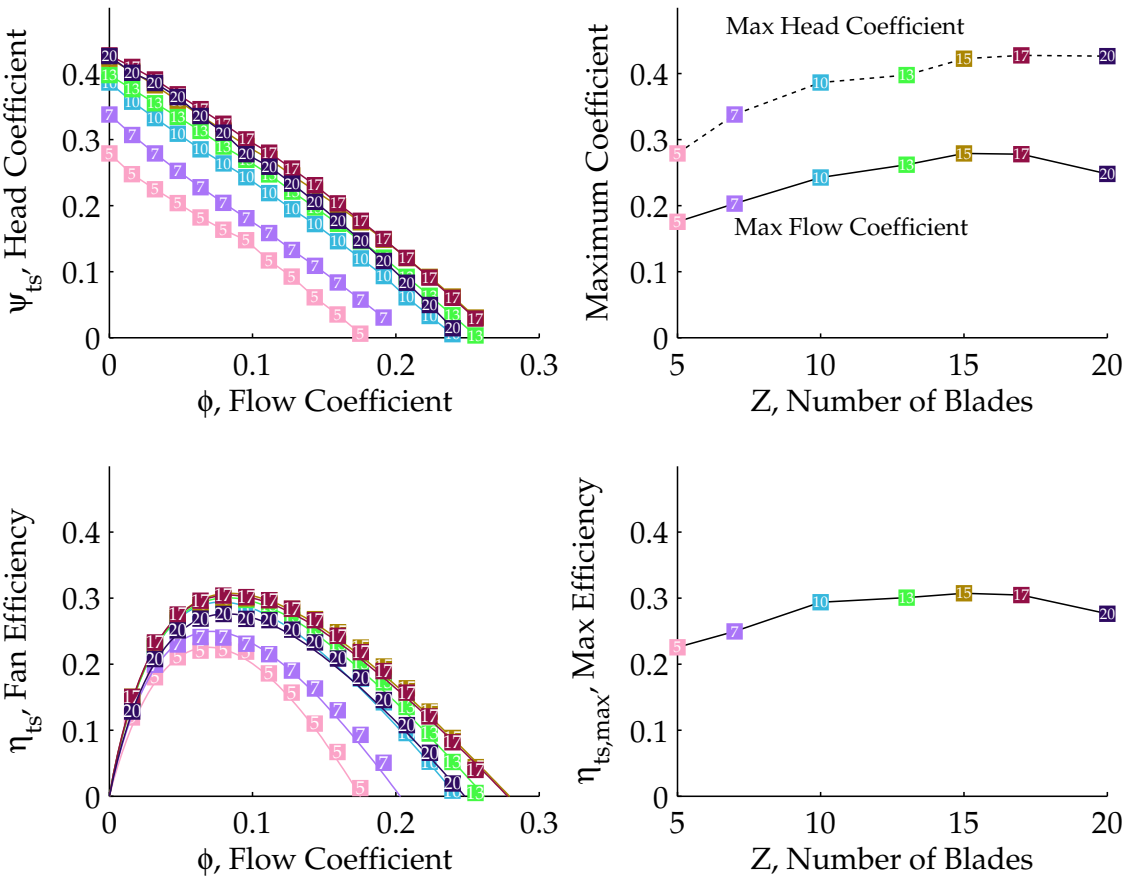

Figure 3-8: CFD simulations were used to predict the fan performance and efficiency curves for radial blade impellers with a fixed outlet diameter (d_2 = 100 mm), fixed blade and gap breadths (b_b = 1.5 mm, b_g = 2.5 mm), and a varying number of blades (Z). Each square represents a single CFD run; the labels in each data point show the number of blades (the 15-blade data points are somewhat concealed by the 17 and 20-blade data points in the upper left plot). The blade shape was the same as that of impeller 5 (and shown in the diagrams of the CFD domain, Figs. 3-1 and 3-2). All of the runs were performed at a rotational speed of 5 krpm. The upper right plot shows the maximum head and flow coefficients (the intercepts of the fan curves in the upper left plot) for each fan; the lower right plot shows the maximum efficiency. An optimum around 15 can be seen in the maximum efficiency and maximum flow coefficient curves; the maximum head coefficient may have a slightly higher optimum, but the slope of the curve is shallow.

For each design, 15 operating points were tested to determine the fan curve. At these 15 points, uniformly spaced values of the flow coefficient ranging from 0–0.11 were prescribed[4]. A random rotational speed between 3 and 9 krpm was then assigned to each of these flow coefficient values. At each operating point, the air velocity at the inlet was determined from the rotational speed and the flow coefficient. The SST turbulence model was used without the energy equation; the total pressure at the inlet and the torque on the impeller blade were used to determine the head and power coefficients, respectively.

Several features can be seen in Fig. 3-9, which shows the results for fans with the aspect ratio AR = 0.015; Fig. 3-10 shows the results for AR = 0.025. In Figs. 3-9 and 3-10, four inlet ratios are shown in each plot as indicated by the legend. Each of these datasets included all 3 scales (0.8, 1, 1.2).

The fill ratio improved the fan curves and the efficiency in most cases, although for the fans with IR = [0.5, 0.6] the efficiency decreased going from FR=0.7 to 0.8. The square data points, corresponding to an inlet ratio of 0.4, had the highest maximum efficiency, which is consistent with the optimal 40 mm diameter inlet suggested by Allison [50]. Increasing the inlet ratio decreased the maximum head coefficient but increased the maximum flow coefficient. A fan with a larger inlet ratio has less restriction of the flow entering the inlet, so this increase in the flow coefficient seems physically reasonable. In a multilayer device, where several fans operating in parallel may share a common inlet, the inlet restriction plays a significant role in determining the operating point of the fans, which will lead to an optimal inlet ratio larger than the best single layer value.

The simulation results for the trials with AR = 0.025, Fig. 3-10, shows that the trends observed in Fig. 3-10 (for AR = 0.015) remain intact. However, the fan and efficiency curves all shift upward, indicating improved performance for the higher aspect ratio impeller. In some of the cases, this performance improvement was drastic (e.g. for IR = 0.6 and FR = 0.8 the maximum fan efficiency increased from 13 to 23%) In a multilayer device, however, the additional vertical space needed by a higher aspect ratio fan may come at a premium and could require that fewer fan layers be used to meet an overall volume specification for the heat sink.

Finally, the data points for each combination of FR, IR, and AR were tightly grouped and well described by the dimensionless fan parameters (ϕ, ψ_{ts}, and ξ or η_{ts}). Implicit in this observation is that the fan and efficiency curves only showed very small changes when the entire fan ranged in scale from 0.8 to 1.2. This provides some confirmation that the dimensionless parameters ϕ, ψ_{ts}, and ξ for this range of scales satisfactorily characterize the fan performance, and the Reynolds number effects can be safely neglected in the size range of 80–120 mm[5].

3.3.3 Inlet Ratio

Finally, the effect of the inlet ratio was studied by performing CFD simulations on Fan 5 (with d_2 = 100 mm, b_g = 2.6 mm, and b_b = 1.6 mm) for various inlet ratios (IR = [0.2, 0.3, 0.4, 0.5, 0.6, 0.7, 0.8]). In these simulations, the rotational speed was fixed at 5 krpm, and the flow coefficient was varied with linear spacing from 0 to 0.2. The resulting fan and efficiency curves are shown in Fig. 3-11. The fan curves retained the linearity that was

[4]The range of flow coefficient values was chosen based on an initial simulation that suggested a maximum flow coefficient of 0.11 for the base geometry.

[5]At significantly smaller scales, the Reynolds number will begin to have an effect, and the dimensionless relationships reported in this work will change.

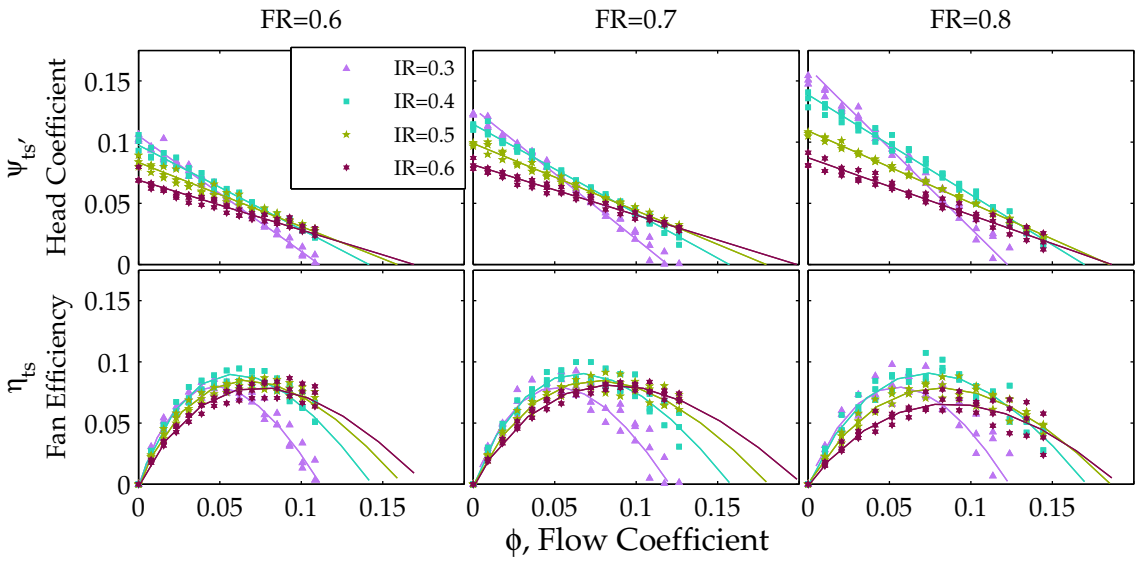

Figure 3-9: CFD simulation results for a study of 72 designs variations of Fan 1, which included variations in the fill ratio (FR = [0.6, 0.7, 0.8]), the aspect ratio (AR = [0.015, 0.025]), the inlet ratio (IR = [0.3, 0.4, 0.5, 0.6]), and overall scale factor (scale = [0.8, 1, 1.2]). This figure only shows the points for which AR = 0.015 (see Fig. 3-10 for the AR = 0.025 points). The top row of plots shows the dimensionless fan curves for fill ratios of 0.6 (left plot), 0.7 (center plot), and 0.8 (right plot). The bottom row shows the respective efficiency curves. In each plot, the inlet ratio is indicated by the data markers: the triangles, squares, pentagrams and hexagrams represent an inlet ratio of 0.3, 0.4, 0.5, and 0.6, respectively. Increasing the fill ratio increased the maximum head coefficient in each fan curve. The fill ratio, surprisingly, seemed to reduce the efficiency for the fans with IR = [0.5, 0.6], but didn't have much effect on the other efficiency curves. An inlet ratio of 0.4 had the highest maximum efficiency for all of the fill ratios.

observed in the studies above; a best-fit line for each fan yielded the ϕ and ψ_{ts} intercepts (i.e. the maximum head and flow coefficients), which are shown in the upper right plot of Fig. 3-11 as functions of the inlet ratio. Neither the flow coefficient nor the head coefficient show a local optimum within the range of inlet ratios tested. The maximum efficiency, shown in the lower right plot of Fig. 3-11, peaked (17.7%) at IR = 0.5, although it was nearly as high (17.6%) at IR = 0.4 ($\eta_{ts,max}$ = 17.6%).

This inlet ratio study shows how the fan curve can be altered with changes to the inlet diameter. In a heat sink with multiple fans, this effect could be used to decrease the inlet flow resistance. At some point, however, the loss in surface area due to the inlet hole would offset the increase in the heat transfer coefficient associated with a higher flow rate. Higher flow rates can also result in increased mechanical power consumption. In Chapter 5, models for multilayer systems will be developed that predict multilayer performance with knowledge of single-fan characteristics. Parametric CFD studies like the three discussed here can be used in combination with the multilayer scaling models developed in Chapter 5 to forecast the performance impact of hypothetical changes in an integrated fan's design.

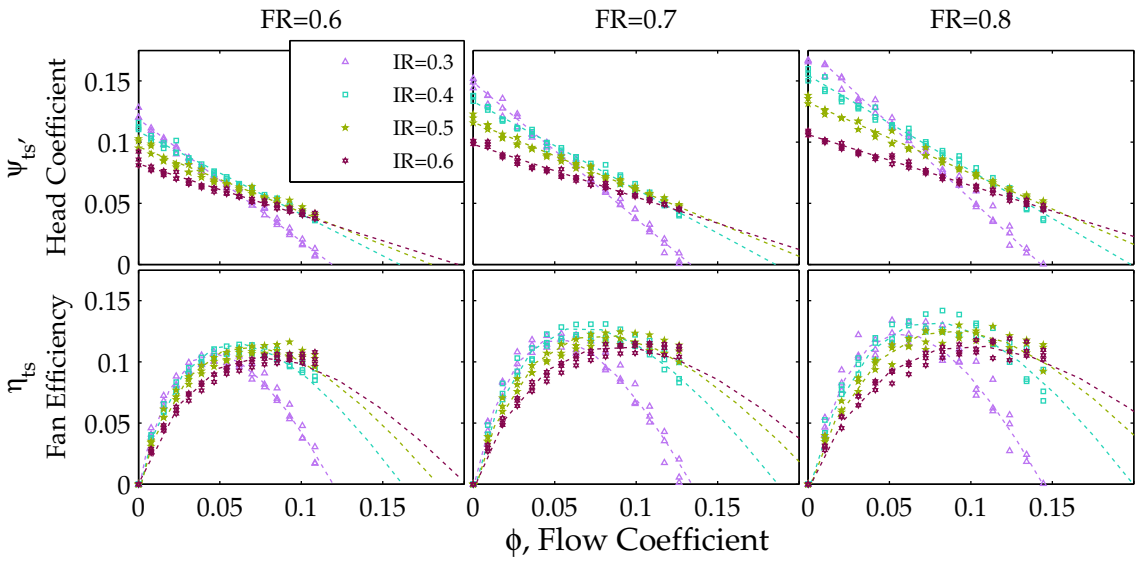

Figure 3-10: CFD simulation results for variations of Fan 1 (described in the caption of Fig. 3-9). This figure only shows the points for which AR = 0.025 (see Fig. 3-9 for the AR = 0.015 points). In these plots, analogous trends to those observed in the AR = 0.015 simulations occurred; in changing from AR = 0.015 to AR = 0.025 (current figure), the fan and efficiency curves shifted slightly upward. This effect could be due to decreased frictional loss in the large aspect ratio passage, which has a lower length-to-hydraulic-diameter ratio.

3.4 Summary

Several benchmark studies were performed to determine if common, steady-state CFD analysis using RANS turbulence models could successfully compute the performance of integrated fans. Of 3 turbulence models, the laminar and SST models gave accurate estimates of the fan performance and efficiency curves, provided a fine enough mesh was used. To a lesser extent, the $k-\epsilon$ model computed the fan performance, but displayed decreased accuracy with mesh refinement beyond a certain point. In computing the heat transfer, the SST unquestionably proved to be the best choice of the 3 models tested. Thus, due to the consistent trends observed in computing the fan and heat transfer performance, the SST model is recommended for CFD simulations of integrated fans.

Despite the successes of the SST model, it was also shown that designers can be misled into trusting a CFD simulation based on satisfactory fan performance curve predictions. A benchmark study of Fan 1 using the SST model showed that simulations with agreement in the fan performance curves can simultaneously compute completely incorrect heat transfer trends. Designers must therefore exercise caution, and conduct careful mesh refinement and CFD parameter sensitivity studies (as recommended, for example, by Pelletier [87]). Better still, CFD simulations can be used to estimate the flow performance of the fan; the results from these simulations can be subsequently combined with the correlations for the dimensionless heat flux (discussed later in Chapter 4) to determine the heat transfer performance of a newly proposed fan design.

Finally, several parametric studies were shown, which give an idea of what outcomes should be expected in the fan performance with changes in the number of blades, fill ratio, inlet ratio, and aspect ratio. For fans similar to Fan 5, CFD simulations suggest that the

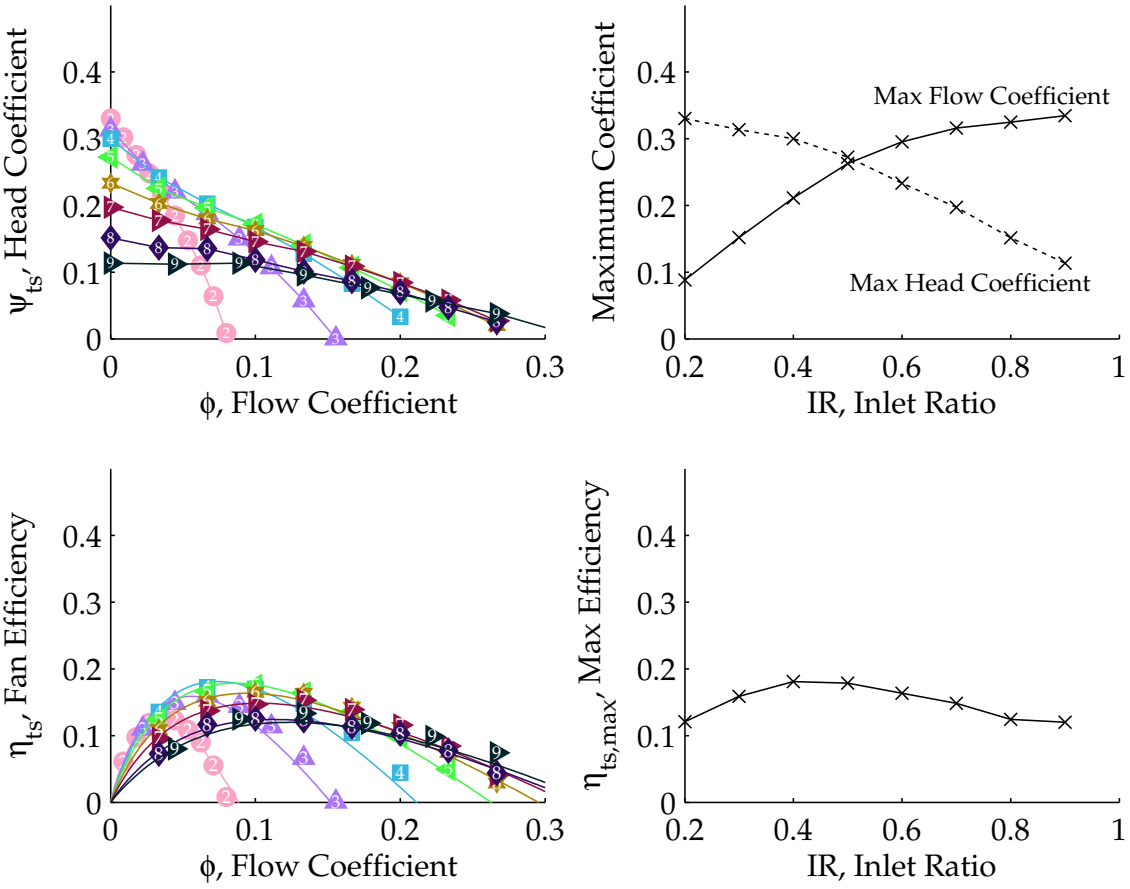

Figure 3-11: CFD simulations were used to predict the fan and efficiency curves for radial blade impellers with varying inlet ratio (IR). Each marker in the leftmost plots represents a single CFD run, and the labels in each marker indicate $10 \cdot \text{IR}$. These tests were performed for Fan 5 (15 blades, $d_2 = 100\,\text{mm}$, $b_g = 2.6\,\text{mm}$, $b_b = 1.6\,\text{mm}$). All of the runs were performed at a rotational speed of 5 krpm. The upper right plot shows the maximum head and flow coefficients (the intercepts of the fan curves in the upper left plot) for each inlet ratio; the lower right plot shows the maximum efficiency. As the inlet ratio is increased, the maximum flow coefficient increases and the maximum head coefficient decreases. The maximum efficiency occurs near an inlet ratio of 0.4, but the maximum efficiency does not change as quickly as the maximum head and flow coefficients.

optimum number of blades is about 15. A more comprehensive study of the aspect and inlet ratios is suggested as a possible direction for further study to improve and better understand the performance of integrated fans.

THIS PAGE INTENTIONALLY LEFT BLANK

CHAPTER 4

EXPERIMENTAL RESULTS AND CORRELATIONS

Integrated fan heat sinks have complex fluid dynamic phenomena. The fully unshrouded nature of the fans in this work gives rise to high leakage flows from the pressure side of the impeller blades to the suction side. This leakage flow results in shear and mixing losses, and ultimately a degradation in the fan performance that exceeds estimates based on conventional centrifugal fan analyses (i.e. the Euler turbomachinery equation with common slip factor correlations). These complexities in the flow field also make analytical estimation of the heat transfer coefficient similarly uncertain.

Engineers often turn to CFD to solve analytically intractable problems involving fluid dynamics and heat transfer. Unfortunately, CFD is known to be of questionable validity in dealing with untested geometries, as was discussed in Chapter 3. Integrated fans have features that pose significant challenges to current CFD software. In particular, the gap between the blade and the stationary wall is very small compared to the streamwise length of the flow passage. These disparate length scales can make it difficult for CFD solvers. The close proximity of the walls to the interface between the stationary and rotating frames can also present problems for the software. Ultimately, experiments give a solid connection to reality that is necessary to provide benchmarking to any numerical simulation for the complex fluid flow.

Accordingly, a suite of experiments was performed to characterize both the pumping and heat transfer characteristics for several basic fan geometries. The experimental results were compared to the computed results from some analytical approaches. Some of these approaches were able to provide the general trends in the fan and heat transfer performance. Correlations were developed to supplement these analytical approaches and provide a method of achieving accurate design estimates. These models are more suitable for integration into the multilayer models that will be described in Chapter 5

In the development of these experimentally based models, it was observed that the heat transfer in the integrated fans is not sensitive to the geometry of the impeller profile. Instead, the heat transfer is a function of the operating point (volume flow and rotational speed) and the aspect ratio (the ratio of blade breadth to impeller diameter, AR = b_b/d_2). This observation greatly simplifies the design process; the fill ratio can be decided based on the application, and the impeller profile design can proceed without detailed consideration of its impact on the heat transfer.

The correlations developed for the heat transfer are a function of the rotational Reynolds

number and the hydraulic diameter Reynolds number. These correlations span the entire operating range of the fans, from 0 net volume flow to near the free delivery point. This comprehensive characterization is useful for estimating the performance in a multiple impeller system (see Chapter 5); these multilayer systems tend to operate in more restricted regimes than a single, unrestricted fan. Interestingly, the heat transfer was observed to be finite for operating points at 0 net volume flow These correlations can be used to accurately estimate the heat transfer for an impeller with a known operating point.

To determine the operating point of an integrated fan, a designer must know its fan performance curve as well as the resistance of the system it pumps against. While the latter is application dependent, the former is a function of the dimensionless fan parameters identified in Section 1.8. Analytical techniques for conventional centrifugal fans capture the gross trends in the integrated fans, but more accurate estimation can be obtained through correlations. A number of fans were characterized experimentally; fits were applied to the experimentally measured fan and power curves, reducing them to several parameters per geometry. These correlation parameters were then related to the basic fan geometry (fill ratio, blade exit angle, and number of blades). These high-level estimates are, of course, less accurate than the impeller-specific correlations, but are useful as design heuristics.

4.1 Average Heat Transfer Coefficient

The average heat transfer coefficient was determined by measuring the heat input ($\dot{Q}$) required to maintain the stators at a constant temperature (T_w). The average heat transfer coefficient is

$$h_{ITD} = \frac{\dot{Q}}{A_s \Delta T_{in}}, \tag{4.1}$$

where A_s is the surface area of the stator plates and ΔT_{in} is the difference between the stator and inlet air temperature. The "ITD" subscript stands for "inlet temperature difference," so as to distinguish this heat transfer coefficient from the conventionally defined average heat transfer coefficient, which references the log-mean temperature difference between the wall and the fluid stream. The inlet temperature difference ($\Delta T_{in} = T_w - T_{in}$) was determined by measuring the wall temperature and inlet air temperature with thermocouples, as described in Section 2.1.1. The high thermal conductivity of the copper stator plates ensured that their temperature remained spatially uniform. The surface area of the plates in these experiments was

$$A_s = 2 \cdot \pi (r_2^2 - r_1^2) \tag{4.2}$$

for the circular stator apparatus, and

$$A_s = 2 \cdot \left(d_2^2 - \pi r_1^2 - 4 \cdot \pi d_{tube}^2 / 4 \right) \tag{4.3}$$

for the square stator apparatus, where r is the radius, d is the diameter, and the subscripts 1 and 2 refer to the core and the impeller blade tip, respectively (following the convention introduced in Fig. 1-9. d_{tube} refers to the diameter of the four support posts located in the corners of the square stator apparatus. Each of these expressions includes the area of both the top and bottom surfaces of the air flow channel.

4.1.1 General Features

The heat transfer coefficient was measured for various rotational speeds and flow rates. A typical measurement of the heat transfer coefficient is shown in Fig. 4-1; h_{ITD} is plotted as a function of the volume flow rate for Fan 5 (15 blades, 90° exit angle, $b_{\mathrm{b}} = 1.6\,\mathrm{mm}$, $b_{\mathrm{g}} = 2.6\,\mathrm{mm}$). As expected, the heat transfer coefficient increases with volume flow; the presence of the rotating impeller also causes a significant increase in the heat transfer coefficient. At a given volume flow, h_{ITD} at the highest rotational speed is sometimes thrice its value in the absence of rotation.

The heat transfer coefficient can be expressed in dimensionless form as the dimensionless heat flux (Φ_{m}). As discussed in Section 1.8.2, Φ_{m} and the Nusselt number (Nu) have similar forms. While the Nusselt number refers to the local or log-mean temperature difference between the wall and the fluid, the dimensionless heat flux instead refers to the inlet temperature difference (the same temperature scale used in h_{ITD})[1].

In the integrated fans, it was observed that using the streamwise meridional flow

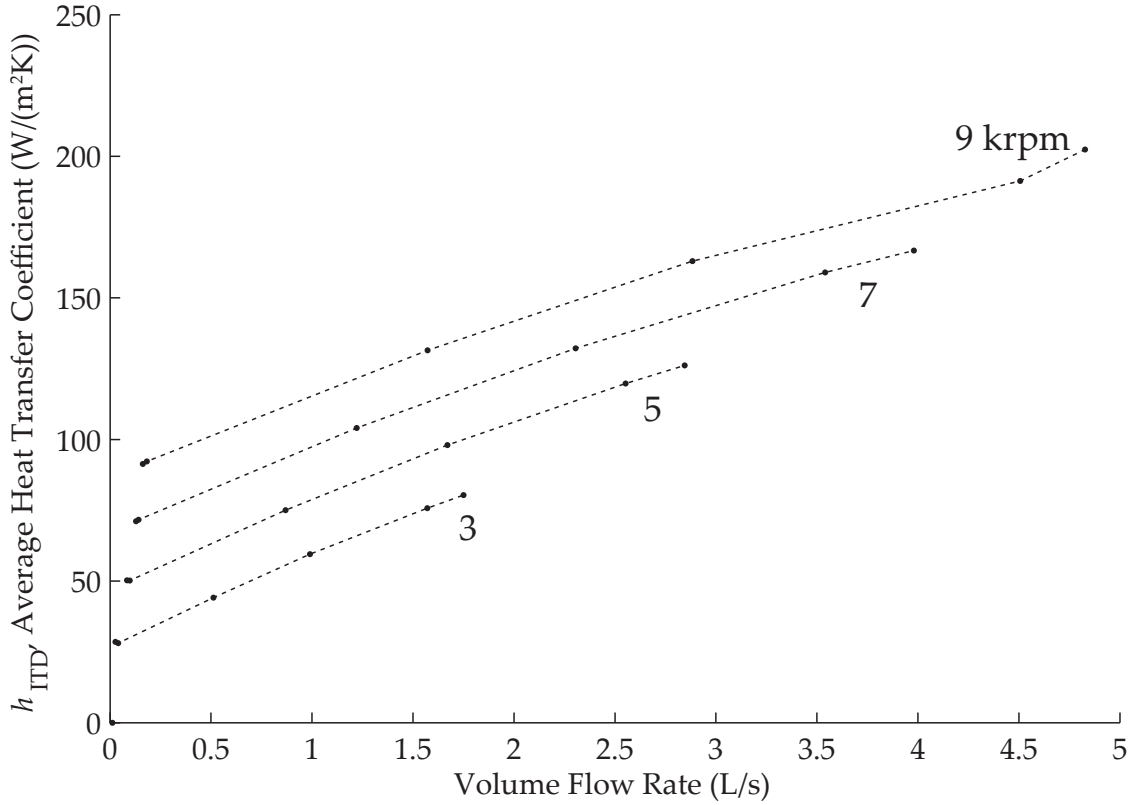

Figure 4-1: The average heat transfer coefficient h_{ITD} increases with volume flow and impeller rotational speed. The data shown correspond to impeller 5 (15 blades, 90° exit angle, $b_{\mathrm{b}} = 1.5\,\mathrm{mm}$, $b_{\mathrm{g}} = 2.5\,\mathrm{mm}$). The data points with common rotational speeds are connected with dashed lines; the higher rotational speeds are capable of inducing a greater volume flow through the system. The enhancement of the heat transfer coefficient due to the impeller can be easily seen by comparing h_{ITD} at a constant volume flow.

[1] A thorough discussion on the subtle differences in the limiting behaviors of Nu and Φ_{m} can be found in Shah and London [61].

length $L_f = r_2 - r_1$ as the characteristic length in the dimensionless heat flux gave a more consistent representation of the experimental data. This modification in the length scale removes the direct dependence on the gap breadth that would exist in Φ_m had the hydraulic diameter been chosen as the length scale. The mean dimensionless heat flux is, thus,

$$\Phi_{m,L} = \frac{h_{ITD} L_f}{k}, \tag{4.4}$$

where k is the thermal conductivity of the air and L_f is the radial flow length along the passage $(r_2 - r_1)$. The additional "L" in the subscript of $\Phi_{m,L}$ serves as a reminder that the length scale is L_f rather than the hydraulic diameter.

The mass flow can be expressed nondimensionally in terms of the channel Reynolds number (evaluated at the arithmetic mean radius, $r_m = (r_2 + r_1)/2$):

$$\mathrm{Re}_{dh} = \frac{\rho v d_h}{\mu} = \frac{\dot{m}}{\pi \mu r_m}, \tag{4.5}$$

where ρ and μ are the density and dynamic viscosity of the air, and d_h is the hydraulic diameter (for parallel discs, the hydraulic diameter is twice the gap spacing: $d_h = 2b_g$).

The dimensionless heat flux was observed to increase linearly with the channel Reynolds number at each rotational speed, as shown in Fig. 4-2. In each characterization, the fan was held at a constant speed and various flow rates were allowed through the system. At constant rotational speed in a particular geometry, the rotational Reynolds number, $\mathrm{Re}_\omega = \frac{\rho \omega r_2^2}{\mu}$, is constant. Therefore, each group of points in a $\Phi_{m,L}$ vs. Re_{dh} plot represents a constant rotational Reynolds number. The dimensionless heat flux was also observed to increase linearly with Re_ω.

The heat transfer is relatively insensitive to the particular profile of the impeller. For example, consider 4 fans: impellers 8, 11, 12 and 13, which are very similar except for the backsweep angle of their blades. The dimensionless heat flux for these impellers is shown in Fig. 4-2.

4.1.2 Analytical Estimates

Surface Renewal Theory

The data shown in Fig. 4-1 can be estimated by the surface renewal theory (discussed in Section 1.4.2), which could lead to the conclusion that some of the heat transfer enhancement is derived from the boundary layer interruption that occurs with successive blade passages. However, some of the trends suggested by the surface renewal theory were not observed experimentally. For example, a series of tests were performed on impellers 5–7, which were identical except for the number of blades. Equation 1.17 predicts that the heat transfer should scale with the square root of the renewal frequency as

$$h = 2\sqrt{\frac{k\rho c_p}{\pi}}\sqrt{f}, \tag{4.6}$$

where in the case of the integrated fans, the frequency is related to the rotational speed and number of blades Z as

$$f = \frac{Z\omega}{2\pi}. \tag{4.7}$$

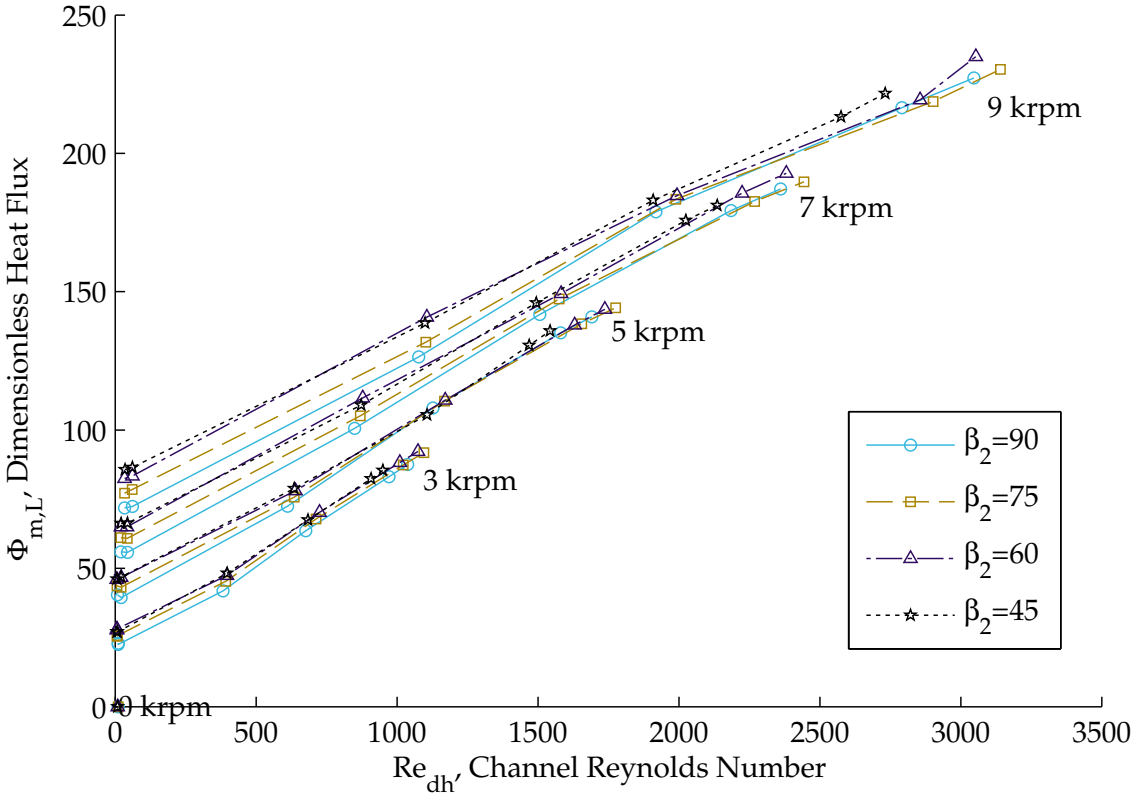

Figure 4-2: The heat transfer in integrated fans is relatively insensitive to the planform profile of the impeller blades. Four impellers are shown, the only difference being the angle of their blades. In this plot, their heat transfer characteristics differ by only 15% at most, a small change considering the drastic difference in their shapes. These impellers have different fan performance curves, which can be partially seen in this plot by noting the maximum channel Reynolds number for each rotational speed; the fans with better pumping capability can reach a higher Re_{dh}. The fans shown in this plot are Fans 8, 11, 12 and 13, all with $b_b = 1.5\,\mathrm{mm}$, $b_g = 2.5\,\mathrm{mm}$, and β_2 as indicated by the legend.

The heat transfer coefficient was calculated, and the total heat transfer determined using the effectiveness-N_{TU} method, in a manner similar to that shown in Section 1.5.1. The inlet-temperature-difference heat transfer coefficient was calculated from this overall heat transfer.

Figure 4-3 shows the surface renewal theory estimates compared with experimental data. The measured heat transfer coefficients are barely different for the 3 impellers; this is in contrast to the surface renewal theory estimates, which are significantly different. The surface renewal theory correctly suggests an enhancement due to increases in rotational speed, but does not appropriately estimate the effect of additional blades. Additionally, the surface renewal theory significantly underestimates the heat transfer at low channel Reynolds numbers (low volume flow rates). This is due to an unmodeled recirculatory flow at the exit plane of the impeller.

When the inlet is blocked and the net flow through the fan is zero, the relative eddy dominates the flow in the blade passage. This eddy, at the exit plane, results in some reentry flow that is likely to have a temperature close to ambient, resulting in a significant cooling effect. The surface renewal theory results above were modeled under the

assumption that the air flows unidirectionally through the passage from inlet to outlet, so of course this recirculation effect did not manifest itself in the estimate shown in Fig. 4-3.

These findings are similar to those of Hagge and Junkhan [38], who studied external flow over a flat plate fitted with a rotating scraper blade. They found that the surface renewal theory was applicable at low freestream Reynolds numbers, and served to estimate the general trends of the heat transfer; however, they also reported that the surface renewal theory was not capable of standing alone as a predictive tool for design purposes. They suggested that the main heat transfer mechanism was instead the turbulent boundary layer established between the blade and the heated wall.

Turbulent Flow

Another approach to modeling the heat transfer in an integrated fan heat sink is to assume that the flow between the blade and the heated wall is turbulent, and calculate the heat transfer using turbulent pipe flow correlations and the effectiveness–N_{TU} method. Several Reynolds numbers were tested in this approach since the choice of length and velocity scale was unclear. Using a Reynolds number based on velocity scale similar to Hagge and Junkhan [38] and a length scale of the hydraulic diameter, reasonable agreement with the experimental data at higher flow rates was achieved. The "effective velocity" used by Hagge and Junkhan was the sum of the blade speed and the flow speed. In the present work, an internal flow analog to this approach was formed, using an effective velocity calculated (as a function of radius r) as the sum of the meridional velocity c_m and the local

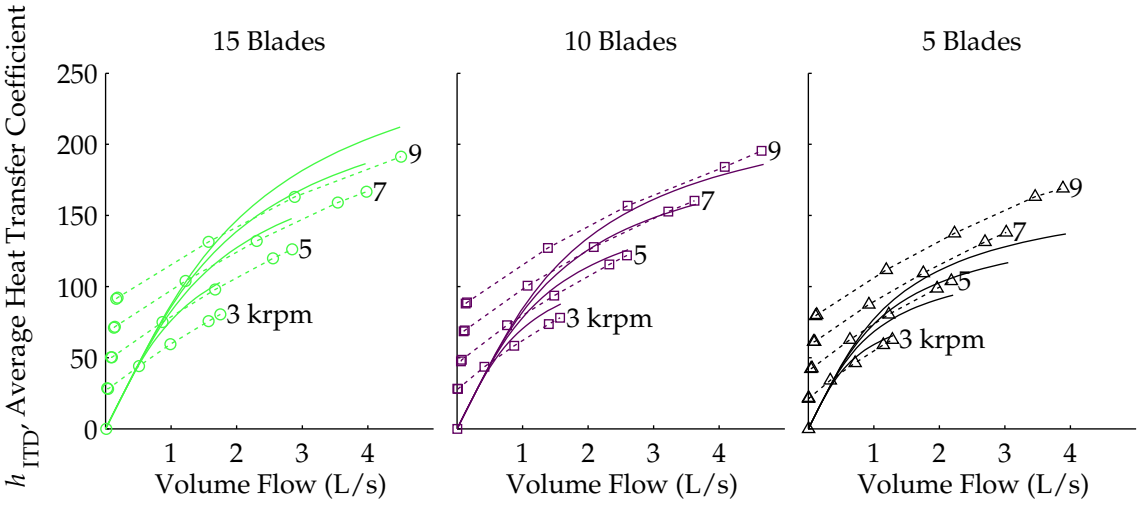

Figure 4-3: The heat transfer in three impellers with various numbers of blades (15, 10 and 5) was predicted to be significantly different by the surface renewal theory; however, experimental data only showed a small difference in the heat transfer coefficient at a fixed volume flow through the fan. In these plots, the experimental data points with the same rotational speed are connected with a dashed line; the solid lines are the surface renewal theory estimates. The main effect of increasing the number of blades to improve the fan performance (the 5-blade impeller cannot pump as much air as the 10- or 15-blade impeller at the same rotational speed).

blade speed u:

$$v_{\text{eff}} = u + c_{\text{m}} = r\omega + \frac{\dot{V}}{2\pi r b_{\text{g}}}. \tag{4.8}$$

The Reynolds number used v_{eff} as the velocity scale and the hydraulic diameter as the length scale:

$$\text{Re}_{\text{eff}} = \frac{\rho v_{\text{eff}} d_{\text{h}}}{\mu} \tag{4.9}$$

The Nusselt number was then calculated using a turbulent flat plate correlation as was done by Hagge and Junkhan:

$$\text{Nu} = 0.0249\text{Re}_{\text{eff}}^{0.8}, \tag{4.10}$$

where Nu is the local Nusselt number. This Nusselt number for flow over a flat plate is defined as

$$\text{Nu} = \frac{hx}{k}, \tag{4.11}$$

where x is the distance from the leading edge of the plate and h is the local heat transfer coefficient (referenced to the local wall-to-bulk temperature difference). The average heat transfer coefficient was determined from this through integration, and the effectiveness-N_{TU} method was used to account for the temperature rise of the air stream. The total heat transfer was used to calculate the inlet-temperature-difference heat transfer coefficient (h_{ITD}).

Figure 4-4 shows the results of this analysis in comparison with experimental data (for Fan 1, a 5-bladed impeller with $b_{\text{g}} = 2.5\,\text{mm}$ and $b_{\text{b}} = 1.5\,\text{mm}$). Hagge and Junkhan's turbulent heat transfer approach accounts for the enhancement due to faster rotational speeds. It predicts no improvement in the heat transfer with the addition of blades, contrary to the surface renewal theory, and is more representative of the experimental observations.

Also shown in Fig. 4-4 are two analytical estimates of the heat transfer from the radially outward flow when the impeller is stationary. Suryanarayana's correlation [42] for radially outward flow is shown to slightly underestimate the heat transfer. Additionally, for reference, a correlation for simultaneously developing laminar flow (hydrodynamic and thermal boundary layer development in concert) is also shown. This correlation is given in Ebadian and Dong [88] for parallel plates with constant temperature walls as

$$\text{Nu} = 7.55 + \frac{0.024x^{*-1.14}\left[0.0179\text{Pr}^{0.17}x^{*-0.64} - 0.14\right]}{\left(1 + 0.0358\text{Pr}^{0.17}x^{*-0.64}\right)^2}, \tag{4.12}$$

where Nu is the local Nusselt number (referenced to the hydraulic diameter). x^* is a dimensionless entry length, defined as

$$x^* = \frac{x/d_{\text{h}}}{\text{RePr}}, \tag{4.13}$$

where x is the distance from the flow entrance. The entry length has a higher heat transfer coefficient than in the fully developed regime. Even accounting for this, the estimated heat transfer is much lower than the experimentally observed heat transfer in the presence of rotation, further supporting the hypothesis that the fan causes turbulence in the channel, despite the relatively low through flow velocities.

Of these methods, the turbulent flow approach (the internal flow analog of Hagge

and Junkhan's method) seems to have the most merit, in that it (1) correctly models enhancement of the heat transfer with higher rotational speed, (2) predicts no significant enhancement with addition of impeller blades, and (3) comes reasonably close to the experimentally observed heat transfers at higher flow rates, where recirculation is likely to be negligible.

As with the surface renewal theory results, the main failure of these turbulent flow estimations occurs at the lower volume flows; the assumption of unidirectional throughflow inherent to these models was observed to be untrue. An attempt was made to correct for this by modeling the outlet recirculation in a manner similar to that of Qiu et al. [89]. In Qiu's model, a blockage in the exit plane is caused by the blade loading in the impeller (that is, the difference in velocity between the pressure and suction sides of the blade that arises due to the Coriolis forces on the flow in the rotating frame). Qiu calculated a velocity difference based on the blade geometry and rotational speed, and established a recirculatory zone so that the main flow maintained this velocity difference without separation on the pressure side of the blade. The problem with Qiu's model when applied to the in-

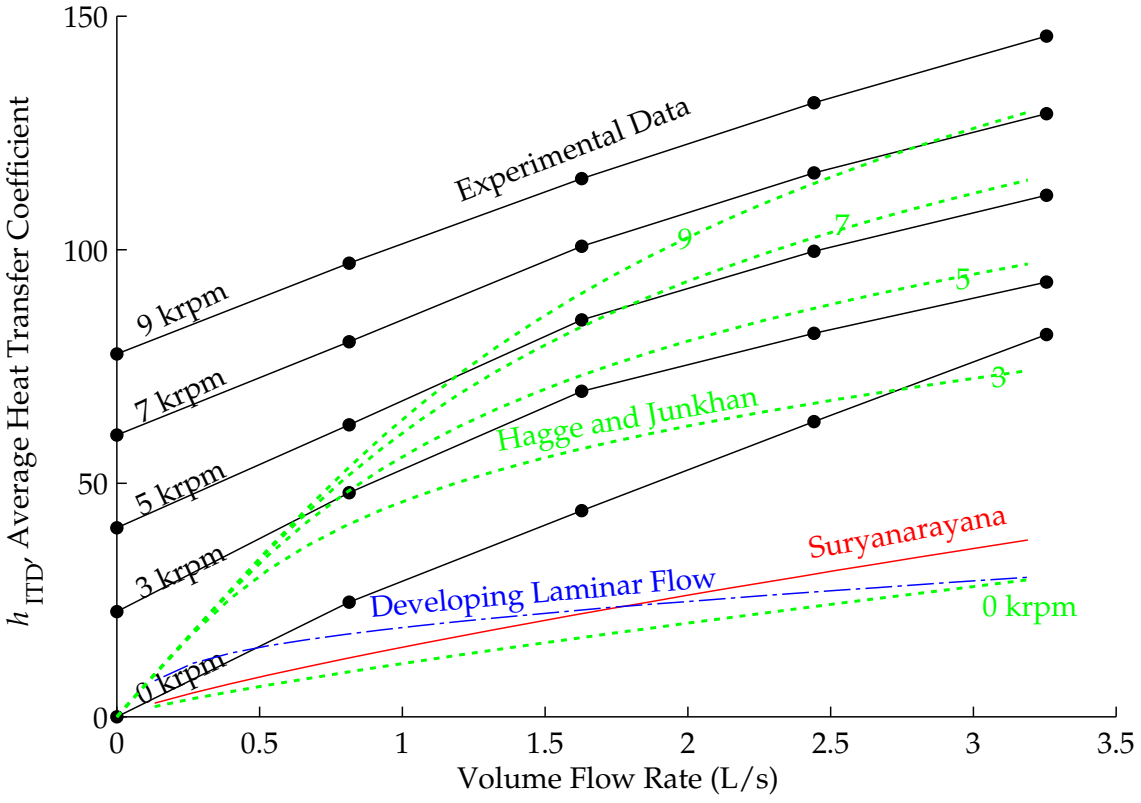

Figure 4-4: Several analytical models were compared to the experimental data. Correlations for simultaneously developing laminar flow and radially outward flow between parallel discs (Suryanarayana's correlation), combined with the effectiveness-N_{TU} method, are shown to estimate smaller-than-observed heat transfer coefficients. Additionally, an internal flow analog of Hagge and Junkhan's external, mechanically induced turbulence model was used to estimate the heat transfer coefficient. This turbulent flow model correctly predicted a heat transfer enhancement associated with impeller rotation and provided reasonable estimates of the heat transfer coefficient at the higher flow rates.

tegrated fans assessed in the present work was that it predicted high flow velocities and large fractions of the exit area as being blocked, even at high flow coefficients. This led to overestimation of the heat transfer at low flow rates. Correction factors were applied to improve agreement with the experimental observations, but these factors needed adjustment for different impeller geometries. It was felt that the application of correction factors to this analytical model that proved inappropriate for the physical phenomena observed in the lab obviated the very insights being sought with the analytical approach.

Rather than supplementing these analytical methods with correction factors to capture the system's behavior, an experimentally based approach using dimensionless parameters was pursued, leading to a more accurate and simpler reduction of the experimental data.

4.1.3 Correlations

Experimentally based correlations were developed to allow for the estimation of the heat transfer in an integrated fan with knowledge of the aspect ratio (AR = b_b/d_2) and operating point (flow rate and rotational speed). A key finding was that the impeller profile and fill ratio did not have a significant, direct effect on the heat transfer, and therefore the heat transfer problem is largely independent of the fan design problem. This is a convenient result because simple fan characterization tests are much easier to perform than heat transfer experiments; these tend to be much more laborious, complicated, and expensive than unheated fan characterizations. A new impeller design can be quickly and efficiently characterized on a relatively simple apparatus, and its heat transfer estimated with confidence using the correlations developed in this section. Generally speaking, an efficient, well designed integrated fan will automatically excel in terms of heat transfer performance.

It's worth clarifying that the insensitivity of the heat transfer to the impeller blade profile doesn't suggest that the impeller profile is unimportant in the design process. On the contrary, the impeller profile has a significant effect on the system performance, because it has a strong effect on the fan performance curve. The flow rate through the fan depends on the fan's pressure rise capability and the flow resistance of the system the fan pumps against. The fan performance curves relate the pressure rise, volume flow, and rotational speed. The fan performance curves are sensitive to the impeller blade profile; since this blade profile affects the operating point, the blade profile indirectly affects the heat transfer performance.

In the heat transfer experiments, the heat transfer required to keep the stators at a constant temperature was measured for various fan speeds and flow rates. The average heat transfer coefficient is often expressed nondimensionally as a mean Nusselt number; however, calculating the mean Nusselt number requires knowledge of the temperature rise in the air stream, and therefore an assumption about the mass flow rate. Although the net mass flow rate is measured, the recirculatory flow at the exit plane of the impeller is uncertain. Assumptions about the air flow through the device are therefore undesirable, as they introduce unnecessary error in the heat transfer estimates. In a heat sink the inlet temperature difference is known a priori, so the dimensionless heat flux $\Phi_{\mathrm{m,L}}$ (defined in Eq. 4.4) proves to be a convenient figure of merit.

The heat transfer coefficient is affected by the flow through the gap as well as the rotational speed of the impeller. Each of these operating parameters can be represented by a respective Reynolds number. The channel Reynolds number, $\mathrm{Re}_{d\mathrm{h}}$, is the Reynolds

number at the arithmetic mean radius r_{m}, which simplifies to

$$\mathrm{Re}_{d\mathrm{h}} = \frac{\dot{V}}{\pi \nu r_{\mathrm{m}}}, \tag{4.14}$$

where ν is the kinematic viscosity of the fluid. The channel Reynolds number uses the hydraulic diameter as its length scale. In the heat transfer experiments, the flow Reynolds number proves more convenient than the flow coefficient (ϕ) because it contains no influence from the rotational speed, allowing decoupling of the two independently controllable parameters, the flow through the system and the rotational speed. The rotational speed ω is represented by the rotational Reynolds number (introduced in Section 1.8.2):

$$\mathrm{Re}_{\omega} = \frac{\omega r^2}{\nu}. \tag{4.15}$$

A two-dimensional linear correlation for the dimensionless heat flux ($\Phi_{\mathrm{m,L}}$) in terms of the two Reynolds numbers in Eqs. 4.14 and 4.15 was formed to fit the data from each experiment. These correlations had the form

$$\Phi_{\mathrm{m,L}} = C_1 \mathrm{Re}_{\omega} + C_2 \mathrm{Re}_{d\mathrm{h}}, \tag{4.16}$$

where C_1 and C_2 were determined through a linear least squares minimization (the "\" command in MATLAB). $\Phi_{\mathrm{m,L}}$ is a dimensionless heat flux that uses the flow length along the plate ($L_{\mathrm{f}} = r_2 - r_1$) as its length scale, defined in Eq. 4.4 as

$$\Phi_{\mathrm{m,L}} = \frac{h_{\mathrm{ITD}} L_{\mathrm{f}}}{k}. \tag{4.17}$$

The experimentally determined heat transfer for all of the heat transfer tests performed in both the square and circular stator apparatuses is shown in Fig. 4-5 as the dimensionless heat flux ($\Phi_{\mathrm{m,L}}$) vs. the channel Reynolds number ($\mathrm{Re}_{d\mathrm{h}}$). These plots each have a label in the upper left corner that corresponds to a row in Table 4.1 that describes the essential features of its underlying experiment. Table 4.1 shows the experimental identifier (EID), fill ratio (FR = $b_{\mathrm{b}}/b_{\mathrm{g}}$), aspect ratio (AR = b_{b}/d_2), blade exit angle (β_2), number of blades (Z), the fit coefficients C_1 and C_2 from Eq. 4.16, and the relative root-mean-squared error (rRMSE) of the correlation fit. This error metric (originally introduced in Eq. 3.2) is defined as

$$\mathrm{rRMSE} = \sqrt{\frac{1}{n}\sum_{i=1}^{n}\left(\frac{x_{\mathrm{p,i}} - x_{\mathrm{m,i}}}{x_{\mathrm{m,i}}}\right)^2}, \tag{4.18}$$

where $x_{\mathrm{m,i}}$ is the measured quantity and $x_{\mathrm{p,i}}$ is the correlation-estimated quantity for data point i of an experiment with n data points. The linear fit proposed in Eq. 4.16 has small values of rRMSE (typically less than 10%) for each experiment, meaning that this form of correlation represents each data set with excellent fidelity.

The individual correlations appear to be successful in reproducing the heat transfer behavior of the entire operating range of the fans, based on the values of the rRMSE shown in Table 4.1. Next, a natural progression is to collapse the experimental data even more by developing an estimator for the correlation coefficients C_1 and C_2. An average value of C_1 and C_2 could be taken over all experiments, but first the distributions of C_1 and C_2 were examined to determine whether they were normally distributed. Figure 4-6 shows

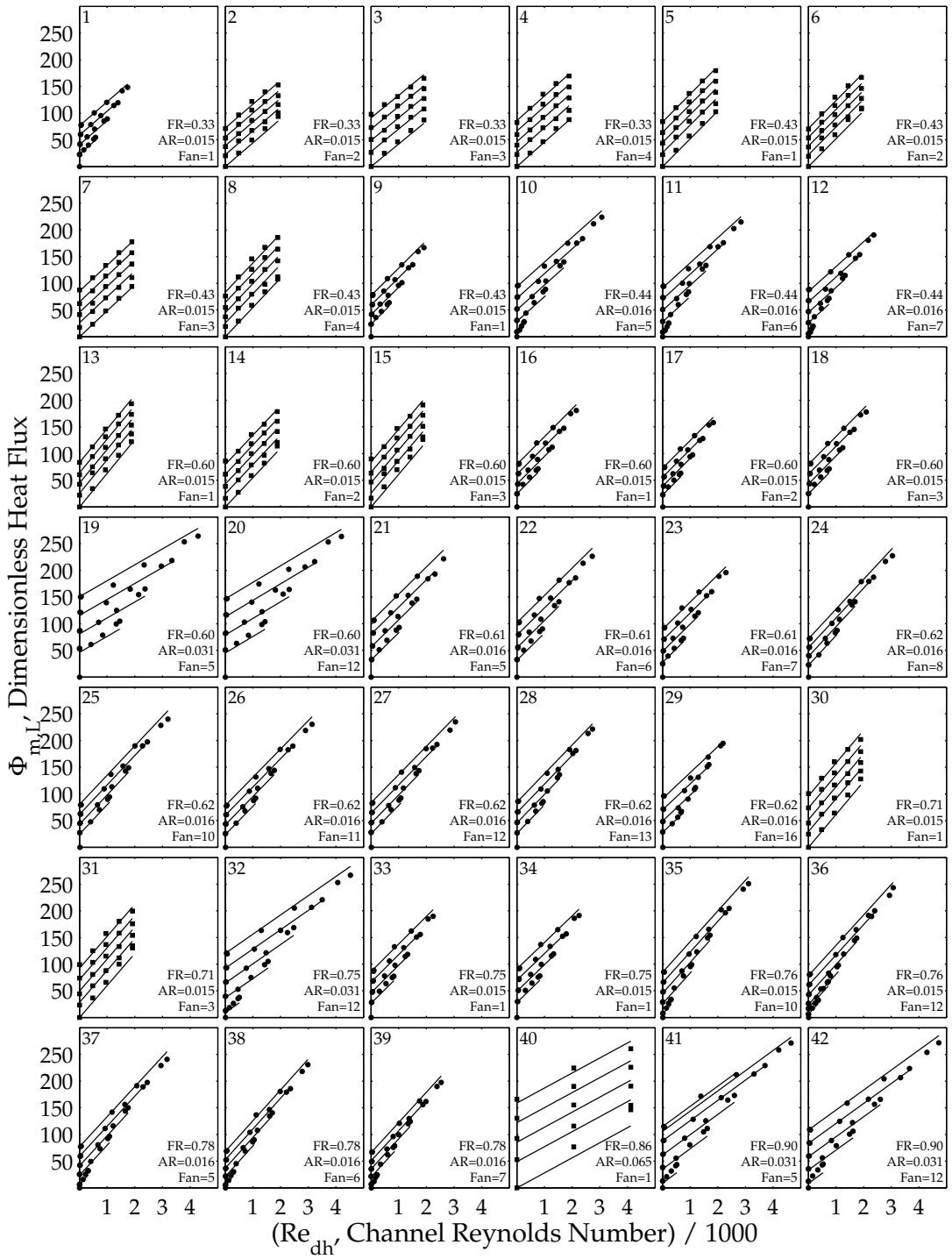

Figure 4-5: The similarity in the trends and magnitude of the dimensionless heat flux over 42 sets of experimental data shows its relative insensitivity to the impeller geometry (except the aspect ratio, which seemed to have a small effect). The dimensionless heat flux was observed to be a function of the channel Reynolds number ($\mathrm{Re}_{d\mathrm{h}}$) and the rotational Reynolds number (Re_{ω}). The square and circular stator apparatus tests are indicated by square and circle shaped markers, respectively. First, the heat transfer appears to be insensitive to the local meridional velocity, because points with substantially different gap spacings have similar dimensionless heat fluxes at the same $\mathrm{Re}_{d\mathrm{h}}$ (i.e. $\dot{Q}$ depends only on $\dot{m}$ and not on the local meridional velocity). The implication is that, in contrast to pipe flow, the average through-flow velocity is not the dominant contributor to the turbulence and heat transfer. Second, the channel Reynolds numbers are quite low and fall solidly within the laminar range; however, the observed heat transfer coefficients are higher than the laminar flow estimates.

Table 4.1: Heat Transfer Correlations Summary

Plot No. in Fig. 4-5	EID	Fan	FR	AR	β_2	Z	C_1	C_2	rRMSE
1	198	1	0.33	0.015	42.5	5	0.00050	0.04488	0.05
2	106	2	0.33	0.015	45	5	0.00047	0.04446	0.07
3	107	3	0.33	0.015	70	5	0.00060	0.04229	0.05
4	108	4	0.33	0.015	30	7	0.00056	0.04602	0.08
5	117	1	0.43	0.015	42.5	5	0.00055	0.05203	0.07
6	118	2	0.43	0.015	45	5	0.00047	0.05214	0.08
7	133	3	0.43	0.015	70	5	0.00056	0.04847	0.14
8	134	4	0.43	0.015	30	7	0.00054	0.05480	0.13
9	196	1	0.43	0.015	42.5	5	0.00050	0.05141	0.04
10	311	5	0.44	0.016	90	15	0.00061	0.04630	0.07
11	312	6	0.44	0.016	90	10	0.00060	0.04696	0.07
12	313	7	0.44	0.016	90	5	0.00055	0.04667	0.06
13	100	1	0.60	0.015	42.5	5	0.00054	0.06284	0.07
14	98	2	0.60	0.015	45	5	0.00052	0.05485	0.15
15	101	3	0.60	0.015	70	5	0.00055	0.06114	0.16
16	195	1	0.60	0.015	42.5	5	0.00052	0.05215	0.06
17	202	2	0.60	0.015	45	5	0.00048	0.05174	0.05
18	203	3	0.60	0.015	70	5	0.00052	0.05220	0.06
19	304	5	0.60	0.031	90	15	0.00099	0.02982	0.05
20	305	12	0.60	0.031	60	15	0.00096	0.03097	0.05
21	205	5	0.61	0.016	90	15	0.00068	0.05104	0.05
22	212	6	0.61	0.016	90	10	0.00067	0.05113	0.06
23	211	7	0.61	0.016	90	5	0.00059	0.05119	0.07
24	298	8	0.62	0.016	90	15	0.00047	0.05578	0.04
25	299	10	0.62	0.016	90	20	0.00053	0.05497	0.04
26	300	11	0.62	0.016	75	15	0.00051	0.05298	0.04
27	301	12	0.62	0.016	60	15	0.00055	0.05293	0.04
28	302	13	0.62	0.016	45	15	0.00055	0.05369	0.03
29	303	16	0.62	0.016	30	15	0.00060	0.04860	0.04
30	105	1	0.71	0.015	42.5	5	0.00063	0.06159	0.08
31	103	3	0.71	0.015	70	5	0.00060	0.05989	0.09
32	316	12	0.75	0.031	60	15	0.00079	0.03606	0.05
33	199	1	0.75	0.015	42.5	5	0.00056	0.05161	0.05
34	201	1	0.75	0.015	42.5	5	0.00059	0.04993	0.05
35	310	10	0.76	0.015	90	20	0.00055	0.05755	0.09
36	306	12	0.76	0.015	60	15	0.00051	0.05695	0.09
37	307	5	0.78	0.016	90	15	0.00050	0.05623	0.06
38	308	6	0.78	0.016	90	10	0.00045	0.05758	0.14
39	309	7	0.78	0.016	90	5	0.00043	0.05660	0.08
40	114	1	0.86	0.065	42.5	5	0.00104	0.02813	0.05
41	314	5	0.90	0.031	90	15	0.00075	0.03785	0.08
42	315	12	0.90	0.031	60	15	0.00071	0.03737	0.09
								Mean	0.07
								St. Dev.	0.03

histograms and Q-Q plots (see Wilk and Gnanadesikan [90] for greater detail) for C_1 and C_2. The data in the Q-Q plots (also referred to as normal probability plots) tend to group along the line drawn through its first and third quartiles if the distribution is normal. Data that is not normally distributed introduces curvature into the plot. Both C_1 and C_2 seemed to have relatively normal distributions, except for a few errant data points. These data points corresponded experiments with larger aspect ratios than the majority of the data.

To improve the estimate of C_1 and C_2, equations were formed involving the aspect ratio. These estimation methods must be used cautiously, because a relatively small amount of experimental data at larger aspect ratios was collected; nonetheless, the improvement in the estimates of C_1 and C_2 proved compelling. Figure 4-7 shows the histograms and Q-Q plots for $C_1/\mathrm{AR}^{1/2}$ and $C_2\mathrm{AR}^{1/2}$; these distributions seemed to be much more normal with the modification associated with the aspect ratio, based on the linearity of the normal probability plots and the shape of the histograms. Taking the mean of this remapped data leads to equations that can estimate C_1 and C_2 for any of the characterized fans. These

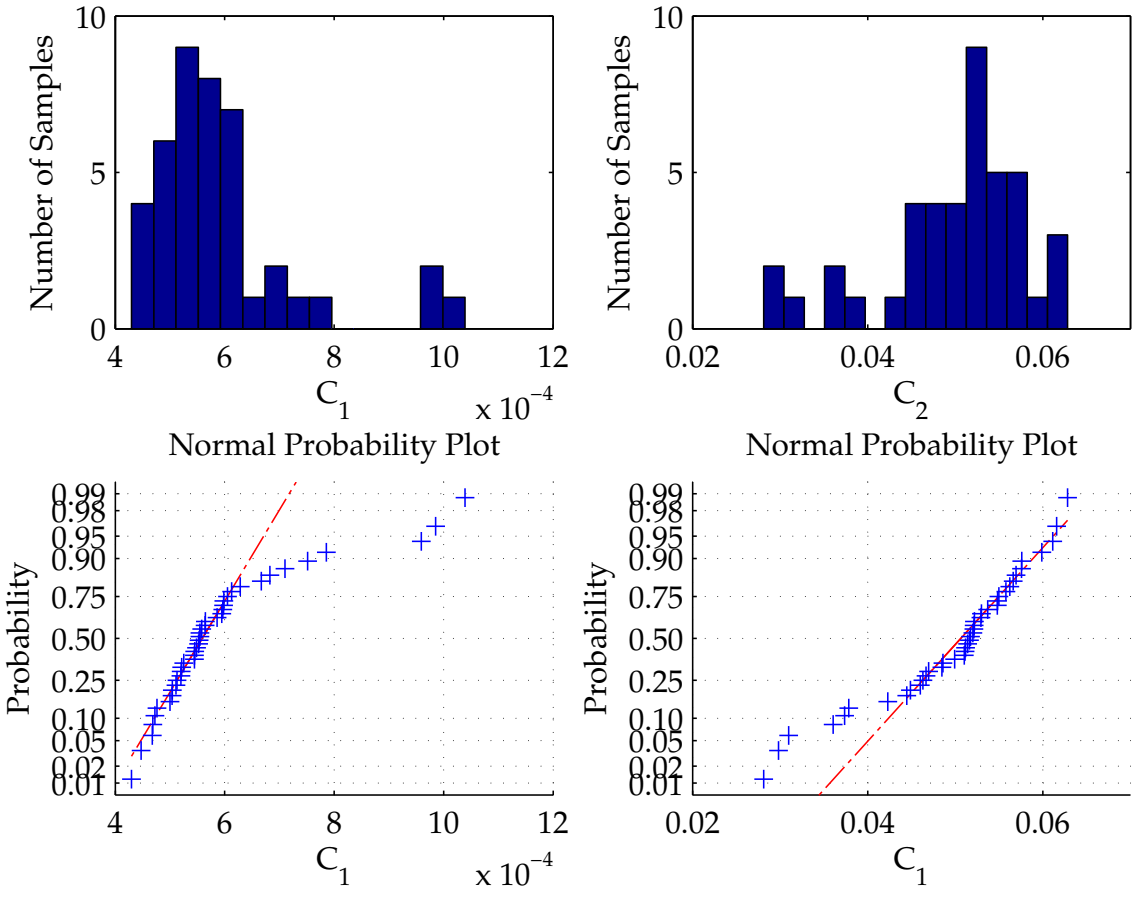

Figure 4-6: Histograms and normal probability plots (also called Q-Q plots; see Wilk and Gnanadesikan [90]) suggested that the correlation coefficients C_1 and C_2 were approximately normally distributed except for a small group of experiments, which were observed to have larger aspect ratios than most of the other data points.

estimates were as follows:

$$C_1 = 0.0044 \cdot \mathrm{AR}^{1/2} \tag{4.19}$$

$$C_2 = 0.0065 \cdot \mathrm{AR}^{-1/2}. \tag{4.20}$$

These equations for C_1 and C_2 can be substituted into Eq. 4.16, yielding

$$\Phi_{\mathrm{m,L}} = 0.0044 \cdot \mathrm{AR}^{1/2}\mathrm{Re}_{\omega} + 0.0065 \cdot \mathrm{AR}^{-1/2}\mathrm{Re}_{d\mathrm{h}}, \tag{4.21}$$

which is a global correlation for the dimensionless heat flux that spans all of the experimental data.

These correlations for C_1 and C_2, of course, result in additional error in reproducing the original experimental data. A comparison of the rRMSE associated with the experiment-specific values of C_1 and C_2 and the estimated values from Eq. 4.19 is shown in Fig. 4-8. The equation-estimated constants generally have a higher rRMSE than the experiment-specific versions; however, the error is still reasonably small, and is likely to be useful in the design phase.

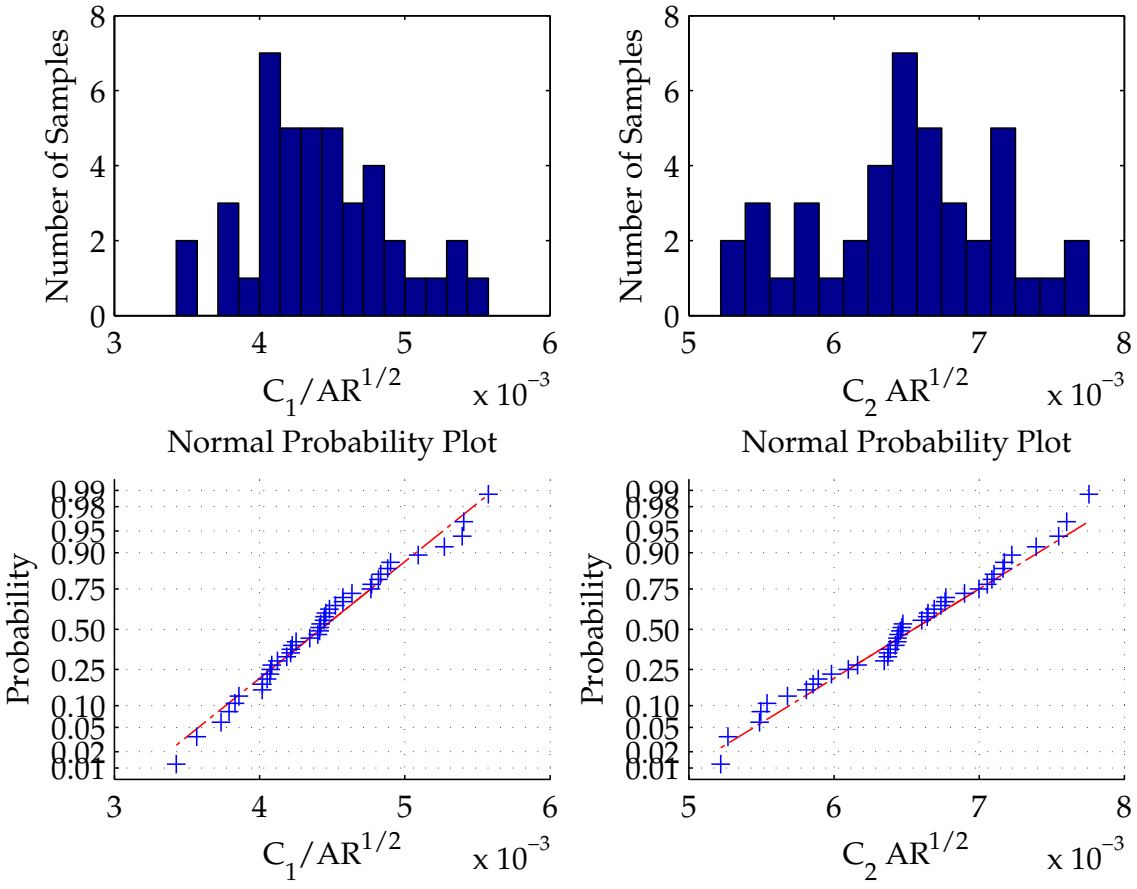

Figure 4-7: The correlation coefficients C_1 and C_2 were modified by multiplying by $\mathrm{AR}^{-1/2}$ and $\mathrm{AR}^{1/2}$, respectively. This transformation improved the estimators; the transformed variables are more closely represented by a normal distribution. The means of these distributions are the coefficients in Eq. 4.19.

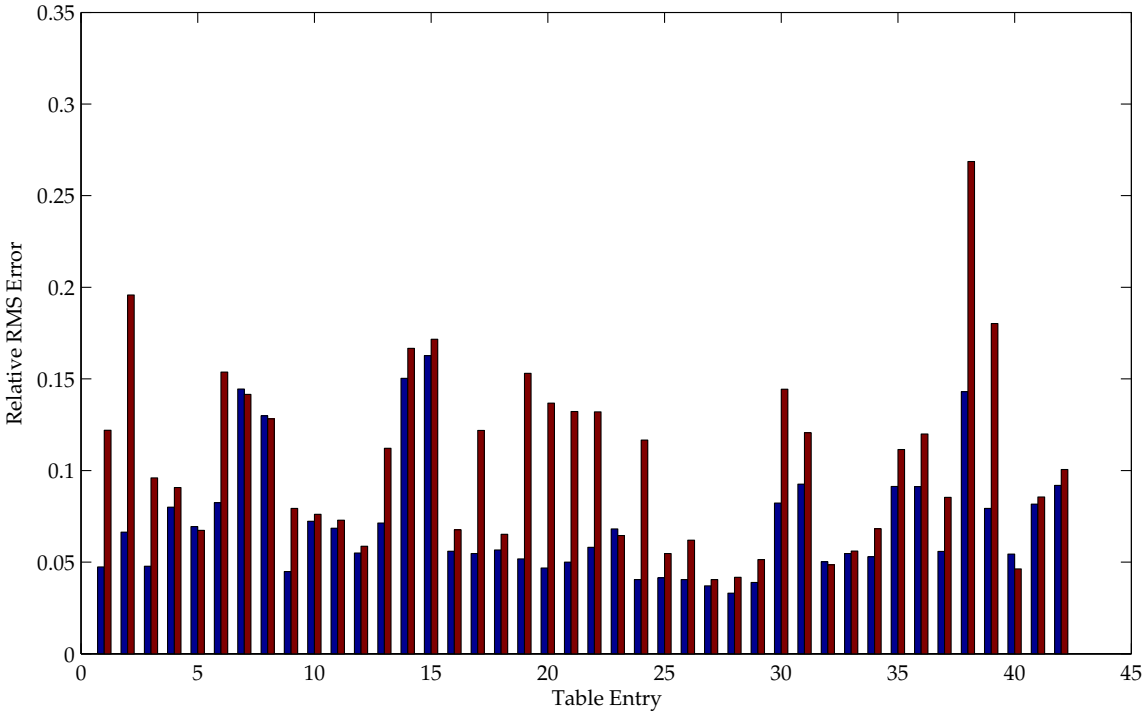

Figure 4-8: The correlation coefficients C_1 and C_2 can be either be determined directly from experimental data or estimated as a function of the aspect ratio using Eq. 4.19. The rRMSE (the error in the estimated heat transfer compared to the measured heat transfer) of these two estimation methods is shown for (1, blue bars) the experiment-specific values of C_1 and C_2 from Table 4.1; and (2, red bars) the equation-estimated values of C_1 and C_2 from Eq. 4.19. Using the equation-based estimate introduces some additional error, but the entirety of each data set can typically be represented with an rRMSE of 20% or less.

In summary, the heat transfer for an integrated fan is well approximated by a two-variable linear correlation for the dimensionless heat flux (Eq. 4.16):

$$\Phi_{\mathrm{m,L}} = C_1 \mathrm{Re}_{\omega} + C_2 \mathrm{Re}_{d\mathrm{h}}. \tag{4.22}$$

The constants C_1 and C_2 can either be determined by consulting Table 4.1 or using Eq. 4.19, which is a function of the aspect ratio of the impeller.

4.2 Fan Performance

Fan and power curves were measured on the square and circular stator apparatuses. Their general form was observed to be consistent for most of the impellers tested, and above a critical rotational Reynolds number the fan and power curves were well described by the dimensionless parameters ϕ, ψ_{ts}, and ξ, the flow, head, and power coefficients, respectively. Correlations in terms of these parameters were formed for each experiment, which allowed the dimensionless fan and power curves to be represented with two parameters each (each experiment had about 110 data points). The correlation parameters describing these fits were compared and some patterns based on the fan geometry became evident. The correlation parameters were related to the fan geometry through some sim-

ple relations. From a design perspective, these relations allow for the fan performance to be quickly estimated for an unknown fan geometry.

4.2.1 General Features

The fan and power curves were observed to be well approximated by linear fits. For example, Fig. 4-9 shows the fan and power curves for Fan 5 (15 blades, 90° exit angle, $b_b = 1.6\,\text{mm}$, $b_g = 2.6\,\text{mm}$). The dashed lines are linear fits for each rotational speed, and the solid lines comprising each point represent the uncertainty bounds in both axes. The uncertainty in the mechanical power input may be slightly underestimated, because the uncertainty in the bearing power was not included in the bounds shown in Fig. 4-9. The estimated bearing power, based on the parabolic fit discussed in Section 2.1.2, was subtracted from the measured motor power to determine the mechanical input power at each point.

The dimensionless fan parameters (the flow coefficient ϕ, the head coefficient ψ_{ts}, and the power coefficient ξ) were found to be effective in collapsing all of these speed-dependent curves onto a single curve. Figure 4-10 shows the dimensionless fan and power curves associated with the experimental data shown in Fig. 4-9. Except for the 1 and 2 krpm data, all of the points seem to be well represented by a single line. The practical

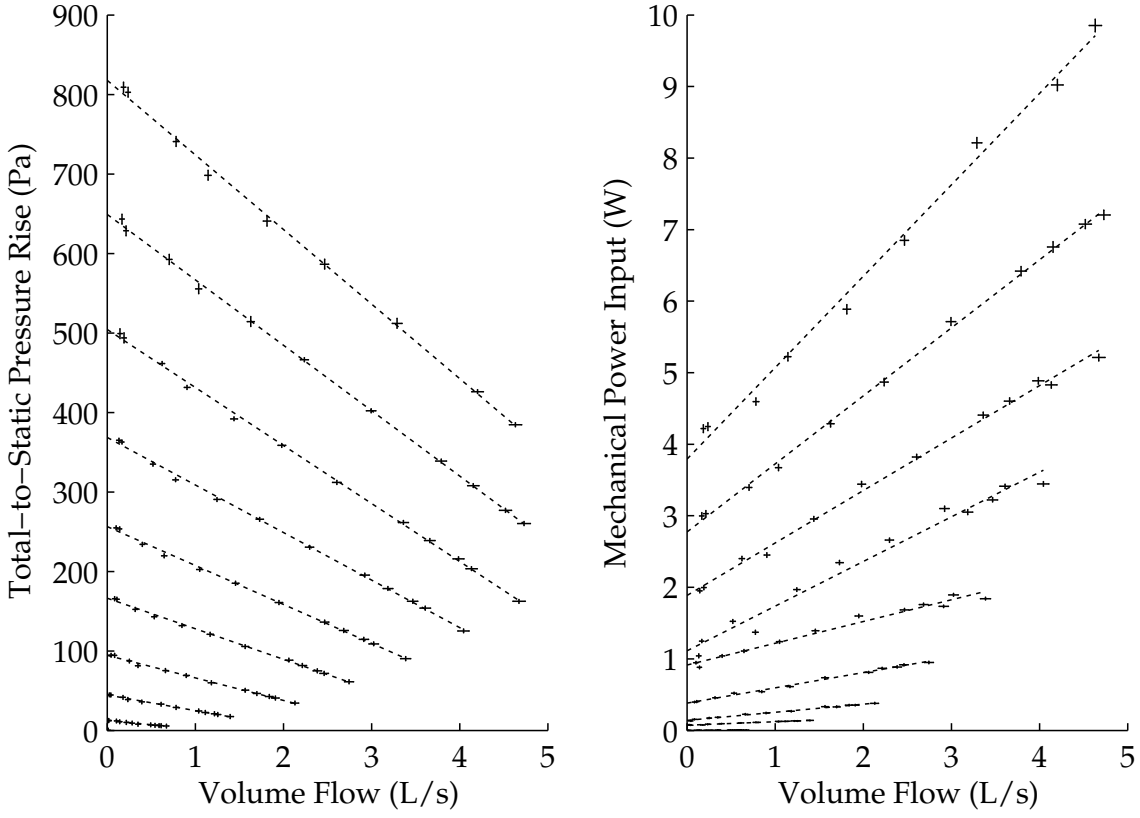

Figure 4-9: The fan and power curves were found to be well described by linear fits; this experimental data is for Fan 5 (15 blades, 90° exit angle, $b_b = 1.6\,\text{mm}$, $b_g = 2.6\,\text{mm}$). The curves shift away from the origin with increasing rotational speed. Fan and power curves for 1–9 krpm are shown in 1 krpm increments.

consequence of this behavior is that the fan and power curves for a particular integrated fan geometry can be compactly represented with two parameters each for ψ_{ts} and ξ. This will be discussed in detail in Section 4.2.3.

Fan Geometry Effects

The fan performance curves were observed to be sensitive to the number of blades (Z), the blade exit angle (β_2), and the fill ratio (FR). For example, Fig. 4-11 shows experimental results for 5, 10, and 15 bladed radial (90° exit angle) fans for various fill ratios. In Fig. 4-11, the top row of plots shows the fan performance curves, the middle row shows the power curves, and the bottom row shows the total-to-static efficiency. The vertical columns of plots correspond to 5, 10, and 15 blade impellers. Finally, the different symbols represent four fill ratios ranging from 0.44 to 0.78.

Increasing the fill ratio resulted in an upward shift of the fan performance curves, which indicates improved performance. Increasing the number of blades was also ben-

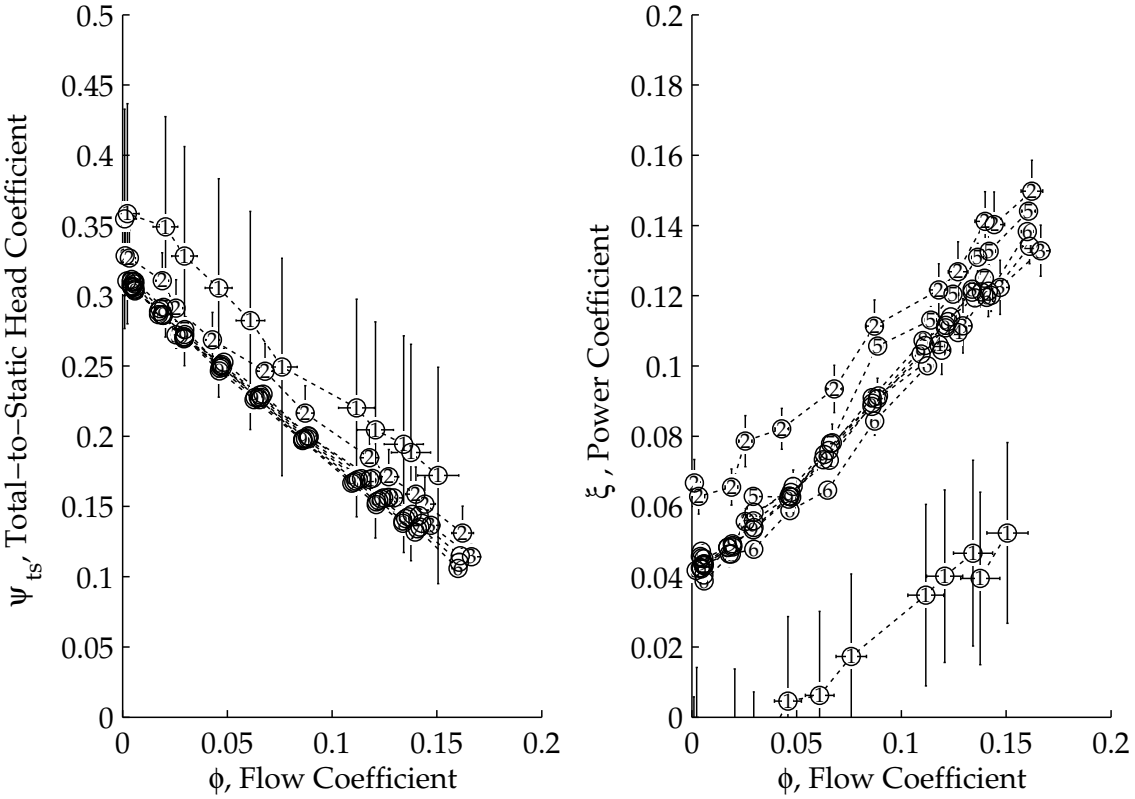

Figure 4-10: The dimensionless fan parameters collapsed all of the dimensional fan performance curves into single fan and power curve for each fan geometry. The number within each data point is the rotational speed (in krpm). The lower rotational speeds (below 3 krpm) tended to have higher uncertainty and did not fall into line with the higher rotational speed curves; this difference was likely due to Reynolds number effects in the fan, suggesting the transition to turbulence is complete by about $\mathrm{Re}_\omega = 5 \cdot 10^4$. The experimental data in this figure correspond to Fan 5 (15 blades, 90° exit angle, $b_b = 1.6\,\mathrm{mm}$, $b_g = 2.6\,\mathrm{mm}$).

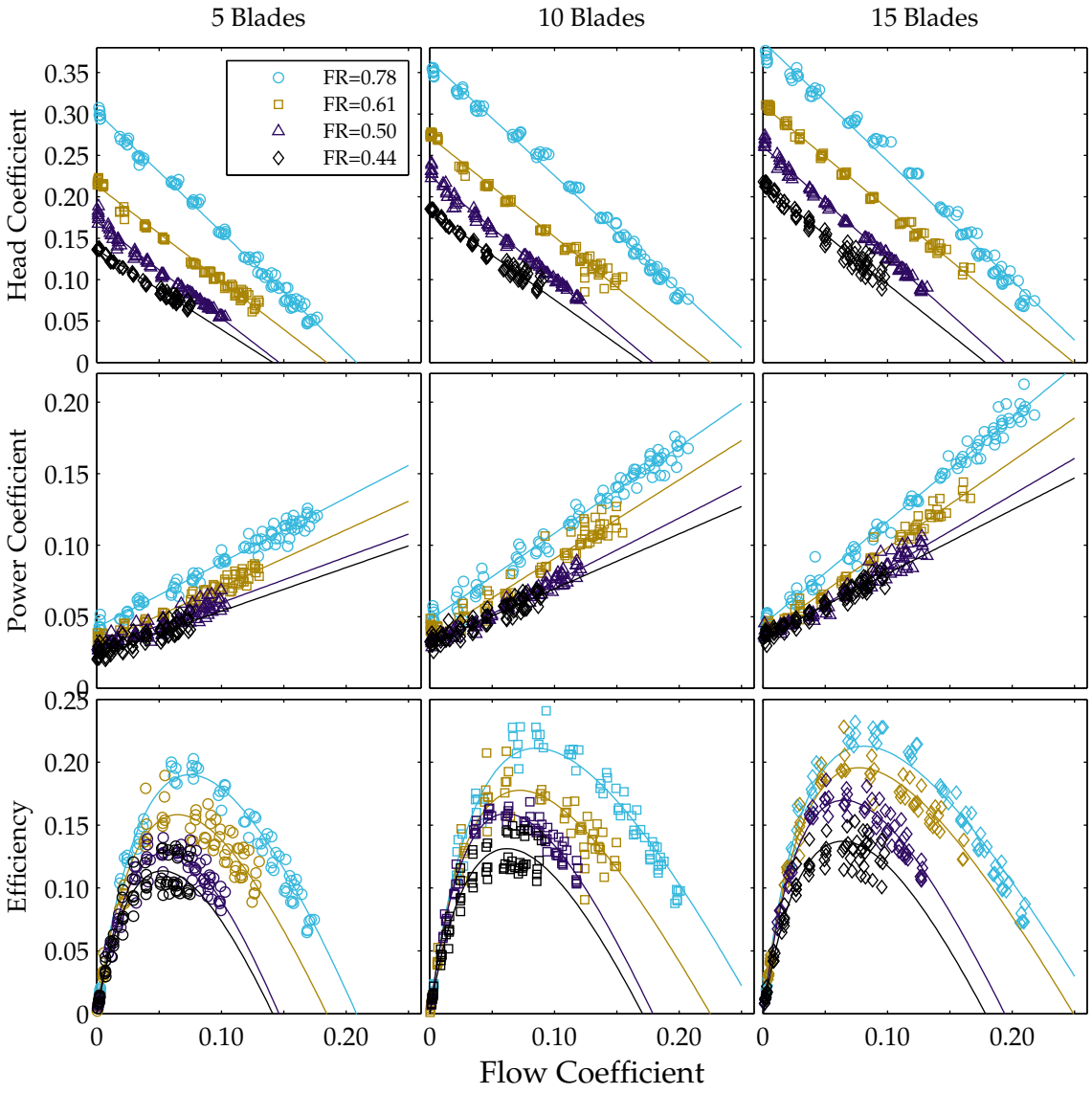

Figure 4-11: Fan performance curves for 3 impeller geometries (Fan 5, 15 blades; Fan 6, 10 blades; and Fan 7, 5 blades) are shown, with 4 fill ratios shown in each plot. As the fill ratio increases, the fan performance curve improves in both the ψ_{ts} and ϕ intercepts. The path for leakage flow from the pressure to the suction side of the impeller blades becomes more restrictive with higher fill ratio, meaning that less of the power supplied goes into dissipative phenomena, allowing a greater fraction to instead goes into the air. Furthermore, increasing the number of blades improves the fan performance curves; this is due to improved guidance of the flow by the impeller blades.

eficial, although this effect diminishes as more blades are added[2]. The fan performance curves maintain their linear form over these significant ranges in the fill ratio and number of blades.

In addition to the fan performance curves, the power curves are also affected by the number of blades. Using Eq. 1.70, the flow, head and power coefficients can be combined at each point to calculate the total-to-static efficiency ($\eta_{ts} = \phi\psi_{ts}/\xi$). The efficiency curves can be seen to improve with increased fill ratio and number of blades; however, the difference in efficiency between the 10- and 15-bladed fans appears to be negligibly small. This may be an indication that the frictional losses in the blade passage begin to outweigh the efficiency improvement associated with better flow guidance. Incidentally, the CFD simulations discussed in Chapter 3 suggested an optimum number of blades around $Z = 17$.

The fan performance curve also depends on the blade angle at the exit plane. This dependence makes sense because the blade angle appears in the Euler turbomachinery equation and therefore changes the theoretical maximum fan performance curve that can be reached (see Eq. 1.52). The blade angle affects the relationship between the meridional and tangential velocity components, which influences the slip and the frictional losses (this will be discussed in more detail in Section 4.2.2). The trends associated with variation of the blade angle, based on the Euler turbomachinery equation, were observed experimentally; Fig. 4-12 shows measurements of the total-to-static head coefficient, the power coefficient, and the efficiency for 90, 60 and 45 degree exit angle impellers. Three values of the fill ratio are shown in each plot.

As the blade angle is reduced (i.e. as the blades become more backswept), the maximum flow coefficient decreases and the maximum head coefficient decreases. The maximum efficiency increases, although diminishing returns appear evident in comparing the 60 and 45° impellers.

4.2.2 Analytical Estimates

The Euler turbomachinery equation (1.52) relates the theoretical performance of an ideal fan to its geometry using the conservation of angular momentum:

$$\psi_{ts} = \frac{1}{2}\left[1 - \left(\frac{\phi}{\sin\beta_2}\right)\right]. \tag{4.23}$$

In an ideal fan, the flow follows the blade contour so that the flow angle is the same as the blade angle at station 2 (the exit plane). This ideal performance is decreased by phenomena such as slip (due to imperfect guiding of the flow) and losses of total pressure such as frictional and incidence loss. The Euler equation for the total-to-static pressure rise can be expressed to include the slip factor. This is done by considering the velocity triangle with slip, and using the expression for the total-to-static pressure rise

$$\Delta p_{ts} = \frac{\rho}{2}\left(u_2^2 - w_2^2\right), \tag{4.24}$$

[2]The analytical estimates shown in Section 4.2.2 confirm that diminishing returns begin to take effect around 15 blades. Recalling that the size of the relative eddy (a loss mechanism associated with imperfect guiding of the flow) is related to the width of the blade passage at the exit, it makes sense that the improvement associated with adding blades would diminish; the pitch between blades at the exit plane does not change as much going from 10 to 15 blades as it does going from 5 to 10.

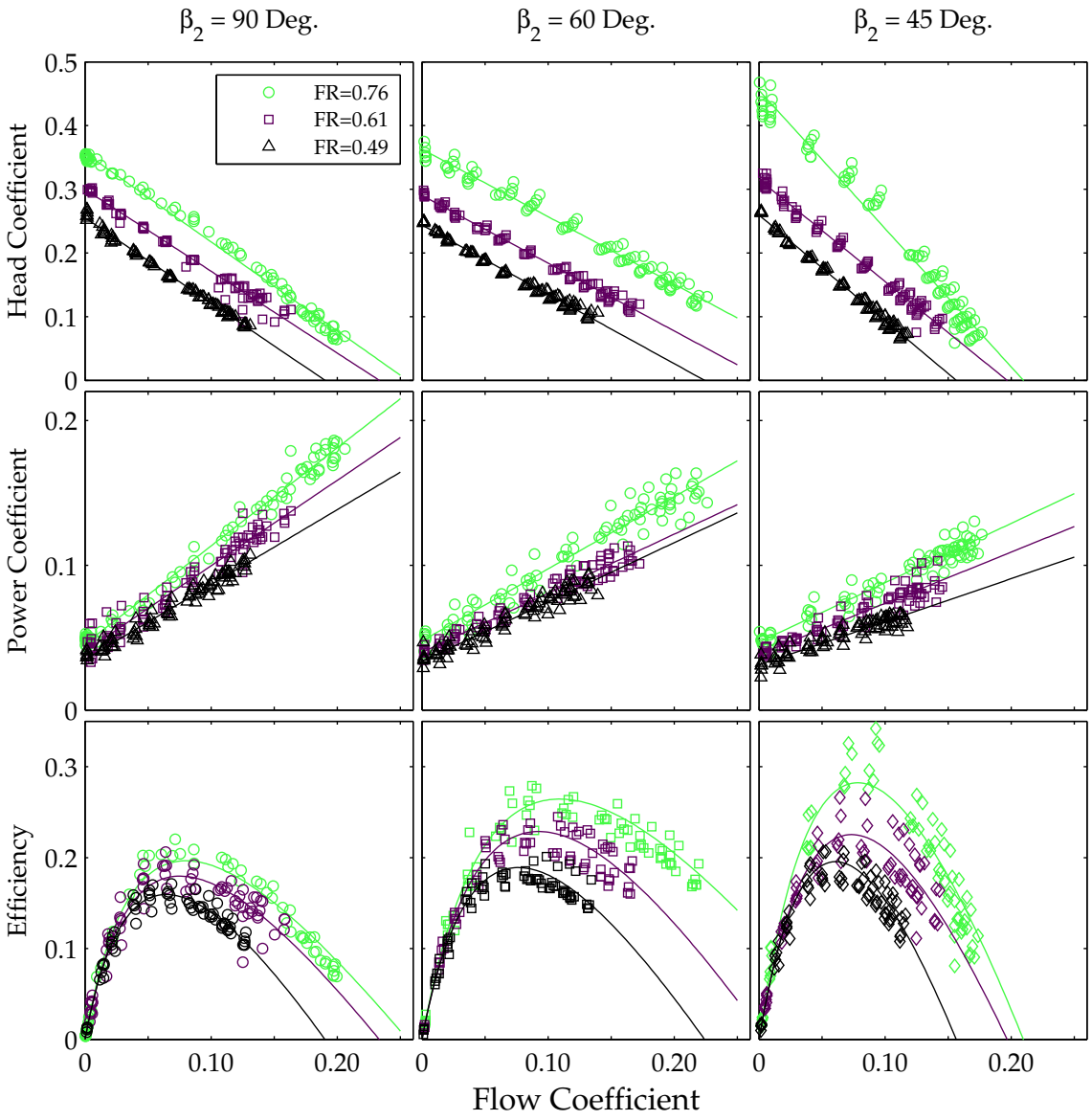

Figure 4-12: Fan performance curves for 3 15-bladed impeller geometries (Fan 8, $\beta_2 = 90°$; Fan 12, $\beta_2 = 60°$; and Fan 13, $\beta_2 = 45°$) are shown, with 3 fill ratios shown in each plot. As in Fig. 4-11, the fan performance curve improves in both the ψ_{ts} and ϕ intercepts as the fill ratio increases. As the exit angle is reduced, the blades become more backswept; as the Euler turbomachinery equation predicts, the maximum flow coefficient decreases and the maximum head coefficient increases. The maximum efficiency increases with decreases in the blade angle.

which is derived from the Euler equation [51]. The relative velocity w_2 can be calculated by applying the Pythagorean theorem to the velocity triangle (Fig. 1-12), as

$$w_2^2 = w_{\mathrm{m}2}^2 + w_{u2}^2, \tag{4.25}$$

where w_{u2} is the tangential relative velocity at the outlet, and is increased over its ideal value by the slip velocity c_{slip}. With this slip-modified velocity, and the definitions of the head coefficient, flow coefficient and slip factor, the ideal estimate of the tangential velocity in the Euler equation can be modified to include the effect of slip:

$$\psi_{\mathrm{ts,s}} = \sigma_{\mathrm{s}} - \frac{\sigma_{\mathrm{s}}^2}{2} - \frac{\phi(1-\sigma_{\mathrm{s}})}{\tan(2\beta_2)} - \frac{\phi^2}{2\sin\beta_2}, \tag{4.26}$$

where β_2 is the blade metal angle at the exit plane. The slip factor, defined in Eq. 1.57, can be estimated based on one of several correlations (e.g. the Wiesner correlation, Eq. 1.58) for substitution into Eq. 4.26, which estimates the total-to-static pressure rise including slip. When the slip factor is 1, Eq. 4.26 reduces to the ideal form of the Euler turbomachinery equation (Eq. 4.23).

Next, the effect of frictional loss in the passage can be estimated. The frictional loss is presumed to be proportional to the relative velocity at the exit plane, w_2:

$$\Delta p_{\mathrm{t}} = K_{\mathrm{f}} \frac{\rho}{2} w_2^2, \tag{4.27}$$

where K_{f} is a minor loss coefficient, assumed to be of order 1. The relative velocity w_2 was calculated with Eq. 4.25, and Eq. 4.27 was nondimensionalized using the reference area (A_2) and reference speed (u_2) for consistency with the head and flow coefficients. In dimensionless form, Eq. 4.27 represents the reduction in the total-to-static head coefficient due to frictional loss:

$$\psi_{\mathrm{friction}} = \frac{K_{\mathrm{f}}}{2}\left[\phi^2\left(1+(\tan\beta_2)^{-2}\right) + (1-\sigma_{\mathrm{s}})^2 + \frac{2\phi(1-\sigma_{\mathrm{s}})}{\tan\beta_2}\right]. \tag{4.28}$$

The reduction in the head coefficient due to frictional loss was subtracted from the expression for the head coefficient including slip (Eq. 4.26) to form an estimate of the fan's operational head coefficient including slip and friction ($\psi_{\mathrm{ts,sf}}$).

$$\psi_{\mathrm{ts,sf}} = \psi_{\mathrm{ts,s}} - \psi_{\mathrm{friction}} \tag{4.29}$$

The slip factor used in Eqs. 4.26 and 4.28 was calculated with Wiesner's correlation (shown in Eq. 1.58):

$$\sigma_{\mathrm{s}} = 1 - \frac{\sqrt{\sin\beta_2}}{Z^{0.7}}. \tag{4.30}$$

This slip factor correlation is affected by the exit blade angle (β_2) and the number of blades (Z). A shallower exit angle (farther from the radial line) also causes the relative velocity to be lower at a given flow rate, as can be seen from the velocity triangle, which decreases the frictional loss.

Figure 4-13 shows the effect of the exit angle and the number of blades. In each subplot, the total-to-static head coefficient (ψ_{ts}) is shown as a function of the flow coefficient. The uppermost, black curve represents the ideal head coefficient, calculated with Eq. 4.23.

The blue curves represent the head coefficient including the effect of slip, for 3 slip factors associated with 15, 10 and 5 blade impellers (the slip factor was calculated with Eq. 4.30). Finally, the red curves represent the head coefficient including the effect of slip and friction (calculated using Eq. 4.29). In each group of curves, the effect of the number of blades can be clearly seen; the total-to-static head coefficient decreases as the number of blades decreases from 15 to 5. The difference in the head coefficient between the 15- and 10-blade impellers can be seen to be small in comparison to the difference between the 10- and 5-blade impellers.

4.2.3 Correlations

Fan Performance Curves

The fan performance curves were well described by the dimensionless forms of the volume flow and pressure rise (the flow coefficient ϕ and the total-to-static head coefficient ψ_{ts}). These dimensionless curves, like their dimensional counterparts, exhibited linear behavior. A linear correlation for the total-to-static head coefficient as a function of the flow coefficient allowed the dimensionless fan performance curves to be approximated with two parameters:

$$\psi_{ts} = \psi_{ts,max} - C_r \phi, \tag{4.31}$$

where $\psi_{ts,max}$ is the maximum or "blocked" head coefficient and C_r is a coefficient that represents the slope of the dimensionless fan performance curve. The maximum flow coefficient can be expressed as a combination of C_r and ψ_{ts} as

$$\phi_{max} = \frac{\psi_{ts,max}}{C_r}; \tag{4.32}$$

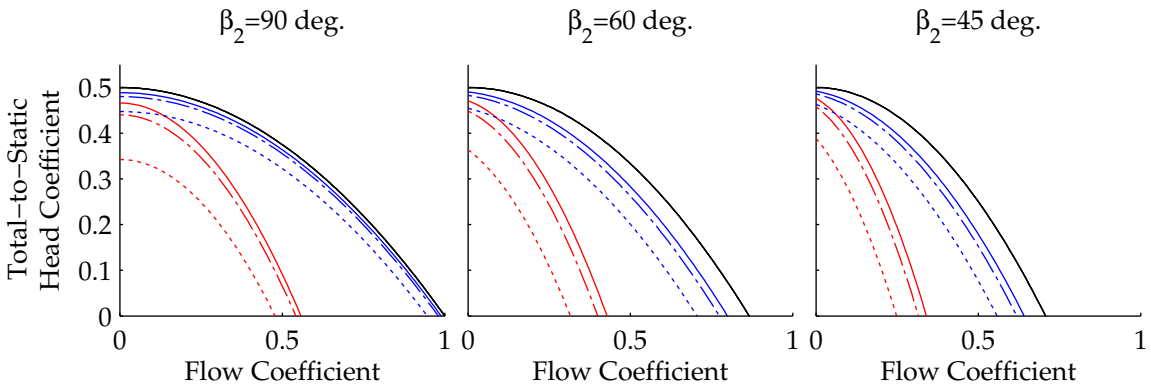

Figure 4-13: The dimensionless Euler turbomachinery equation was modified to include the effects of slip and friction. The slip factor was calculated using Wiesner's correlation, which accounts for the blade exit angle and number of blades. The frictional loss was assumed to scale with the square of the relative velocity; in this figure, the minor loss coefficient was assumed to be 1. The uppermost line in each plot is the Euler-estimated head coefficient, which changes with the exit angle β_2. Just below the Euler head coefficient line, the next set of 3 (blue) lines shows the head coefficient including the effect of slip (Eq. 4.26); the slip factor was computed with Wiesner's correlation (Eq. 4.30). Finally, the lowest group of 3 lines shows the estimated head coefficient including slip and friction (Eq. 4.29). In each group of 3 lines, the solid, middle dashed, and lowest dashed lines represent 15, 10, and 5-blade fans.

this parameter is convenient because of its physical meaning, which is a dimensionless form of the free delivery flow rate, the flow which occurs when pumping against a resistance-free system. In general, this linear, dimensionless correlation for the fan performance curves resulted in accurate estimates of the fan performance. Table 4.3 shows the values of $\psi_{ts,max}$, ϕ_{max}, and C_r for the fans tested in the circular stator apparatus, as well as the goodness of the correlation fit (expressed as the relative root mean squared error, rRMSE). Table 4.3 lists the details of each fan performance curve experiment, including the experiment identifier (EID), the fill ratio (FR), the aspect ratio (AR), the inlet ratio (IR), the blade exit angle (β_2), and the number of blades (Z). The circular stator tests were thought to be the most accurate, based on the method of pressure and flow measurement, consistency of the measured data, and simplicity of the stator geometry[3]. The relative RMS error (rRMSE) indicates that most of the geometries' correlations represented the data to within 10%.

The correlation parameters ($\psi_{ts,max}$ and ϕ_{max}) themselves were examined to see if any geometry dependence could be ascertained. A correlation related to the geometry of the impellers would be useful in the early phase of a design, when it is desirable to have rough estimates of a hypothetical fan's performance based on high-level design parameters. A reasonable agreement with the data was obtained by fitting these parameters as follows:

$$\phi_{max} = \mathrm{FR}\,(a_1 + a_2 Z \sin(\beta_2)) \tag{4.33}$$

$$\psi_{ts,max} = \mathrm{FR}\left(b_1 + b_2 Z^{-1}\right), \tag{4.34}$$

where a and b are constants with values shown in Table 4.2. With this form, both coefficients approach zero as FR approaches zero. The $\sin(\beta_2)$ term was motivated by the velocity triangle and seemed to provide a good fit for the various blade angle data. Using this reduced form, the fan performance curves can be estimated as a function of the fan geometry (Z, FR, and β_2). The error associated with using these correlation constant estimators can be seen in Fig. 4-14.

Table 4.2: Fan Performance Curve Parameter Estimators

	1	2
ϕ_{max} estimator (a)	0.2257	0.0104
$\psi_{ts,max}$ estimator (b)	0.5970	-1.1246

Table 4.3: Fan Performance Correlations Summary

Fan Characteristics						ψ_{ts} Correlation				ξ Correlation		
EID	FR	AR	IR	β_2	Z	$\psi_{ts,max}$	ϕ_{max}	C_r	rRMSE (ψ_{ts})	ξ_0	C_w	rRMSE (ξ)
189	0.60	0.02	0.400	42.5	5	0.222	0.162	1.37	0.081	0.029	0.244	0.089
190	0.75	0.02	0.400	42.5	5	0.340	0.210	1.62	0.114	0.044	0.282	0.078
191	0.43	0.02	0.400	42.5	5	0.136	0.109	1.24	0.080	0.018	0.178	0.103
192	0.33	0.02	0.400	42.5	5	0.107	0.077	1.39	0.083	0.013	0.163	0.076
197	0.43	0.02	0.400	42.5	5	0.121	0.108	1.12	0.057	0.018	0.175	0.819
200	0.75	0.02	0.400	42.5	5	0.279	0.195	1.43	0.120	0.042	0.230	0.079

(continued on next page)

[3]The square stator apparatus had corner posts that were specific to the PHUMP heat pipe application. The circular stator apparatus only measured the performance of the fan, and did not implicitly contain any resistances to the flow.

Table 4.3 (continued from previous page)

	Fan Characteristics					ψ_{ts} Correlation				ξ Correlation		
EID	FR	AR	IR	β_2	Z	$\psi_{ts,max}$	ϕ_{max}	C_r	rRMSE (ψ_{ts})	ξ_0	C_w	rRMSE (ξ)
204	0.61	0.02	0.400	90	15	0.267	0.243	1.10	0.044	0.047	0.542	0.099
209	0.61	0.02	0.400	90	10	0.233	0.204	1.14	0.071	0.047	0.514	0.092
210	0.61	0.02	0.400	90	5	0.180	0.165	1.09	0.049	0.034	0.354	0.110
213	0.44	0.02	0.400	90	10	0.183	0.171	1.07	0.044	0.031	0.383	0.093
214	0.44	0.02	0.400	90	5	0.136	0.141	0.96	0.036	0.024	0.304	0.125
215	0.44	0.02	0.400	90	15	0.214	0.179	1.20	0.059	0.036	0.446	0.064
216	0.60	0.02	0.400	90	15	0.289	0.241	1.20	0.030	0.037	0.573	0.089
225	0.61	0.02	0.400	90	15	0.300	0.233	1.29	0.088	0.041	0.590	0.099
226	0.61	0.02	0.400	90	20	0.320	0.243	1.31	0.093	0.044	0.632	0.080
227	0.61	0.02	0.400	75	15	0.322	0.246	1.31	0.103	0.043	0.534	0.062
228	0.61	0.02	0.400	60	15	0.317	0.245	1.29	0.048	0.042	0.441	0.082
229	0.61	0.02	0.400	45	15	0.315	0.197	1.60	0.081	0.038	0.354	0.079
230	0.59	0.02	0.400	42.5	5	0.230	0.157	1.46	0.093	0.027	0.237	0.129
231	0.61	0.02	0.400	90	15	0.310	0.249	1.25	0.027	0.038	0.604	0.059
232	0.61	0.02	0.400	90	10	0.273	0.225	1.21	0.070	0.036	0.550	0.100
233	0.61	0.02	0.400	90	5	0.214	0.184	1.16	0.049	0.031	0.399	0.087
235	0.76	0.02	0.400	60	15	0.431	0.280	1.54	0.077	0.051	0.507	0.073
236	0.76	0.02	0.400	45	15	0.455	0.210	2.17	0.177	0.047	0.410	0.075
237	0.75	0.02	0.400	42.5	5	0.341	0.212	1.61	0.118	0.043	0.275	0.095
238	0.76	0.02	0.400	90	20	0.389	0.268	1.45	0.227	0.047	0.749	0.091
239	0.76	0.02	0.400	75	15	0.410	0.274	1.49	0.253	0.047	0.625	0.073
240	0.76	0.02	0.400	75	15	0.412	0.264	1.56	0.118	0.048	0.613	0.063
241	0.76	0.02	0.400	90	15	0.357	0.256	1.40	0.074	0.046	0.678	0.056
242	0.86	0.02	0.400	60	15	0.505	0.286	1.77	0.171	0.058	0.550	0.092
244	0.50	0.02	0.400	60	15	0.258	0.191	1.35	0.042	0.033	0.406	0.081
246	0.40	0.02	0.400	60	15	0.215	0.153	1.41	0.057	0.027	0.397	0.087
247	0.40	0.02	0.400	60	15	0.213	0.164	1.30	0.035	0.028	0.336	0.057
248	0.30	0.02	0.400	60	15	0.175	0.104	1.68	0.065	0.023	0.330	0.083
249	0.30	0.02	0.400	60	15	0.172	0.114	1.51	0.049	0.023	0.294	0.073
250	0.20	0.02	0.400	60	15	0.127	0.059	2.17	0.067	0.019	0.240	0.091
251	0.10	0.02	0.400	60	15	0.064	0.031	2.10	0.054	0.013	0.105	0.058
252	0.86	0.02	0.500	60	15	0.440	0.390	1.13	0.080	0.061	0.507	0.077
253	0.76	0.02	0.500	60	15	0.363	0.342	1.06	0.051	0.048	0.498	0.088
254	0.61	0.02	0.500	60	15	0.290	0.273	1.06	0.037	0.040	0.408	0.065
255	0.51	0.02	0.500	60	15	0.244	0.224	1.09	0.038	0.034	0.410	0.082
256	0.40	0.02	0.500	60	15	0.200	0.171	1.17	0.048	0.029	0.350	0.076
257	0.30	0.02	0.500	60	15	0.163	0.120	1.35	0.052	0.024	0.300	0.071
258	0.20	0.02	0.500	60	15	0.115	0.072	1.61	0.047	0.020	0.215	0.050
259	0.10	0.02	0.500	60	15	0.057	0.039	1.46	0.037	0.013	0.085	0.052
260	0.76	0.02	0.400	60	15	0.418	0.263	1.59	0.092	0.047	0.494	0.059
261	0.61	0.02	0.400	60	15	0.324	0.221	1.46	0.046	0.039	0.421	0.053
262	0.76	0.01	0.417	90	15	0.353	0.264	1.34	0.038	0.052	0.695	0.052
263	0.61	0.01	0.417	90	15	0.284	0.212	1.34	0.019	0.039	0.604	0.050
264	0.50	0.01	0.417	90	15	0.252	0.174	1.45	0.025	0.033	0.544	0.051
265	0.40	0.01	0.417	90	15	0.217	0.143	1.52	0.070	0.029	0.458	0.049
274	0.76	0.02	0.400	30	15	0.520	0.133	3.90	0.371	0.053	0.259	0.069
276	0.78	0.02	0.400	90	5	0.303	0.208	1.45	0.069	0.042	0.454	0.052
277	0.78	0.02	0.400	90	10	0.364	0.263	1.39	0.053	0.048	0.606	0.067
278	0.78	0.02	0.400	90	15	0.387	0.269	1.44	0.085	0.044	0.723	0.052
279	0.50	0.02	0.400	90	15	0.261	0.194	1.34	0.025	0.033	0.510	0.073
280	0.50	0.02	0.400	90	10	0.225	0.179	1.26	0.026	0.030	0.446	0.062
281	0.50	0.02	0.400	90	5	0.170	0.146	1.16	0.036	0.028	0.320	0.084
282	0.49	0.02	0.400	90	15	0.255	0.190	1.34	0.025	0.035	0.518	0.063
284	0.50	0.02	0.400	90	20	0.282	0.203	1.39	0.021	0.033	0.586	0.078

(continued on next page)

Table 4.3 (continued from previous page)

	Fan Characteristics					ψ_{ts} Correlation				ξ Correlation		
EID	FR	AR	IR	β_2	Z	$\psi_{ts,max}$	ϕ_{max}	C_r	rRMSE (ψ_{ts})	ξ_0	C_w	rRMSE (ξ)
285	0.50	0.02	0.400	75	15	0.264	0.195	1.36	0.034	0.032	0.475	0.067
286	0.50	0.02	0.400	45	15	0.259	0.156	1.66	0.051	0.031	0.298	0.093
287	0.49	0.02	0.400	30	15	0.229	0.115	1.99	0.032	0.029	0.205	0.126
288	0.61	0.02	0.400	30	15	0.319	0.127	2.50	0.080	0.038	0.207	0.133
289	0.39	0.02	0.400	30	15	0.179	0.097	1.84	0.055	0.021	0.182	0.163
290	0.90	0.03	0.400	90	15	0.452	0.358	1.26	0.035	0.035	0.870	0.059
291	0.90	0.03	0.400	60	15	0.491	0.315	1.56	0.046	0.040	0.637	0.058
292	0.80	0.03	0.400	60	15	0.435	0.281	1.55	0.029	0.036	0.628	0.049
293	0.80	0.03	0.400	90	15	0.408	0.325	1.25	0.019	0.036	0.786	0.062
294	0.70	0.03	0.400	90	15	0.370	0.280	1.32	0.012	0.036	0.724	0.055
295	0.70	0.03	0.400	60	15	0.380	0.245	1.55	0.022	0.036	0.580	0.041
296	0.60	0.03	0.400	60	15	0.332	0.194	1.71	0.026	0.033	0.552	0.043
297	0.60	0.03	0.400	90	15	0.337	0.224	1.51	0.016	0.036	0.632	0.048

Power Curves

The mechanical input power curves for the fans were also correlated in a manner similar to that of the fan performance curves. The dimensionless power curve, expressed in terms of the power coefficient ξ (defined in Eq. 1.64), was observed to be linear as mentioned above. ξ was correlated using a form similar to Eq. 4.31:

$$\xi = \xi_0 + C_w \phi, \tag{4.35}$$

where ξ_0 is the power coefficient at zero flow coefficient, and C_w is the slope of the dimensionless power curve. The values of ξ_0 and C_w for each experiment are shown in Table 4.3; this linear correlation resulted in 10% or better rRMSE in all but 6 of the experiments. Additionally, the correlation parameters ξ_0 and C_w were observed to have a relationship to the fan geometry:

$$\xi_0 = e_1 + e_2 \mathrm{FR} \sin(\beta_2) \tag{4.36}$$

$$C_w = f_1 \mathrm{FR} \sin(\beta_2) Z^{1/2}. \tag{4.37}$$

Equation 4.36 allows the two parameters that define the power curve for each fan (ξ_0 and C_w) to be estimated based on the fan geometry. The agreement between Eq. 4.36 and the power curve parameters determined from each experiment is shown in Fig. 4-15. Most of the power curve parameters are estimated to within 20% by Eq. 4.36.

4.3 Thermo-mechanical Coupling

In the previous sections, the effects of the fan geometry on the heat transfer, fan performance curves, and efficiency were shown. Considering the thermal performance at the same time as the fan performance reveals an interesting relationship. Figure 4-16 shows the thermal resistance and mechanical input power for several fans. Each plot show the effect of one geometrical parameter by comparing 3 fans. The leftmost plot shows the effect of fill ratio, the center plot shows the effect of number of blades (Z) and the rightmost plot shows the effect of the exit blade angle (β_2). On each plot, groups of constant rotational speed are connected by lines, with the higher speeds on the right.

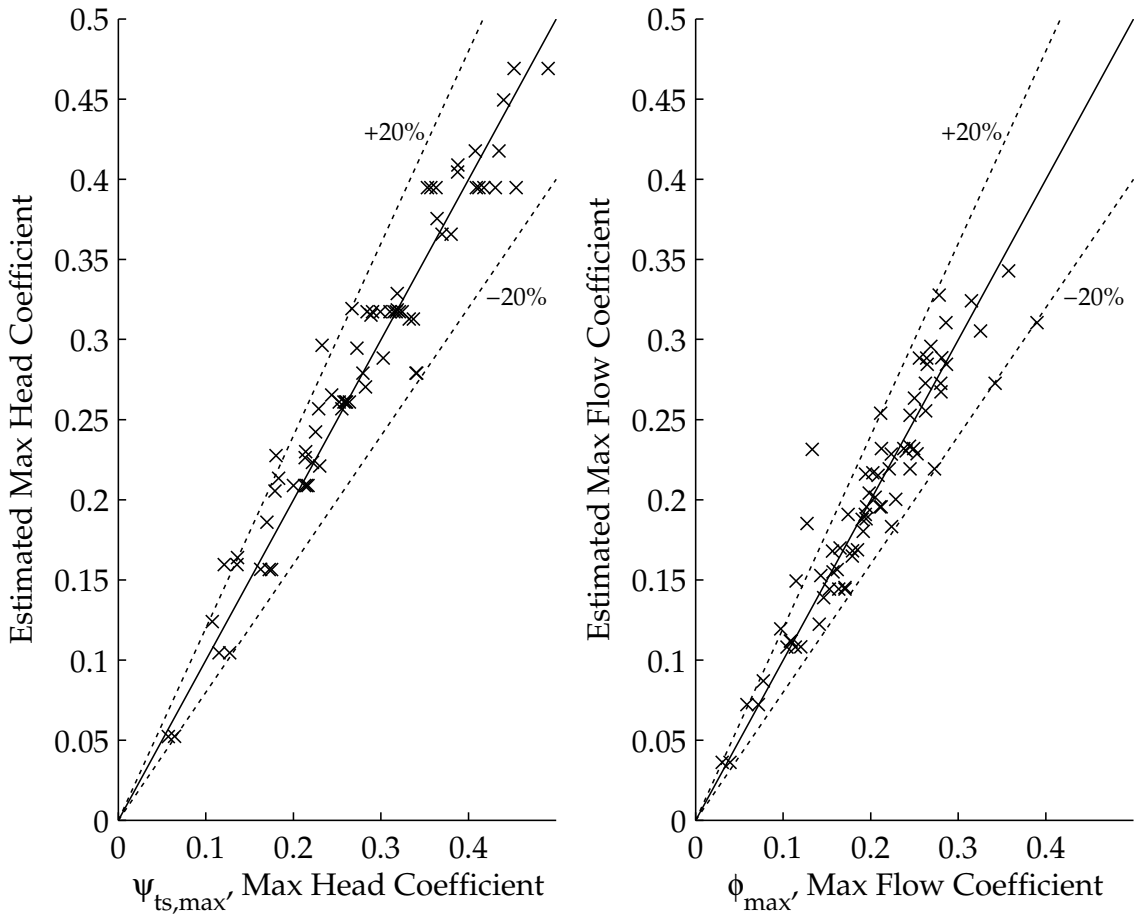

Figure 4-14: The correlation parameters $\psi_{ts,max}$ and ϕ_{max} were related to the fan geometry using Eq. 4.33; the estimates produced using Eq. 4.33 can be seen agree to within 20% for most of the experiments. Lines of ±20% are shown as dashed lines; the solid line indicates a perfect estimate.

The thermal resistance vs. mechanical power plot can easily lead to misinterpretations about the thermo-mechanical performance of the fan. For example, at first glance, the center plot seems to indicate that the 5-blade fan performs better than the 10- and 15- blade fans, because it has a lower thermal resistance at the same speed and constant mechanical power (e.g. at about 6 W, the 5-blade trace has a value of 0.55 K/W while the 15-blade trace has a value of 0.46 K/W). However, the other fans can reach a lower thermal resistance at a slower speed. The rightmost point on each connected series of constant-speed points represents the highest flow rate measured at that speed. Again referring to the center plot, the 10- and 15- bladed impellers were capable of reaching a higher flow rate at a given speed, so their curves extend farther right and allow lower thermal resistances to be achieved. The solid black lines near the bottom of each data set is the best performance frontier (also known as a Pareto frontier) based on all of the data observed in the circular stator apparatus.

A fan's operating range consists of the entire envelope of points shown on the R vs. $\dot{W}$ plot since it can operate at speeds between those shown in Fig. 4-16. The best points are the lowest thermal resistance at a given mechanical power input. The bounding en-

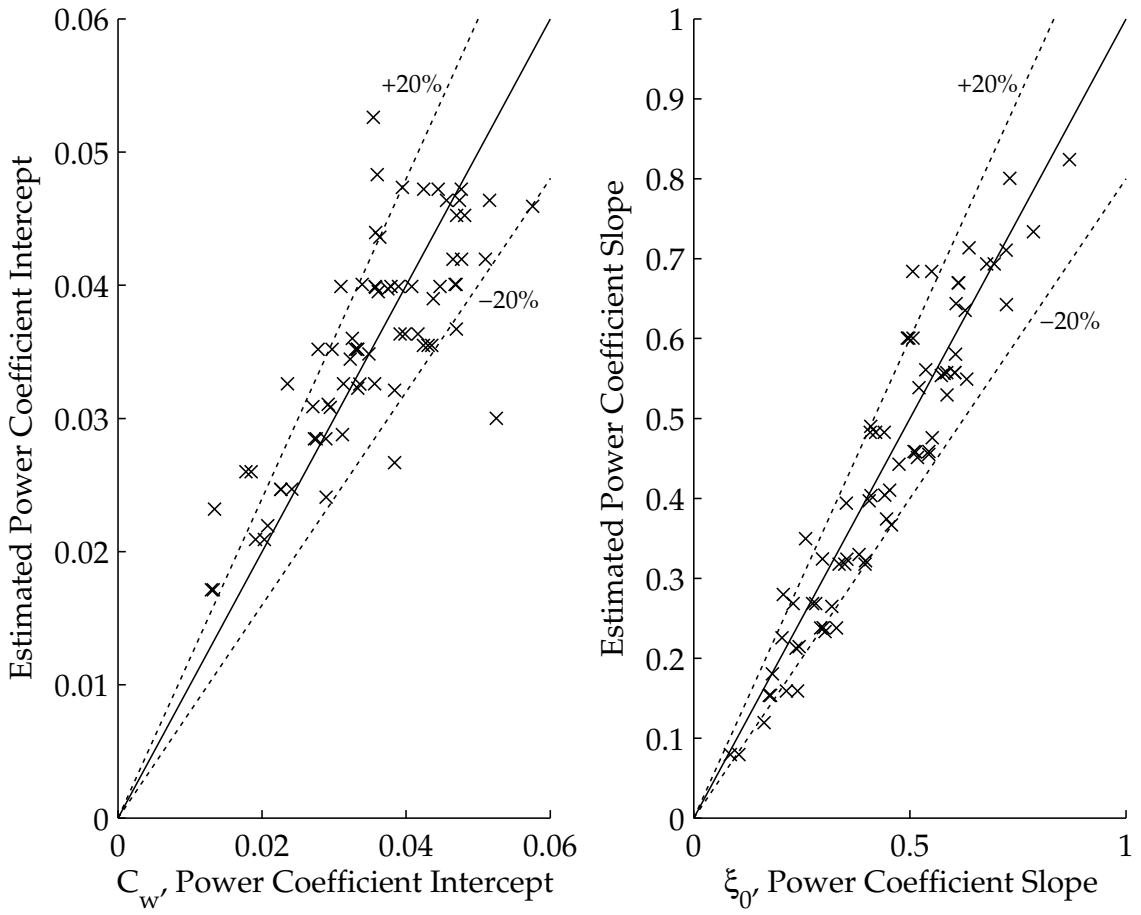

Figure 4-15: The power curve parameters ξ_0 and C_w were correlated to the fan geometry using Eq. 4.36; the estimates produced using Eq. 4.36 can be seen agree to within 20% for most of the experiments. Lines of ±20% are shown as dashed lines; the solid line indicates a perfect estimate.

velope of each data set looked similar, because small changes in the heat transfer appear as even smaller changes in R. To better compare the best operating points, all of the heat transfer data were viewed in a different representation of the fan–heat transfer coupling. Figure 4-17 shows the mechanical power plotted as a function of the average heat transfer coefficient (h_{ITD}). In Fig. 4-17, a frontier of points can clearly be seen. This frontier was found to be well represented by a power law fit for $\dot{W}$ in terms of h_{ITD}, namely

$$\dot{W} = m h_{\mathrm{ITD}}^4, \tag{4.38}$$

where the constant m has a value of $m = 6.04 \cdot 10^{-9}\,\mathrm{m^7K^4W^3}$. This dimensional representation, although not as elegant as a dimensionless approach, used a very minimal amount of data processing prior to fitting; h_{ITD} and $\dot{W}$ are essentially direct measurements. The curve defined by Eq. 4.38 is shown as a solid black line in Fig. 4-17. Fan 12 (15 blades, 60° exit angle) appears to occupy many points along the frontier, suggesting that Fan 12 is one of the best designs studied in the present work.

The frontier of best operating points can be expressed in terms of thermal resistance

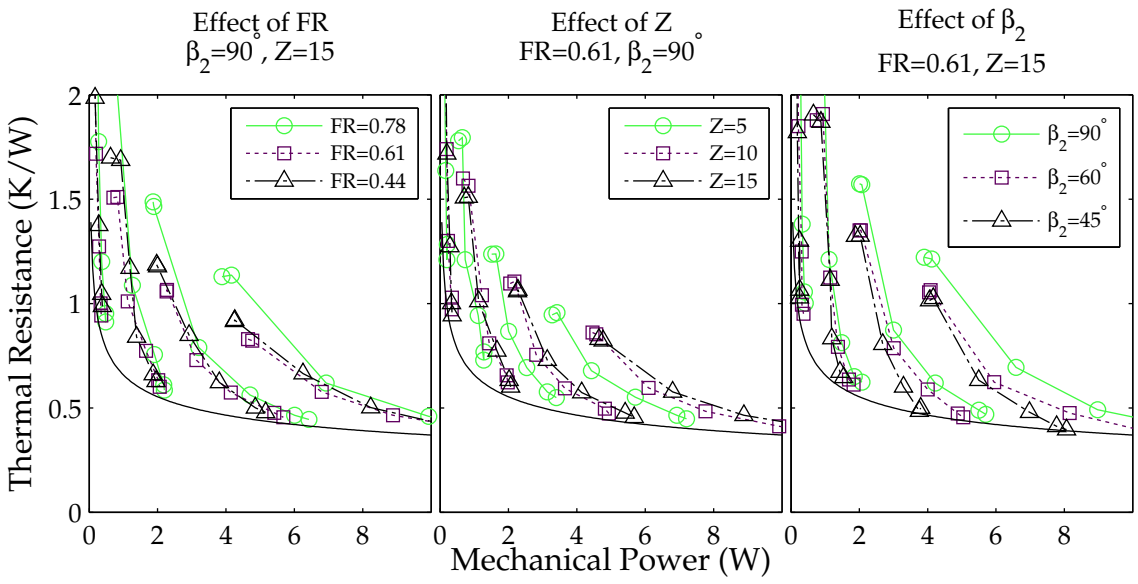

Figure 4-16: The thermal resistance decreases as the mechanical power input to the fan increases. The effects of fill ratio (FR), number of blades (Z), and blade angle (β_2) are shown in the left, center, and right plots, respectively. The left plot uses data from Fan 5; the center plot uses data from Fans 7 (○), 6 (□), and 5 (△); and the right plot uses data from Fans 8 (○), 12 (□), and 13 (△). Each plot shows three fan geometries; each of these geometries has 4 curves that correspond to 3, 5, 7, and 9 krpm rotational speeds (in left-to-right order on the plots). At each rotational speed, the thermal resistance decreases as the flow rate of air through the fan increases. The solid black lines represent the locus of points (from the entire range of heat transfer experiments) with the best performance, meaning the lowest thermal resistance for a given mechanical power input.

by manipulating Eq.4.38 using the relationship between h_{ITD} and R from Table 1.2,

$$R = \frac{m^{1/4}}{\dot{W}^{1/4} A_s}, \tag{4.39}$$

where A_s is the heated surface area of the stator gap (defined in Eq. 4.2). Equations 4.38 and 4.39 can be used as a best-case estimate of the achievable thermal performance of a single integrated fan given a mechanical power constraint. For reference, the DARPA MACE goal sought a thermal resistance of 0.05 K/W with an electrical power input of 33 W. Assuming that 33 W of mechanical power was available for the fan, a single integrated fan could only reach a thermal resistance of 0.275 K/W according to Eq. 4.39. In Chapter 5, it will be shown that a simple solution to this apparent limitation is to use multiple integrated fans in a single device. The thermal resistance in these multilayer heat sinks can be much lower than Eq. 4.39 would suggest.

Incidentally, some prior work on the heat transfer in integrated fans was reported by Allison [50], who gives two equations for R representing the best design points. These were as follows:

$$R = 0.387\dot{W}^{-0.333} \quad \text{(Experimental Measurements [50])} \tag{4.40}$$

$$R = 0.339\dot{W}^{-0.643} + 0.373 \quad \text{(CFD Simulations [50])} \tag{4.41}$$

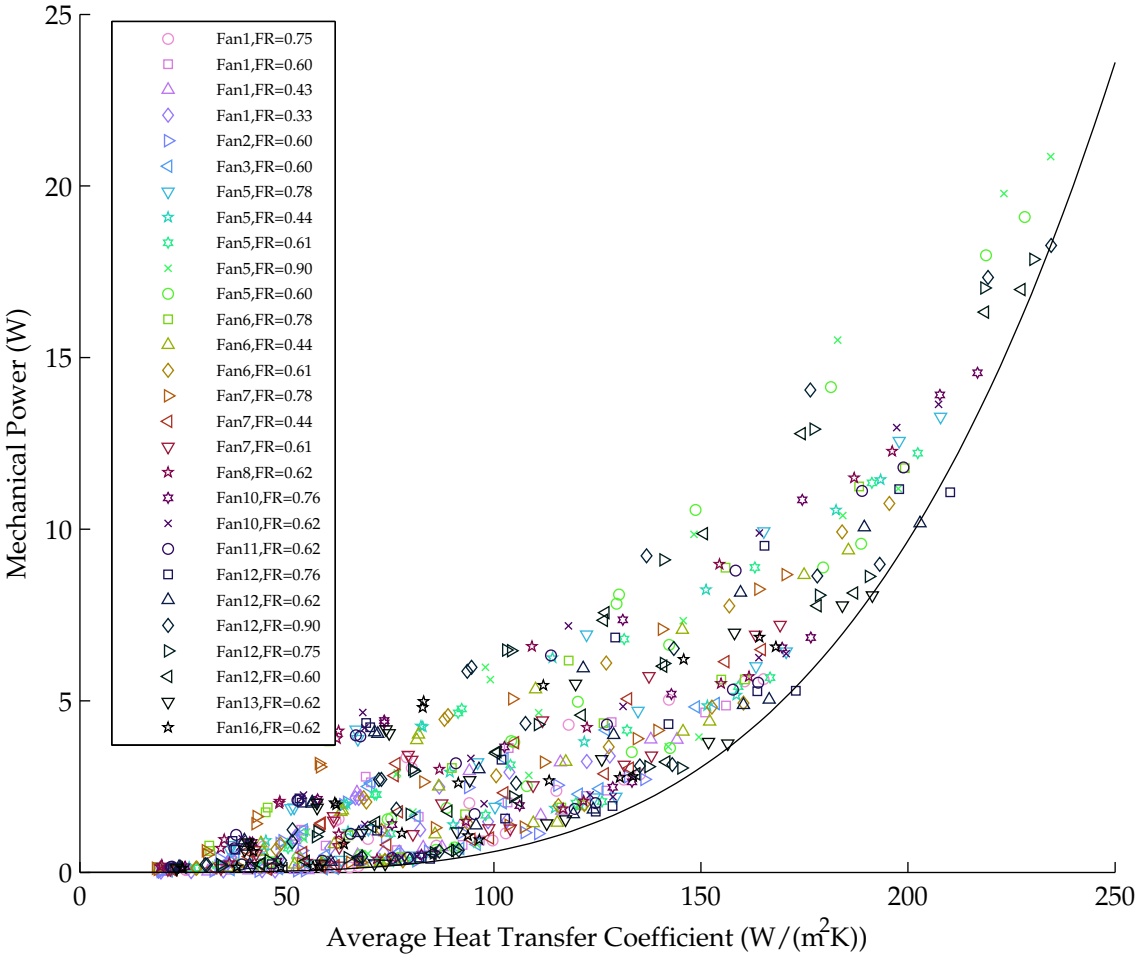

Figure 4-17: The experimental data from the circular stator apparatus are shown to approach a maximum heat transfer coefficient at each value of mechanical power input. This frontier represents the best observed fan designs. Many of the points along the frontier are for Fan 12, a 15-blade, 60° exit angle impeller. The frontier was observed to have the form shown in Eq. 4.38.

Both the experimental measurements and CFD simulations conducted by Allison focused only on the free delivery point. Since the free delivery point was observed to be the best operating point in the present work, Allison's results should be consistent. However, they were observed to be substantially lower in thermal resistance. This could have occurred for several reasons. First, the heat losses were only estimated rather than experimentally characterized, which could have led to underestimates of the heat loss (in this scenario, some of the lost energy due to conduction through the insulation, for example,would be counted as part of the reported convective heat transfer). Second, the bottom heated plate appears to extend right up to the impeller shaft, where there is some additional heat transfer surface area that was possibly unaccounted for on the bottom plate within the core. The heat transfer in this region could be significant, because the flow entering the eye is likely to impinge upon the bottom plate; impingement zones are known to have thin boundary layers and high heat transfer coefficients. In the present work, this core region had an identical hole in the top and bottom plates, so this difference in the setups could explain why Allison's reported thermal resistances are lower. The optimal design frontiers reported by Allison are compared to Eq. 4.39 in Fig. 4-18. Allison's CFD-computed frontier shows reasonably good agreement with the present experimental data; however, his experimental-measurement-based correlation for the frontier estimates substantially lower thermal resistances.

Referring back to Fig. 4-16, this frontier seems to be close to the experimental data, although some points approach the frontier closer than others. Notably, the 60° and 45° exit angle blades in the rightmost plot come very close to the frontier. In fact, the 60° points shown in Fig. 4-16 are Fan 12, which was also identified as one of the best designs in Fig. 4-17. In addition to showing the best geometrical designs, the best operating points for a given design can be identified in Fig. 4-16. The points with the least flow restriction (the rightmost points on each line of constant speed) approach the frontier more closely than the restricted points, confirming that operating with minimal flow restriction (highest flow coefficient) is preferable to achieve the best performance. Although this may seem obvious in hindsight, these points do *not* represent the best efficiency point of the fan; the best efficiency point occurs when the fan operates at a flow coefficient less than the maximum flow coefficient (e.g. see Fig. 4-12). This will have consequences in Chapter 5 when the scaling of multilayer devices is discussed.

4.4 Local Heat Transfer Coefficient

A heated-thin-film infrared thermography method was developed (introduced in Section 2.2.4) to characterize the local heat transfer coefficient. Two PCBs, each with 12 independently controllable heater traces, served as stators for an integrated fan. The lower stator's temperature field was measured with a thermal camera. In combination with knowledge of the thermal power input, this temperature field was used to determine the heat flux associated with the forced convection of the integrated fan.

The new IR thermography method was used to test the sensitivity of the heat transfer in the integrated fan to its thermal boundary condition. A fan was subjected to back-to-back tests with two different thermal boundary conditions: (1) constant heat flux and (2) constant temperature. These tests followed the procedure described in Section 2.2.4. The freedom to control the thermal boundary condition is usually absent in IR thermography methods, presumably because of the additional complexity required to have inde-

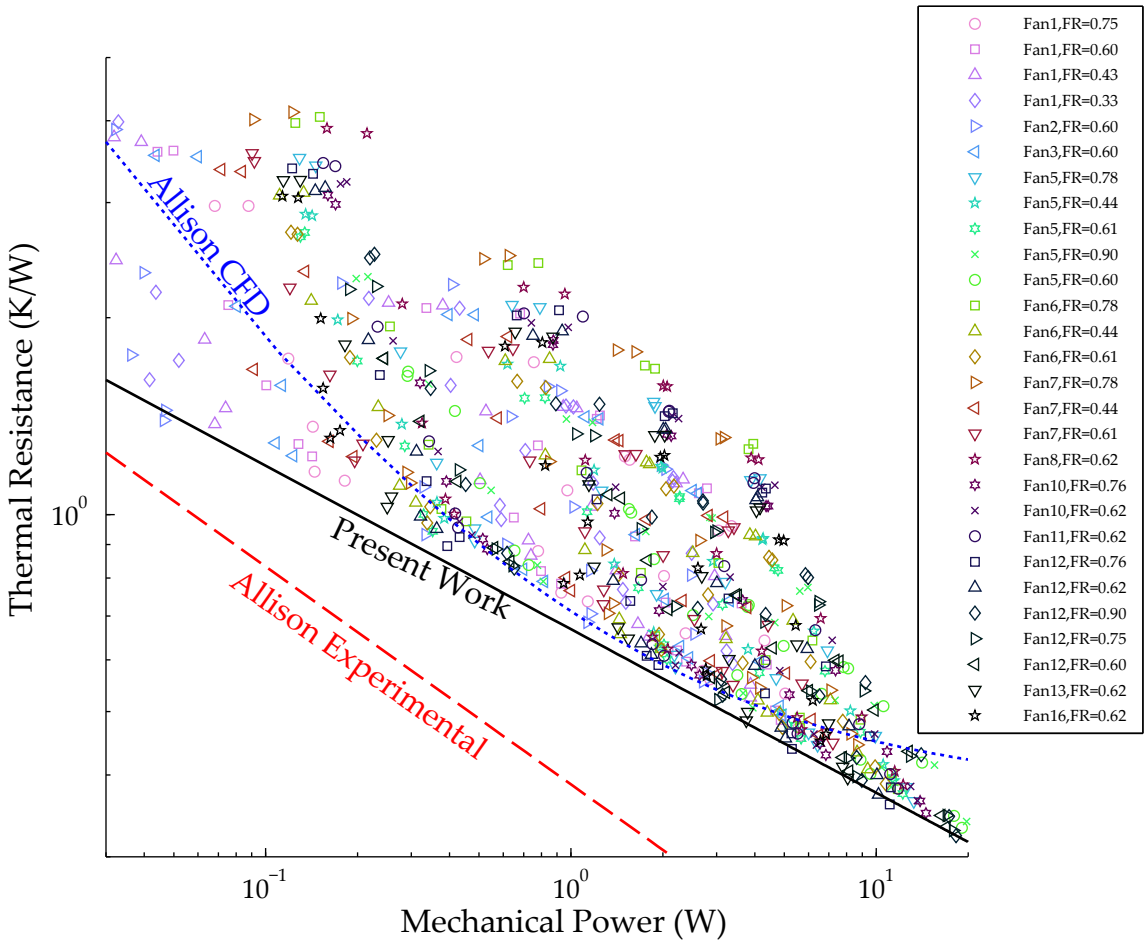

Figure 4-18: The experimental heat transfer data exhibits a frontier in the R vs. $\dot{W}$ plane representing the designs that have the lowest thermal resistance for a given mechanical power. Equation 4.39 is shown as a black line; this effectively bounds all of the experimental data. For comparison, the estimates of Allison [50], who studied a very similar integrated fan in unrestricted flow scenarios, are also shown. Allison's CFD computations are close to the frontier in the present work, but his experimentally based frontier equation overestimates the thermal performance.

pendently controlled zones; most thin film IR thermography experiments use only the constant heat flux boundary condition or some variant which cannot locally react to temperature feedback. The results from the IR thermography setup in the present work show that the heat transfer is insensitive to the thermal boundary condition, further supporting the notion that turbulence from the impeller governs the character of the heat transfer in the system (even in cases when the channel Reynolds number would suggest laminar flow).

The local heat transfer coefficient, $h_{\mathrm{ITD,loc}}$, is defined as

$$h_{\mathrm{ITD,loc}} = \frac{\dot{q}''_{\mathrm{fc}}(r)}{T(r) - T_{\mathrm{in}}}, \tag{4.42}$$

where r is the radius, $\dot{q}''_{\mathrm{fc}}(r)$ is the heat flux associated with the forced convection, $T(r)$ is the surface temperature, and T_{in} is the temperature of the inlet air. $\dot{q}''_{\mathrm{fc}}(r)$ and $T(r)$ in Eq. 4.42 are circumferentially averaged quantities, not including a range of angles that included the power and thermocouple wires going into the PCB. Figure 4-19 shows $h_{\mathrm{ITD,loc}}$ for 4 rotational speeds (3, 5, 7, and 9 krpm) and 4 flow coefficients at each rotational speed. The heat transfer coefficient has maxima at the entry and exit of the channel. The entry to the channel should have a high value of $h_{\mathrm{ITD,loc}}$ because (1) the entry tends to have a very thin boundary layer, leading to high heat transfer; and (2) the local temperature difference between the stator and the air is large, giving more driving potential for heat transfer. One disadvantage to using the inlet temperature difference as the temperature scale in $h_{\mathrm{ITD,loc}}$ is that temperature increases in the air manifest themselves as lower values of $h_{\mathrm{ITD,loc}}$. In contrast, a conventionally defined h references the local bulk temperature of the fluid, and the effects of the fluid temperature rise must be accounted for using the conservation of energy (often conveniently packaged into the effectiveness-N_{TU} method). These conventionally defined heat transfer coefficients are independent of the local fluid temperature. In this heat sink, however, calculating a conventionally defined h introduces a significant uncertainty, because the character of the air flow is not well defined or well known. For example, if one assumes unidirectional flow through the integrated fan, effectivenesses higher than 1 are often discovered. Of course, this seemingly unphysical behavior is merely due to improper accounting of the mass flow in the fan (namely, a failure to consider the recirculatory flow at the exit plane). As discussed in Section 1.8.2, the average value of h_{ITD} is a useful heat sink design parameter that can be directly related to R (see Table 1.2). Thus, despite its inclusion of air-flow-temperature-rise effects, h_{ITD} is a convenient way to express the measured heat flux that does not rely on assumptions about the flow characteristics in the system.

The second peak in $h_{\mathrm{ITD,loc}}$ occurs at the exit of the flow channel. Several phenomena likely contribute to this high heat transfer coefficient at the exit. First, the aforementioned recirculatory flow causes cool air from the surroundings to enter the flow channel through the exit plane. This cool air, like the air entering the inlet, has a higher local temperature difference relative to the wall (compared to the air flowing through the channel, which must absorb thermal energy from the hot walls). Second, complex flow patterns occur at the tip of the blade, where the pressure side and suction side of the blade meet. This pressure difference across the blade results in leakage flows and vortices which are likely to improve the turbulent mixing and the heat transfer coefficient.

Finally, although care was taken to subtract this effect from the results, these peaks could be an artifact of the experimental processing because large gradients in temperature

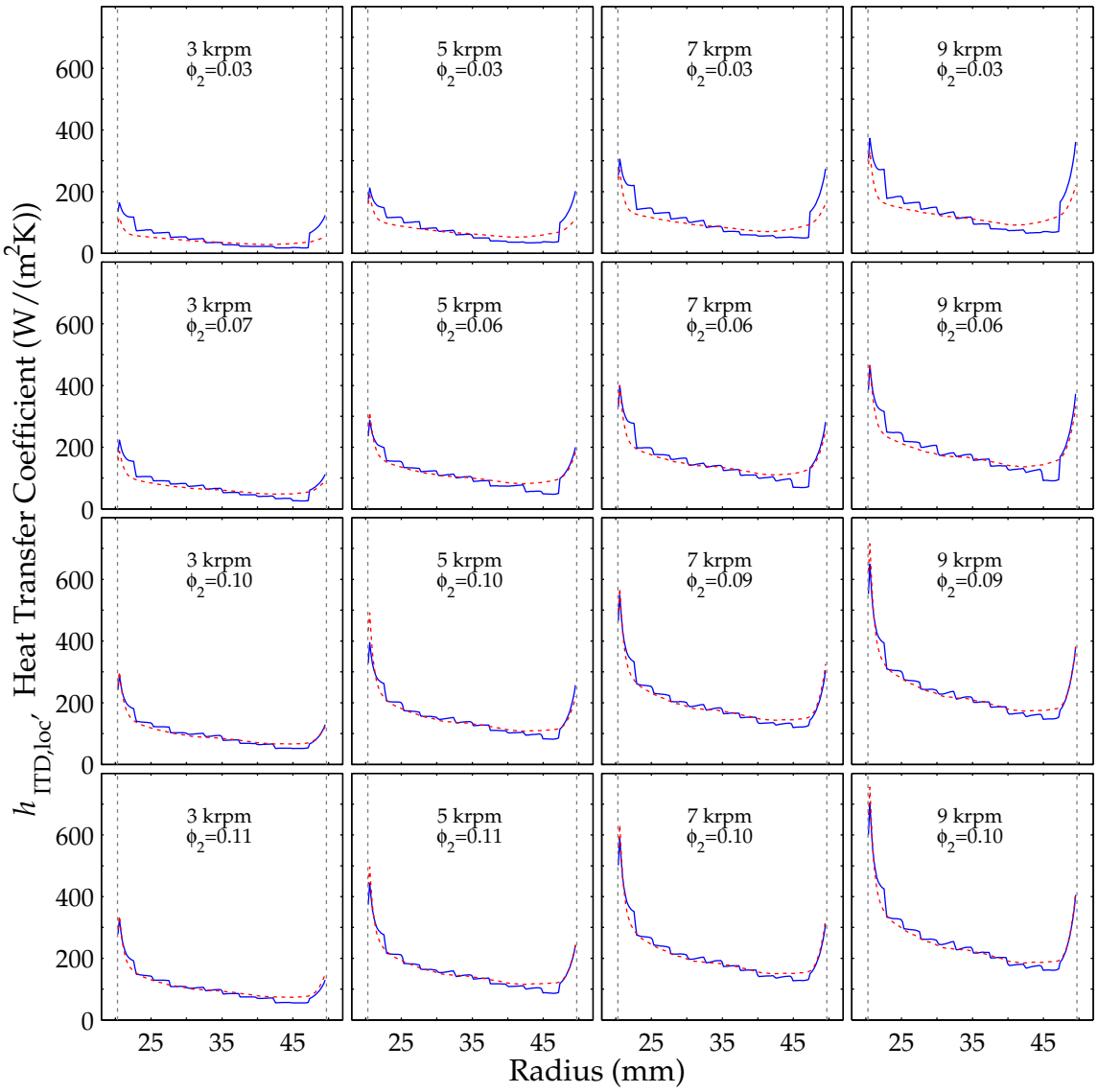

Figure 4-19: The local heat transfer coefficient $h_{\mathrm{ITD,loc}}$ was measured for two thermal boundary conditions: constant heat flux (dashed red lines) and constant temperature (solid blue lines). Results for Fan 1 with $b_b = 1.5\,\mathrm{mm}$ and $b_g = 2.5\,\mathrm{mm}$ are shown; each plot shows the $h_{\mathrm{ITD,loc}}$ vs. the radius r for a single operating point (the rotational speed and exit plane flow coefficient ϕ_2 are indicated in each plot). The vertical, dashed gray lines indicate the inner and outer edges of the heated zones on the PCBs. The data for the constant temperature tests appear jagged because of the discrete nature of the independently controlled zones. The heat transfer coefficients appear to be insensitive to the thermal boundary condition, due to the agreement of the two data sets in each operating point.

occur near the inner radius and outer radius of the annular PCB. The heat losses were characterized in a zero flow, zero rotational speed trial. A voltage was applied to the heater traces to increase the PCB's temperature. First, the lateral conduction loss was determined from the observed temperature gradients in the plate (in a procedure analogous to Stafford et al. [73]). Next, radiation loss was calculated by applying the Stefan-Boltzmann law to the measured temperature field. Third, the heat flux associated with the heated channels was calculated. Finally, an effective "lost heat transfer" was determined by an energy balance as

$$\dot{q}''_{\text{loss}} = \dot{q}''_{\text{gen}} - \dot{q}''_{\text{rad}} + \dot{q}''_{\text{cond}}, \tag{4.43}$$

where $\dot{q}''_{\text{gen}}$ is the heat flux associated with the heater traces, $\dot{q}''_{\text{rad}}$ is the radiation heat flux, and $\dot{q}''_{\text{cond}}$ is the lateral conduction; the sign convention follows Stafford et al. [73]. These quantities are all calculated locally over the entire PCB. The heat loss can be expressed as a local heat transfer coefficient, namely

$$h_{\text{loss}} = \frac{\dot{q}''_{\text{loss}}}{T - T_{\text{in}}}, \tag{4.44}$$

where T is the local temperature of the PCB as measured by the IR camera. This heat transfer coefficient (h_{loss}) was subsequently used in the experimental runs, so that the forced convection heat flux (q''_{fc}) was calculated as follows

$$\dot{q}''_{\text{fc}} = \dot{q}''_{\text{gen}} - \dot{q}''_{\text{rad}} + \dot{q}''_{\text{cond}} - h_{\text{loss}}(T - T_{\text{in}}). \tag{4.45}$$

It is conceivable that a small error in h_{loss} could result in erroneous interpretations of the results near the edges, so the exact values of $h_{\text{ITD,loc}}$ near the edges should be interpreted with caution.

The experimentally measured heat transfer coefficient $h_{\text{ITD,loc}}$ shown in Fig. 4-19 was nondimensionalized as the local dimensionless heat flux,

$$\Phi_{\text{m,loc}} = \frac{h_{\text{ITD,loc}} d_{\text{h}}}{k}, \tag{4.46}$$

where k is the thermal conductivity of the air and d_{h} is the hydraulic diameter ($d_{\text{h}} = 2b_{\text{g}}$). The mass flow of air was nondimensionalized using the local Reynolds number, which varies inversely with r as

$$\text{Re}_{d\text{h,loc}} = \frac{\dot{m}}{\mu \pi r}. \tag{4.47}$$

The constant temperature and constant heat flux data shown in Fig. 4-19 are shown in Fig. 4-20. The innermost and outermost heated channel are excluded so that the peaks in $h_{\text{ITD,loc}}$ are not shown in Fig. 4-20. The data from the constant temperature tests are in good agreement with the data from the constant heat flux tests. This insensitivity to the thermal boundary condition is a feature of turbulent flow, even though the local Reynolds number (calculated using the hydraulic diameter and the average meridional velocity rather than the local air velocity) is below the critical value for internal pipe flow in most of the data points. This further supports the notion that the rotating impeller introduces turbulent flow structures in the air flow, thereby enhancing the convective heat transfer from the walls.

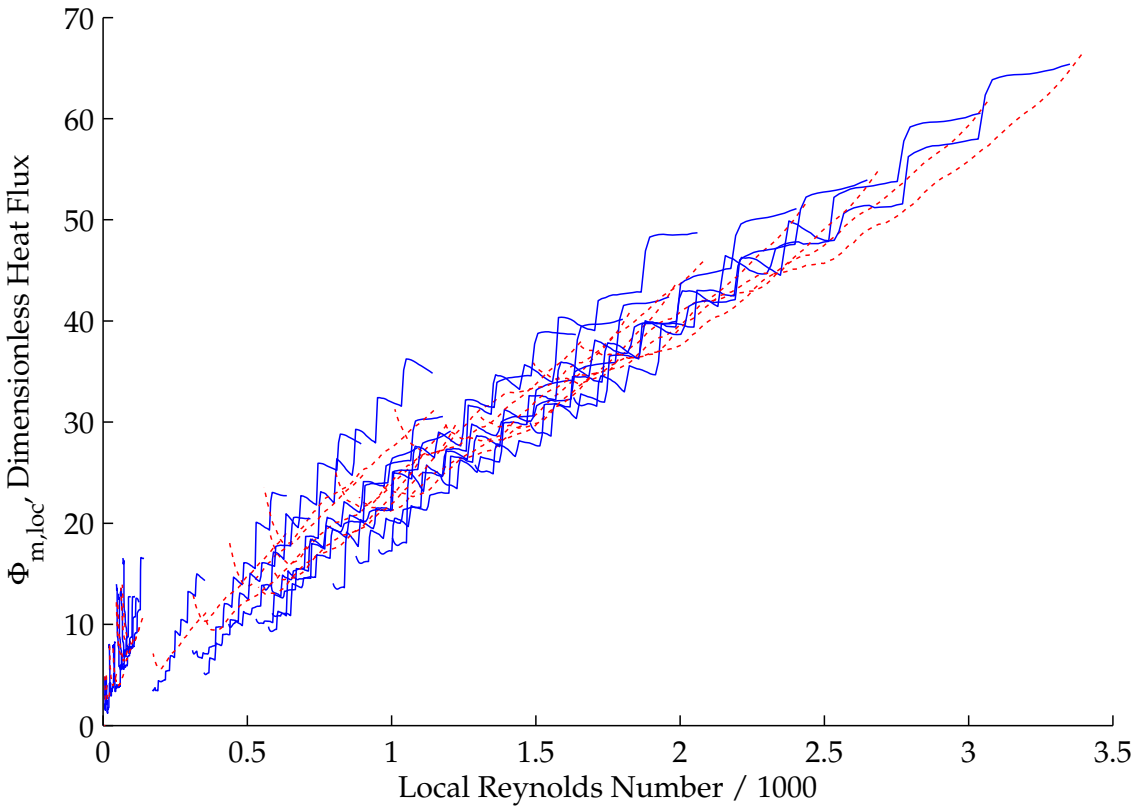

Figure 4-20: The data shown in 4-19 were nondimensionalized as the local dimensionless heat flux (Eq. 4.46) and the local Reynolds number (Eq. 4.47). The innermost and outermost zones, which had higher heat transfer coefficients, are not shown. The data with a constant heat flux boundary condition are shown as dashed red lines; the data with a constant temperature boundary condition are shown as solid blue lines. Each contiguous line represents an operating point; the innermost radius has the highest local Reynolds number, so the flow direction in each data set shown is from right to left. The jaggedness of the blue lines arises from differences in heat flux in adjacent heater zones; the discrete channel control attempts to approximate a constant wall temperature but must have small discontinuities in the heat flux to do so. Once again, the differences between the constant-heat-flux and constant-temperature results appear very small; this insensitivity to the thermal boundary condition is a feature of turbulent heat transfer.

4.5 Impeller Design Considerations

4.5.1 Wiper Blades

Increasing the fill ratio seemed to improve the fan performance curve, efficiency and heat transfer coefficient. However, manufacturing tolerances and material properties limit the achievable fill ratio. In the experiments, fill ratios of up to 90% were tested, but great care was taken to ensure proper alignment and positioning of the impeller in the experimental apparatus. This attention to the manufacturing tolerances exercised in the experimental setup may not be achievable in every real-world application. To achieve very high fill ratios without requiring high-precision impeller and stator gap tolerances, a new type of impeller was devised that used thin sheets of plastic as "wipers," which either physically rubbed against the stator surfaces or acted as hydrodynamic air bearings. With these wipers attached to the impeller blades, the breadth of the metal part of the impeller blade could be made much thinner compared to the breadth of the stator gap while still effectively maintaining very small gaps between the wipers and the stator walls.

To test the concept, two impellers (with the profile of Fan 1) were modified to have wipers on the leading edge of each blade, as shown in Fig. 4-21. The wipers were cut from a sheet of 25 μm thick polyimide film and adhered to the pressure side of each blade. The wipers were 2.5 mm and 4.6 mm in width, and were sized to cover the entire length of each blade. The effective fill ratio for the wiper impeller ($\mathrm{FR_w}$) can be expressed as

$$\mathrm{FR_w} = b_{\mathrm{wiper}}/b_{\mathrm{g}}, \tag{4.48}$$

by replacing the blade breadth b_{b} in the original definition of FR with the wiper breadth (b_{wiper}).

The fan performance of the wiper impellers was measured and compared to that of conventional impellers. The wiper impeller, compared to an identical wiperless impeller

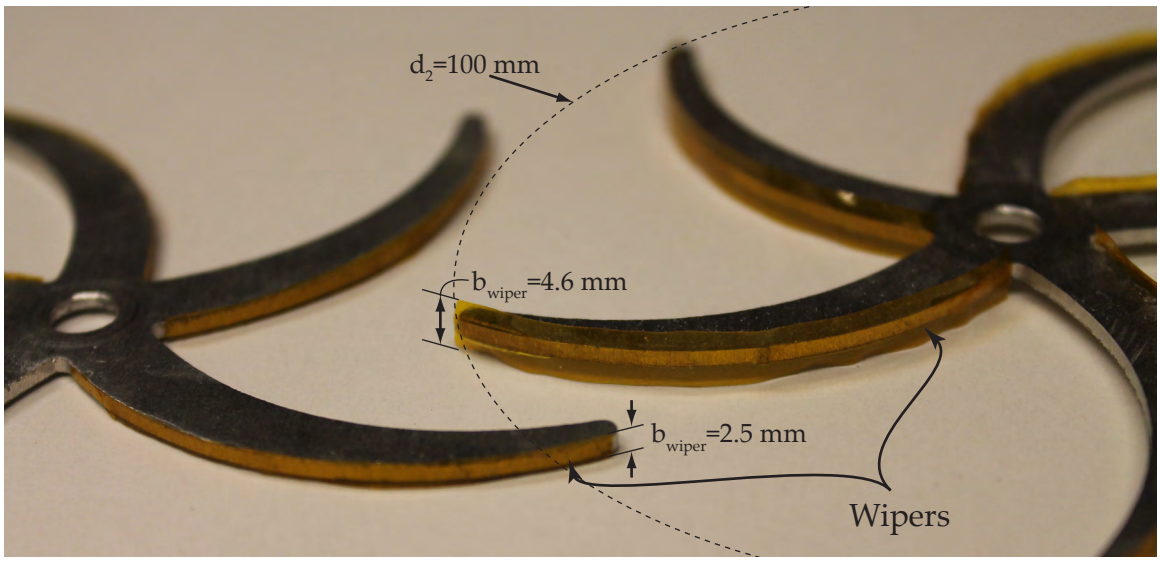

Figure 4-21: Wipers were cut from a sheet of 25 μm polyimide film and adhered to the pressure side each blade. The compliance of these wipers allows for high fill ratios to be achieved without the risk of damage due to the metal blades scraping against the stator surfaces.

in the same stator gap, showed a significant improvement in the fan performance curve and efficiency curve, as shown in Fig. 4-22. This improvement appears to be due to the increase in the fill ratio that the addition of the wiper causes. To test this hypothesis, a wiperless impeller with the same FR as the wiper impeller's FR_w was also tested. In Fig. 4-22, this wiperless fan indicated by the blue dots had a fill ratio of 0.61, compared to the wiper fan's effective fill ratio of 0.63; these two fans can be seen to have very similar performance in both pumping and efficiency.

The fan performance and efficiency of a wiper impeller is shown in Fig. 4-23. The wiper impeller had a blade breadth of 1.5 mm and a wiper breadth of 2.5 mm, and was placed between stators with a gap breadth of 2.67 mm. The effective fill ratio (FR_w) was 0.95; as expected, the pressure rise is quite high compared to similar fans without wipers (e.g. see Fig. 4-22). The efficiency of the wiper impeller, in contrast to the unmodified impeller, seems to be a function of the rotational speed. This phenomenon could be explained by the wiper forming an air bearing against the stator wall. At the lower rotational speeds, the wiper is very close or even rubbing against the wall; as the speed increases, the air bearing effect causes the wiper to separate slightly from the surface, reducing the friction and by extension the power consumption of the fan. In the 7–9 krpm range the efficiency curves begin show much smaller increases; this may indicate that the air bearing is fully lifted off of the surface.

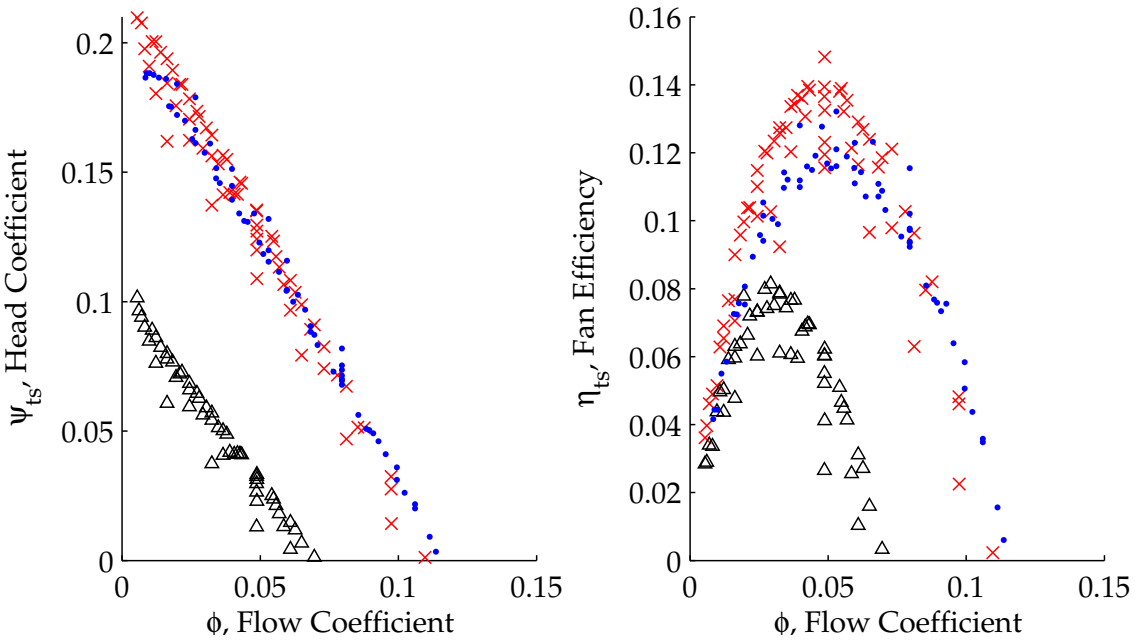

Figure 4-22: The addition of wipers to an impeller (while maintaining the same stator gap breadth b_g) causes a significant improvement in the fan performance curve and efficiency, due to the increased effective fill ratio. The black triangles indicate results for a fan without wipers (b_g = 4.1 mm, FR = 0.37, Fan 1, no wipers); the red x's indicate test results for the same impeller with wipers added (b_g = 4.1 mm, FR_w = 0.63, Fan 1, with wipers). The blue dots indicate the same impeller, with no wipers, but with the gap breadth adjusted to produce a fill ratio close to the wiper impeller's effective fill ratio (b_g = 2.5 mm, FR = 0.61, Fan 1, no wipers). The performance of the wiper impeller and regular impeller with the same effective fill ratios seems to be very close.

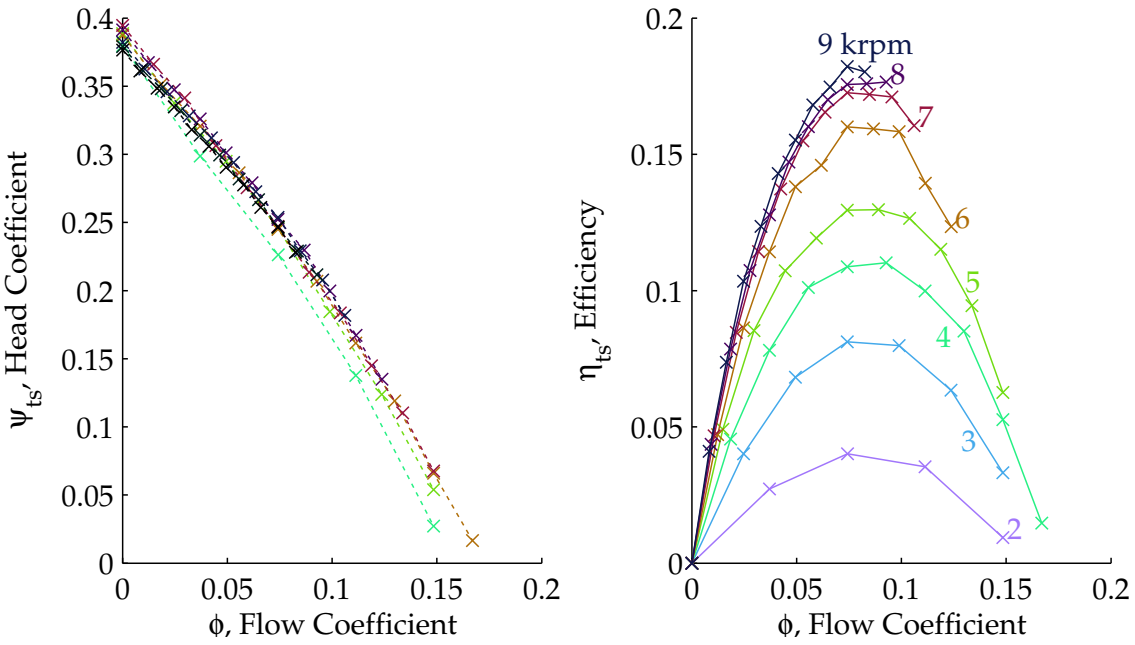

Figure 4-23: A wiper impeller with a very high effective fill ratio (FR_w = 0.95) exhibited a speed-dependent efficiency curve. This speed dependence is thought to occur due to an air-bearing effect with the wiper and the stator wall; as the speed increases, the pressure force on the wiper causes it to deflect and separate from the wall. Eventually, the wiper is sufficiently far from the wall that no further reductions in the frictional drag occur, and the efficiency curves begin to lose their speed dependence. The x's represent data points; the data points having a common rotational speed are connected with lines.

The wiper impellers also exhibited a slight change in their heat transfer characteristics. Figure 4-24 shows a comparison between a conventional impeller (blue dots) and a wiper impeller (red x's). The data points that share a common rotational speed are connected with a lines. These two fans have the same gap breadth (b_g = 3.6 mm) and blade breadth (b_b = 3.6 mm), but the wiper impeller has a 2.5 mm breadth wiper adhered to the leading edge of each blade. This resulted in a slight improvement in the dimensionless heat flux at higher rotation speeds. This improvement could be due to the increase in the effective aspect ratio, which has been shown to have an effect on the correlation coefficients (C_1 and C_2) for $\Phi_{m,L}$. Increasing AR should increase C_1 and decrease C_2, although the relative increase in C_1 should be greater than the relative decrease in C_2. C_1 describes the proportionality of $\Phi_{m,L}$ with Re_ω; thus, the increased improvement at higher rotational speed makes sense in light of Eq. 4.19. Additionally, the thermal resistance at the same mechanical power input was slightly lower in the wiper impeller, meaning that the wiper impeller would have a higher coefficient of performance in a heat sink.

Clearly, the addition of wipers has potential to improve performance in integrated fans, and may warrant further study for certain applications.

4.5.2 Support Ring

It was shown that increasing the number of blades can improve the performance of the fans. With fully unshrouded fans, the center region begins to fill with material as more blades are added because the blades must be thick enough to support the loads imposed

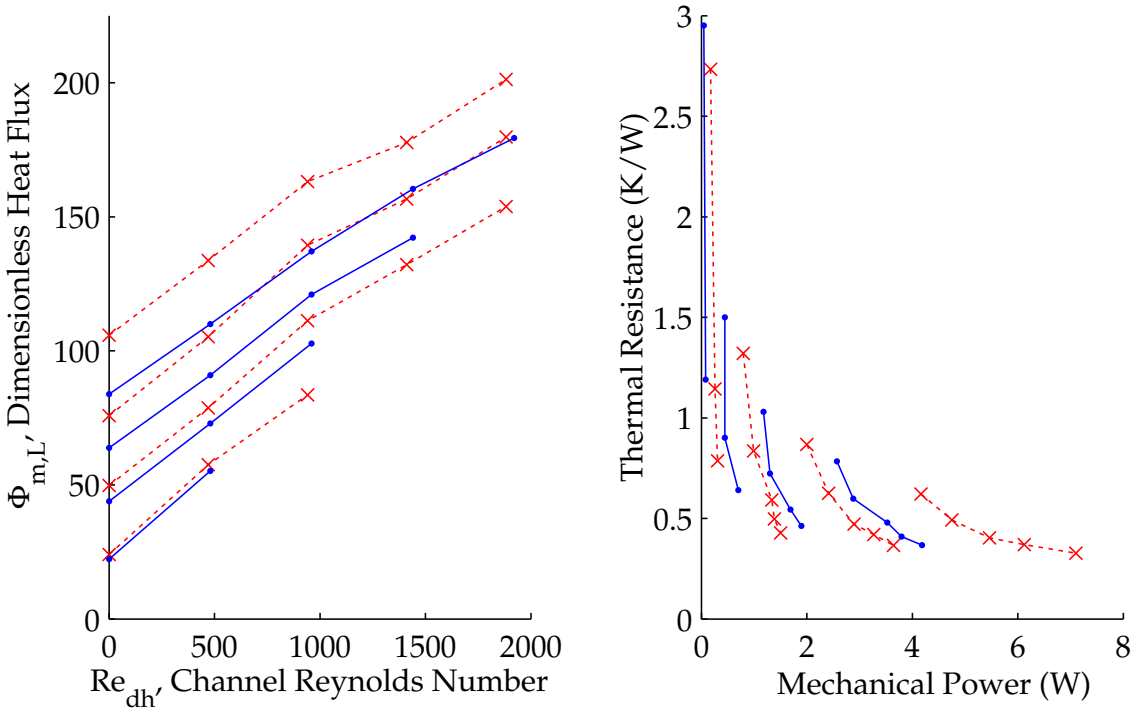

Figure 4-24: The addition of wipers to an impeller results in a slight change in the dimensionless heat transfer characteristics. In the figure, the blue dots indicate a conventional impeller (Fan 1, $b_b = 1.5\,mm$, $b_g = 3.6\,mm$) and the red x's indicate a wiper impeller (Fan 1, $b_b = 1.5\,mm$, $b_w = 2.5\,mm$, and $b_g = 3.6\,mm$). The slight improvement in the dimensionless heat flux makes sense in light of the previous heat transfer observations: the effective aspect ratio of the wiper impeller increases (the addition of the wiper increases the effective breadth of the impeller), and Eq. 4.19 suggests an increase in the proportionality of $\Phi_{m,L}$ with an increase in AR, explaining the wider spacing between the lines of constant rotational speed. The thermal resistance for the same mechanical power appears to be slightly improved with the wiper impeller.

by centrifugal force. In straight radial blades (e.g. Fans 5, 6 and 7), these centrifugal loads are tensile, so the blades do not need a large cross section to minimize deflection. Blades with curvature, however, must resist a bending moment when the fan rotates. The width of each blade must be increased to avoid excessive deflection, further increasing the blockage in the center core of the fan. It will be shown in Chapter 5 that blockage in the central core can adversely affect the performance of multilayer devices.

To maintain an open region in the center, a "support ring" was added to the impellers, as shown in Fig. 4-25 Three spokes connected the center shaft to the support ring, from which the blades extended to the periphery of the impeller. The support ring, in addition to opening up the center core of the impeller to reduce the flow restriction to subsequent layers in a stack, served to shorten the length of each impeller blade, reducing the centrifugal bending moment and the effective beam length.

The support ring was situated about 2.5 mm (1 gap breadth) upstream of the entry of the air flow gap. This distance was chosen so the support ring would not excessively block the flow entering the gap; since the pressure field satisfies Laplace's equation, the upstream pressure effect of the gap entry was expected to be on par with its transverse length scale [91]. Fan 8 was designed to be identical to Fan 5 except for the addition of

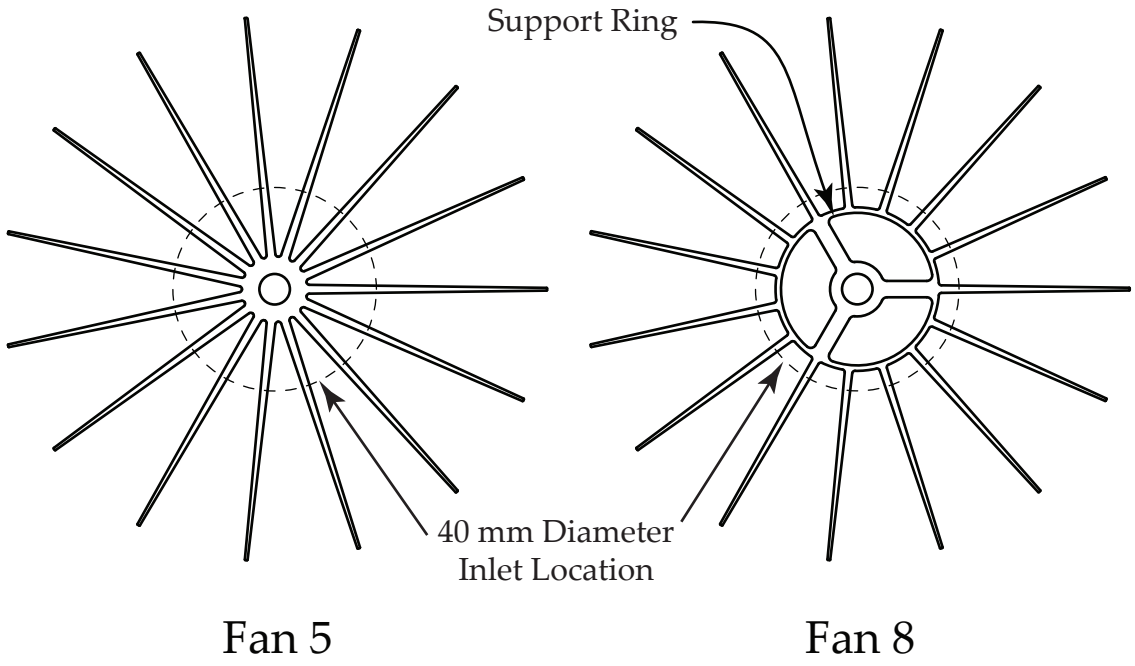

Figure 4-25: Fans 5 and 8 were identical except for the addition of a support ring in Fan 8, which served to reduce the blockage in the core of the fan. This blockage was shown to be harmful to the performance of a multilayer system, which will be discussed in Chapter 5.

the support ring to test whether it would introduce any adverse effects on the fan performance. Figure 4-26 shows a comparison of the fan and efficiency curves two identical fans, one with a support ring and the other with straight radial blades (Fans 8 and 5, respectively). The support ring seems to have caused a slight reduction in the fan and efficiency curves; however, since the support ring shortens the effective blade length that is affected by centrifugal bending, backswept blades can be used without reducing the number of blades. With a support ring, a 15-bladed 60° exit angle fan exceeded the performance of 15-bladed radial fan with no support ring.

4.6 Summary

Experiments were performed to gain an understanding of the heat transfer and fan performance of integrated fan heat sinks and provide better performance estimates than current analytical approaches. Correlations for the dimensionless heat flux, head coefficient, and power coefficient were developed based on the fan's operating conditions. These correlations were also expressed in terms of the basic fan geometry, so that designers may quickly estimate the performance of a hypothetical design.

Viewing the heat transfer and fan performance simultaneously led to some interesting conclusions. First, a frontier of best designs was identified that gave the lowest thermal resistance for a given mechanical power input. Second, it was shown that integrated fans exhibit the best heat transfer performance per unit power input when operating unrestricted,

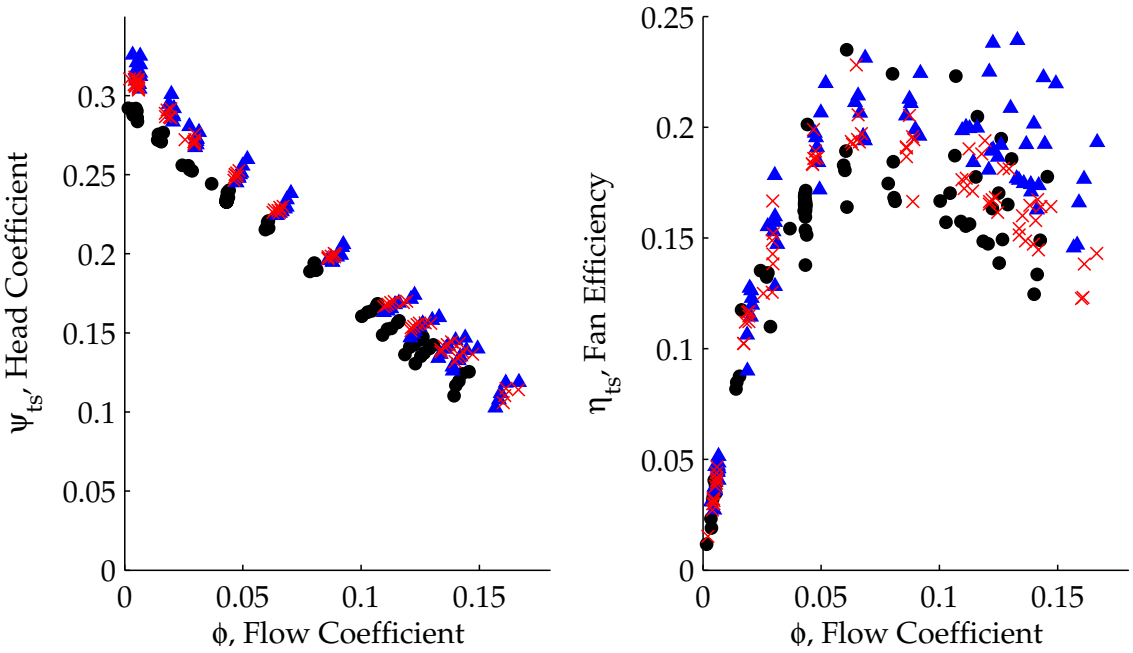

Figure 4-26: The effect of the support ring on the fan performance was tested by comparing experimental results from Fans 5 and 8 (see Fig. 4-25). The impeller with the support ring (Fan 8: black circles) had slightly reduced fan and efficiency curves compared to the original design (Fan 5: red x's). However, by adding the support ring, backswept blades could be added without excessive deflection from centrifugal bending. A fan with a 60° exit angle and the same number of blades is shown (Fan 12: blue triangles) to improve the fan and efficiency performance over the original design.

even though these unrestricted points have a very low fan efficiency. This serves as a reminder that the goal of integrated fan heat sink design (minimization of thermal resistance and mechanical power input) has a different ultimate goal than fan design (maximization of hydraulic efficiency).

Finally, several practical design modifications for integrated fans were developed. A support ring opened the center area of the fan to minimize blockage of the core, while also reducing the length of each beam to minimized deflection caused by centrifugal force. Additionally, flexible plastic wipers attached to the leading edge of an impeller's blades were shown to give performance increases comparable to increasing the fill ratio; these flexible blades are unlikely to cause any damage to the stators. Since very tight clearances are difficult to manufacture, the wipers allow a thinner metal blade to have a higher effective fill ratio and achieve performance comparable to a thicker impeller.

THIS PAGE INTENTIONALLY LEFT BLANK

CHAPTER 5

SCALING IN MULTILAYER DEVICES

A NATURAL QUESTION in designing multilayer heat sinks is how the performance scales with the addition of fan layers. The relationship between the fan performance and the heat transfer is important in engineering a device with multiple fan layers. In a single layer device, the air flow is relatively unimpeded and the heat transfer performance can be characterized as solely a function of the impeller's rotational speed. In contrast, in multilayer devices the pressure drop from the stagnant ambient pressure surroundings to the inlet of the device limits the air flow to each layer, requiring the impellers to pump against a more severe pressure gradient. In these operating regimes, the characteristic pumping curve of the fan becomes an important consideration in the system design. Fortunately, methods to counteract this starvation can be implemented. For example, an impeller can be removed from a layer to create an opening for additional inward air flow.

A multilayer device is desirable from a thermal perspective, because by adding additional surface area for convective heat transfer, the effective UA of the air side increases. Put another way, the thermal resistance ($R = \frac{1}{UA}$) of the convective heat transfer decreases. To frame this in the familiar thermal/electrical analogy, a single layer device may be thought of as a circuit in which thermal energy flows from the wall temperature (e.g. the exterior surface of a condenser in a heat pipe) to the air flow induced by the impeller. If each layer comprises such a thermal resistance, additional layers in parallel act analogously to electrical resistors in parallel; that is, they reduce the overall resistance of the circuit, causing the equivalent resistance of the ensemble to decrease hyperbolically with the number of layers (see Fig. 5-1). Unfortunately, if the air flow layers draw from a shared core (as they do in the PHUMP), the nonlinear scaling of the inlet pressure drop forces the fans to pump against an increasingly adverse pressure difference, reducing the flow rate per layer. This decreased flow reduces the heat transfer per layer. Indeed, the scaling of a multilayer device cannot be readily deduced from single layer results; forecasting the performance of a multilayer system demands a simultaneous understanding of the fan characteristics and the system in which the fans operate. Despite these difficulties, it will be shown that multilayer integrated fan heat sinks can achieve levels of performance significantly beyond the current state of the art.

In this chapter, methods of predicting the performance of multilayer integrated fan heat sinks will be discussed. A simple analytical method and a more powerful numerical flow circuit model were used to solve the flow through the system, based on its geometry

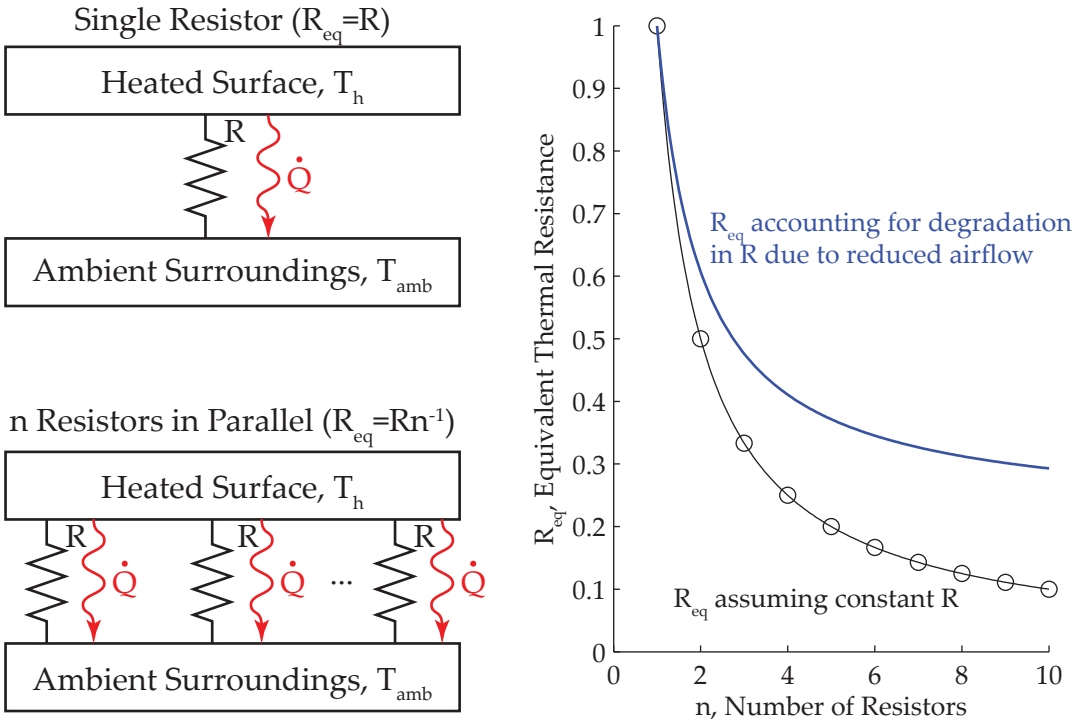

Figure 5-1: Thermal resistances in parallel between a heated surface at T_h and ambient surroundings at T_{amb} reduce the equivalent overall resistance in the system. The equivalent thermal resistance decreases hyperbolically with the number of resistors placed in parallel. However, the addition of layers also requires more air flow through the inlet of the device, creating a lower pressure in the core of the device and reducing the air flow per layer. This leads to decreased heat transfer per layer, and the overall equivalent resistance does not decrease as quickly as one would predict without accounting for this coupling in the thermal and hydraulic performance of the system.

and the fan curves of each integrated fan layer. The heat transfer in each layer was calculated subsequently, based on the predicted fan operating points, to predict the overall multilayer device performance. The flow circuit model was then used to explore the effects on multilayer devices of adding fan layers, adding inlets, and changing the flow resistance in the core of the device. Finally, the multilayer scaling estimates were compared to the experimental results of two prototype integrated fan, loop heat pipes, and were observed to satisfactorily predict their performance.

5.1 Analytical Flow Network Model

A common problem in fan engineering is to find the flow rate through a system with a fan and a network of ducts. This can be done by determining the system flow resistance curve (pressure drop as a function of volume flow); the intersection of this system resistance curve and the fan curve is the operating point, where the fan's pressure rise balances the pressure drop through the system. In the integrated fan heat sink, a similar methodology was used to yield insight into the multilayer scaling. To make this approach as general as possible, the fan curve and system resistance curve were nondimensionalized to remove

any dependence on the rotational speed.

5.1.1 Addition of Parallel Fans

The integrated fan heat sink consists of a central core that supplies cool air to the fan layers, which pump against the low pressure in the core and discharge air to the ambient. If the interlayer flow resistances in the core are assumed to be small, the fans in this arrangement can be said to act purely in parallel. Fans acting in parallel can be thought of as having a single composite fan curve that is formed by adding the volume flows of the constituent fan curves at a given pressure rise. This effect is shown in Fig. 5-2 for 1–4 fans pumping against a fixed system resistance. For n identical fans in parallel (each having linear fan curves), the composite fan curve is:

$$\Delta p_{\mathrm{ts}} = \Delta p_{\mathrm{ts,max}} - \frac{R_1}{n}\dot{V}, \tag{5.1}$$

where $-R_1$ is the slope of the fan curve and $\Delta p_{\mathrm{ts,max}}$ is the maximum (or blocked) total-to-static pressure rise. Adding multiple fans in parallel essentially "stretches" the fan curve along the $\dot{V}$ axis. The maximum pressure rise does not change when fans are added in parallel[1]. By substituting $\phi = \dot{V}/(A_2 u_2)$ and $\psi_{\mathrm{ts}} = \Delta p_{\mathrm{ts}}/(\rho u_2^2)$ into Eq. 5.1, the composite fan curve becomes

$$\psi_{\mathrm{ts}} = \psi_{\mathrm{ts,max}} - \frac{R_1 A_2}{\rho u_2 n}\phi. \tag{5.2}$$

The resistance term R_1, representing the fan curve's slope at a particular speed, can be expressed in terms of the dimensionless constant C_{r} ($\psi_{\mathrm{ts}} = \psi_{\mathrm{ts,max}} - C_{\mathrm{r}}\phi$) from the dimensionless fan curve relationships in the previous chapter:

$$R_1 = \frac{\rho u_2 C_{\mathrm{r}}}{A_2}, \tag{5.3}$$

where $-C_{\mathrm{r}}$ is the slope of the dimensionless fan curve (C_{r} is the dimensionless analog of R_1). Substituting this expression for R_1 into Eq. 5.2, the composite dimensionless fan curve becomes

$$\psi_{\mathrm{ts}} = \psi_{\mathrm{ts,max}} - \frac{C_{\mathrm{r}}}{n}\phi. \quad \textbf{\textit{n}-layer Fan Curve} \tag{5.4}$$

This dimensionless form does not depend on the rotational speed of the fan, and predicts the relationship between flow coefficient and total-to-static head coefficient for n fans in parallel. One subtle aspect of Eq. 5.4 is that the reference area A_2, used in the definition of ϕ, *still refers to the exit area of a single fan, not the combined exit area*. A consequence of this is that ϕ calculated from Eq. 5.4 in a multilayer system can have values larger than the ϕ-intercept on the dimensionless fan curve for a single fan.

5.1.2 Addition of Parallel Inlets

The fans must pump against a system resistance that arises from the inlets, which can either be in the axial or radial direction. In general, system resistances in flow networks can take several forms with various proportionality of the pressure drop to the volume

[1] In contrast, for fans in series, the maximum flow rate does not change, and the fan curves add along the Δp_{ts} axis.

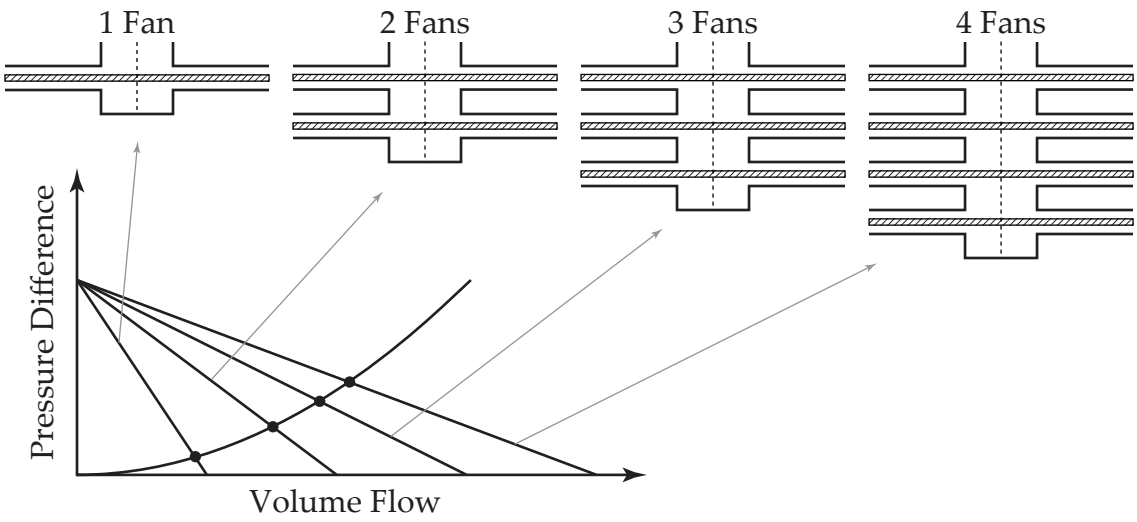

Figure 5-2: Fans in parallel add along the volume flow axis; the maximum pressure rise does not change. The intersection points between the composite fan curves and the system resistance curve are the operating points. Addition of fans to a fixed system resistance results in diminishing returns in the total volume flow through the system. The blockages between the fan layers are assumed to be negligible.

flow. Fan systems typically experience a system resistance proportional to the square of the volume flow, due to most system level resistances arising from turbulent phenomena. The system resistance curve is

$$\Delta p_\mathrm{t} = R^\dagger \dot{V}^2, \tag{5.5}$$

where $R^\dagger$ is the "modified resistance", a constant describing the resistivity of the system. $R^\dagger$ can be estimated from equations for minor losses in flow networks. In general, the minor loss in a flow is defined as

$$\Delta p_\mathrm{t} = K_\mathrm{m} \frac{\rho v^2}{2}, \tag{5.6}$$

where v is the average velocity at the inlet and K_m is the minor loss coefficient, which can be found in a table (e.g., see White [56]) or determined with experimental or computational tools. The modified resistance can be expressed in term of the minor loss coefficient:

$$R^\dagger = \frac{\rho K_\mathrm{m}}{2A_\mathrm{c}^2}, \tag{5.7}$$

where A_c is the cross sectional flow area, conventionally the smallest area in flow elements that have multiple choices, such as a contraction. $R^\dagger$ is a constant for a system and does not depend on the flow rate through the system.

Much like fans, flow resistances can be combined in parallel to form a composite system with a lower equivalent resistance. This is of consequence to multilayer integrated fan heat sinks because additional inlets can be added to lower the overall system resistance and increase the total flow rate through the system. Parabolic system resistances add along the $\dot{V}$ axis in the same fashion as fan curves; this is illustrated in Fig. 5-3. However, the modified resistances cannot simply be arithmetically combined. Furthermore, different types or sizes of inlets can have different values of $R^\dagger$, so it is undesirable to make

the equivalent modified resistance purely a function of the number of inlets. Two inlets in parallel (having volume flows $\dot{V}_1$ and $\dot{V}_2$), leading to the same plenum from ambient, have the same pressure drop. An equivalent modified resistance for these two inlets is defined as

$$R^{\dagger}_{\mathrm{eq}} = \frac{\Delta p_{\mathrm{t}}}{\dot{V}^2}, \tag{5.8}$$

where $\dot{V}$ is the total flow rate ($\dot{V} = \dot{V}_1 + \dot{V}_2$). Equation 5.8 can be combined with the individual pressure balances for each inlet, and the system of equations solved to express $R^{\dagger}_{\mathrm{eq}}$ in terms of $R^{\dagger}_1$ and $R^{\dagger}_2$:

$$R^{\dagger}_{\mathrm{eq}} = \frac{R^{\dagger}_1 R^{\dagger}_2}{\left(\sqrt{R^{\dagger}_1} + \sqrt{R^{\dagger}_2}\right)^2}. \tag{5.9}$$

Multiple inlets can be treated as a single, less restrictive inlet using Eq. 5.9; negligible interlayer flow resistance is an inherent assumption in Eq. 5.9. This assumption is justified provided that (1) the core is free of significant flow blockages (this effect will be discussed in Section 5.3.3), and (2) the frictional loss in the core is small. The frictional pressure drop in a duct is given by the Darcy-Weisbach equation (Eq. 1.7),

$$\frac{\Delta p_{\mathrm{t}}}{\rho v^2/2} = f\frac{L}{d_{\mathrm{h}}} \tag{5.10}$$

, where L is the duct length, v is the average velocity, and f is the Darcy friction factor. In the core of a multilayer heat sink, the velocity v in Eq. 5.10 is the same as the velocity in Eq. 5.6, so the magnitude of the terms $f\frac{L}{d_{\mathrm{h}}}$ and K_{m} indicates when the frictional loss in the core can be neglected (i.e. when $f\frac{L}{d_{\mathrm{h}}} << K_{\mathrm{m}}$). K_{m} is typically of order 1, and f can be bounded as less than 0.1 by examining a Moody chart (e.g. see White [56]). Accordingly, a criterion for neglecting the frictional pressure drop in the core is when $\frac{L}{d_{\mathrm{h}}} << 10$. Most compact heat sinks will strive to minimize the vertical height above the heat input surface, so the length-to-diameter ratio of the core can be expected to be quite small. In the experimentally characterized heat sinks, the core diameter is 40 mm and the distance between layers is about 2.5 mm, giving a value of $\frac{L}{d_{\mathrm{h}}} \sim 0.06$ and confirming that frictional loss in the core (in the absence of flow blockages) can be neglected.

A further simplification can be made to Eq. 5.9 if n_{in} inlets that have identical modified resistances ($R^{\dagger}$) operate in parallel; in this case, the equivalent modified resistance for the n_{in} inlets is

$$R^{\dagger}_{\mathrm{eq}} = \frac{R^{\dagger}}{n^2_{\mathrm{in}}} \quad \text{(for } n_{\mathrm{in}} \text{ identical inlets)} \tag{5.11}$$

With these methods to calculate $R^{\dagger}_{\mathrm{eq}}$, the composite resistance curve for multiple parallel inlets can be determined, and the intersection of this curve with a fan's pressure rise curve represents the operating point of the system. An additional design convenience is to transform the pressure balance for the inlets into the same nondimensional space as the fan curves, so as to remove any dependence on the rotational speed. For consistency with the fan curves, the total pressure balance for the inlet flows is nondimensionalized using

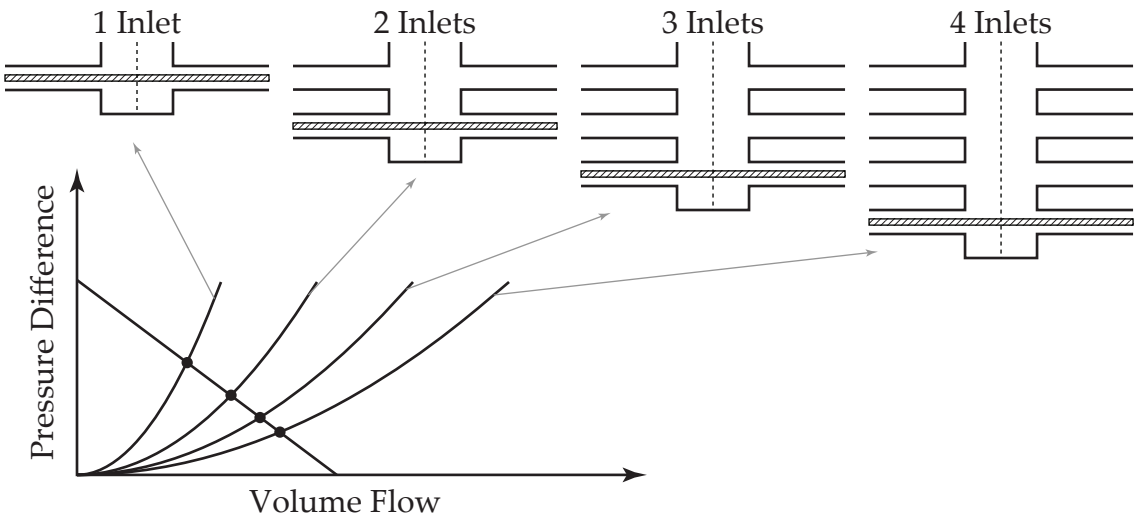

Figure 5-3: Inlets in parallel add along the volume flow axis in the same fashion as fans. The intersections points between the fan curve and the composite system resistance curves are the operating points. Decreasing the overall system resistance can be helpful when the addition of fans shows diminishing returns. The pressure loss in the core is negligible compared to the loss associated with the inlet flow.

the tip speed (u_2) and the exit area of a single fan layer (A_2):

$$\psi_t = \frac{R^{\dagger}_{eq} A_2^2}{\rho} \phi^2, \quad \textbf{Composite Inlet Resistance Curve} \tag{5.12}$$

where ψ_t is the total head coefficient, defined analogously to the total-to-static head coefficient as:

$$\psi_t = \frac{\Delta p_t}{\rho u_2^2}. \tag{5.13}$$

Even though the impeller is separate from the inlets, it is useful to employ a velocity scale that is consistent with the dimensionless fan curves in a multilayer device. Equation 5.12 expresses the composite resistance of all inlets leading to a common plenum from a stagnant, ambient reservoir. Combined with a composite fan curve, the flow through a multilayer device can be determined.

5.1.3 Determination of the Operating Point

The operating point of a system with multiple inlets and multiple fans is the intersection of the composite fan curve (Eq. 5.4) and the composite inlet resistance curve (Eq. 5.12). The total pressure loss from stagnant conditions at ambient pressure to the core balances the total-to-static pressure rise across the fans at this operating point:

$$\Delta p_{t,in} = \Delta p_{ts,fan}. \tag{5.14}$$

Since both of these use the same references in their nondimensional forms, an equivalent statement is

$$\psi_{t,in} = \psi_{ts,fan}. \tag{5.15}$$

Equations 5.12 and 5.4 can be used to recast Eq. 5.15 in terms of the flow coefficient:

$$\frac{R_{\text{eq}}^{\dagger} A_2^2}{\rho} \phi^2 = \psi_{\text{ts,max}} - \frac{C_{\text{r}}}{n} \phi, \tag{5.16}$$

which can be rearranged as

$$0 = \frac{1}{2} \phi^2 + \frac{\rho C_{\text{r}}}{2 R_{\text{eq}}^{\dagger} A_2^2 n} \phi - \frac{\rho}{2 R_{\text{eq}}^{\dagger} A_2^2} \psi_{\text{ts,max}}. \tag{5.17}$$

Equation 5.17 represents the intersection between the composite fan curve and the composite inlet resistance curve (see Fig. 5-4). This quadratic equation can be solved to obtain the values of ϕ that satisfy the dimensionless pressure balance in Eq. 5.15:

$$\phi = \frac{-\rho C_{\text{r}}}{2 R_{\text{eq}}^{\dagger} A_2^2 n} + \sqrt{\frac{\rho^2 C_{\text{r}}^2}{4 (R_{\text{eq}}^{\dagger})^2 A_2^4 n^2} + \frac{\rho}{R_{\text{eq}}^{\dagger} A_2^2} \psi_{\text{ts,max}}} \tag{5.18}$$

The negative root is discarded as it has no physical meaning. With Eq. 5.18, the total volume flow through the system can be found by calculating the flow coefficient and then converting back to dimensional volume flow (a rotational speed must be specified to calculate u_2 and convert ϕ back to $\dot{V}$).

In Eq. 5.18, as the number of layers n approaches infinity, only the second term under the square root remains; the maximum flow coefficient for $n \to \infty$ is

$$\phi_{\infty} = \lim_{n \to \infty} \phi = \sqrt{\frac{\rho \psi_{\text{ts,max}}}{R_{\text{eq}}^{\dagger} A_2^2}} \tag{5.19}$$

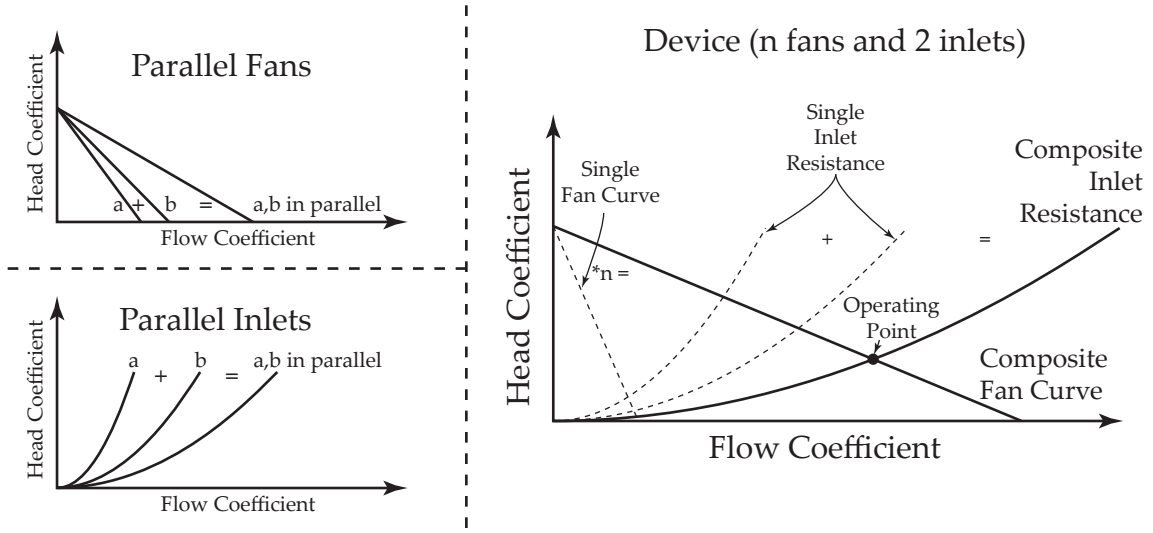

Figure 5-4: Fans in parallel and inlets in parallel add along the flow coefficient axis to generate dimensionless composite curves; the reference speed and area are the impeller tip speed (u_2) and the exit area of a single fan layer (A_2). The fan curves add according to Eq. 5.4 and the inlet resistance curves add according to Eq. 5.9. The intersection point between the fan curve and the inlet resistance curve is the operating point, which can be determined using Eq. 5.18.

The maximum attainable flow coefficient depends on three designer-controlled parameters: the maximum head coefficient ($\psi_{ts,max}$), the composite modified resistance of the inlets ($R^{\dagger}_{eq}$) and the exit area of the fan (A_2). However, volume constraints will often constrain a design before the addition of layers causes the flow coefficient to saturate.

Once the operating point is determined, the flow per layer and rotational speed are known; the volume flow exiting the device is equally distributed among the fans due to the assumption of negligible interlayer resistance. These operating parameters can be used to determine the heat transfer in each layer using the correlations developed in the previous chapter.

5.2 Numerical Flow Circuit Model

In a multilayer integrated fan heat sink, the heat transfer and pumping power in each layer depend on the air flow and rotational speed. For a particular rotational speed, the fan curve and efficiency curve can be estimated based on experimental or analytical models, such as those developed in the Chapter 4. The system resistance combined with these fan curves determines the operating point. Incorporating the fans into a network model representing the multilayer system yielded additional insight into how the multilayer performance scales with the addition of fan layers, and how to best manipulate the system to obtain better performance. This network model, called the "flow circuit model," allows for additional complexity compared to the analytical approach in Sec. 5.1. Particularly, the effect of interlayer resistance (that is, flow through the core of the device) can be explored using the flow circuit model.

The first step in estimating the thermal performance of a multilayer system is to determine the air flow in each of its passages. The flow through the system can be thought of using an electrical analogy: pressure difference (analogous to voltage) causes volumetric flow of air (analogous to electric current). Such a system can be divided into discrete components. In multilayer integrated fan heat sinks, three fundamental components were identified: fans, axial inlets and radial inlets. A model for the pressure change[2] as a function of volume flow for each component was developed; these models were then generalized and incorporated into a network representing the heat sink. Figure 5-5 shows a schematic of a multilayer integrated fan heat sink and its fundamental components.

Each fan was modeled as a battery in series with a resistor; this was chosen from the observation that each fan curve has a negative-slope, linear relationship between pressure rise and volume flow. Next, the axial inlet (i.e. the opening on the top of the heat sink to draw in cool air) was modeled as a nonlinear resistor, due to the quadratic scaling of the pressure drop with the volume flow rate. Since only one axial inlet can be introduced in a multilayer stack, it is common for the inlet to become starved if too many fans are added. The possibility of adding more inlets was introduced by using an air flow layer without an impeller. This radial inlet allowed additional air flow into the low pressure core and out the fan layers. The radial inlet, like the axial inlet, was modeled as a nonlinear resistor.

The models comprising these components are discussed below; these models were generalized and incorporated into the flow circuit model, which was solved numerically to yield the volume flows and pressures throughout the system. The heat transfer was calculated with this knowledge of each operating point within the system, using the correlations developed in the Chapter 4.

[2]This can be a rise or drop in pressure, depending on the component.

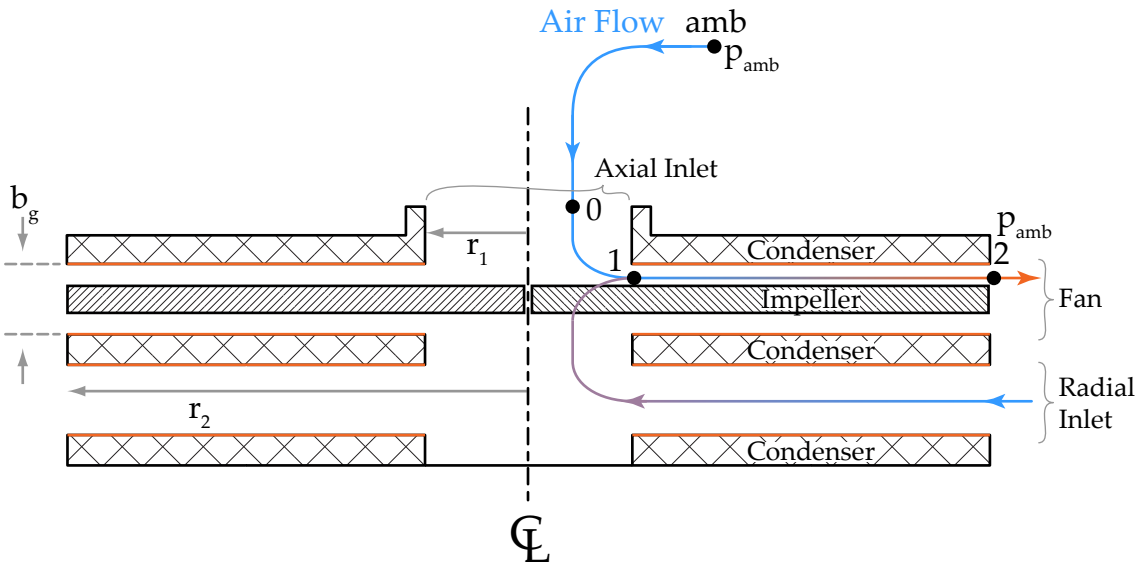

Figure 5-5: A multilayer integrated fan heat sink can be modeled as a network of fans and flow resistances. This network has three fundamental components: a fan, an axial inlet, and a radial inlet. This cross sectional view shows an integrated fan heat sink that contains one of each of these components. The inlets act as nonlinear resistances to the flow, while the fans can be modeled as a battery with an internal linear resistance.

5.2.1 Fans

The fans were modeled as a pressure source in series with a linear flow resistance. This, in electrical terms, is analogous to an ideal battery in series with a linear resistor. At a particular rotational speed, the total-to-static pressure can be determined as a function of the volume flow using the fan curve. The dimensionless representation of a linear fan curve is

$$\psi_{ts} = \psi_{ts,max} - C_r \phi, \tag{5.20}$$

where ψ_{ts} is the total-to-static head coefficient and ϕ is the flow coefficient. $\psi_{ts,max}$ and C_r are constants, determined from a correlation or an analytical model. The dimensional fan curve at rotational speed ω is determined from the definitions of ψ_{ts} and ϕ:

$$\Delta p_{ts} = \rho u_2^2 \psi_{ts,max} - C_r \frac{\rho u_2 \dot{V}}{A_2}, \tag{5.21}$$

where $u_2 = r_2 \omega$ is the blade tip speed and $A_2 = 2\pi r_2 b_g$ is the area of the impeller exit plane. For convenience, this can be expressed in terms of the rotational speed, impeller diameter d_2, and gap breadth b_g:

$$\Delta p_{ts} = \frac{1}{4}\rho d_2^2 \omega^2 \psi_{ts,max} - \frac{C_r \rho \omega}{2\pi b_g} \dot{V}. \tag{5.22}$$

The first term on the right hand side of Eq. 5.22 is the battery voltage in the electrical analogy, which represents a constant total-to-static pressure rise:

$$\Delta p_{\mathrm{ts,max}} = \frac{1}{4}\rho d_2^2 \omega^2 \psi_{\mathrm{ts,max}}, \tag{5.23}$$

where $\Delta p_{\mathrm{ts,max}}$ is the pressure rise developed across the fan when the net volume flow is zero, sometimes referred to as the "blocked pressure rise." The second term on the right hand side of Eq. 5.22 represents the decrease in the pressure rise as the flow increases. This term contains the flow resistance,

$$R = \frac{C_{\mathrm{r}}\rho\omega}{2\pi b_{\mathrm{g}}}. \tag{5.24}$$

The maximum pressure rise and the flow resistance of the fan can be calculated from geometrical parameters and knowledge of the dimensionless fan curve and rotational speed. Once these two terms are known, the fan curve can be rewritten as

$$\Delta p_{\mathrm{ts}} = \Delta p_{\mathrm{ts,max}} - R\dot{V}, \tag{5.25}$$

allowing the pressure rise across a fan to be related to its volume flow.

5.2.2 Axial Inlets

The axial inlet, located at the top of the heat sink, is where cool air enters the core of the device. Air flow enters the device inlet from an large, stagnant reservoir at ambient pressure (point "amb" in Fig. 5-5). Air must be accelerated from the stagnation state at ambient pressure ($p = p_{\mathrm{amb}}$ and $v = 0$) to some velocity at the entrance to the core. The stagnant condition implies that the ambient total pressure[3] $p_{\mathrm{t,amb}}$ is equal to the ambient static pressure p_{amb}. Examining a streamline that begins at the ambient stagnation state and enters the core, the total pressure loss can be modeled using the energy equation with a minor loss term:

$$p_{\mathrm{t,amb}} - p_{\mathrm{t},0} = K_{\mathrm{in}}\frac{\rho v_0^2}{2}, \tag{5.26}$$

where $p_{\mathrm{t,amb}}$ is the ambient pressure, $p_{\mathrm{t},0}$ and v_0 are the total pressure and the average velocity in the inlet, and K_{in} is the minor loss coefficient associated with the inlet (point 0 in Fig. 5-5). This minor loss coefficient associated with the entry flow from an infinite reservoir is $K_{\mathrm{in}} = 0.4$ [44], but it can take a different value depending on the structure of the flow. For example, a bell shaped inlet (e.g. a "velocity stack" in the automotive industry) would reduce K_{in}. In the PHUMP, however, there are rotating spokes that support the motor rotor that interfere with the inlet flow, resulting in larger values for K_{in}.

Equation 5.26 can be expressed in terms of the volume flow $\dot{V} = A_0 v_0$ as

$$\Delta p_{\mathrm{t}} = \frac{\rho K_{\mathrm{in}}}{2A_0^2}\dot{V}^2, \tag{5.27}$$

where A_0 is the cross sectional area of the inlet. Equation 5.27 describes a loss in total pressure that increases parabolically with volume flow. The term that multiplies $\dot{V}^2$ is

[3] It is convenient to work in terms of the total pressure, since static pressure changes occur due to both velocity changes and dissipative phenomena.

analogous to a resistance, but where conventional resistance describes a linear voltage-current relationship, the modified resistance ($R^\dagger$) describes a parabolic dependence of the current on voltage:

$$R^\dagger_{\text{in}} = \frac{\rho K_{\text{in}}}{2A_0^2}. \tag{5.28}$$

Thus, the relationship between volume flow and total pressure loss in an axial inlet is

$$\Delta p_{\text{t}} = R^\dagger_{\text{in}} \dot{V}^2. \tag{5.29}$$

As a side note, when the fans were tested on the circular stator apparatus, the plenum was designed to behave like an infinite reservoir, rendering the dynamic pressure upstream of the inlet negligible. It may seem paradoxical, then, that the flow circuit model separates the axial inlet from the fan layers, since the entry effect of the axial inlet was included in the fan curve measurements. While this entry loss is significant in multilayer systems, it is negligible in a single layer. This can be shown with a simple scaling analysis. The total pressure loss associated with the entry flow (Eq. 5.27) can be nondimensionalized using the same reference speed (u_2) and area (A_2) as were used in ψ_{ts} and ϕ of the dimensionless fan curves. After this nondimensionalization, Eq. 5.27 becomes:

$$\psi_{\text{t,in}} = K_{\text{in}} \frac{A_2^2}{2A_0^2} \phi^2. \tag{5.30}$$

In terms of the diameters of the impeller (d_2) and the fan inlet hole (d_1), Eq. 5.30 reduces to

$$\psi_{\text{t,in}} = K_{\text{in}} \frac{8 d_2^2 b_{\text{g}}^2}{d_1^4} \phi^2. \tag{5.31}$$

The maximum dimensionless total pressure loss ($\psi_{\text{t,in}}$) occurs when the flow coefficient (ϕ) is maximum. ϕ was typically less than 0.3 in the experiments; evaluating Eq. 5.31 with the typical dimensions of the fans tested and $\phi = 0.3$ indicates that this inlet loss was at worst 2% of the measured total-to-static head coefficient (and usually much lower).

The minor loss coefficient K_{in} was difficult to accurately quantify. Based on previous experiments [92] that attempted to measure the volume flow through a multilayer integrated fan, this minor loss coefficient was thought to be between 5 and 10. This high value can be attributed to the high-shear flows in the inlet caused by the motor spokes of the loop-heat-pipe design in the present work. Figure 5-6 shows an early prototype integrated fan with a permanent magnet motor powering the fans. Referring to the top view in Fig. 5-6, the air flow path passes through the rotating motor spokes, followed by the stationary bearing support spokes, causing shearing and flow disruption that increases the loss in total pressure. To err on the side of a more conservative model, $K_{\text{in}} = 10$ was assumed in the flow circuit models of the present work. It will be shown that this assumption results in excellent agreement with experimental data from multilayer integrated fan heat sink prototypes.

5.2.3 Radial Inlets

The addition of impeller layers causes the inlet total pressure loss to rise rapidly. In the multilayer integrated fan heat sink, one way to ameliorate this unfavorable scaling is to

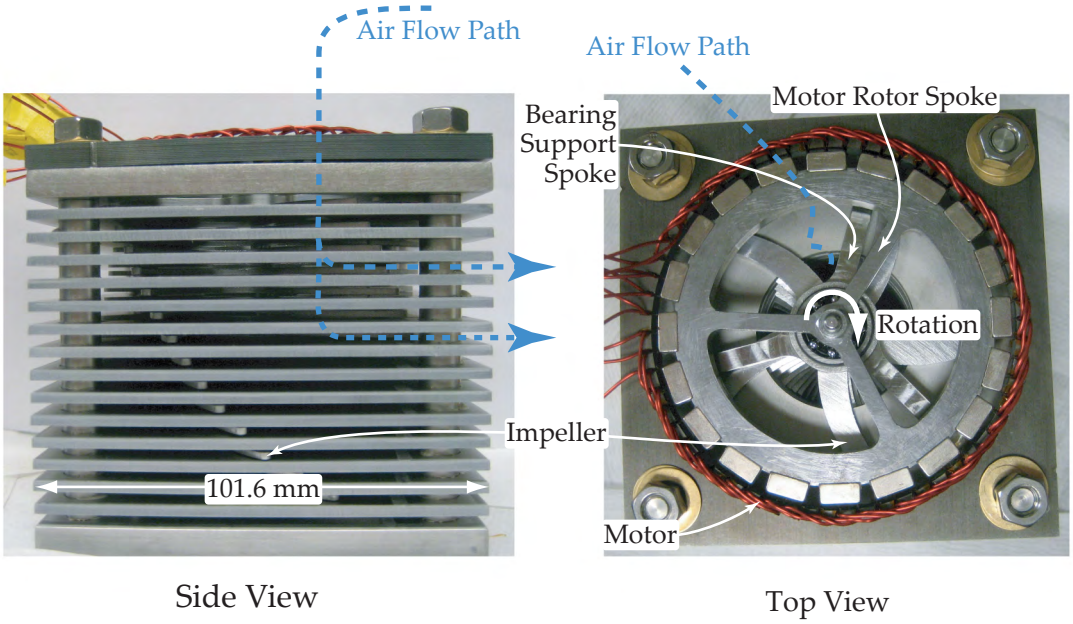

Figure 5-6: The permanent magnet motor driving the fans of a prototype integrated fan heat sink causes an impediment to the air flow. The rotating motor rotor spokes and the stationary bearing support spokes cause shearing and an indirect flow path for the incoming air, resulting in a high minor loss coefficient compared to a rotation-free inlet.

use a radial inlet layer.

The radial inlet was devised to allow greater inlet flow area in an integrated fan heat sink. In a radial inlet (see Fig. 5-5), an impeller is omitted from one parallel plate gap, allowing a direct flow of air from the outer periphery into the low pressure core. This essentially gives the air flow into the device a parallel entry path and lowers the total inlet resistance. When this inlet resistance is reduced, the total air flow increases and the thermal power input can increase.

A radial inlet layer often must be situated between condensers, so some heat transfer to the incoming air occurs. In the flow circuit model, this heat input to the air stream in the radial inlet is accounted for; the air temperature rises as a result of this heat transfer. The temperature in the core of the device is assumed to be the mass averaged temperature of all incoming flows. To account for the heat transfer and pressure change in the radial inlet, correlations for the pressure drop and heat transfer were developed based on CFD simulations. In these simulations, two square-shaped, parallel plates were spaced by a gap of breadth b_g, as shown in Fig. 5-7. These plates had circular holes in the center leading to a small cylindrical plenum, which represented the core of the multilayer device. A mass flow outlet boundary condition was applied to the end faces of this cylindrical core. A total pressure boundary condition was applied to a large diameter cylindrical face upstream of the square periphery of the plates. The resulting total pressure on the mass flow outlet faces was calculated. Meanwhile, a constant temperature boundary condition was applied to the faces of the square plates, so that their temperature was 50 K higher than the inlet air temperature; the heat flux on these surfaces was integrated to obtain the total heat transfer. The SST turbulence model was used with the total energy equation. The CFD simulations consisted of 450 runs, with ranges in b_g and d_1 of 1.25–10 mm and 30–50 mm,

respectively. The side length of the square defining the outer boundary of the plates was 101.6 mm.

The minor loss coefficient for the radial inflow was calculated from the CFD results as

$$K_{\mathrm{ri}} = \Delta p_{\mathrm{t}} \left(\frac{\rho v_1^2}{2} \right)^{-1}, \tag{5.32}$$

where v_1 is the average velocity at the entrance to the core, following the general convention that the minor loss coefficient references the dynamic pressure $\frac{\rho v^2}{2}$ where the velocity is highest. The results of the CFD simulations were correlated as

$$K_{\mathrm{ri}} = 0.170 \left(\frac{b_{\mathrm{g}}}{d_1} \right)^{-0.538}; \tag{5.33}$$

this expression correlated the entire range of data to within 20%, except for about 25 errant points slightly outside that range.

A power law correlation for the mean dimensionless heat flux in the radial inlet ($\Phi_{\mathrm{m,ri}}$)

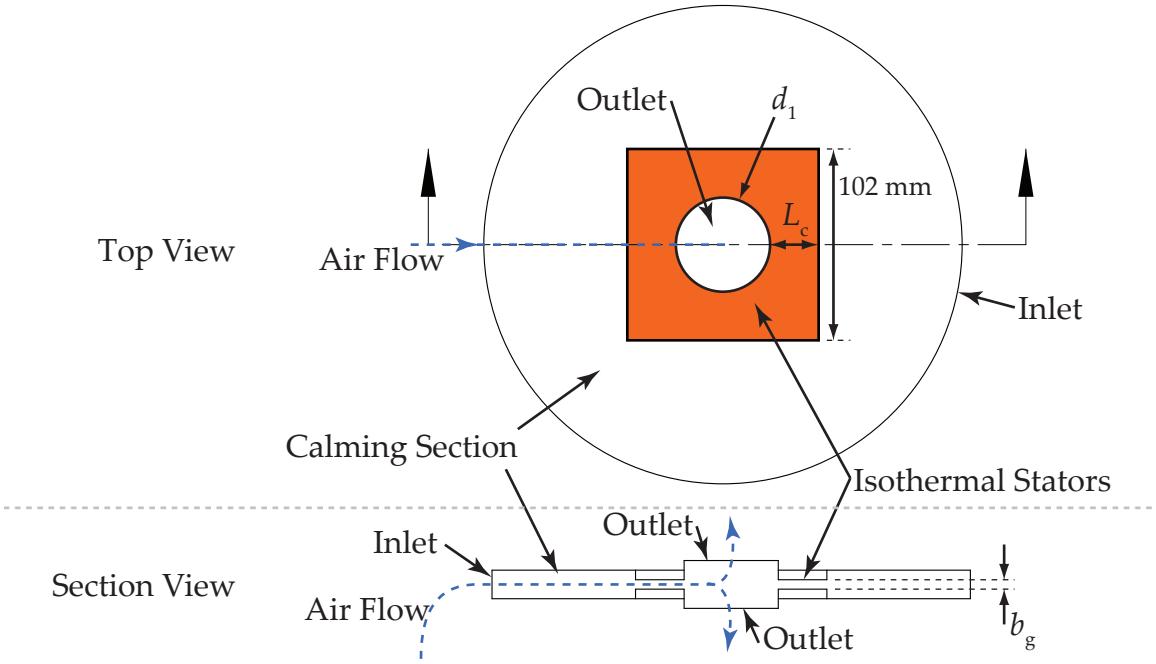

Figure 5-7: The heat transfer and minor loss coefficients for radial inlets of various b_{g} and d_1 were determined using a CFD simulation. In these simulations, a total pressure inlet and a mass flow outlet were used as the boundary conditions. The orange shaded region indicates the isothermal stator walls, which were set to 50 K above the inlet air temperature. The large circle in the top view is the calming section, which ensured that the inlet flow could establish itself naturally prior to entering the square stator gap. The total pressure at the outlet was calculated to determine the total pressure change from the ambient to the core; the heat flux was integrated over the stator surfaces to determine the total heat transfer into the air flow.

was formed:

$$\Phi_{\mathrm{m,ri}} = \frac{\dot{Q} L_{\mathrm{c}}}{A_{\mathrm{s}} \Delta T_{\mathrm{in}} k} = 0.463 \mathrm{Re}_L^{0.373} (b_{\mathrm{g}}/d_2)^{-0.359}, \tag{5.34}$$

where $\dot{Q}$ is the total heat transfer, $L_{\mathrm{c}} = r_2 - r_1$ is the characteristic length associated with the inward flow, A_{s} is the wetted surface area, ΔT_{in} is the temperature difference between the wall and the incoming flow, and k is the thermal conductivity of the air. Re_L is the Reynolds number with length scale L_{c} velocity scale v_1 (the same velocity scale as in the minor loss coefficient). The correlation for the dimensionless heat flux represented the data with an R^2 value of 0.96, and comprised a range of $1.3 \cdot 10^3 < \mathrm{Re}_L < 1.6 \cdot 10^5$.

5.2.4 Generalized Component

Fans, axial inlets, and radial inlets express a relationship between volume flow and pressure difference. The pressure-volume flow relationship can be generalized into a single equation capable of representing any of these components. A generalized model of the pressure change across a layer i is

$$\Delta p_i = R_{i,0} + R_{i,1} \dot{V} + R_{i,2} \dot{V}^2 = \sum_{a=0}^{2} R_{i,a} \dot{V}^a, \tag{5.35}$$

where R_i is one component of a composite resistance that consists of three parts: a DC offset ($R_{i,0}$), a linear resistance ($R_{i,1}$), and a modified resistance ($R_{i,2}$) identical in form to $R^\dagger$ in Eq. 5.29. Representations of these three components (fans, axial inlets, and radial inlets), along with interlayer resistances (discussed in the next section), are shown in Fig. 5-8, alongside the equations representing their composite resistances. Equation 5.35 follows a sign convention for Δp_i and $\dot{V}$: positive pressure differences tend to cause flow into the device, and positive volume flow goes into the device. In the core, volume flow is defined as positive when it flows downward (from layer i to layer $i+1$). In Eq. 5.35, the right hand side can reproduce the pressure change equations for either of the inlets or fans, provided the correct values or R are used and the sign convention is preserved. Summarizing the previous 3 subsections, the values of R in Eq. 5.35 for the three components are shown in Table 5.1:

In the case of axial and radial inlets, the pressure difference (Δp_{i} in Eq. 5.35) is total-to-total, since their loss equations describe flow from the total pressure at ambient ($p_{\mathrm{t,amb}}$) to the total pressure in the core. In contrast, the fans draw air from the core and discharge it at the periphery. The outlet flow resembles a jet; due to the negligible streamline curvature immediately at the outlet, the *static* pressure here is equal to the ambient pressure. Thus, the fans express a relationship between volume flow and the total-to-static pressure

Table 5.1: Resistance Values for a Generalized Component

	$R_{i,0}$	$R_{i,1}$	$R_{i,2}$
Axial Inlet	0	0	$\frac{\rho K_{\mathrm{in}}}{2A_0^2}$
Fan	$\rho u_2^2 \psi_{\mathrm{ts,max}}$	$\frac{A \rho u_2}{A_2}$	0
Radial Inlet	0	0	$\frac{\rho K_{\mathrm{ri}}}{2A_2^2}$

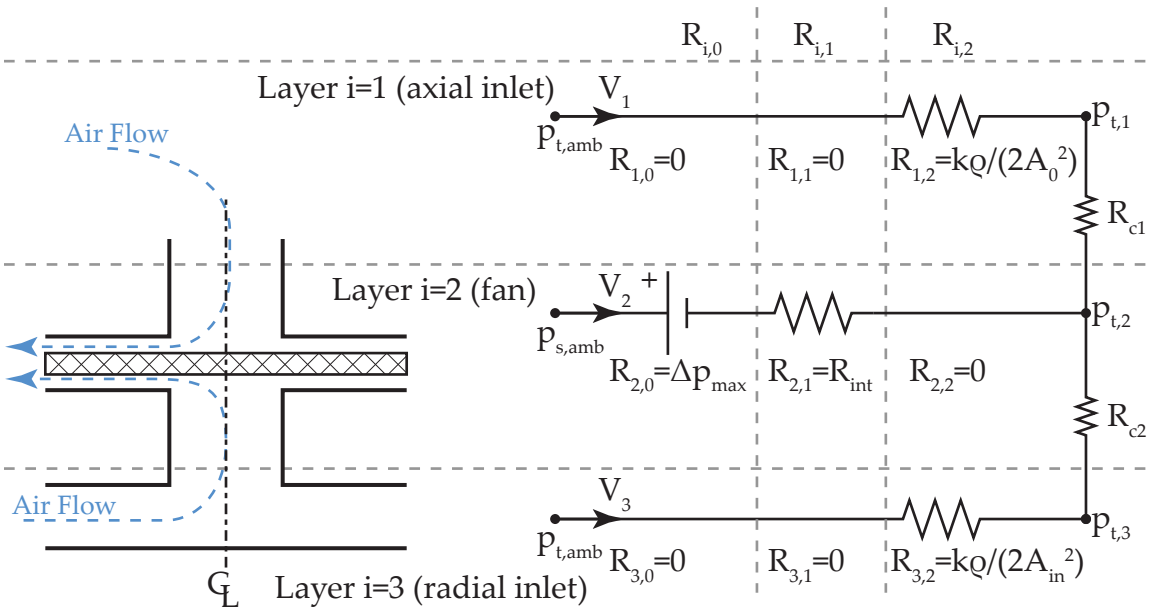

Figure 5-8: A multilayer integrated fan heat sink can be modeled as a network of fans and flow resistances. Each layer can be represented using a general formulation for the pressure change, which contains 3 resistance terms (R_0, R_1, and R_2). Three fundamental components are shown: fans, axial inlets, and radial inlets. The inlets act as nonlinear resistances to the flow ($p_{\text{t,amb}} - p_{\text{t,i}} = R_{i,2}\dot{V}_i^2$), while the fans can be modeled as a battery with an internal resistance ($p_{\text{s,amb}} - p_{\text{t,i}} = R_{i,0} + R_{i,1}\dot{V}_i$).

difference between the core and the ambient. This total-to-static pressure difference in the flow circuit model is convenient because the experimental fan results were directly measured as total-to-static pressure differences. The correlations from Chapter 4 can therefore be directly used in the flow circuit model.

5.2.5 Interlayer Flow Resistance

In addition to flow resistance from the ambient into the core, the flow circuit model can also account for flow resistances *within* the core. The flow in the core, between components 1 and 2, must traverse the portion of the impeller that is within the core. The impeller blades block some of the cross sectional area in the core. The flow between layers 1 and 2 in the core was modeled as a sudden contraction immediately followed by a sudden expansion[4]. The minor losses associated with each of these area changes can be summed because they both reference the velocity at the smaller cross sectional area. The minor loss coefficient for a sudden contraction (K_c) is [44]

$$K_c = 0.4\left(1 - \frac{A_S}{A_L}\right), \tag{5.36}$$

where A_S is the smaller area and A_L is the larger area. In the interlayer flow, the larger area is the cross sectional area of the core (A_0) and the smaller area is $A_0 - A_B$, where A_B is the

[4]The flow does not become fully developed between the contraction and expansion; however, these relations were meant to provide general estimates of the pressure drop.

area blocked by the impeller and shaft. The minor loss coefficient for a sudden expansion (K_e) is [44]

$$K_e = \left(1 - \frac{A_S}{A_L}\right)^2. \tag{5.37}$$

The total minor loss from the contraction-expansion is the sum of these losses,

$$K_{ce} = 0.4\left(1 - \frac{A_S}{A_L}\right) + \left(1 - \frac{A_S}{A_L}\right)^2; \tag{5.38}$$

the losses associated with the contraction and expansion can be added because they both reference the velocity at the small area.

The blockage ratio (BR) is defined as the fraction of the core's cross sectional area that is blocked by the impeller and shaft:

$$\mathrm{BR} = \frac{A_B}{A_L} = \frac{A_L - A_S}{A_L}. \tag{5.39}$$

The minor loss of the contraction-expansion (Eq. 5.38) can be expressed in terms of the blockage ratio as

$$K_{ce} = 0.4\mathrm{BR} + \mathrm{BR}^2. \tag{5.40}$$

This minor loss coefficient only ranges from 0 to 1.4 as the blockage ratio varies from 0 to 1. The pressure loss, however, increases drastically at high blockage ratios because the dynamic pressure in the small area becomes very large. The scaling of K_{ce} with the blockage ratio is shown in Fig. 5-9. The ratio of the dynamic pressure in the small area compared to the large area is also shown as a function of the blockage ratio (calculated from continuity). The dynamic pressure ratio diverges; the loss in total pressure is proportional to the dynamic pressure in the small area, so it follows that the total pressure loss can be quite significant at high blockage ratios, and its rate of increase is drastic beyond about BR = 0.5.

The blockage ratios of the experimentally characterized impellers were calculated by measuring the blocked area within the 40 mm diameter core using CAD software. These blockage ratios ranged between 0.3 and 0.5, corresponding to minor loss coefficients of 0.22 to 0.42. Of course, the additional shearing associated with the rotating blades could cause these minor loss coefficients to be higher than anticipated by this simple model.

The pressure change from the core of layer i to the core of layer $i+1$ is modeled as a minor loss, using the coefficient from Eq. 5.40:

$$p_i - p_{i+1} = \frac{K_{ce}\rho\dot{V}^2}{2A_0^2(1-BR)^2} \cdot \mathrm{sign}(\dot{V}), \tag{5.41}$$

where $A_0 = \pi d_1^2/4$ is the area of the unblocked core. The volume flow is defined as positive when flowing downward in the device (from layer i to layer $i+1$; layer 1 is the axial inlet on the top of the device). The "sign" operator is defined as

$$\mathrm{sign}(x) = \begin{cases} -1, & \text{if } x < 0 \\ 0, & \text{if } x = 0 \\ 1, & \text{if } x > 0 \end{cases}. \tag{5.42}$$

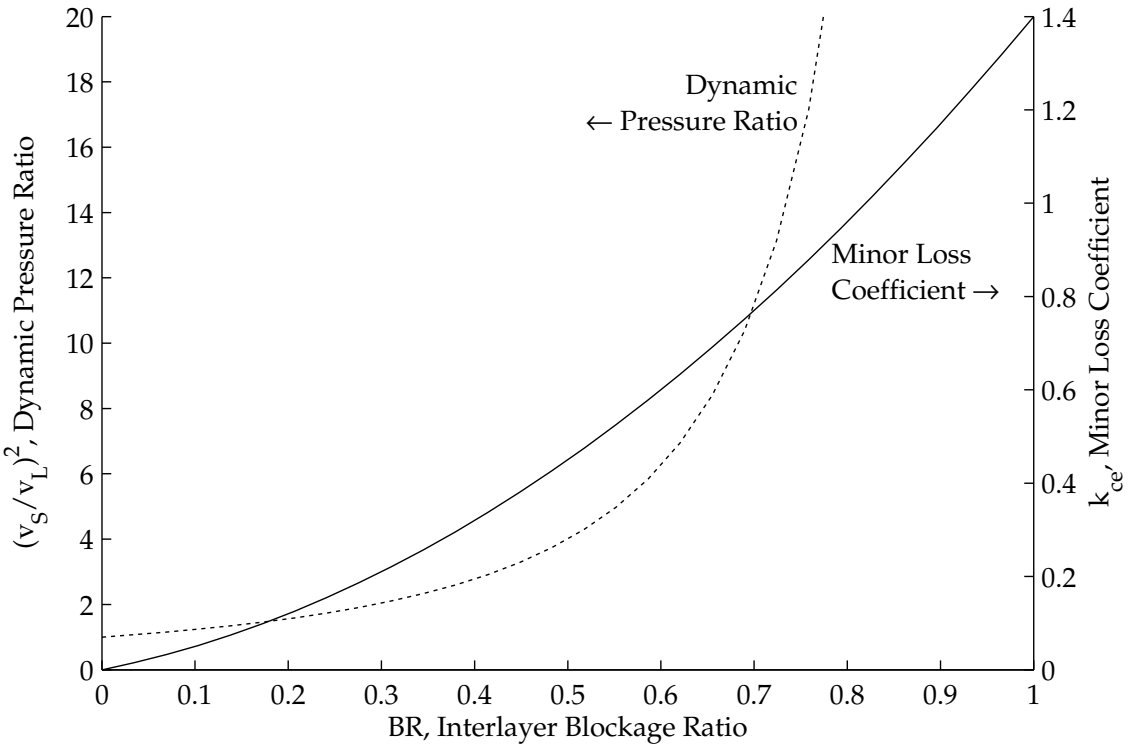

Figure 5-9: The minor loss coefficient for the contraction-expansion in the interlayer flow increases parabolically with the blockage ratio. However, the dynamic pressure ratio between the open (large) area and the obstructed (small) area diverges as the blockage ratio approaches 1, leading to significant total pressure loss in the interlayer flow. v_S and v_L are the velocities in the small and large areas, respectively.

In Eq. 5.41, the sign operator ensures that the pressure gradient opposes the flow. For example, if $\dot{V} < 0$ (i.e. upward flow from layer $i+1$ to layer i), Eq. 5.41 would correctly indicate that $p_{i+1} > p_i$.

If the interlayer flow resistance can be neglected, the closed form solution in Eq. 5.18 can be used. However, this interlayer resistance is not always negligible, and the numerical flow circuit model gives the designer the ability to include these resistances for more accurate system modeling. In Sec. 5.3.3, the effect of the interlayer blockage ratio is discussed further. A conclusion from this section is that as long as BR does not exceed about 0.5, the interlayer resistance results in less than a 10% degradation in the multilayer performance.

5.2.6 Solution Procedure

Each component introduces one equation (the pressure-volume flow relationship, Eq. 5.35) and two unknowns (the volume flow $\dot{V}_i$ and total pressure in the core $p_{t,i}$), which leaves n unknown variables that must be determined. An additional $n-1$ equations come from the flow through the interlayer resistances in the core, governed by Eq. 5.41. Finally, 1 equation comes from the conservation of mass, which can be expressed in terms of volume

flow (since the air is modeled as incompressible) as

$$0 = \sum_{i=1}^{n} \dot{V}_i, \tag{5.43}$$

where $\dot{V}_i$ is the volume flow in component i, adhering to the positive-inward sign convention. This set of $2n$ simultaneous equations can be solved using a numerical technique (in the present work, the equations were solved using the fsolve function in MATLAB).

After the volume flows and pressures are determined throughout the device, the heat transfer in each layer can be computed. The dimensionless heat flux (Φ_m) was calculated in each of the fan layers using the appropriate correlation (Eq. 4.16). The temperature of the air in the core was determined as the mass averaged temperature of the air entering the core. The air temperature entering from the axial inlet was simply the ambient temperature. On the other hand, the radial inlets experience heat transfer, because the air flow enters through a passage with heated walls (condensers). This heat transfer increases the temperature of the air flowing in through the radial inlet, and must be accounted for as it reduces the heat transfer in the other layers. The total heat transfer in the inlet layer was calculated by using Eq. 5.34 to determine the dimensionless heat flux, and then using Eq. 1.67 to calculate the total heat transfer into the radial inlet air flow. The air's temperature at the entrance to the core was determined by an energy balance.

The air was assumed to mix in the core so that the temperature of the air entering each fan layer was the same. Since the properties were approximated as constant, the temperature in the core reduces to

$$T_{\text{core}} = \frac{\sum_{i=1}^{n_{\text{in}}} \dot{m}_{\text{in},i} T_{\text{in},i}}{\sum_{i=1}^{n_{\text{in}}} \dot{m}_{\text{in},i}}, \tag{5.44}$$

where T_{core} is the temperature of the air entering the fan layers from the core, n_{in} is the number of inlets, $\dot{m}_{\text{in},i}$ is the mass flow rate though inlet i, and $T_{\text{in},i}$ is the temperature of the air entering the core from inlet i.

The mechanical power consumption of the multilayer device arises from mechanical power input required by the fans as well as from bearing losses. The fan power input was calculated with knowledge of the fans' operating points, using a correlation based on experimental data (Eq. 4.35). The bearing losses were calculated with a parabolic fit to the experimentally measured bearing losses (Eq. 2.17)[5]. These bearing losses were added to the calculated fan power input to determine the required mechanical power to run the fans:

$$\dot{W} = \left(\sum_{i=1}^{n_{\text{fans}}} \dot{W}_{\text{fan},i} \right) + \dot{W}_{\text{brg}}, \tag{5.45}$$

where $\dot{W}$ is the mechanical power required to run the multilayer device, n_{fans} is the number of fans, $\dot{W}_{\text{fan},i}$ is the mechanical fan power associated with layer i, and $\dot{W}_{\text{brg}}$ is the mechanical power loss associated with one pair of bearings that act to support the shaft.

[5]The bearing losses associated with the square stator apparatus were used, because these bearings were thought to be likely candidates for use in a functional prototype device.

5.3 Performance Estimation

The flow circuit model was used to explore various parameters and their effects on the performance of a multilayer integrated fan heat sink. The effects of adding fan layers, inlet layers, and changing the interlayer flow resistance are discussed below.

5.3.1 Effect of Additional Fans

As expected, the addition of fan layers causes the overall thermal resistance of the heat sink to decrease due to the addition of surface area. An example of this is shown in Fig. 5-10. Figure 5-10 represents a simulation of a device with a single axial inlet and a varying number of fans. This device used Fan 12, with blade and gap breadths of $b_b = 1.5\,\text{mm}$ and $b_g = 2.5\,\text{mm}$, respectively. The total heat transfer ($\dot{Q}$), input mechanical power ($\dot{W}$), and total volume flow ($\dot{V}$) were calculated and normalized to their values in a single fan device. The total heat transfer increases with the number of fans; the pumping power increases at a similar rate. As predicted by the closed form solution for ϕ as $n \to \infty$ (Eq. 5.19), the volume flow saturates; it ceases to increase appreciably after about 10 layers. Curiously, the heat transfer continues to increase despite this saturation; this makes sense, however, in the context of the experimental results for a single fan layer. It was observed that, even at zero net volume flow, there is a finite heat transfer due to the recirculatory flow at the exit plane of the fan. Thus, even though the volume flow per layer decreases with additional layers, the total heat transfer can continue to increase. The rise in pumping power also makes sense because, as the volume flow per layer (and hence the flow coefficient) approaches zero, the fan efficiency vanishes.

As Fig. 5-1 suggests, the scaling of the heat transfer does not increase linearly with the number of fans; the hyperbolic decrease in the thermal resistance is less rapid than a crude prediction based on a fixed thermal resistance of a single layer. This sublinear scaling is a direct result of the reduction in heat transfer caused by the restricted flow (as was suggested in Fig. 5-1). The degradation in volume flow per layer due to inlet starvation shifts the fan's operating point and increases the effective thermal resistance of each fan layer. This effect must be accounted for to properly design an integrated fan heat sink, as can be seen by the rapid departure of the actual heat transfer from the linear scaling indication in Fig. 5-10.

Figure 5-10 shows that the heat transfer increases (although sublinearly) and does not asymptotically approach a constant value as does the volume flow. However, beyond a certain point, the device begins to rely on recirculatory flow to sustain the predicted heat transfer. In other words, at a certain volume flow the air temperature must reach the temperature of the wall before it exits the device in order to sink the predicted thermal power input. This regime has only been experimentally characterized for a single layer; operating a multilayer device in this fashion may have unintended consequences. For example, in a tall multilayer device, there may be reingestion of warm air exiting a neighboring layer. This would decrease the heat transfer compared to estimates from the experimentally based correlations for a single layer, where no adjacent layers are present to thermally contaminate the surrounding air. Therefore, it is inadvisable to design a device to operate with more fans than indicated by the vertical dashed line (marked $\epsilon = 1$) representing an effectiveness of unity in Fig. 5-10. This point is the First Law limit, when the net air flow through the system absorbs enough thermal energy to bring its temperature up to the stator wall temperature.

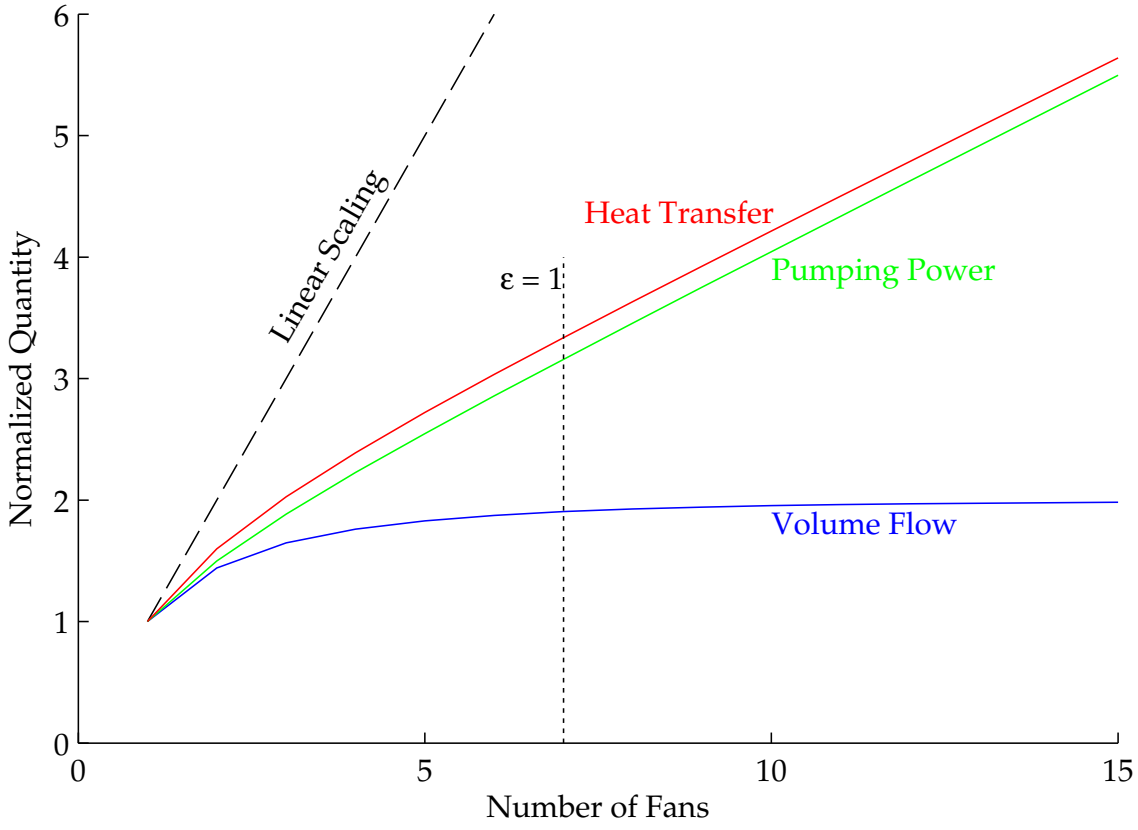

Figure 5-10: As fans are added, the total volume flow saturates but the heat transfer and pumping power continue to increase, although at a sublinear rate. The recirculatory flow at the fan exit plane (i.e. the periodic inflow of air at the impeller periphery) results in a finite heat transfer rate even with no net volume flow through the fan. In this figure, the flow circuit model was run with 1–15 fan layers (Fan 12, $b_b = 1.5\,\text{mm}$, $b_g = 2.5\,\text{mm}$) with an axial inlet. In this case, a heat sink with more than 7 layers is predicted to have a total heat transfer rate higher than the maximum predicted by an energy balance on the air stream; that is, the effectiveness is greater than unity beyond 7 layers. Thus, in this example, for $n > 7$ the heat sink relies on the recirculatory flow for operation. This is probably undesirable, because warm air from adjacent layers may reenter at the periphery in a multilayer stack.

Fortunately, additional fans can be added to a multilayer stack more effectively by using radial inlets to decrease the pressure drop of the incoming flow. This reduction of the inlet resistance allows more fan layers to be added without reaching saturation in the volume flow, and results in better scaling of the system's performance with the number of layers.

5.3.2 Effect of Radial Inlets

Sometimes a multilayer device's performance does not improve significantly with additional fan layers, or the addition of fans pushes the device into an unfavorable operating regime that relies on recirculatory flow. The parabolic increase in the inlet pressure drop tends to render additional fan layers ineffective beyond a certain number (see Fig. 5-2). Addition of radial inlets lessens the slope of the composite system resistance curve and shifts the operating point to a higher overall volume flow. Sometimes this can have a drastic effect on the system's overall performance. For example, Fig. 5-11 shows the performance in heat transfer, pumping power, and volume flow (compared to their respective single-fan values). Compared to Fig. 5-10, which shows the performance for an identical device with only one axial inlet, the difference is striking. In the axial inlet case (the solid lines in Fig. 5-11), the volume flow quickly plateaus and causes the heat sink to rely on recirculation flows for additional heat transfer. By adding a single radial inlet, this same device's performance changes to that of the middle dashed lines. The volume flow now plateaus at a higher level and saturates at a higher number of fans. Also, the heat transfer's departure from linear scaling does not occur as rapidly. Finally, the effectiveness does not reach unity until 27 layers, which is probably a larger-than-practical heat sink size. Thus, recirculation at the outlet (and the associated risk of reingesting warm air) can be avoided by using radial inlets. The pumping power increases with the addition of radial inlets due to the increase in volume flow. The model results shown in Fig. 5-11 do not include the effect of interlayer blockage, so the position of the inlet layers does not have an effect on the results.

The heat transfer and pumping power increase together; this concurrent increase shows one of the tradeoffs in heat sink design. The thermal resistance of the device is inversely proportional to the heat transfer (ΔT_{in} is constant). Increasing the pumping power results in improved heat transfer. The pumping power can increase by (1) increasing the rotational speed, or (2) adding an inlet layer to increase the volume flow. The intersection of the fan curves and system resistance curves *is independent of the rotational speed*, meaning that changing the rotational speed does not change the fan efficiency of a device. On the other hand, by adding an inlet layer, the operating point can shift along the dimensionless fan curve to one of higher efficiency.

The tradeoff between R and $\dot{W}$ can be seen in Fig. 5-12. In this figure, the upper plot shows a device with 1 axial and 1 radial inlet, while the lower plot shows a device with 1 axial and 2 radial inlets. The solid lines represent fixed geometries with various numbers of fan layers; lines of constant rotational speed are indicated by gray dashed lines. As the rotational speed increases, the thermal resistance decreases and the pumping power increases. These operating curves shift closer to the origin as the number of fans is increased; the addition of a second radial inlet shifts the entire family of curves closer to the origin. The maximum thermal resistance and pumping power specified by the DARPA MACE program (see Sec. 1.2) are shown as dashed lines. In comparing the upper and lower plots, it can be seen that these design requirements can be met with fewer layers

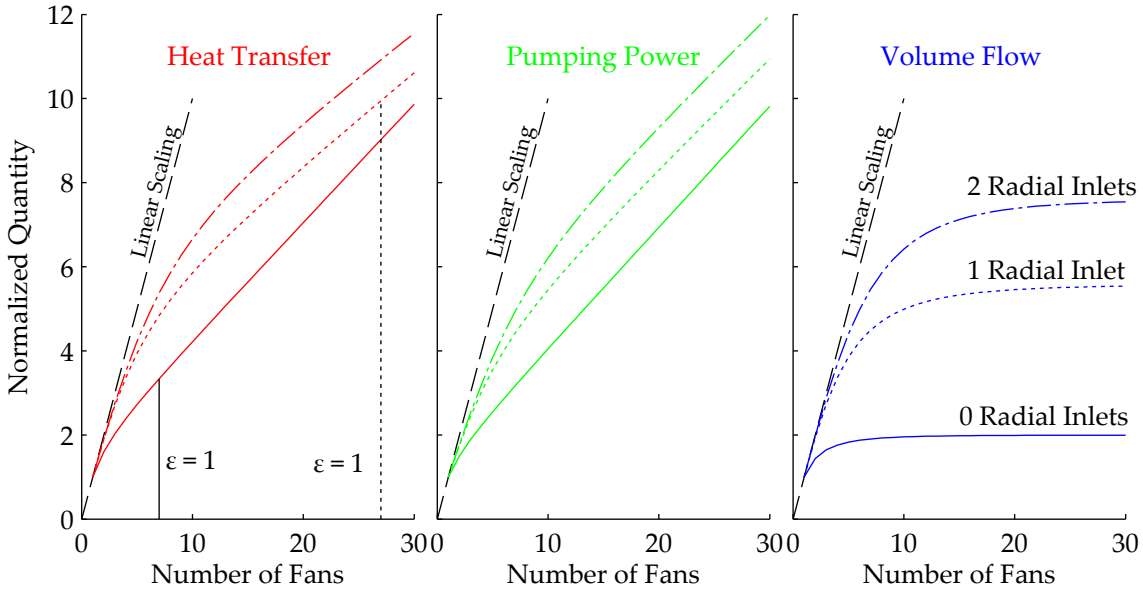

Figure 5-11: The addition of inlet layers results in a significant change in the scaling of heat transfer, pumping power and volume flow with the number of fans. In this figure, the solid lines are the same data as is shown in Fig. 5-10. The dashed lines show how the performance changes with the addition of radial inlet layers. The largest effect is in the volume flow. Initially, the axial inlet causes the volume flow to quickly saturate. The addition of 1 radial inlet increases the volume flow enough to change the point at which the first law limit is reached (the vertical dashed lines in the left plot) from 7 to 27 fans. This improvement is drastic, because while 7 fans is within the range of practical devices, it is unlikely that a 27-fan device would be built (it would be an unusually tall heat sink). Thus, the radial inlet layer significantly broadens the available design space.

and at a lower rotational speed in the device containing two radial inlet layers.

An alternative way of showing the effect of inlet layers is to examine the scaling of thermal resistance, pumping power, and overall volume occupied by the heat sink. Figure 5-13 shows how these parameters vary relative to the specifications of the DARPA metric ($R_{\max} = 0.05\,\mathrm{K/W}$, $\dot{W}_{\max} = 33\,\mathrm{W}$, and $V_{\max} = 1.05\,\mathrm{L}$). A design that satisfies these metrics must have all of the lines (for R, $\dot{W}$, and V) below the black dashed line simultaneously. Three device layouts were considered: the left column shows devices with no radial inlets ($n_{\mathrm{ri}} = 0$); the devices in middle column have 1 radial inlet ($n_{\mathrm{ri}} = 1$); and the right column shows devices with 2 radial inlets ($n_{\mathrm{ri}} = 2$). The upper and lower plots represent fans with different fill ratios (the upper 3 plots have a fill ratio of FR=0.62, and the lower 3 plots have a fill ratio of FR=0.77). Aside from these geometrical differences, everything else about the devices shown in Fig. 5-13 is identical. The rotational speed is 6 krpm for all of the points. All of the designs that meet the DARPA metric are shown with a thickened portion of the curves.

First, the heat sink volume, indicated by the blue lines (labeled "Vol") in Fig. 5-13, increases with (1) the larger gap spacing associated with lower fill ratio and (2) additional vertical space occupied by radial inlet layers. Second, the thermal resistance decreases with increasing fill ratio and addition of radial inlets. However, the improvement in thermal resistance generally accompanies a steeper pumping power curve that exceeds the DARPA maximum with fewer fans. The lower-middle and lower-right plots show how

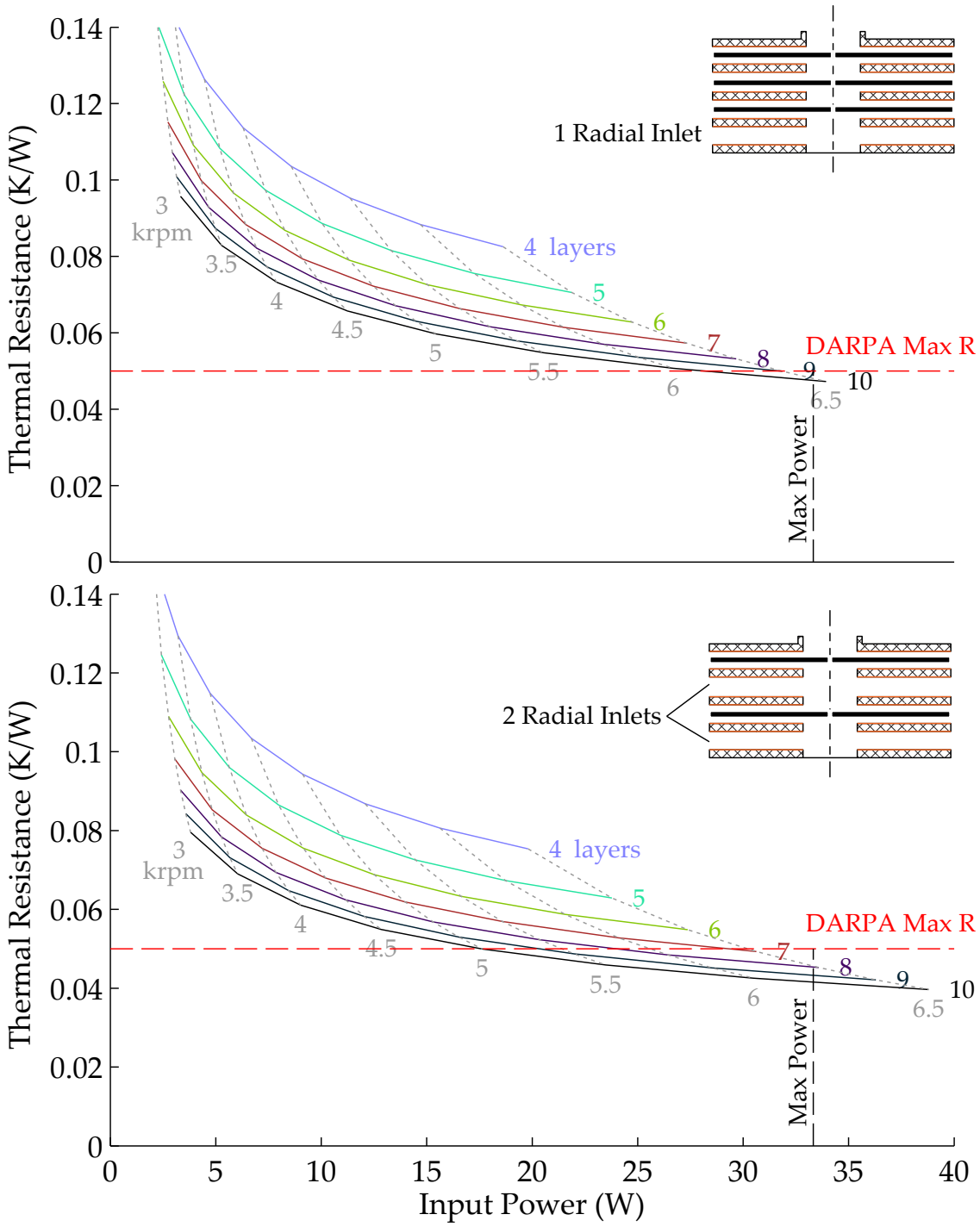

Figure 5-12: Thermal resistance decreases as the rotational speed increases and with the addition of fan layers. The upper plot shows the thermal resistance vs. input power for 4–10 fan layers with 1 radial inlet ($b_{ri} = 3b_g$); the lower plot is identical except that it has 2 radial inlets. The addition of inlet layers shifts the operating curves toward the origin. The DARPA maximum thermal resistance and power consumption are shown as dashed lines; points inside this region meet the DARPA requirements. Unlike the hypothetical heat sinks discussed in Section 1.5 (Figs. 1-6 and 1-8), these pumping powers and thermal resistances are experimentally based, and include losses due to fan and bearing inefficiency.

the pumping power can exceed the metric and narrow the design space. Still, in comparing these figures, the case with 2 radial inlets meets the requirements with fewer layers compared to the case with 1 radial inlet.

One reason that these radial inlets are so effective is that with a reasonable vertical space, they can be considerably less restrictive ($K_{ri} \sim 1$) than the axial inlet ($K_{in} \sim 10$). This difference is likely due to the radial inlet's absence of dissipative, high-shear flows present near the motor spokes in the axial inlet. The radial inlet also results in a small amount of additional heat transfer from the walls bounding the inward flow. In the next section, the distribution of flow among the layers will be explored. One feature that becomes evident in this flow distribution study is the difference in flow between the axial and radial inlet.

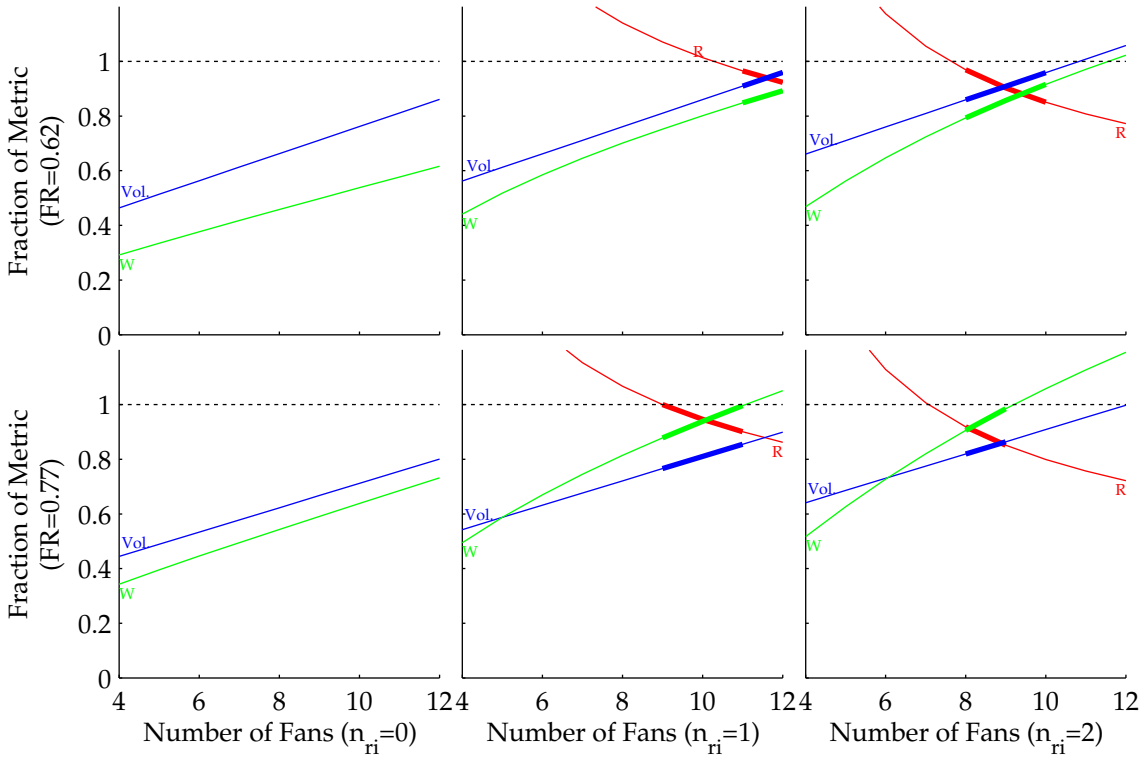

Figure 5-13: The flow circuit model was run for 4–12 layers with Fan 12 (with b_b = 1.5mm) rotating at 6 krpm. The thermal resistance ("R"), overall device volume ("Vol."), and mechanical power input ("W") were calculated at each operating point, and were normalized to the DARPA metrics in Table 1.1(viz. R = 0.05 K/W, Vol.=1 L, $\dot{W}$ = 33 W). The fill ratio (FR) was 0.62 in the top 3 plots and 0.77 in the bottom 3 plots; the number of radial inlets (n_{ri}) was varied 0, 1 and 2 for the left, middle, and right plots. In these plots, a design that meets the DARPA metrics *must have all 3 quantities below the dashed line for a given number of fans*. These valid design points are shown with thicker lines.

Radial inlets tend to reduce the thermal resistance but increase the pumping power. The volume steadily increases with the addition of layers. Increasing the fill ratio also improves the thermal performance at the expense of pumping power, but also results in a leftward shift in the R and $\dot{W}$ curves, meaning that the metrics can be satisfied with fewer fan layers.

5.3.3 Effect of Interlayer Resistance

The flow circuit model simulations suggested that the interlayer resistance has a noticeable effect on the device performance; fortunately, as long as the blockage ratio can be kept below about 0.5, the degradation in performance is minimal. To demonstrate this effect, a 6-fan device with axial and radial inlets was simulated in the flow circuit model for various blockage ratios. The resulting decrease in heat transfer and volume flow is shown in Fig. 5-14. The heat transfer decreases faster than the pumping power, meaning that the COP decreases as the blockage ratio increases. One simple way to mitigate the effect of interlayer blockage due to the impellers is to use a support ring (see Fig. 2-24). A support ring serves as the starting point of the impeller blades, and attaches to the shaft via 3 spokes, leaving most of the area unimpeded. In impellers with many blades, this support ring results in a significant reduction in the blockage ratio. Fan 12, for example, used a support ring to reduce its blockage ratio from 0.470 (if the blades extended all the way to the center shaft as in Fan 1) to 0.324. This improvement in performance, although minimal according to Fig. 5-14, comes at very low cost; planar manufacturing techniques (e.g. waterjet or laser cutting) can easily incorporate the additional features of the support ring.

In addition to reducing the overall performance of the device, interlayer blockage also changes the *distribution* of flow among the layers. Figure 5-15 shows the distribution of volume flow and heat transfer among the layers of a 6-fan device with axial and radial inlets for 5 blockage ratios. First, increasing the blockage ratio decreases the total flow through the device, as indicated by Fig. 5-14. This is most evident in Fig. 5-15 by visually comparing the size of the flows in the two inlet layers. Second, as the blockage ratio increases, the inner-most fan layers receive a smaller share of the total flow. In the unblocked case, the pressure in the core is the same in each layer, since the air flows unimpeded from one layer to the next. With blockage, however, the fans in the inner-most layers must fight a stronger pressure gradient because the flow undergoes additional pressure drops to arrive at their section of the core. Third, the relative flow resistance of the axial and radial inlets can be seen easily in Fig. 5-15; this disparity becomes less pronounced with more blockage, because the higher velocities in the core near the radial inlet are penalized by the restrictive interlayer blockages. Finally, a curious phenomenon occurs in the axial inlet and in the lowest fan layer. In these cases, the flow *increases* with increasing blockage ratio. Of course, these increases are only local, and result from more restrictive flow paths elsewhere in the system. The overall performance of the system always decreases with increased blockage ratio; losses in total pressure imply generation of entropy, a sure sign of degraded performance.

5.4 Multilayer Design Example

The methods of modeling multilayer systems developed in the present work (Sections 5.1 and 5.2) allow multilayer performance to be estimated based on knowledge of a single fan layer. These multilayer scaling models can also be used to select the best fan designs for an application with design constraints. To illustrate this application of the scaling models, a design that meets the DARPA metrics summarized in Table 1.1 is outlined. In this design example, the volume of the device was constrained and needed to fit within a cube with 102 mm sides. Additionally, the maximum electrical power input was specified as 33 W.

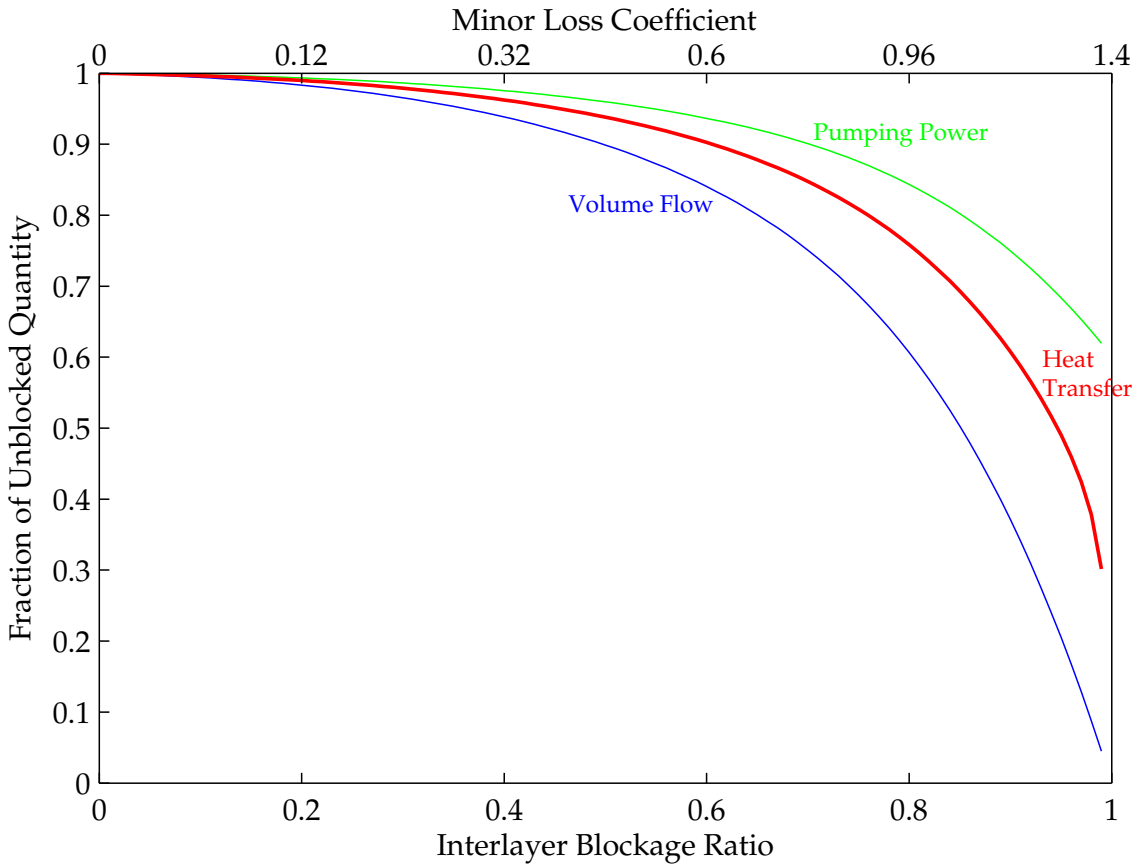

Figure 5-14: The interlayer resistance can significantly degrade the performance of a multilayer device. A 6-fan device was simulated using the flow circuit model for various interlayer blockage ratios. This device used Fan 1 in the fan layers (with $b_b = 1.5$mm and $b_g = 2.5$mm), and had an axial inlet and one radial inlet (with $b_{ri} = 3b_g$). At a blockage ratio of 0.6, the heat transfer is reduced to 90% of its unblocked value. The minor loss coefficient associated with each blockage ratio (calculated using Eq. 5.40) is shown on the upper horizontal scale.

The thermal resistance of a multilayer device using 33 W of electrical power input[6] was chosen as a figure of merit for this device; this metric will be referred to as R_{33}. Several fan designs were evaluated in terms of their multilayer R_{33} value. Each fan design corresponded to an experimentally characterized design (these 42 experimental results are shown in Fig. 4-5 and summarized in Table 4.1). The number of condensers that could fit in a 100 mm vertical space was calculated based on the expected component breadths of the condensers (b_{cond}), the evaporator (b_{evap}), and the electric motor to drive the impellers (b_{motor}) [45]. These breadths were estimated as $b_{cond} = 2.5$mm, $b_{evap} = 17$mm, and $b_{motor} = 10$mm in this example. The total breadth of the multilayer device was calculated as

$$b_{total} = b_{evap} + b_{motor} + (b_{cond} + b_g)n_{fans} + (b_{cond} + b_{ri})n_{ri}, \tag{5.46}$$

where b_g is the breadth of the parallel plate gap in each fan layer and b_{ri} is the breadth of a radial inlet layer. For manufacturing convenience, b_{ri} was taken to be $b_{ri} = b_{cond} + 2b_g$, so that a condenser and two impellers could be removed from a multilayer stack to create a

[6] A motor efficiency of 90% was assumed (i.e. $\dot{W}_{mech}/\dot{W}_{elec} = 0.9$).

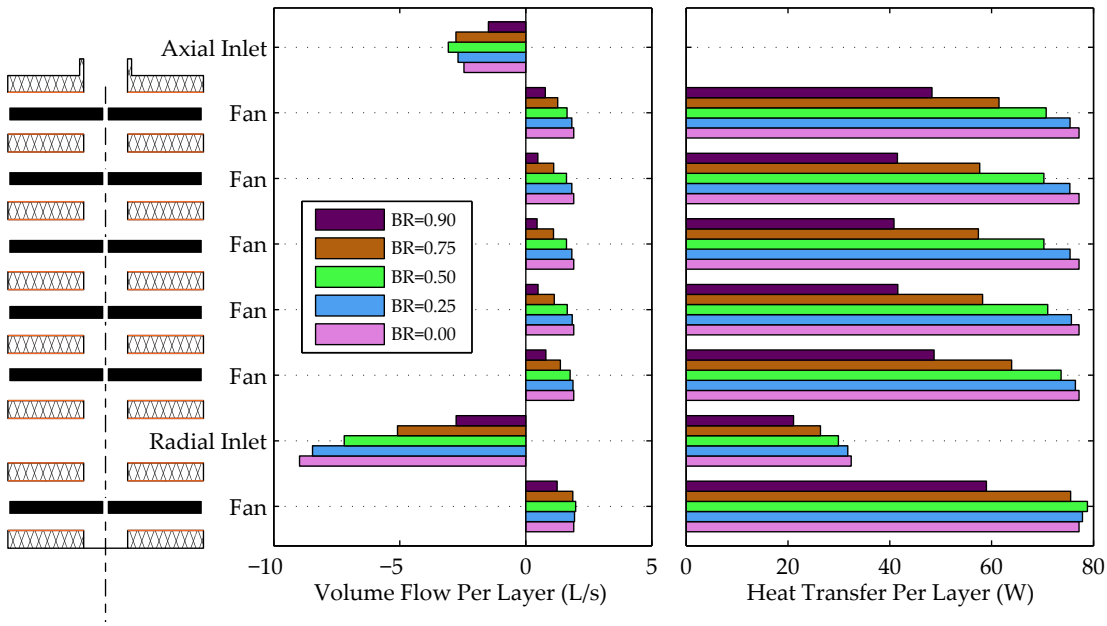

Figure 5-15: In addition to changing the overall performance of a multilayer device, interlayer resistance results in a different *distribution* of volume flow and heat transfer among the layers. A 6-fan device was simulated using the flow circuit model for various interlayer blockage ratios (BR). This device used Fan 1 in the fan layers (with $b_b = 1.5$mm and $b_g = 2.5$mm), and had an axial inlet and one radial inlet (with $b_{ri} = 3b_g$). The overall volume flow, defined in this figure as positive for flow exiting the device, decreases as BR increases (seen most clearly by summing the volume flows in the inlets). Higher BR also causes the layers farthest from the inlets to receive a smaller share of the net flow, with similar behavior in the heat transfer. Curiously, the axial inlet and lowest fan layer show a slight *increase* in $\dot{V}$ and $\dot{Q}$ with increasing BR. This marginal local increase occurs at the expense of neighboring layers.

radial inlet layer while maintaining the same pitch between condensers[7].

The experimentally based heat transfer and fan correlations (Eqs. 4.16 and 4.31) were used in the numerical flow circuit model to calculate the thermal resistance at various rotational speeds. The speed that resulted in an electrical power input of just under 33 W was chosen to compute R_{33}. Using Eq. 5.46, the number of condensers and fans that could fit within a specified total breadth ($b_{total} = 100$mm) was calculated. The number of fans and condensers that would fit within the maximum breadth also depended on how many radial inlets were used; in this example, for each fan design, multilayer devices with 1, 2, and 3 radial inlets were simulated, and the design whose R_{33} was lowest was chosen.

Figure 5-16 shows the results of the 42 fan designs that were evaluated. In Fig. 5-16, different fan designs have a differing number of condensers, because the various breadths of these fans allow only a certain number of layers to fit in the maximum total breadth constraint. Devices with more condensers tend to have a lower R_{33}. the best fan design for a particular number of condensers can be selected based on the application. For example, a high end application may warrant a design with many condensers, but in other applications the cost of manufacturing condensers may be a more important concern. In-

[7]The vertical fluid tubes that allow water to enter and exit the condensers have small transverse passages into each condenser. These tubes can be manufactured with a uniform pitch ahead of time for flexibility in relocating the radial inlet layers.

terestingly, Fan 12, which was on the Pareto frontier for single fans (Fig. 4-18), is also the best design for many of the multilayer scenarios (Fan 12 has the lowest R_{33} value of the 6, 7, 9, and 12 condenser designs). This example shows how the multidimensional space in the design of a multilayer integrated fan heat sink can be reduced by applying design constraints (in this case, a maximum volume and electrical power input) and coupling the modeling techniques (either the analytical or numerical approach) with an external optimization routine. Figure 5-16 presents a clear, concise evaluation of 42 potential fan designs and their multilayer performance under volume and input power constraints, allowing a design to be chosen depending on the cost to manufacture condensers. In this example, the best single-layer fan design (Fan 12) also yielded several of the best multilayer designs.

5.5 Experimental Validation

Two prototype heat pipes with integrated fans were built: a single condenser loop heat pipe with 2 fan layers, and a 6-condenser loop heat pipe with 6 fans and 1 radial inlet. These heat pipes underwent thermal testing, whereby the vapor-to-ambient temperature difference was measured for various heat loads. The data from these tests were compared to the results of the flow circuit model and found to agree to within 25% for the 2-fan prototype and 10% for the 6-fan prototype. A comparison between the experimental data and the estimates of the flow circuit model is shown in Fig. 5-17.

The construction details of the single condenser loop heat pipe with two integrated fans is discussed by Kariya [45], and is shown in Fig. 5-18. In this prototype, the fans had a breadth of 6.5 mm, and the air flow gap had a breadth of 7.5 mm. The fans had the profile of impeller 1; they were designed to be unusually thick to generate more air flow. Ultimately, the purpose of this heat pipe was to test the evaporator and condenser rather than to achieve efficient heat transfer, so every effort was taken to maximize the heat transfer into the air regardless of the pumping power ramifications. In the flow circuit model estimates, the pressure rise, pumping power, and heat transfer characteristics for these impellers were derived from correlations based on measurements in the square stator apparatus.

The overprediction of the flow circuit model compared with the single condenser heat pipe experiments likely occurred due to unaccounted for heat loss from the apparatus. For example, in the side view of Fig. 5-18, an unheated aluminum plate can be seen above the top fan. In the flow circuit model, this plate was treated as adiabatic. However, in the actual device, it is in intimate thermal contact with the four corner tubes, which contain hot working fluid. Certainly, heat leak from these corners into the aluminum plate represented a heat loss from the system that was not accounted for in the flow circuit model. Additionally, the copper chamber near the top of the device (under the motor) was a fluid reservoir [8]. This reservoir also contained hot working fluid, and additional surfaces from which thermal energy could leak to the ambient surroundings. These heat leaks would act to lower the thermal resistance, bringing the predicted curves closer to the experimental measurements. Furthermore, these heat losses are a larger fraction of the total heat transfer compared to a device with more condensers (and a higher overall heat input), and thus may contribute more substantially to decreasing the thermal resistance.

[8] A "reservoir" in a heat pipe serves as a heatable space that is used (1) to control the liquid side pressure and (2) to provide space for changes in the liquid volume with operating temperature.

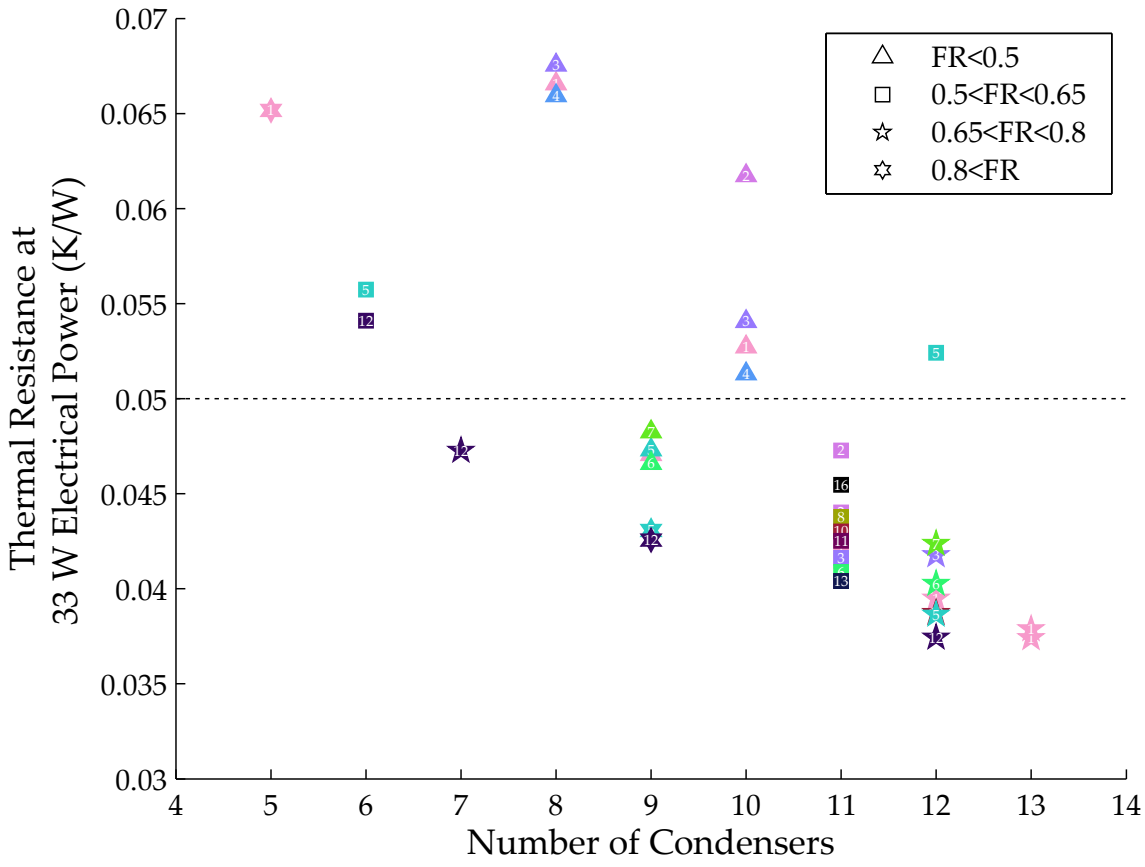

Figure 5-16: The multilayer scaling models can be used in constrained optimization problems to determine a multilayer design. In this example, the total breadth of the device was limited to 100 mm and the thermal resistance at the maximum electrical input power (viz. 33 W) was computed. For each fan design (corresponding to the designs in Table 4.1), a multilayer device with 1, 2, and 3 radial inlets was simulated and the design with the minimum thermal resistance (at 33 W electrical input power) is plotted. The marker shapes indicate the fill ratio (FR = b_b/b_g); the number in each marker represents the fan type (as indicated in Fig. 2-24). All markers that share a certain fan type have the same color. As the number of condensers increases, the minimum thermal resistance decreases. Furthermore, Fan 12 (which had several designs along the Pareto frontier in Fig. 4-18) has the lowest thermal resistance at 6, 7, 9, and 12 condensers.

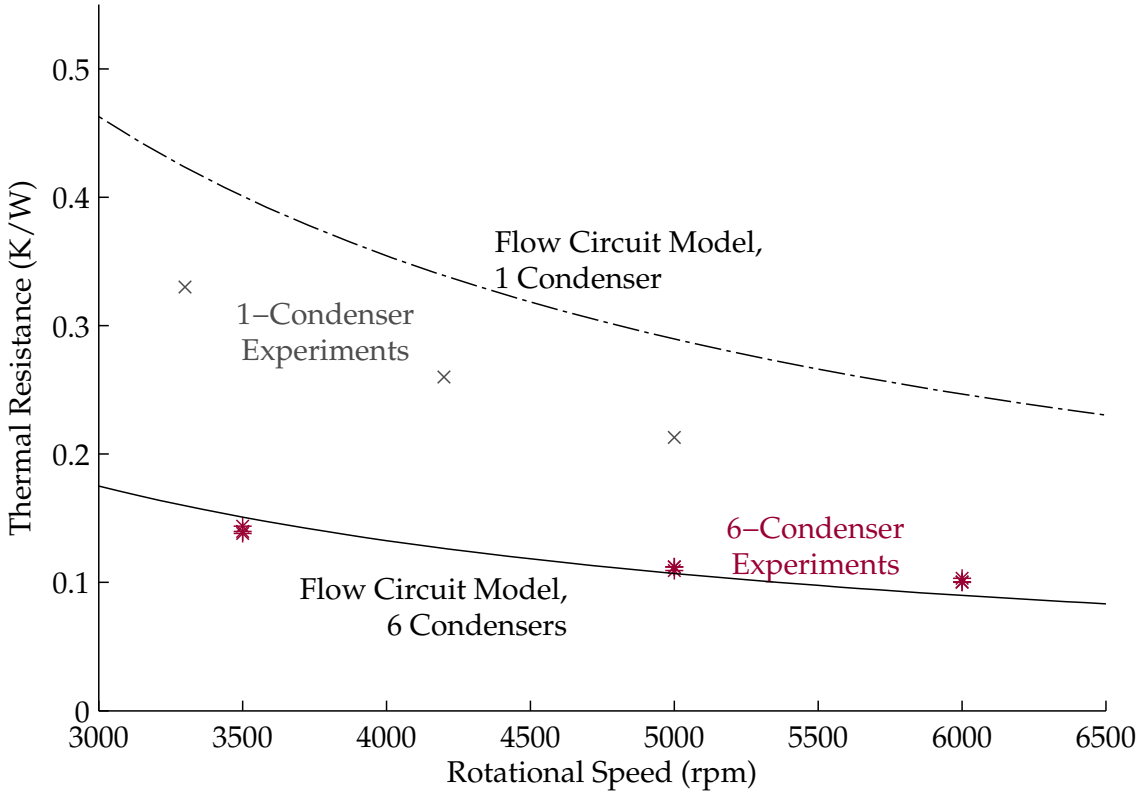

Figure 5-17: The flow circuit model predicted a higher thermal resistance than was measured experimentally in the single condenser prototype. This was likely due to heat loss that was not accounted for in the flow circuit model (e.g. natural convection loss from the vertical tubes and compensation chamber). The model estimates were more accurate for the 6-condenser prototype; the largest error was 15%.

In the 6-condenser prototype (Fig. 5-19), the flow circuit model predictions were very close to the experimentally measured thermal resistances. In this device, 6 fans cooled 6 condenser plates and the top surface of the evaporator. The impellers in this system used the profile of Fan 1, had a breadth of $b_b = 1.5\,\text{mm}$, and operated in gaps of breadth $b_g = 2.5\,\text{mm}$. The flow circuit model, once again, used experimentally based correlations based on the single layer measurements of the fan curves, heat transfer, and pumping power. Interlayer resistance was accounted for in both the 1-condenser and 6-condenser simulations.

The excellent agreement between the experimental data and the flow circuit model suggests that the basic physics of the model are correct. Furthermore, the values assumed for the various loss coefficients seem to provide a good representation of the system, at least in the aggregate. A more thoroughly instrumented, future multilayer prototype could yield further insight into the validity of the various assumptions in the flow circuit model. Additional experimental work could also be useful in improving the model's accuracy; in particular, an experimental characterization of the loss coefficients of the axial and radial inlets could be a useful exercise.

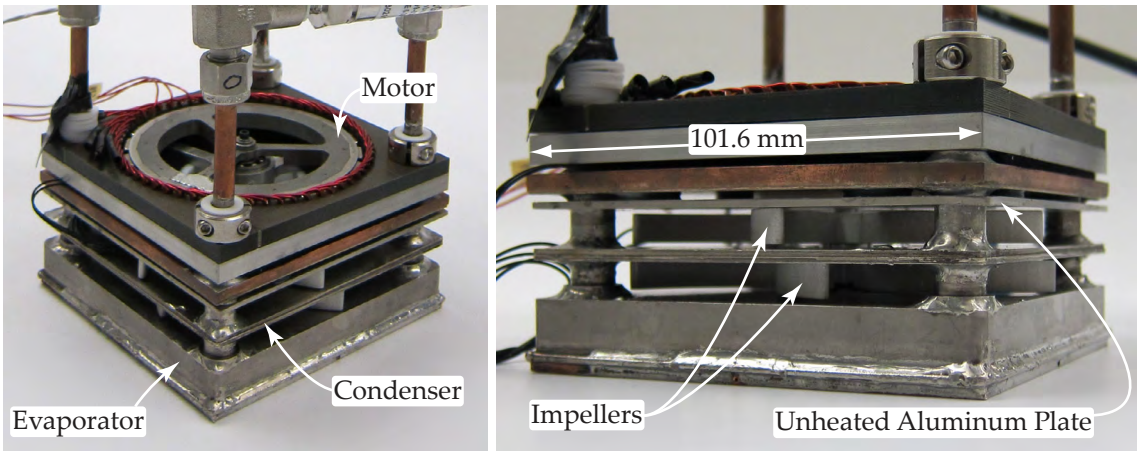

Figure 5-18: A prototype integrated fan heat sink centered around a single condenser loop heat pipe had 2 fan layers and an axial inlet. The flow circuit model overestimated the thermal resistance of the device. This discrepancy between the model and the experiment most likely arose due to additional losses of heat from the prototype which were not accounted for in the flow circuit model. Unmodeled heat losses occurred from the copper compensation chamber, the vertical fluid tubes, and the sides of the evaporator and condenser. The unheated aluminum plate, which was also not modeled in the flow circuit model, acted as a fin that allowed heat to flow from the vertical fluid tubes to the air flow in the top fan. In this single condenser prototype, these heat losses represent a more significant fraction of the total heat transfer than in larger devices with more condensers.

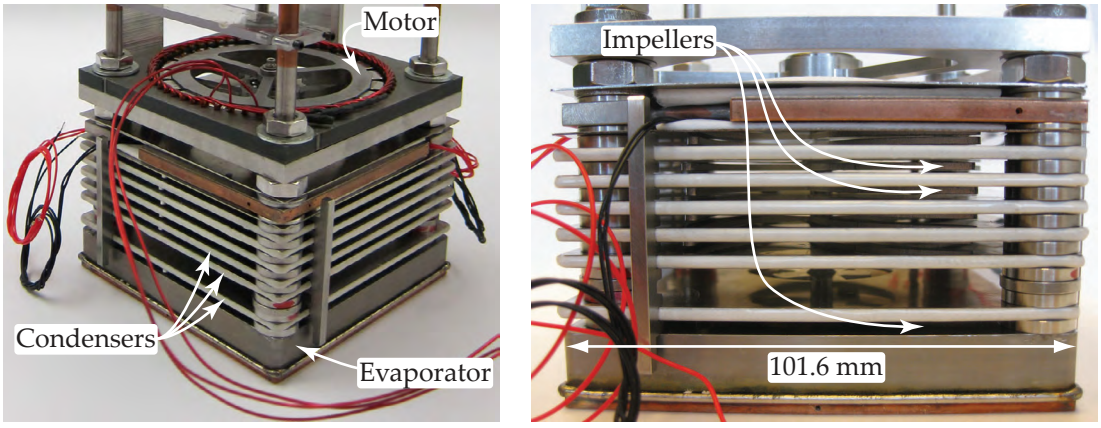

Figure 5-19: A prototype integrated fan heat sink centered around a 6-condenser loop heat pipe had 6 fan layers, an axial inlet and a radial inlet. The flow circuit model predictions for the overall heat transfer from this device were within 15% of the experimentally measured values (see Kariya [45] and Hanks [46] for details of the heat pipe construction).

5.6 Summary

The design of a multilayer integrated fan heat sink must be undertaken with an understanding of the various limitations imposed by the interactions of the fans, inlets, and interlayer blockages. An analytical, closed form solution for the operating point of a multilayer heat sink was developed by assuming negligible interlayer resistance in the core. Next, building blocks were developed to represent the various subcomponents of a multilayer heat sink (fans, axial inlets, radial inlets, and interlayer blockages). These components were then incorporated into a numerical model of a network representation of a multilayer device; the model solved for the flow state of the system. The heat transfer and pumping power rates were calculated based on the flow states and correlations developed in Chapter 4.

The effect of adding fan layers and radial inlet layers was explored using the numerical flow circuit model. Addition of fans becomes ineffective when the inlet restriction is too high; for example, in a design with a single axial inlet, the performance per layer decreased starting at about 3 layers. The scaling of the total heat transfer noticeably departed from linearity by this point as well. The volume flow through this device saturated after several layers as well. Addition of radial inlet layers delayed this saturation and significantly improved the heat transfer scaling. Inlet layers also were observed to shift the thermal resistance vs. pumping power curve toward more favorable operating points (near the origin) at the expense of heat sink volume. The addition of radial inlet layers allows for better balancing of the composite system resistance and the composite fan curve. Finally, interlayer blockage was observed to have a deleterious effect on the multilayer system performance, but with careful design this effect is easily mitigated.

The flow circuit model was compared to the experimental results from two prototype integrated fan heat sinks. These heat sinks were centered around planar heat pipes and used impeller geometries that were very similar to those characterized in Chapter 4, so the thermal and fluidic boundary conditions closely matched the experiments discussed in Chapter 2. The predictions of the flow circuit model agreed with the experimentally measured thermal resistances to within 25 and 10% for the 1- and 6-condenser prototypes, respectively.

CHAPTER 6

CONCLUSIONS

6.1 Summary of Present Work

The present work sought to build an understanding of the heat transfer and fan performance of integrated fan heat sinks. The main conclusions of this study are:

- Integrated fan heat sinks offer significant improvement in the balance of thermal resistance, coefficient of performance, and overall volume that epitomizes heat sink design. A compact air cooled heat sink design is suggested that improves on the current state-of-the-art by 4x in thermal resistance and 3x in coefficient of performance [12]. This heat sink design has thermal resistance of $R < 0.05\,\mathrm{K/W}$, coefficient of performance of COP > 33, and a volume of $V < 1$ L; these performance forecasts are based on experimental results for single fans and a multilayer scaling model (Chapter 5).

- In Chapter 1, two traditional compact heat sink designs were analyzed; they could not match the performance estimates of integrated fan heat sinks (Chapter 5) while still maintaining a comparable volume. Integrated fans complement emerging planar heat pipe technology, as well. The designs explored in the present work focused on an integrated fan combined with a planar multicondenser loop heat pipe.

- 3-D CFD simulations based on commonly used RANS turbulence models were shown to produce reasonable estimates of the fan performance, though only for a limited set of boundary conditions, turbulence models and mesh sizes. Agreement with the experimentally measured heat transfer was not as good as the fan performance, but with sufficient mesh size the SST turbulence model seems to give reasonably accurate predictions. The trends observed in CFD parameter studies of the blade angle and number of blades were used to develop better impeller designs for experimental characterization.

- The heat transfer in a single integrated fan was experimentally characterized for 13 different impeller profiles with various impeller thicknesses and stator gap spacings. The dimensionless heat flux was observed to increase linearly with both the flow Reynolds number and the rotational Reynolds number. Based on this observation, a

two-parameter correlation was developed for each experiment that predicts the data to within a relative RMS error of less than 13% (with a 95% confidence interval). A global correlation for the heat transfer was also developed and fits the data from 41 of the 42 experiments to within 20%.

- The convective heat transfer in an integrated fan heat sink exhibits a marked enhancement compared to a pressure driven flow at a similar flow Reynolds number, due to the presence of the rotating impeller in the flow passage. This heat transfer enhancement can be ascribed to turbulent flow structures induced by the impeller. The number of blades had only a minor effect on the heat transfer, suggesting that surface renewal theory (i.e. mechanical boundary layer disruption) does not adequately explain the heat transfer enhancement. Experiments designed to measure the local heat transfer coefficient demonstrated that the heat transfer coefficient was independent of the thermal boundary condition, which is another characteristic of turbulent flow.

- The fan performance (specifically, the pressure rise and mechanical power requirement), was correlated with a pair of 2-parameter correlations for each of 73 experiments performed on the circular stator apparatus. These correlations (for the head and power coefficients associated with a given flow coefficient) predicted the data for each experiment with a relative RMS error of less than 19% for the pumping and 27% for the mechanical power (within 95% confidence intervals). The correlation parameters were then expressed as functions of the fan geometry; these functions could estimate the correlation parameters to within 20%, and serve as high-level design tools for integrated fans.

- The tradeoff between thermal resistance and pumping power was observed, along with a Pareto frontier representing the best design points. Designs that minimized the thermal resistance at a given pumping power approached this optimal frontier. For a particular fan design, the operating points that most closely approached the optimal frontier were the points with the highest volume flow (least flow restriction) at each rotational speed. These optimal operating points did not correspond to the points of highest fan efficiency, serving as a reminder that integrated fan heat sink design has different goals than conventional fan design.

- The performance of integrated fan heat sinks improves significantly when multiple fan layers are used. A multilayer scaling model showed that the overall device performance depends on the pumping and power characteristics of the integrated fans as well as the flow resistance of the inlet to the heat sink's core. Radial inlet layers were investigated as a way to decrease the overall inlet resistance, and were shown to result in drastic performance improvements under certain conditions (namely, when the inlet resistance dominates the flow in the fan layers). The flow resistance in the central core was shown to have an effect, albeit one that may be neglected when the fans have a sufficient open area in the core region. The multilayer model results were shown to agree with experimental data from two integrated fan heat sink prototypes to within 15%.

6.2 Contributions

- The first full characterization of integrated fans that comprises the full range of the fans from the blocked condition to the maximum flow rate at a variety of rotational speeds.
- Experimental data for internal flow of a gas with active mechanical enhancement. Hagge and Junkhan [38] studied active enhancement of external air flow, and many others (e.g. Uhl [36]) have studied active enhancement of viscous liquids or slurries, but the literature on active mechanical enhancement of gases is sparse.
- Demonstration that the heat transfer in integrated fan heat sinks can be treated separately from the fan design problem. The fan design (which can be completed under isothermal conditions) determines the operating point in a system, and the heat transfer is a function of this operating point (not of the basic fan geometry). This separability of the fan and heat transfer designs greatly simplifies the design of integrated fan heat sinks, because the fan design and characterization (either from experiments or CFD) is much simpler than a full heat transfer characterization.
- Correlations of fan and heat transfer performance of single integrated fan heat sinks.
- Geometry-based estimates of fan and heat transfer performance. These can be used as design heuristics to form performance estimates of new integrated fan designs.
- Development of a new heated thin film IR thermography method that allows arbitrary thermal boundary conditions to be approximated on the surface of the thin film. This method uses independently controlled traces on a printed circuit board as the heat source. In the present work, this method was used to study the local heat transfer coefficient in integrated fan heat sinks. This method could find other uses in characterizing internal or external laminar flows in complex geometries. Previous heated thin film IR thermography methods (e.g. Stafford et al. [73], Astarita et al. [93]) can only apply a single type of boundary condition such as a prescribed heat flux. The method developed in the present work also uses multichannel closed-loop control to allow an approximation of a constant temperature boundary condition.
- Development of multilayer scaling models for integrated fan heat sinks that extend single-fan knowledge to multilayer performance estimates. The numerical flow circuit model uses a simple hydraulic-electrical analogy and allows various fluidic components (viz. fans, inlets, and flow obstructions) to be represented with a generalized, nonlinear resistor. This method of hydraulic circuit modeling could be useful in other applications, as it provides a simple way of visualizing and solving a complex flow network.

6.3 Suggested Future Work

Several possible avenues for future research could lead to further understanding of integrated fan heat sinks:

- First, the recirculatory flow at the exit plane of the fans was shown to have a significant effect on the heat transfer at low values of the flow coefficient. A model

that accurately predicts the size of this recirculatory zone would be useful because it would allow an energy balance to be performed on the air flowing through the fan layer; this would enable the determination of the wall-to-bulk temperature based heat transfer coefficient. This conventionally defined heat transfer coefficient is useful because it does not have any dependence on the local temperature of the air flow and is only a function of flow characteristics. Furthermore, a model of the recirculatory zone could serve to bridge the gap between the analytical models and the experimental data (see Section 4.1.2).

- Additional CFD studies are warranted based on the agreement of some of the benchmark tests in the present work. More sophisticated studies such as LES simulations could lead to insight into the microscale phenomena (e.g. vortex shedding) near the impeller blade and the recirculatory flows at the exit plane.

- Another direction for future work is to further characterize the local heat transfer coefficient in integrated fans using the modified heated thin film IR thermography method developed in the present work. In particular, combining the IR thermography measurements with particle image velocimetry (much like the combined IR thermography and PIV setup in Stafford et al. [77]), some useful insight into the local heat transfer coefficient could be obtained. An accurate energy balance on the air flow could be performed with the flow field information gained from PIV. Such flow field measurements could also serve as very useful benchmarks for CFD simulations.

- The fans could be further optimized. In the present work, some of the geometry of the fans was constrained by the experimental apparatus. For example, only a single inlet ratio could be tested, but CFD studies suggested that there may be a benefit to using a different inlet ratio in multilayer systems. Additionally, the fans characterized in the present work had simple, fundamental forms (radial blades or logarithmic spirals); performance improvements could likely be achieved by departing from these fundamental shapes.

- In the design of multilayer devices, several experiments could increase the accuracy of the flow circuit model of Chapter 5. First, the loss coefficients associated with the components in the flow circuit model could be characterized (in particular, the axial inlet and interlayer blockages). This could be done on a flow bench similar to the circular stator apparatus used in the present work. Additionally, a multilayer test with instrumentation (e.g. pressure taps in the core, or thermocouples in the exit air stream) could give clues about the accuracy or shortcomings of the flow circuit model. A measurement of the total volume flow in a multilayer device would be particularly useful for validating the flow circuit model results.

- Finally, further optimization studies of multilayer integrated fan heat sinks could yield better multilayer device performances. The multilayer scaling models can be used to perform constrained optimization on multilayer devices. One potential study would involve generating a cost function for the competing optimization objectives (e.g. thermal resistance, input power, and overall volume). With such a cost function, constrained optimization software could be used to determine the best device for a certain application. Additionally, a sensitivity analysis could be performed using the multilayer scaling models by (1) designing and optimizing a device, (2) perturbing the inputs to the model (such as the parameters defining the fan performance curve

or the inlet flow resistance), and (3) examining the effect of these perturbations on the overall behavior of the system. This sensitivity analysis would reveal the most effective places to focus design effort to improve a device's overall performance.

THIS PAGE INTENTIONALLY LEFT BLANK

APPENDIX A

PROPERTIES OF AIR

The properties of air used in the present work (at standard conditions of 25 C and 101300 Pa) were determined from REFPROP 8.0 [94] as a mixture of 77% nitrogen and 23% oxygen by mass:

Density: $\rho = 1.17944 \frac{\text{kg}}{\text{m}^3}$

Dynamic Viscosity: $\mu = 1.84145 \cdot 10^{-5} \frac{\text{kg}}{\text{m} \cdot \text{s}}$

Thermal Conductivity: $k = 0.0259100 \frac{\text{W}}{\text{m} \cdot \text{K}}$

Isobaric Specific Heat: $c_p = 1013.4 \frac{\text{J}}{\text{kg} \cdot \text{K}}$

BIBLIOGRAPHY

[1] M. Webb, "Smart 2020: Enabling the low carbon economy in the information age," tech. rep., London, U.K., 2008.

[2] S. E. Thompson and S. Parthasarathy, "Moore's law: the future of Si microelectronics," *Materials Today*, vol. 9, no. 6, pp. 20 – 25, 2006.

[3] J. G. Koomey, S. Berard, M. Sanchez, and H. Wong, "Assessing trends in the electrical efficiency of computation over time," *IEEE Annals of the History of Computing*, 2009.

[4] W. Krueger and A. Bar-Cohen, "Optimal numerical design of forced convection heat sinks," *Components and Packaging Technologies, IEEE Transactions on*, vol. 27, pp. 417 – 425, june 2004.

[5] Intel, "Intel core i7 processor family for the LGA2011-0 socket: Thermal/mechanical specification and design guide," Tech. Rep. Document Number: 326199-001, Intel Corp., November 2011.

[6] N. Kim, T. Austin, D. Baauw, T. Mudge, K. Flautner, J. Hu, M. Irwin, M. Kandemir, and V. Narayanan, "Leakage current: Moore's law meets static power," *Computer*, vol. 36, pp. 68 – 75, dec. 2003.

[7] U. E. I. Administration, "Electric power monthly: July 2012," tech. rep., U.S. Department of Energy, 2012.

[8] G. I. Meijer, "Cooling energy-hungry data centers," *Science*, vol. 328, no. 5976, pp. 318–319, 2010.

[9] J. Koomey, "Growth in data center electricity use 2005 to 2010," tech. rep., Analytics Press, Oakland, CA, July 2011.

[10] "2011 iNEMI roadmap, executive summary." http://thor.inemi.org/webdownload/RM/2011RM_ExSum.pdf, 2011. Accessed: July 21, 2012.

[11] "International Technology Roadmap for Semiconductors (ITRS)." http://www.itrs.net/Links/2010ITRS/Home2010.htm, 2009. Accessed: July 29, 2012.

[12] "Broad agency announcement, microtechnologies for air-cooled exchangers (MACE), BAA 08-15," tech. rep., DARPA MTO, 2008.

[13] S. S. Anandan and V. Ramalingam, "Thermal management of electronics: A review of literature," *Thermal Science*, vol. 12, no. 2, pp. 5–26, 2008.

[14] S. Sathe and B. Sammakia, "A review of recent developments in some practical aspects of air-cooled electronic packages," *ASME J. Heat Transfer*, vol. 120, pp. 830–839, 1998.

[15] A. Bar-Cohen, "Thermal management of microelectronics in the 21st century," in *Electronic Packaging Technology Conference, 1997. Proceedings of the 1997 1st*, pp. 29 –33, oct 1997.

[16] Noctua, "NH-D14." `http://www.noctua.at/main.php?show=productview&products_id=34&lng=en`. Accessed: July 7, 2012.

[17] D. Tuckerman and R. Pease, "High-performance heat sinking for VLSI," *Electron Device Letters, IEEE*, vol. 2, no. 5, pp. 126–129, 1981.

[18] R. W. Knight, J. S. Goodling, and D. J. Hall, "Optimal thermal design of forced convection heat sinks-analytical," *Journal of Electronic Packaging*, vol. 113, no. 3, pp. 313–321, 1991.

[19] P. Teertstra, M. Yovanovich, J. Culham, and T. Lemczyk, "Analytical forced convection modeling of plate fin heat sinks," in *Semiconductor Thermal Measurement and Management Symposium, 1999. Fifteenth Annual IEEE*, pp. 34–41, 1999.

[20] A. Bejan, *Entropy generation minimization*. CRC Press, Inc., 1996.

[21] A. Bejan, "Fundamentals of exergy analysis, entropy generation minimization, and the generation of flow architecture," *International Journal of Energy Research*, vol. 26, no. 7, pp. 0–43, 2002.

[22] J. Culham and Y. Muzychka, "Optimization of plate fin heat sinks using entropy generation minimization," *Components and Packaging Technologies, IEEE Transactions on DOI - 10.1109/6144.926378*, vol. 24, no. 2, pp. 159–165, 2001.

[23] W. Khan, J. Culham, and M. Yovanovich, "Optimization of pin-fin heat sinks using entropy generation minimization," *Components and Packaging Technologies, IEEE Transactions on*, vol. 28, pp. 247 – 254, june 2005.

[24] A. Bar-Cohen and M. Iyengar, "Least-energy optimization of air-cooled heat sinks for sustainable development," *Components and Packaging Technologies, IEEE Transactions on*, vol. 26, pp. 16 – 25, march 2003.

[25] M. Iyengar and A. Bar-Cohen, "Minimum energy design for manufacturability of air cooled heat sinks," *ASME Conference Proceedings*, vol. 2009, no. 43604, pp. 319–326, 2009.

[26] T. Furukawa and W.-J. Yang, "Reliability of heat sink optimization using entropy generation minimization," in *8th AIAA/ASME Joint Thermophysics and Heat Transfer Conference*, (St. Louis, Missouri), American Institute of Aeronautics and Astronautics, June 2002.

[27] V. Egan, P. Walsh, E. Walsh, and R. Grimes, "Thermal analysis of miniature low profile heat sinks with and without fins," *Journal of Electronic Packaging*, vol. 131, September 2009.

[28] J. Stafford, E. Walsh, V. Egan, P. Walsh, and Y. S. Muzychka, "A novel approach to low profile heat sink design," *Journal of Heat Transfer*, vol. 132, no. 9, p. 091401, 2010.

[29] J. P. Koplow, "A fundamentally new approach to air-cooled heat exchangers.," Technical Report SAND2010-0258, Sandia National Laboratories, 2010.

[30] E. C. Cobb and O. A. Saunders, "Heat transfer from a rotating disk," *Proceedings of the Royal Society of London. Series A, Mathematical and Physical Sciences*, vol. 236, no. 1206, pp. pp. 343–351, 1956.

[31] A. F. Mills, *Heat and Mass Transfer*. CRC Press, 1994.

[32] G. E. Karniadakis, B. B. Mikic, and A. T. Patera, "Minimum-dissipation transport enhancement by flow destabilization: Reynolds' analogy revisited," *Journal of Fluid Mechanics*, vol. 192, pp. 365–391, 1988.

[33] A. E. Bergles, *Handbook of Heat Transfer*, ch. 11: Techniques to Enhance Heat Transfer. McGraw–Hill, 1998.

[34] M. W. Rubesin, M. Inouye, and P. G. Parikh, *Handbook of Heat Transfer*, ch. 6: Forced Convection, External Flows. McGraw–Hill, 1998.

[35] F. Herrault, P. Hidalgo, C.-H. Ji, A. Glezer, and M. Allen, "Cooling performance of micromachined self-oscillating reed actuators in heat transfer channels with integrated diagnostics," in *Micro Electro Mechanical Systems (MEMS), 2012 IEEE 25th International Conference on*, pp. 1217 –1220, 2012.

[36] V. W. Uhl, "Mechanically aided heat transfer to viscous materials," in *Augmentation of Convective Heat and Mass Transfer*, pp. 109–117, New York: ASME, 1970.

[37] S. S. Chauk and L.-S. Fan, *Handbook of Heat Transfer*, ch. 13: Heat Transfer in Packed and Fluidized Beds. McGraw–Hill, 1998.

[38] J. K. Hagge and G. H. Junkhan, "Mechanical augmentation of convective heat transfer in air," *Journal of Heat Transfer*, vol. 97, no. 4, pp. 516–520, 1975.

[39] S. Mochizuki and W.-J. Yang, "Local heat-transfer performance and mechanisms in radial flow between parallel disks," *Journal of Thermophysics and Heat Transfer*, vol. 1, pp. 112–116, April 1987.

[40] S. Mochizuki and W.-J. Yang, "Self-sustained radial oscillating flows between parallel disks," *Journal of Fluid Mechanics*, vol. 154, pp. 377–397, 1985.

[41] S. Mochizuki, W.-J. Yang, Y. Yagi, and M. Ueno, "Heat transfer mechanisms and performance in multiple parallel disk assemblies," *Journal of Heat Transfer*, vol. 105, no. 3, pp. 598–604, 1983.

[42] N. V. Suryanarayana, T. Scofield, and R. E. Kleiss, "Heat transfer to a fluid in radial, outward flow between two coaxial stationary or corotating disks," *Journal of Heat Transfer*, vol. 105, no. 3, pp. 519–526, 1983.

[43] P. Moller, "Radial flow without swirl between parallel discs," *The Aeronautical Quarterly*, vol. 14, pp. 163–186, 1963.

[44] J. Fay, *Introduction to Fluid Mechanics*. Cambridge USA: MIT Press, 1994.

[45] H. A. Kariya, *Development of an Air-cooled, Loop-type Heat Pipe with Multiple Condensers*. PhD thesis, Massachusetts Institute of Technology, 2012.

[46] D. F. Hanks, "Design, fabrication, and characterization of a multi-condenser loop heat pipe," Master's thesis, Massachusetts Institute of Technology, 2012.

[47] R. M. Manglik and A. E. Bergles, "Heat transfer and pressure drop correlations for the rectangular offset strip fin compact heat exchanger," *Experimental Thermal and Fluid Science*, vol. 10, no. 2, pp. 171 – 180, 1995. ¡ce:title¿Aerospace Heat Exchanger Technology¡/ce:title¿.

[48] C. E. Brennen, *Hydrodynamics of Pumps*. Concepts NREC and Oxford University Press, Jan. 1994.

[49] C. Ding, G. Soni, P. Bozorgi, B. Piorek, C. Meinhart, and N. MacDonald, "A flat heat pipe architecture based on nanostructured titania," *Microelectromechanical Systems, Journal of*, vol. 19, pp. 878 –884, aug. 2010.

[50] J. Allison, "Air flow in a high aspect ratio heat sink," Master's thesis, Massachusetts Institute of Technology, June 2010.

[51] P. Epple, *Modern Design and Applications to Radial Fans*. PhD thesis, Der Technischen Fakultat der Universitat Erlangen-Nurnberg, 2009.

[52] B. Eck, *Fans*. Pergamon Press, 1975.

[53] S. L. Dixon, *Fluid Mechanics and Thermodynamics of Turbomachinery*, p. 227. Elsevier Butterworth-Heinemann, fifth ed., 1998.

[54] X. Qiu, D. Japikse, J. Zhao, and M. R. Anderson, "Analysis and validation of a unified slip factor model for impellers at design and off-design conditions," *Journal of Turbomachinery*, vol. 133, no. 4, p. 041018, 2011.

[55] T. W. von Backstrom, "A unified correlation for slip factor in centrifugal impellers," *Journal of Turbomachinery*, vol. 128, no. 1, pp. 1–10, 2006.

[56] F. M. White, *Fluid Mechanics*, pp. 760–761. McGraw–Hill, fifth ed., 2003.

[57] T. Wright, *Fluid machinery: performance, analysis, and design*. CRC Press, 1999.

[58] M. Boyce, *Gas Turbine Engineering Handbook*. Elsevier Science, 2011.

[59] R. Lewis, *Turbomachinery Performance Analysis*. New York: Wiley, 1996.

[60] D. Japikse and N. C. Baines, *Introduction to Turbomachinery*. Concepts ETI, Inc. and Oxford University Press, 1997.

[61] R. K. Shah and A. L. London, *Laminar flow forced convection in ducts: a source book for compact heat exchanger analytical data*. Academic Press, Inc., 1978.

[62] M. Page, "FrostyTech — Best Heat Sinks & PC Cooling Reviews." http://www.frostytech.com. Accessed: March, 2012.

Num.	Author	Date	URL
1.	Max Page	12-May-10	http://www.frostytech.com/articleview.cfm?articleID=2521
2.	"	12-Jan-10	http://www.frostytech.com/articleview.cfm?articleID=2480
3.	"	27-May-10	http://www.frostytech.com/articleview.cfm?articleID=2525
4.	"	12-May-10	http://www.frostytech.com/articleview.cfm?articleID=2521
5.	"	18-May-10	http://www.frostytech.com/articleview.cfm?articleID=2523
6.	"	2-Jan-10	http://www.frostytech.com/articleview.cfm?articleID=2481
7.	"	26-Oct-09	http://www.frostytech.com/articleview.cfm?articleID=2461
8.	"	23-Mar-09	http://www.frostytech.com/articleview.cfm?articleID=2383
9.	"	10-May-10	http://www.frostytech.com/articleview.cfm?articleID=2518
10.	"	3-Nov-09	http://www.frostytech.com/articleview.cfm?articleID=2467
11.	"	30-Apr-08	http://www.frostytech.com/articleview.cfm?articleID=2271
12.	"	17-Feb-10	http://www.frostytech.com/articleview.cfm?articleID=2497
13.	"	26-Feb-10	http://www.frostytech.com/articleview.cfm?articleID=2500
14.	"	6-Mar-10	http://www.frostytech.com/articleview.cfm?articleID=2498
15.	"	23-Dec-08	http://www.frostytech.com/articleview.cfm?articleID=2348
16.	"	7-Feb-11	http://www.frostytech.com/articleview.cfm?articleID=2562
17.	"	27-Apr-12	http://www.frostytech.com/articleview.cfm?articleID=2657
18.	"	28-Jan-11	http://www.frostytech.com/articleview.cfm?articleID=2587
19.	"	23-Nov-09	http://www.frostytech.com/articleview.cfm?articleID=2486
20.	"	9-Nov-11	http://www.frostytech.com/articleview.cfm?articleID=2614

Sources for Heat Sinks Surveyed in Table 1.5.

[63] R. Jorgensen, ed., *Fan Engineering: An engineer's handbook on fans and their applications*. Buffalo, NY: Buffalo Forge Company, 8 ed., 1983.

[64] *Energy efficiency guidebook*, ch. Chapter 5. Fans and Blowers, pp. 93–112. Bureau of Energy Efficiency (BEE), Government of India, 2004.

[65] M. Turner, "All you need to know about fans," *Electronics Cooling*, vol. 2, no. 2, 1996.

[66] "Electronic Components Distributor | DigiKey Corp. | US Home Page." http://www.digikey.com, November 2010.

[67] B. Tummers, "Datathief III." http://datathief.org, 2006.

[68] L. Newborough, M. Newborough, and S. Probert, "Electronically commutated direct-current motor for driving tube-axial fans: A cost-effective design," *Applied Energy*, vol. 36, no. 3, pp. 167 – 190, 1990.

[69] P. R. Bevington and D. K. Robinson, *Data Reduction and Error Analysis for the Physical Sciences*. McGraw–Hill, 2003.

[70] T. G. Beckwith, R. D. Marangoni, and J. H. Lienhard V, *Mechanical Measurements*. Addison-Wesley, 5 ed., 1993.

[71] "Arduino - homepage." http://arduino.cc/.

[72] J. A. Harvey, *Machine Shop Trade Secrets: A Guide to Manufacturing Machine Shop Practices*. Industrial Press, Inc., 2005.

[73] J. Stafford, E. Walsh, and V. Egan, "Characterizing convective heat transfer using infrared thermography and the heated-thin-foil technique," *Measurement Science and Technology*, vol. 20, no. 10, p. 105401, 2009.

[74] T. Astarita and G. Cardone, "Thermofluidynamic analysis of the flow in a sharp 180 turn channel," *Experimental Thermal and Fluid Science*, vol. 20, no. 34, pp. 188 – 200, 2000.

[75] J. Stafford, E. Walsh, V. Egan, and R. Grimes, "Flat plate heat transfer with impinging axial fan flows," *International Journal of Heat and Mass Transfer*, vol. 53, no. 2526, pp. 5629 – 5638, 2010.

[76] J. Stafford, E. Walsh, and V. Egan, "Local heat transfer performance and exit flow characteristics of a miniature axial fan," *International Journal of Heat and Fluid Flow*, vol. 31, no. 5, pp. 952 – 960, 2010.

[77] J. Stafford, E. Walsh, and V. Egan, "A study on the flow field and local heat transfer performance due to geometric scaling of centrifugal fans," *International Journal of Heat and Fluid Flow*, vol. 32, no. 6, pp. 1160 – 1172, 2011.

[78] K. Anderson, "NASA's Anderson loop," *Instrumentation Measurement Magazine, IEEE*, vol. 1, pp. 5 –15, 30, mar 1998.

[79] E. H. Banner, "Flattening thin metal sheets," *Journal of Scientific Instruments*, vol. 4, no. 1, p. 26, 1926.

[80] W. Rice, "Tesla turbomachinery," in *Handbook of Turbomachinery*, pp. –, CRC Press, May 2003.

[81] P. Harwood, "Further investigations into tesla turbomachinery," M. Sc., The University of Newcastle, Australia, 2008. SID:3046768.

[82] "ANSYS Academic Research, Release 14.0."

[83] *ANSYS Academic Research, Release 13.0, Help System, 2.3.2. Recommended Configurations of Boundary Conditions, ANSYS, Inc.*

[84] J. Noh, E. Lee, J. Kim, and D. Lee, "CFD analysis of a partial admission turbine using a frozen rotor method," *Proceedings of the Conference on Aerospace Propulsion*, vol. 44, pp. 746–751, 2004.

[85] F. Menter, M. Kuntz, and R. Langtry, "Ten years of industrial experience with the SST model.," in *Turbulence, Heat and Mass Transfer 4* (K. Hanjalić, Y. Nagano, and M. Tummers, eds.), 2003.

[86] C. Rumsey, "Turbulence modeling resource," 2012.

[87] D. Pelletier, "Verification, validation, and uncertainty in computational fluids dynamics," *Canadian Journal of Civil Engineering*, vol. 37, no. 7, pp. 1003–1013, 2010.

[88] M. Ebadian and Z. Dong, *Handbook of Heat Transfer*, ch. 5: Forced Convection, Internal Flow in Ducts, p. 5.63. McGraw–Hill, 1998.

[89] X. Qiu, D. Japikse, and M. Anderson, "A meanline model for impeller flow recirculation," *ASME Conference Proceedings*, vol. 2008, no. 43161, pp. 1687–1694, 2008.

[90] M. B. Wilk and R. Gnanadesikan, "Probability plotting methods for the analysis for the analysis of data," *Biometrika*, vol. 55, no. 1, pp. 1–17, 1968.

[91] E. Greitzer, C. Tan, and C. Graf, *Internal Flow: Concepts and Applications*. Cambridge University Press, 2004.

[92] W. L. Staats, T. B. Peters, J. M. Allison, M. McCarthy, E. N. Wang, and J. G. Brisson, "Investigation of a multiple impeller design for a high performance air-cooled heat sink," *ASME Conference Proceedings*, vol. 2010, no. 44441, pp. 313–320, 2010.

[93] T. Astarita, G. Cardone, and G. Carlomagno, "Infrared thermography: An optical method in heat transfer and fluid flow visualisation," *Optics and Lasers in Engineering*, vol. 44, pp. 261 – 281, 2006.

[94] E. Lemmon, M. Huber, and M. McLinden, "NIST Standard Reference Database 23: Reference Fluid Thermodynamic and Transport Properties-REFPROP, Version 8.0, National Institute of Standards and Technology, Standard Reference Data Program, Gaithersburg," 2007.